

# **MultiMo-Bat: Biologically Inspired Integrated Multi-Modal Locomotion**

Submitted in partial fulfillment of the requirements for

the degree of

Doctor of Philosophy

in

Mechanical Engineering

Matthew A. Woodward

B.S., Mechanical Engineering, San Diego State University

M.S., Mechanical Engineering, Carnegie Mellon University

Carnegie Mellon University  
Pittsburgh, PA

December, 2017

© Matthew A. Woodward, 2017  
All Rights Reserved

**Keywords:** Bioinspired Robotics, Integrated Multi-Modal Locomotion, Jumping and Gliding, Miniature Robots, Flexible Wing Design, Mechanism Design, Shape Memory Alloy, Permanent Magnet, Locust Jumping, Slipping, Foot Design



## Abstract

The combination or integration of locomotion modes, is analyzed through the design, development, and verification of a miniature integrated jumping and gliding robot, the MultiMo-Bat, which is inspired by the locomotion strategies of vampire bats, locusts, and pelicans. This robot has a mass of between 100 and 162 grams and exhibits high jumping and gliding performance, reaching heights of over 4.5 meters, to overcome obstacles in the environment. Integration results in a smaller, lighter robot with high cooperation between the modes. This thesis presents a previously unstudied robot design concept and highlights the understudied evolutionary concept within organism mobility of integration of locomotion modes.

High performance locomotion modes also require high energy density actuators. To this end, a design methodology is developed for tailoring magnetic springs to the characteristics of shape memory alloy-actuated mechanisms, which allow the MultiMo-Bat to reach jumping heights of 3.5 m with active wing deployment and full controller. Through a combinations of permanent magnets, a magnetic spring can be customized to desired characteristics; theoretically any well-defined function of force vs. displacement can be created. The methodology is not limited to SMA but can be adapted to any smart actuator, joint, or situation which requires a fixed complex force-displacement relationship with extension other interactions and magnetic field design.

Robotic locomotion is also much more idealized than that of their biological counter parts. This thesis serves to highlight just how non-ideal, yet robust, biological locomotion can inspire concepts for enhancing the robustness of robot locomotion. We studied the desert locust (*Schistocerca gregaria*), which is adapted for jumping at the extreme limits of its surface friction, as evident by its morphological adaptations for not only jumping, but slipping. Analysis of both foot morphology and jumping behavior are used to understand how the feet interact with different surfaces, including hydrophobic glass, hydrophilic glass, wood, sandstone, and mesh. The results demonstrate a complex interplay of embodied mechanical intelligence, allowing the foot to interact and adapt passively to different surfaces without burdening the organism with addi-

tional tasks. The key morphological and dynamical features are extracted to create a concept for developing multi-Surface Locust Inspired Passively-adaptable (SLIP) feet. A simple interpretation of the concepts are then used to construct a SLIP foot for the MultiMo-Bat. These feet allow the MultiMo-Bat to reach jumping heights of well over 4 m, greater than any other electrically powered robot, and this is achieved on a 45 degree angled surface while slipping. The SLIP foot concept can be directly applied to a wide range of robot size scales, thus enhancing their dynamic terrestrial locomotion on variable surfaces.

## Acknowledgments

My parents, Sharon Novak and Russell Woodward, and my family have provided significant support and encouragement to me. I thank them greatly for the experiences which inspired my interest in science and drive to explore.

I thank my advisor and committee chair Metin Sitti for accepting me into the NanoRobotics Lab and for his support, encouragement, advice, and freedom to search for a topic which inspired me. I also thank my thesis committee members Carmel Majidi, Steven H. Collins, and Yong-Lae Park for their time and guidance.

I thank in particular Casey Kute for encouraging me to seek my doctorate after my masters studies and Steven Floyd, Chytra Pawashe, Slava Arabagi, Lindsey Hines, and Yigit Menguc for welcoming me to the lab and continuing advice and critiques which helped shape the focus of my research. Eric Diller, both as a friend and colleague, provided significant academic and personal support throughout my research. His friendship was invaluable. I would like to thank Joshua Giltinan and Guo Zhan Lum for spirited research discussions and ideas as well as all the past and presents members of the NanoRobotics lab for their encouragement, critiques and ideas throughout my study. These include Rika Wright Carlsen, David Colmenares, Randall Kania, Hamid Marvi, Veikko Sariola, Shuhei Miyashita, Zhou Ye, Taewon Seo, Onur Ozcan, Sehyuk Yim, Jiho Song, Jiang Zhuang, Xiaoguang Dong, Donghoon Son, Nitish Thatte, Sukho Song, Matthew Edwards, Uyiosa Abusomwan, and Yizhu Gu.

I would like to thank all the past and presents members of the Max Plank Institutes's Physical Intelligence department for their support, encouragement, and friendship. These include Guillermo Amador, Muhammad Yunusa, Ahmet Tabak, Kirstin Petersen, Hakan Ceylan, Utku Culha, Zoey Davidson, Dirk Drotlet, Kristen Kozielski, Wenqi Hu, Byung-Wook Park, Ajay Vikram, Morgan Stanton, Wendong Wang, Morteza Amjadi, Anuj Agrawal, Önder Erin, Chantal Goettler, HyungGyu Kim, Varun Sridhar, Ceren Yasa, Oncay Yasa, Thomas Endlein, Zeinab Hosseini, Gilbert Hunter, Massimo Mastrangeli. Babak Mostaghaci, Alex Spröwitz, Svetlana

Zakharchenko, and Alejandro Posada.

Throughout my graduate studies I had the opportunity to work with several undergraduate and M.S. students including Meghan Downie, Davide Bray, Elaine Wong, Thomas Castner, Miki Basse, Maunel Schlegel, Mukul Bhatt, Chiedozie Okafor, and Cenk Oğuz Sağlam. I thank them for the opportunity and experience of being a mentor.

My transition to the Max Planck Institutes's Physical Intelligence department in Stuttgart Germany was greatly assisted by Janina Sieber. I thank her for her above and beyond assistance and friendship. Jörg Einfeld also assisted greatly in lab setup and I thank him for his efforts in facilitating the process.

Financial support for this project and myself was provided by the Max Planck Institute Fellowship, Carnegie Institute of Technology Deans Fellowship, and Carnegie Mellon University GuSH grants.

# Contents

	<b>Abstract</b>	<b>v</b>
	<b>Acknowledgments</b>	<b>vii</b>
	<b>List of Figures</b>	<b>xiii</b>
	<b>List of Tables</b>	<b>xvii</b>
<b>1</b>	<b>Introduction</b>	<b>1</b>
1.1	Motivation . . . . .	1
1.2	Research Objectives . . . . .	6
1.3	Organization . . . . .	7
1.4	Contributions . . . . .	8
<b>2</b>	<b>MultiMo-Bat: Biologically Inspired Integrated Multi-Modal Jumping and Gliding Robot</b>	<b>11</b>
2.1	Introduction . . . . .	11
2.2	Biological Inspiration . . . . .	13
2.3	Design Concept . . . . .	16
2.3.1	Phases of Operation . . . . .	22
2.4	Locomotion Mode Coupling . . . . .	24
2.4.1	MultiMo-Bat Coupling . . . . .	26
2.5	Jumping Mode . . . . .	28

2.5.1	Jumping Dynamic Model . . . . .	29
2.5.2	Four-bar Leg Dynamics . . . . .	33
2.5.3	Biologically Inspired Joint Design . . . . .	36
2.5.4	Energy Storage Mechanism . . . . .	38
2.6	Gliding Mode . . . . .	45
2.6.1	Gliding Phase Dynamic Model . . . . .	45
2.6.2	Wing Design . . . . .	55
2.7	Prototype and Experiments . . . . .	59
2.7.1	Jumping Performance . . . . .	59
2.7.2	Gliding Performance . . . . .	63
2.7.3	Robot Performance . . . . .	66
2.8	Integrated Locomotion Metrics . . . . .	68
2.8.1	Mass Integration Metric . . . . .	69
2.8.2	Performance Integration Metric . . . . .	70
2.9	Robot Scaling . . . . .	71
2.10	Discussion . . . . .	75
2.11	Chapter Summary . . . . .	77
<b>3</b>	<b>MultiMo-Bat: Tailored Magnetic Springs for Detwinning of Shape</b>	
	<b>Memory Alloy-Actuated Mechanisms in Miniature Robots</b>	<b>79</b>
3.1	Introduction . . . . .	79
3.2	Concept Development . . . . .	84
3.3	Characteristics for Shape Memory Alloy-Actuated Mechanisms . . . . .	90
3.3.1	Detwinning Force . . . . .	90
3.3.2	Holding Force . . . . .	91
3.3.3	State Transition . . . . .	92
3.3.4	Off-Axis Force and Torque Equalization . . . . .	92

3.3.5	Actuator Mounting . . . . .	93
3.4	Tailored Magnetic Spring Design . . . . .	93
3.5	Irreducible Set . . . . .	95
3.6	Energy Storage Mechanism Design . . . . .	97
3.6.1	Desired Characteristics and Tailored Magnetic Spring . . . . .	98
3.6.2	Driving Circuit . . . . .	100
3.7	Wing Lock Design . . . . .	100
3.7.1	Desired Characteristics and Tailored Magnetic Spring . . . . .	101
3.8	Experimental Characterization . . . . .	102
3.8.1	Materials and Methods . . . . .	102
3.8.2	Results . . . . .	102
3.9	MultiMo-Bat: Results and Discussion . . . . .	105
3.10	Custom Complex Spring Design Methodology . . . . .	107
3.11	Analytical Design . . . . .	109
3.11.1	Solution . . . . .	111
3.11.2	Solution Behavior . . . . .	112
3.12	Numerical Refinement of the Analytical Solutions . . . . .	114
3.13	Methodology Results and Discussion . . . . .	117
3.14	Manufacturing Feasibility . . . . .	119
3.15	Extensions of the Methodology . . . . .	121
3.15.1	Additional Interaction Types . . . . .	121
3.15.2	Multidimensional Magnetic Field Design . . . . .	122
3.16	Adaptability of the Methodology . . . . .	124
3.16.1	Scaling . . . . .	124
3.16.2	Segment Set . . . . .	124
3.17	Chapter Summary . . . . .	125

<b>4</b>	<b>MultiMo-Bat: multi-Surface Locust Inspired Passively-adaptable (SLIP) Foot</b>	<b>127</b>
4.1	Introduction . . . . .	127
4.2	Locust: Morphological Results and Discussion . . . . .	131
4.2.1	Spine: Surface Interaction . . . . .	131
4.2.2	Adhesive Pads: Surface Interaction . . . . .	133
4.2.3	Multi-Surface Foot . . . . .	134
4.3	Locust: Experimental Results and Discussion . . . . .	136
4.3.1	Spine: Slip vs. Re-engagement . . . . .	137
4.3.2	Adhesive Pads: Slip vs. Re-engagement . . . . .	137
4.3.3	Spines vs. Adhesive Pads . . . . .	137
4.3.4	Creating vs. Locating Asperities . . . . .	138
4.3.5	Hydrophobic vs. Hydrophilic Surfaces . . . . .	138
4.4	Robot: Biologically Inspired Design . . . . .	140
4.4.1	SLIP Foot . . . . .	140
4.4.2	Experimental Results and Discussion . . . . .	142
4.5	Chapter Summary . . . . .	144
<b>5</b>	<b>Summary</b>	<b>146</b>
5.1	Thesis Summary . . . . .	146
5.2	Current and Future Research . . . . .	146
5.3	Publications . . . . .	151
	<b>Appendix</b>	<b>153</b>
Appendix A	Preliminary Prototypes and Experiments . . . . .	153
A.1	Modular Independent Jumping Mode . . . . .	153
A.2	Proof-of-Concept Integrated Jumping and Gliding Robot . . . . .	156
Appendix B	Derivation of the Spring Design Equations . . . . .	159

Appendix C	Airfoil CFD . . . . .	161
Appendix D	MultiMo-Bat CAD Drawings . . . . .	163
Appendix E	Manufacturing: Soft Molding Process . . . . .	165
E.1	Procedure . . . . .	166
Appendix F	Distributed Dipole Model . . . . .	167
Appendix G	Internal Energy Storage Mechanism Characterization . . . . .	168
Appendix H	Small Segment Set Example . . . . .	170
Appendix I	Robot Controller . . . . .	171
Appendix J	Experimental Testing Facility . . . . .	172
Appendix K	Materials and Methods . . . . .	175
Appendix L	Locust Adaptation to Jumping . . . . .	176
Appendix M	Dynamics: Robot and Jump Test Rig . . . . .	176
Appendix N	Material Properties: Experimental . . . . .	179
	<b>Bibliography</b>	<b>180</b>

## List of Figures

1.1	Motivation for multi-modal locomtion. . . . .	2
1.2	Variability in the combining strategies of locomotion modes. . . . .	3
2.1	Integrated locomotion in the common vampire bat. . . . .	14
2.2	MultiMo-Bat and its phases of operation show experiemntally. . . . .	16
2.3	CAD model of the MultiMo-Bat and four-bar leg positioning. . . . .	17
2.4	Jumping phase images showing the wing and four-bar leg behaviors. . . . .	19
2.5	Section veiw of the MultiMo-Bat showing internal components. . . . .	20

2.6	MultiMo-Bat locomotion phases. . . . .	22
2.7	Jumping phase multi-body dynamic model. . . . .	29
2.8	Simulated jumping behavior. . . . .	32
2.9	Comparison of the contribution to the dynamics of the mass, drag, and friction in the dynamic model. . . . .	33
2.10	Sensitivity analysis of the four-bar leg dynamics. . . . .	34
2.11	Biologically inspired robotic knee joint. . . . .	36
2.12	Internal energy storage mechanism (IESM). . . . .	39
2.13	Optimal helical extension spring design model results. . . . .	44
2.14	Airfoil model configuration for aerodynamic coefficient calculation. . . . .	48
2.15	Airfoil surface pressure distribution at AoAs. . . . .	50
2.16	Characteristic of a flat plate airfoil. . . . .	52
2.17	Non-steady state gliding behavior and embodied intelligence. . . . .	53
2.18	Simulated non-steady state gliding behavior. . . . .	54
2.19	Simulated jumping and non-steady state gliding behavior. . . . .	54
2.20	Collapsible airfoil design. . . . .	56
2.21	Tensioning the rigid airfoil membrane. . . . .	57
2.22	Jumping experimental results. . . . .	60
2.23	Example jumping trajectories. . . . .	62
2.24	Gliding and jumping-gliding experimental results. . . . .	63
2.25	Example gliding trajectories. . . . .	64
2.26	Example jumping and gliding trajectory. . . . .	67
3.1	MultiMo-Bat CAD model with integrated tailored magnetic spring based actuators.	81
3.2	Helical springs are mounted between surfaces while tailored magnetic springs are embedded into them. . . . .	82

3.3	Introduction to the basic magnet set and the resulting force vs. displacement relationships. . . . .	85
3.4	Tailored magnetic spring design: force vs. displacement relationships, out-of-place forces, segments, and superimosed forces. . . . .	86
3.5	The magnetic dipole distribution within a simulated permanent magnet. . . . .	87
3.6	Characteristics of shape memory alloy actuators, helical springs, and tailored magnetic springs. . . . .	89
3.7	Transformation and variability of a tailored magnetic spring. . . . .	96
3.8	Internal energy storage mechanism design and characteristics. . . . .	97
3.9	Wing lock design and characteristics. . . . .	99
3.10	Experiential characterization procedure of a tailored magnetic spring. . . . .	103
3.11	Isolating the magnetic force from the frictional force. . . . .	104
3.12	Experimental trials of the MultiMo-Bat with integrated energy storage and wing locking mechanisms. . . . .	105
3.13	The regions of non-negligible forces between the magnets of the chosen configurations. . . . .	108
3.14	The small segment set consisting of only 20 segments. . . . .	110
3.15	Initial solution of the large segment set and the filtering techniques used to condense it. . . . .	112
3.16	Mutation algorithm used by genetic algorithm based optimization. . . . .	115
3.17	Comparison between the solutions from various stages and segment sets of the custom complex spring design methodology. . . . .	118
3.18	Modeling the magnet mounting areas to estimate the total surface area required for integration. . . . .	120
3.19	Methodology extension: additional interaction types. . . . .	121
3.20	Methodology extension: multidimensional magnetic field design. . . . .	123

4.1	Images of the desert locust ( <i>Schistocerca gregaria</i> ) and its feet. . . . .	128
4.2	The configuration of the adhesive pads and spines on desert locust's feet leads to several types of surface interactions and embodied intelligence. . . . .	130
4.3	The desert locust's slipping behavior is highly dependent on the surface and the relative stage (planting, early, middle, and late) of the jumping behavior. . . . .	135
4.4	Design, integration, and experimental characterization of multi-Surface Locust Inspired Passively-adaptable (SLIP) feet. . . . .	139
4.5	Experiential trials of the MultiMo-Bat with integrated SLIP feet. . . . .	141
5.1	MutliMo-Bat with combined inertial and aerodynamic tail. . . . .	147
5.2	Gliding control through active wing deformation. . . . .	148
5.3	Wind tunnel for characterization and optimization of the collapsible airfoils. . . .	150
5.4	Experimental trials of the desert locust on granular media. . . . .	151
A.1	Modular jumping and gliding robot. . . . .	154
A.2	Image of the modular jumping and gliding robot. . . . .	155
A.3	Proof-of-concept jumping and gliding robot deisgn. . . . .	156
A.4	Images of the two proof-of-concept jumping-gliding and jumping robots. . . . .	157
A.5	Experiential trials of the two proof-of-concept robots. . . . .	158
C.1	Flat plate airfoil: relative pressure and velocity stream lines for AoAs of 0, 4, and 6 deg. . . . .	161
C.2	Flat plate airfoil: relative pressure and velocity stream lines for AoAs of 45 and 90 deg. . . . .	162
D.1	CAD model of the MultiMo-Bat's gliding configuration. . . . .	163
D.2	CAD model of the MultiMo-Bat's jumping configuration. . . . .	164
E.1	Soft mold manufacturing of components. . . . .	165
F.1	Example distribution of dipoles in two 3.2 mm permanent magnets. . . . .	167
G.1	Power characterization of the internal energy storage mechanism. . . . .	169

H.1	Family of solutions example obtained from the analytical design stage of a tailored magnetic spring. . . . .	171
I.1	Robot controller PCB and schematic views. . . . .	172
J.1	Experiential testing facility for miniature robots and biological organisms. . . . .	173
L.2	Image and high resolution laser profilometer scans of the forelegs of the desert locust. . . . .	177
M.3	The jump testing rig and dynamic comparison to the robot with material characterization. . . . .	178

## List of Tables

2.1	The constituent component masses of the MultiMo-Bat. . . . .	21
2.2	Calculated aerodynamic coefficients for all angles-of-attack of a flat plate airfoil from computational fluid dynamics. . . . .	51
2.3	MultiMo-Bat configurations used in testing of the jumping and gliding performance. . . . .	60
2.4	Mass and Performance Integration metrics of the MultiMo-Bat. . . . .	69
2.5	Scaling relationship of general properties such as mass, volume, and stiffness. . . . .	72
2.6	Scaling relationships of spring, friction, and aerodynamic forces. . . . .	72
2.7	Scaling relationships of spring, battery, and capacitor energy storage. . . . .	73
2.8	Scaling relationships of electric motor and shape memory alloy-actuator properties. . . . .	74
2.9	Scaling relationships of the locomotion modes, structures, and actuators of the MultiMo-Bat. . . . .	74

2.10	Comparing performance metrics of jumping, jumping-gliding, and the MultiMo-Bat robots. . . . .	76
3.1	Tailored magnetic spring of the self-contained internal energy storage mechanism.	100
3.2	Tailored magnetic spring of the wing locking mechanism. . . . .	101
3.3	Magnetic segment filtering options. . . . .	114
3.4	Estimated mounting areas for designed tailored magnetic springs based on relative positions. . . . .	120
4.1	Roughness characterization of the materials used in the locust jumping experiments.	132
4.2	Angular configuration of the desert locust’s tibia spines. . . . .	132
4.3	Experiential results of the multi-Surface Locust Inspired Passively-adaptable (SLIP) foot concept. . . . .	143
A.1	Constituent component masses of the Jumping-Gliding and Jumping prototypes and performance. . . . .	157

# Chapter 1

## Introduction

### 1.1 Motivation

Mobility of miniature robotic platforms is an important challenge as it is a crucial step towards closing the gap between them and the biological world [136]. Operation in unstructured environments poses an additional challenge to miniature robots, due to the extreme variability found in the morphology of the locomotion domain, defined as the region containing all terrestrial, aquatic, and aerial environments, Fig. 1.1. These challenges create regions in the environment where particular locomotion strategies are applicable. The size of these regions is a function of not only the locomotion strategy but, very importantly, the relative size of the robot compared to the obstacles it will encounter in the environment. One of the most challenging regions for locomotion is terrestrial environments where the robot is much smaller than the majority of the obstacles it encounters. However, nature has already had to address this challenge and has developed a conceptually simple solution. If a specific locomotion mode cannot successfully and/or efficiently operate in a given environment, and this environment offers some significant benefit, then another strategy is evolved. These modes include but are not limited to: walking/running, jumping, flying, swimming, climbing, crawling, and brachiating.

Robots, however, have a distinct disadvantage as the number of locomotion modes is increased. This is due to the current actuator, power storage, and transmission technologies which create significant limitations to their uses; due to their size, weight, efficiency, and versatility.

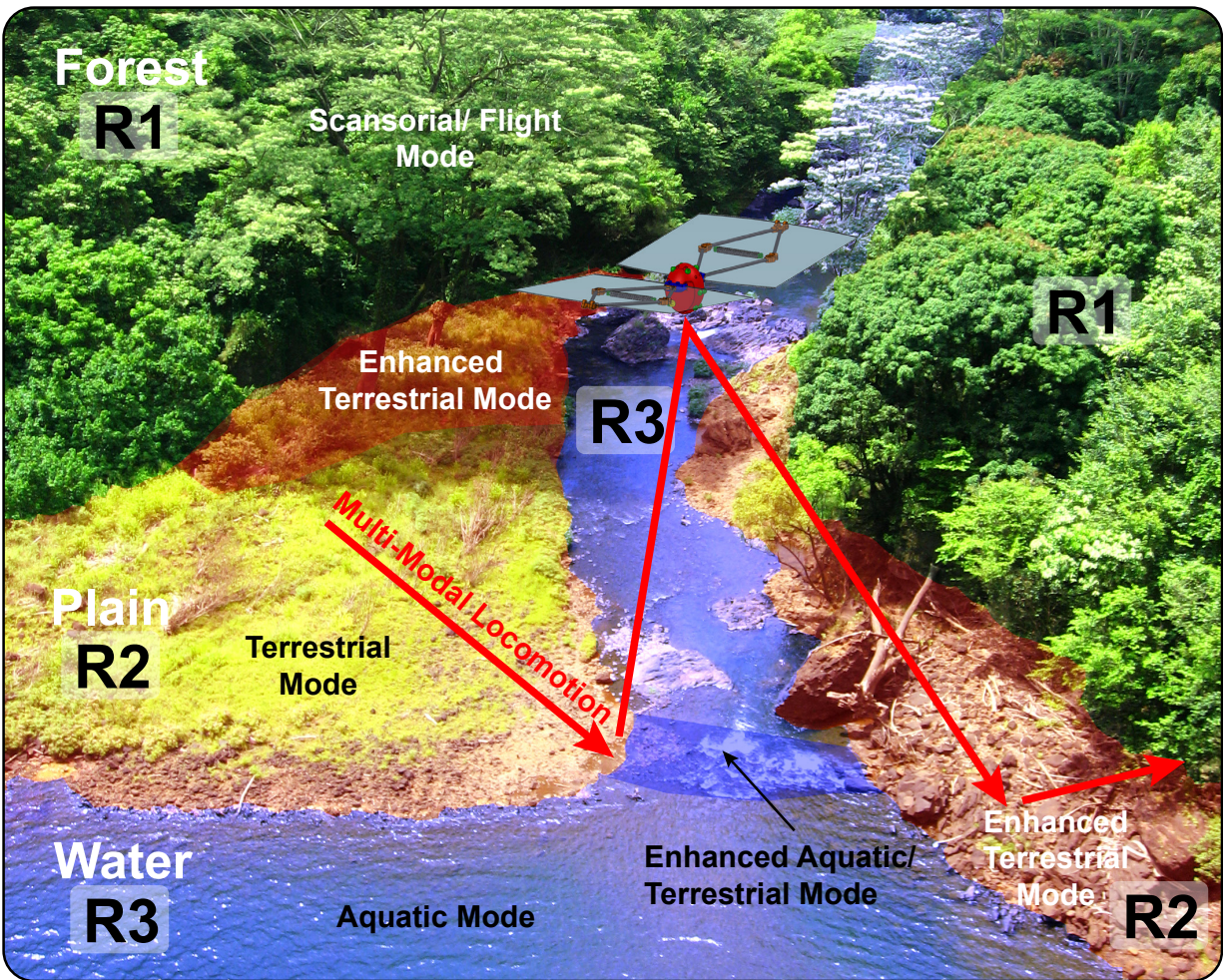


Figure 1.1: The locomotion domain consists of islands where individual modes are applicable; such as regions R1, R2, and R3. Multi-modal locomotion can help to overcome obstacles and connect the islands which require the same locomotion characteristic thus greatly enhancing the robot's range.

Whereas animals, Figs. 1.2a,b, have light weight high power muscles utilizing chemical energy, currently, robots must rely mainly on electromagnetic motors and batteries which are significantly heavier and less efficient. Therefore, the simple addition of independent locomotion modes, Fig. 1.2c to Fig. 1.2d, will significantly reduce the performance of all modes, possibly to the extent that they are no longer viable. Integration is the solution; if some of the components of one locomotion mode can be used for another without significant alterations, such as a shared body Figs. 1.2e, then the additional mode can be added without as substantial a performance

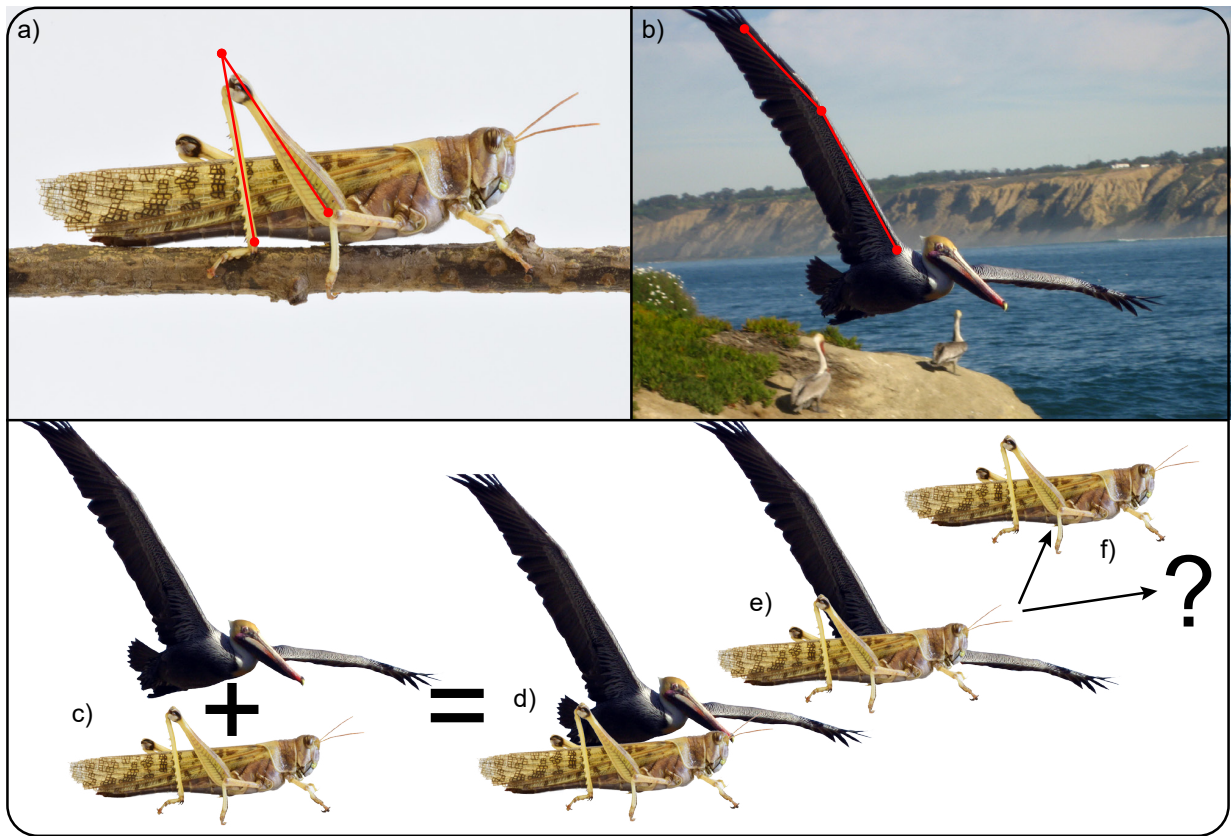


Figure 1.2: **a)** Desert locust (*Schistocerca gregaria*) exhibits high performance jumping. **b)** Brown Pelican (*Pelecanus occidentalis*) exhibits high performance gliding. **c)** Multi-modal jumping and gliding locomotion, inspired by the desert locust (**a**) and brown pelican (**b**), respectively. **d)** Simplest addition through connecting fully independent modes. **e)** Shared body, independent locomotion mode addition; current stage of robotic research. **f)** At this point either a well adapted independent, as in the desert locust, or possibly an integrated approach can be taken to add additional modes.

cost. Further improvements to the integration strategy can increase the cooperation between the modes, Fig. 1.2f, or seek to find strategies for sharing even more of the components. Integration is therefore a method for preserving the performance of individual locomotion modes, through an overall reduction of the number of necessary components, making the system smaller, lighter, and more robust. This concept of integration is ubiquitous in the biological world, where animals universally employ some level of integration between multiple locomotion modes, some with very high levels of integration, highlighting the fact that even seemingly dissimilar modes can utilize significant portions of the structure and actuation of another.

Integration is not a binary quantity but a multi-dimensional continuum where depending on the modes selected, a wide range of strategies and integration levels are possible from nearly zero integration (Fig. 1.2d) to nearly 100 % integration; where 100 % means the modes are mechanically equal. To develop the field, explore the concept, and demonstrate the benefits to robotics of a highly integrated approach to multi-modal locomotion, two modes, which are not commonly known to be highly integrated within the biological world, but commonly exist together as they have complimentary dynamic behaviors, are selected. These modes are jumping and gliding. Jumping can be a very efficient method for overcoming obstacles in the environment; reducing the overall cost of transport [2] however it is also a very effective method for transitioning to flight. A catapult jump is a particular jumping method utilized by many insects [14, 15] including the leafhopper which has one of the highest known jumping performances at accelerations of up to 225 times that of gravity [22]. This method is characterized by the relatively slow storage of elastic energy and its subsequent rapid release, allowing for much smaller actuators and, with the addition of a recharging capability, a smaller energy source as well. Taking advantage of the height potential generated during the jumping mode, the gliding mode can then be used to further control the motion trajectory, creating a more capable system, as well as reduce ground impact forces and thus structural stress.

To develop the jumping and gliding robot, initial inspiration is sought through investigation of biological organisms which have desirable jumping and/or gliding traits. Due to the unpowered nature of the gliding mode it is desirable to have a very high performance jumping mode to create the most potential energy for the gliding mode to utilize. Therefore, to inspire the jumping mode's development, insects are investigated which exhibited high performance jumping. The order *Orthoptera*, which includes desert locusts (*Schistocerca gregaria*), is initially selected as the inspiration for the jumping mode; as seen in Fig. 1.2a. Observations of Brown Pelicans (*Pelecanus occidentalis*) and Red-tailed Hawks (*Buteo jamaicensis*) during gliding flight, revealed the potential of an unpowered gliding locomotion mode; as seen in Fig. 1.2b. As the underlying

structure and actuation of the organisms are examined, despite the significant biological differences, many mechanical similarities are observed; such as the highlighted leg and arm structures in Figs. 1.2a,b. This led us to search for an organism which utilized these mechanical similarities to highly integrate these modes.

The jumping and gliding robot is inspired by not only the mobility afforded by jumping and gliding modes but more importantly, this thesis focuses on the particular method by which these two locomotion modes are combined in the common vampire bat (*Desmodus Rotundus*). These bats utilize the same major actuation and structural components to achieve high performance in both jumping and flying. Within the biological world many organisms use the synergy between jumping and flying modes to improve their mobility such as: ants, grasshoppers, locusts, birds, bats, squirrels, frogs, and snakes. Over the last decade, scientist and engineers have tried to achieve a successful combination of these two modes with initial work conducted in 2007 by Megill W, *et al.* [7]. Subsequent research has attempted to improve on the combination of these locomotion strategies; however, due to the challenges discussed previously, no work has focused on and thus demonstrated a successful highly integrated combination of these two modes.

To realize an integrated jumping and gliding robot, requires not only the integrated approach but also a reinvestigation into the underlying components of these locomotion modes. Within the size scale of miniature robots, which occupy the region of 10s to 100s of grams, every gram is significant. Further more, the emerging field of mechanical, physical, or embodied intelligence suggests that significant portions of the kinematic and dynamic behavior of an organism can be encoded into the physical system, allowing the organism to passively adapt to the situation thus reducing the required computational power and controlled degrees-of-freedom. Embodied intelligence is well aligned with the integration strategy which looks to reduce the number of components and increase the functionality of individual components.

We feel that just as it has been important for the research community to study individual strategies used to move through the environment, it is also important to understand how these

individual modes may be combined and the possible benefits unique to this type of combination. No previous work has attempted to highlight integration as a viable method for the combination of locomotion modes as well as attempt to enhance the design of the underlying components and create metrics to begin to quantify and compare this technique.

In the field of robot mobility, we look to biology and biologists for inspiration on methods to improve robotic systems. However, insufficient information on the integration strategies used and the cost or effect, to a particular organism, for a particular locomotion mode exists. This thesis serves to highlight this potentially beneficial area of research through the case study of a particular integration strategy. This miniature jumping and gliding robot can be used to explore, inspect, and monitor unstructured or hostile environments and deployed in large numbers could be used within the context of a swarm to more rapidly and robustly complete a desired task.

## **1.2 Research Objectives**

The objective of this research is to enhance the mobility of miniature robotic systems through the study of the methods by which multiple locomotion modes are combined in the biological world, actuator and energy storage devices, and embodied intelligence. This thesis serves to highlight the potential of an integrated multi-modal locomotion concept through the development of a system employing this strategy to combine jumping and gliding locomotion. One of the biggest challenges to robot mobility, and a focus area of this research, is the power, actuation, and transmission systems which tend to have limited functionality and low energy density. Therefore, in addition to directly seeking to enhancing actuator performance, embodied intelligence will be employed to encode passive adaptations into the kinematics and dynamics of the robot to reduce the number of actuators required. The combination of these modes requires the development of many specialized components and concepts beneficial to further research into integrated locomotion modes. Therefore, in addition to the development of a high performance, untethered, integrated jumping and gliding robot, areas of broader impact will be set to expand

the applicability of the research to the broader robotics community.

## 1.3 Organization

The thesis is organized as follows: Chapter 2 presents the development of the biologically inspired, integrated, multi-modal, jumping and gliding robot, MultiMo-Bat. The chapter begins by introducing the biological inspiration for the development of the MultiMo-Bat, and then proceeds to the overall design of the MultiMo-Bat using the integration concepts abstracted from the organism. This integration results in coupling between the modes which increases design complexity however, through application of presented coupling parameters the design complexity can be managed. The dynamics and individual components necessary for the jumping and gliding locomotion modes are then developed, followed by experiential characterization of the performance. The chapter finishes with the development of metrics to quantify the integration performance and allow for comparison to future integrated multi-modal locomotion robots as well as their biological counterparts.

Chapter 3 presents the development of a custom complex magnetic spring design methodology for shape memory alloy-actuated mechanisms in the MultiMo-Bat. The chapter begins by introducing the concept of magnetic segments which are combined to create the magnetic springs and the characteristics of shape memory alloy-actuated mechanisms. A simple design methodology is presented to develop two coupling mechanisms for the MultiMo-Bat which are experientially shown to significantly improve locomotion performance. The chapter then proceeds to expand the methodology to any well-defined function of force vs. displacement and demonstrate the relationship between adaptability and computational efficiency through complex examples which highlight the potential power of the custom complex magnetic spring design methodology.

Chapter 4 presents the development of a biologically inspired robotic foot design concept which allows the MultiMo-Bat to passively adapt and interact with a wide range of surfaces

at variable angles. The chapter begins by introducing the desert locust (*Schistocerca gregaria*) and the motivation for examining its feet, followed by a morphological analysis of the feet to understand their potential interaction with the surface. After which, the organism's jumping locomotion is analyzed to understand the interplay between the friction mechanisms on variable surfaces. The chapter finishes with the elucidated concepts being combined to develop the multi-Surface Locust Inspired Passively-adaptable (SLIP) foot for the MultiMo-Bat which is then experientially verified.

Chapter 5 concludes the thesis with summary, future work, and publications. As the focus of each chapter deals with specific but not directly related components of the development of the MultiMo-Bat each chapter will include a separate literature survey.

## 1.4 Contributions

### Biologically Inspired Integrated Multi-Modal Locomotion

- Presented and developed the concept of integrated multi-modal locomotion and highlighted the benefits and challenges associated with this strategy for combining locomotion modes.
- Motivated and validated the concept of integrated multi-modal locomotion through inspiration taken from biological organisms.
- Abstracted and discussed key integration concepts from the Common Vampire Bat which form the foundation of all integrated locomotion strategies.
- Created coupling parameter based methods for reducing the design complexity of integrated locomotion systems.
- Developed high strength multi-functionality joints inspired by the mammalian knee.
- Developed optimal energy density helical spring design equations based on constraints of the system.

- Developed an entirely passive strategy for transitioning between jumping and gliding locomotion which employs significant embodied intelligence encoded into the dynamics and kinematics of the miniature robot.
- Developed of a class of collapsible airfoils with no span-wise support to facilitate the integration of a gliding locomotion mode.
- Designed, developed, and experimental verified a high performance integrated multi-modal locomotion robot which combines jumping and gliding locomotion strategies.
- Developed metrics to quantify the integration strategy and allow for comparison to other robots and their biological counterparts.

### **Tailored Magnetic Spring Design**

- Developed and experimentally verified a custom complex spring design methodology which is able to theoretically create any well-defined function of force vs. displacement using sets of discrete permanent magnets.
- Presented key characteristics and their associated magnetic segments for detwinning shape memory alloy-actuated mechanisms.
- Developed the concept of irreducible sets which allow for the translation of tailored magnetic spring properties to other applications.
- Designed, developed, and experimentally verified a shape memory alloy-actuated high energy storage mechanism for enhanced jumping performance.
- Designed, developed, and experimentally verified a shape memory alloy-actuated wing locking and control mechanism for enhanced jumping to gliding transitions.
- Developed estimations of the integration area necessary for a tailored magnetic spring.
- Extended the custom complex spring design methodology to any interaction forces over any distance using large segment sets as well as multi-dimensional design of magnetic

fields.

### **multi-Surface Locust Inspired Passively-adaptable (SLIP) Foot**

- Discovered the desert locust operates at the extreme limits of friction on a variety surfaces, due to its adhesive pads, spines, and buckling joint.
- Characterized all aspects of the locust's feet which may interact with variable surfaces based on their morphology.
- Discovered the role of the tibia spines in jumping locomotion from variable surfaces.
- Characterized, through significant in-vivo experimentation, the resulting behavior of locust's feet on variable surfaces to understand the interplay between adhesive pad and spine based friction.
- Discovered the planting type jump used by the desert locust which broadened the applicability of the findings to dynamic multi-surface attachment.
- Developed the design concept of the multi-Surface Locust Inspired Passively-adaptable (SLIP) Foot.
- Designed, Developed, and experimentally verified a SLIP foot on the MultiMo-Bat.

## Chapter 2

# MultiMo-Bat: Biologically Inspired Integrated Multi-Modal Jumping and Gliding Robot

### 2.1 Introduction

Enhanced mobility can be achieved by enhanced adaptability of existing locomotion modes thereby increasing the region of the locomotion domain in which they can operate. However, the potential increase in mobility is limited by the underlying characteristics of the mode whereas the addition of a new locomotion mode adds a whole new region of applicability thus significantly increasing overall robot mobility and is therefore the method which will be the focus of this chapter.

The advantages of jumping are just as applicable to robotics as they are to the biological world, and thus has resulted in the development of many jumping robots. The smallest of these are centimeter sized and around a gram in weight; such as the flea inspired [78, 100] and water strider inspired [79] robots which uses shape memory alloy as the main actuation. A combustion powered robot [30] has also been shown which employs nano-porous silicon to store chemical energy for jumping. The next order of magnitude in jumping robots is where DC motors become widely available actuators. The smallest of these systems are the 7 g jumper [82, 83, 84], Grillo robots [89, 126, 127, 128], MSU jumper [174, 175, 176, 177], and others [6] of which some variant can self-right and orient the jump direction. This size scale also includes robots

which combine rolling and jumping [59], such as the Mini-Wegs robot [85], as well as a snap through buckling concept for jumping locomotion [162, 163]. The next order of magnitude are the robots in the kilogram region. Two of which use the combination of wheeled and jumping locomotion; the Rescue Robot [149] which uses pneumatics to power its jump and the Sand Flea [18] which uses combustion to propel itself into the air as well as several other systems under development [140, 143]. However, there still exist performance challenges to these systems. Systems employing non-renewable strategies such as combustion or pneumatics can have very high energy density however, they cannot be easily recharged in the field therefore limiting their range. For electrically powered robots the challenge is to achieve sufficient energy density in the energy storage devices to allow for additional components, payload, or even in some cases the inclusion of the actuators themselves on board. Many of these high performance jumping systems show significant reduction in jumping performance when any additional components are added. There exist several robots which have both jumping and gliding locomotion strategies; however each requires certain assumptions for locomotion. The addition of wing membranes to the Glumper robot is not shown to produce gliding behavior, as the trajectory remains ballistic, resulting in only a reduction of the jumping performance [7]. The 7 g jumper shows good jumping performance however, with the addition of the gliding structure the jump height is reduced by almost 87% requiring the robot to jump from an elevated platform to achieve gliding [81]. The Jump Glider shows both good jumping and gliding performance however, the rigid airfoils restrict the jumping variability and the focus is on efficiency rather than broad robot design concepts [39, 40]. These challenges are the inspiration for this chapter, to show that integrated multi-modal locomotion design strategies can produce systems capable of more than one high performance mode with all necessary actuation on-board. Only a few robots are capable of two locomotion modes and even less are well adapted for both. Also, of all the existing robots that do have multiple locomotion strategies, to the author's knowledge, none focuses on integration to combine high performance locomotion modes.

This chapter focuses on integration of locomotion modes as a method to achieve increased mobility in robotic systems with minimal performance degradation. It is discussed in the context of the design, development, experimentation, characterization, and evaluation of a robotic system with two highly integrated locomotion modes: jumping and gliding. These modes have very different and conflicting structural and actuation requirements. Therefore, the challenge is in the extraction of important concepts of the integrated multi-modal locomotion design approach taken by organisms and the application of these concepts to the robot development along with well adapted, high performance, actuation mechanisms.

The chapter is organized as follows: Section 2 introduces the biological inspiration for the jumping and gliding robot. Section 3 presents the design concept for the robot along with key performance features. Section 4 gives experimental demonstrations of the jumping and gliding robot. Section 5 develops metrics to quantify the integrated design characteristics. Section 6 discusses the overall outcome of the work, and Section 7 provides conclusions.

## 2.2 Biological Inspiration

The order *Chiroptera* (bats) provides a unique case study to examine the combination of terrestrial and aerial locomotion modes. It includes over 1000 species of similar morphology which exhibit significant dissimilarities in terrestrial mobility, ranging from limited crawling to performance comparable to that of many small rodents, as seen in *Desmodus Rotundus* (common vampire bat). *D. Rotundus*, Fig. 2.1, is a sanguinivore, feeding exclusively on blood from terrestrial organisms. This ecology has driven the development several high performance terrestrial locomotion modes, including jumping [4, 120, 121, 129, 157]. Originally thought to have fed on small animals, pursuit of moving prey necessitated the bat's specialization in terrestrial locomotion; its jumping behavior was probably developed as an escape mechanism and/or as a means to transition to flight when highly loaded after feeding.

*D. Rotundus* shows specialization for jumping, however a recent study shows that bat mor-



Figure 2.1: Common vampire bat (*D. Rotundus*) is shown both jumping (a) and flying (b) to highlight the integration of the arm bones into each of these locomotion modes. The wing membrane however, being necessary only for flying, is collapsed during the jumping mode. The configuration of the arm bones, humerus, radius and ulna, are highlighted in each mode. (source: www.arkive.com)

phology in general may facilitate jumping. Several other bats with similar jumping strategies, albeit much lower performance, show performance dictated simply by body size and not ecological pressure [51]. This morphological predisposition toward jumping may be due to the high level of integration between the jumping and flying locomotion strategies in bats as they are developed around the same primary musculoskeletal components. The main actuation of both modes is built around the largest muscle in the organism, the *m. pectoralis profundus* (posterior division). Both modes also share three main bones, comprising the main arm structure, which are the humerus, radius and ulna. This sharing of components, or integration, between locomotion

modes can preserve a significant portion of the flight mode performance as the major components required for jumping already exist for flight. However, this alone does not guarantee the preservation of performance as the shared components themselves may be modified to accommodate the jumping mode.

An approximation of the cost, associated with modification to the major components, can be elucidated from a comprehensive study of the shoulder morphology of 29 species which includes *D. Rotundus* [142]. The two major muscles, used for both modes, show scaling well within the range of the other species; implying no additional major muscle mass is required to power the terrestrial mode. The arm bones are slightly more robust and fusion of the radius and ulna has occurred increasing strength to accommodate the ground reaction forces. The bat's jumping performance is therefore achieved through minor modifications to the shared flight structures, which tend to increase range of motion and independence of control. These changes result in low overall cost to the organism's flight mode and indicate the success of this particular integration strategy. Applying the concept of integration to robotic systems is especially useful as the number of actuators that can be feasibly incorporated into a system and adequately powered is limited. The goal then is to abstract this particular integration strategy, from the organism, and apply it to the development of a high performance jumping and gliding robot.

Analysis of the bat's integration strategy yields two key design abstractions which are necessary for the successful integration of the jumping and gliding modes. As the bat uses its forelimbs to both jump and fly [4, 129], the major abstracted concept from this integration strategy is the sharing of similar structures. Widening the focus to other organisms which have either jumping, flying or both locomotion strategies, one underlying structure, utilized by the bat, which is seen in both of these two modes is the 2-link-2-joint structure shown in Figs. 1.2a,b. The wing membrane is then supported by these shared components as well as the significantly extended metacarples and phalangeal bones; thereby coupling the wing shape to the leg configuration. Therefore, the bat is able to collapse the wing membrane, to reduce drag during the coast phase of the jump, im-

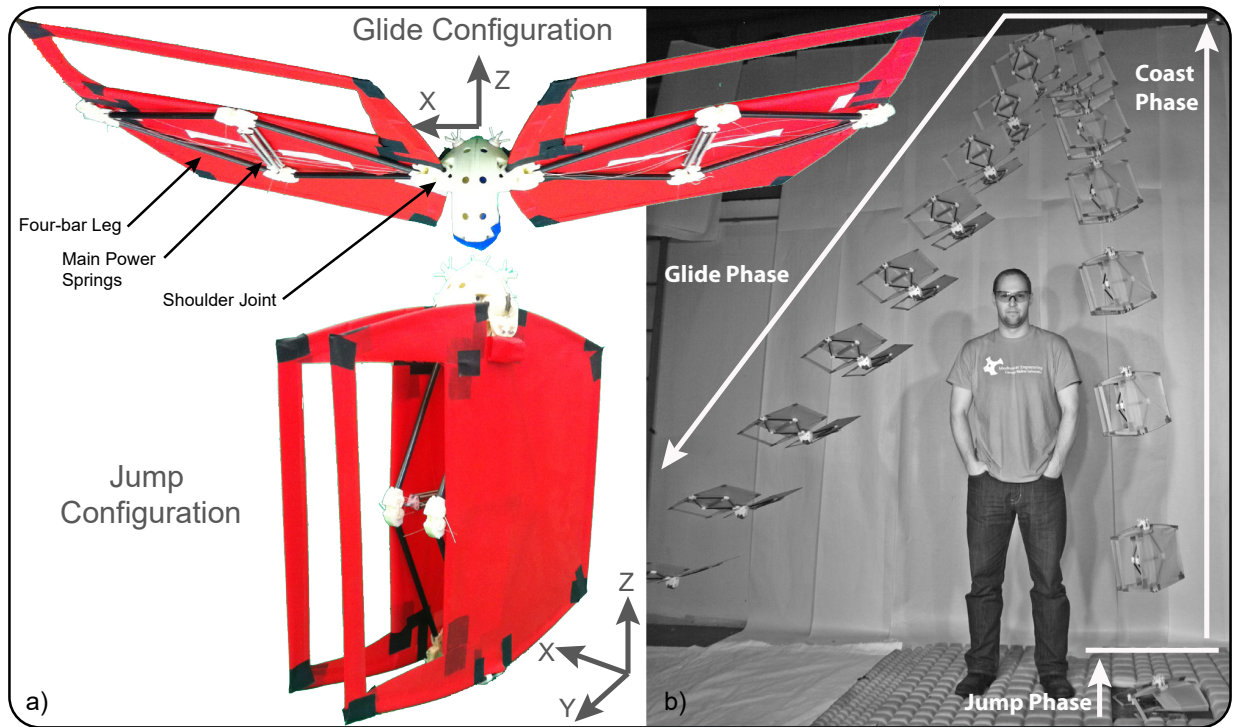


Figure 2.2: **a)** Photos of the proposed jumping and gliding robot, the MultiMo-Bat, shown in the gliding (upper photo) and jumping (lower photo) configurations. **b)** The MultiMo-Bat is shown overcoming an obstacle with three of the four phases of operation labeled. The energy storage phase is not shown but would occur before the jumping phase.

proving jumping performance. Interestingly, in the case discussed and many others, animals that utilize multi-locomotion strategies are able to reduce the effect that each mode has on the other by modifying the configuration of components not needed for a specific mode. These integration concepts of shared similar structures and passive component configuration change represent the foundation of integrated locomotion design concepts and are applied to the development of the MultiMo-Bat.

## 2.3 Design Concept

The design concept behind the MultiMo-Bat, shown in Fig. 2.2 and Fig. 2.3, uses two key abstractions from the vampire bat's locomotion strategy which tend to minimize the number of components and maximize their functionality. The primary abstraction is taken from the mor-

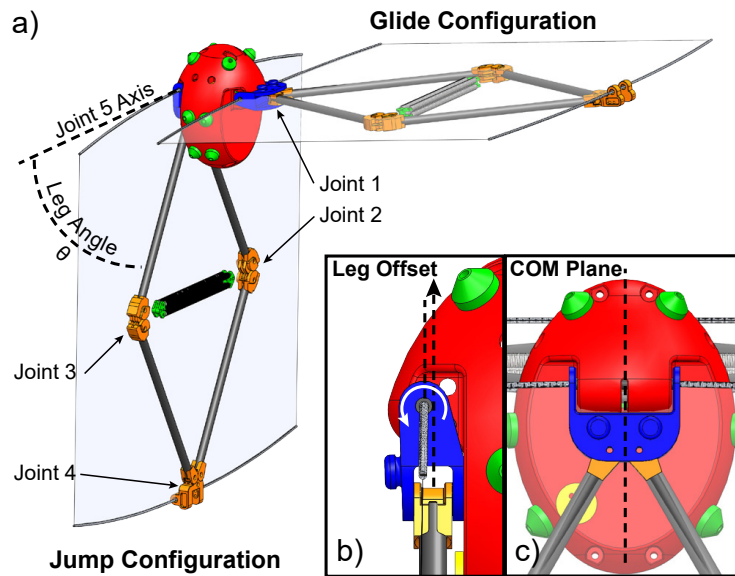


Figure 2.3: **a)** Concept shown with one leg in the jumping configuration and one in the gliding configuration. Joints 1-4 are responsible for the leg extension/retraction whereas Joint 5 is responsible for the transition between jumping and gliding configuration. **b)** Leg offset utilized for configuration change. **c)** The center-of-mass (COM) plane is positioned at the center of the leg assembly.

phology of the arm structure and its function within the context of both modes; this dual functionality inspires the robot's leg design. The second abstraction is associated with the connection between the added wing structure and the shared leg structure. This connection results in inherent motion coupling between these two structures creating the possibility of passively reconfiguring and collapsing the wing.

In the vampire bat, the humerus and fused radius and ulna are the primary arm components used for both locomotion strategies. However, due to the inherently high degrees-of-freedom (DOF), in the vampire bat's musculoskeletal system, significant additional support and constraining components would be necessary to achieve the desired motion. Therefore, to mechanically reduce the DOF of the leg structure, the two arm components are mirrored over the center plane (Fig. 2.2). This creates the four-bar leg structure of the MultiMo-Bat which, being fixed at one joint, results in only two independent DOF. The most important of which, the compression/extension of the diamond shape, allows for the motion necessary for both modes. This DOF

serves to stretch the main power springs, transmit the jumping force to the ground, and tension the airfoil. The second is the rotation of the entire structure around the fixed joint. The second DOF can be used in the future for controlling the jump direction. Finally, attachment of the four-bar leg to the shoulder adds an additional DOF which allows for the two mode configurations shown in Fig. 2.2 and Fig. 2.3a. As the flight mode is currently unpowered, the direct sharing of actuation components will not be necessary for this prototype. Several proof-of-concept prototypes (Appendix A) were constructed to test key design features of the MultiMo-Bat.

To achieve the passive motion coupling between the wing and leg, components which alter their relative position as compared to the rest of the robot are identified. The foot of the MultiMo-Bat is such a component. It changes both its relative distance during compression of the four-bar and angular position according to the shoulder angle from the body. Therefore, connecting the wing to the body and foot will create two coupled DOFs which can be used to modify the wing components. This reduces the controlled DOF necessary for the configuration change because changing the leg configuration changes the wing configuration. However, the jumping mode has priority over these DOFs as both are essential to the jumping mode's performance. The objective then is to design this coupling such that it reduces any detrimental effects associated with the added wing structure. The wing is designed to be highly collapsible, as with the vampire bat, so as to not interfere with the jumping mode. The wing membrane is connected directly to the shoulder joint and the foot; therefore, as the leg structure is compressed, storing the jumping energy, the wing membranes are passively collapsed, as seen in Fig. 2.4. As the legs extend, powering the jump, the wing membranes are extended as well; preparing them for the coming glide phase. However, the integration of the wings and legs also causes the wings, even when fully extended in the coast phase, to remain beside the body parallel to the flow which reduces their drag and preserves jumping performance. In fact this configuration, acting like a tail, actually helps to stabilize the robot about the velocity vector, potentially improving performance.

An exoskeleton can reduce the overall mass of the system while improving the durability,

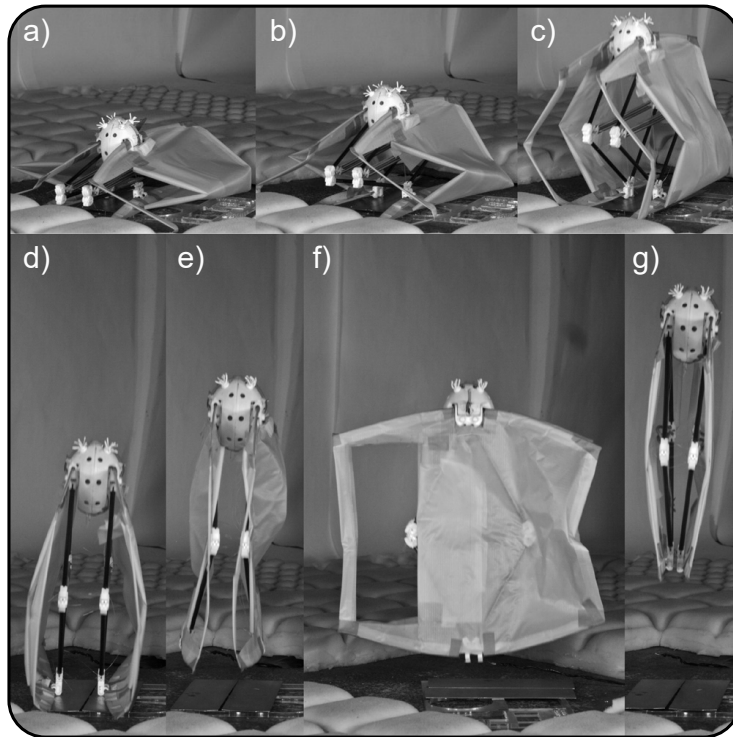


Figure 2.4: Video snapshots of the liftoff behavior of the MultiMo-Bat prototype which illustrates the wing membrane tensioning and the effects of the out-of-plane torques produced by the airfoils. **a)** Initial jumping position with the membranes collapsed. **b)** The four-bar legs begin to extend, powering the jump. **c)** The membranes are reaching full extension. **d)** The MultiMo-Bat just before it leaves the ground showing the airfoils inflated by the escaping air mass between them. **e,f)** Front and side views of the robot at the point of maximum out-of-plane deformation. **g)** The wings quickly stabilize at about a body length above the ground and remain beside the body until the robot nears the apex of the coast phase.

robustness, and protection of sensitive components. This structure is significant to the development of the MultiMo-Bat because occupying the extremities of the system creates significantly more surface area for the integration of attachment points for internal and external components. Engineered components, especially actuators and their transmissions, are typically much larger than their biological counterparts and therefore, the significant increase in attachment area facilitates design and development; as stated previously the goal of integrated design is to reduce the number of components and increase component functionality. Exoskeletons, like their internal counterparts, are used to constrain components and produce fixed points for the actuators to pull against, with articulation only where necessary to facilitate locomotion. This concept is used in

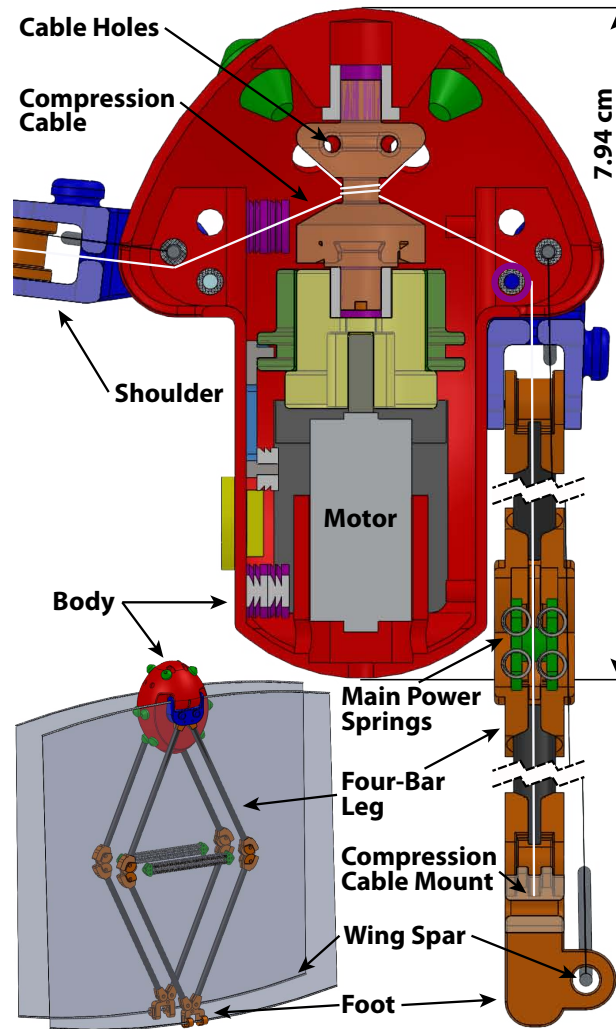


Figure 2.5: A CAD drawing of the half body of the robot showing the integration of the internal energy storage mechanism and SMA clutch. The full system is also shown for reference with the legs fully extended in the jumping configuration.

the development of the body structure for the jumping and gliding robot which consists of only two different components, the half body and the shoulder, symmetric about the  $yz$ -plane (Fig .2.2) resulting in a total of four components to create the entire structure, as seen in Fig. 2.5. This results in very few connection points between components which creates a very strong structure as connections typically result in stress concentrations and therefore weak points in the system. Connection points also require additional features for fortification such that they are of equal strength to a solid single piece, resulting in added mass and volume to the system. All of these

integrated features result in a total body mass of only 23 grams.

Table 2.1: Prototype Component Masses

Subsystems	Mass (g)
<b>Body ASM, <math>M_B</math></b>	<b>78.08</b>
Body	23.3
Shoulders	3.0 (2ea)
Wing Structure (Additional)	16.1
Internal Energy Storage Mechanism	19.5
Misc Components (hardware, cables, etc.)	13.18
<b>Four-bar Leg ASM</b>	<b>12.2</b> (2ea)
Leg Link, $M_L$	2.63 (4ea)
Foot, $M_F$	1.7 (2ea)
<b>Main Power Spring ASM, <math>M_S/2</math></b>	<b>6.56</b> (2ea)
<b>MultiMo-Bat</b>	<b>115.6</b>

The MultiMo-Bat is composed of just over 20 different components. Six, relatively basic, components are CNC machined (HAAS, Office Mill) to allow for the necessary materials; however, the remaining complex components, seen in white in Fig. 2.2, are first 3D printed (Invision HR) and then replicated in a polyurethane, TC-892 (BJB Enterprises), through soft molding (Appendix E). This molding process allows for the creation of components which otherwise would be impossible to create, as individual pieces, as the part can be removed by deformation of the mold. This process facilitates the increase in component functionality while reducing robot cost; the full mass breakdown can be seen in Table 2.1. The body is designed with sufficient space around the internal energy storage components for on-board battery and control electronics. The major components are connected as follows, the four-bar legs attach to the shoulders which in turn attach to the protrusions on the body, as seen in Fig. 2.5. The compression cable is routed from the internal energy storage mechanism into the protrusions on the body and out through small slits. It is then passed through the small hole in the top of the shoulder and continues through the center of the springs and attaches at the foot of the robot. This routing of the com-

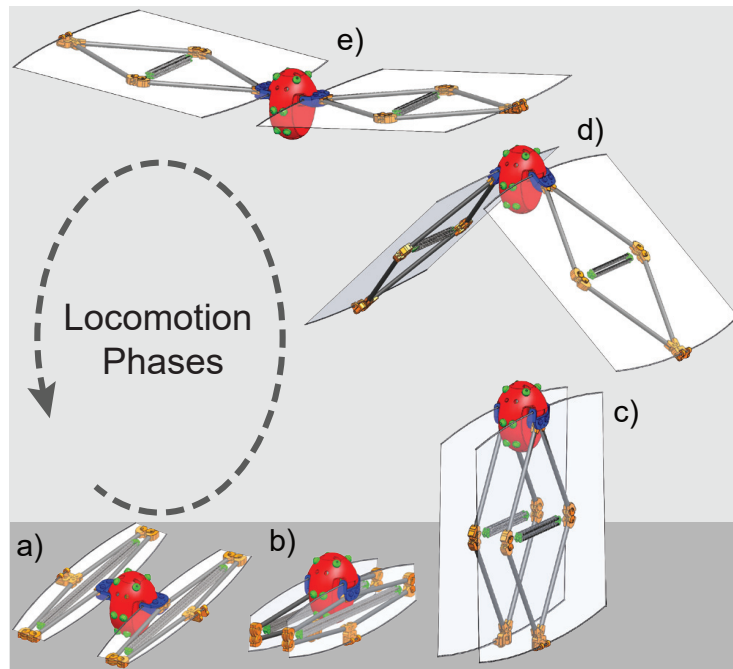


Figure 2.6: Schematic of the operation phases of the MultiMo-Bat: **a)** four-bar legs compressed, **b)** four-bar legs reconfigured for jumping, **c)** lift-off, **d)** four-bar legs reconfiguring for gliding, and **e)** gliding. The **energy storage** phase begins when **(e)** lands and continues until the legs are reoriented for jumping **(b)**. The **jumping phase** begins at **(b)** and ends at lift-off **(c)**. The **coast phase** begins at lift-off **(c)** and continues until the wings are fully deployed **(e)**. Followed finally by the **gliding phase** **(e)** which continues until the robot lands. This process is repeated for locomotion.

pression cable constrains it to the plane of the legs which ensures the compression force produces no moment on the four-bar.

### 2.3.1 Phases of Operation

The proposed design results in four phases of operation: energy storage, jump, coast, and glide which are repeated for locomotion; as in Fig. 2.6 (see video at [158]).

#### Energy Storage Phase

The energy storage phase mainly consists of the accumulation of energy in the main power springs through the compression of the four-bar legs, as seen in Fig. 2.6. In addition, due to a leg offset shown in Fig. 2.3b, the leg compression process also produces a torque around the

shoulder joint which reconfigures the legs for jumping. Using the same actuation force created by the energy storage mechanism thereby minimizes the required mass necessary for these two tasks. Once the energy is completely stored, the system is then prepared for the jumping phase.

### **Jump Phase**

The jumping phase utilizes the four-bar to transfer the spring force to the ground, as seen in Fig. 2.6. This phase employs an passive configuration change in the wing structure due to the integration level of the modes. The wings are initially fully collapsed and extend throughout the jumping phase, however, they remain parallel to the flow, significantly reducing drag and thus minimizing the negative effects of the added structure. Shown in Fig. 2.3c the legs are mounted such that they exert a combined force directly through the center of mass (COM) of the entire system. This restricts the force generated by the legs from generating a torque about the COM, improving the system efficiency and performance by not wasting energy on undesired motions. The off-axis mounting of the leg, discussed in the energy storage phase, also results in a torque about the Joint 5 axis, in the jump phase, that restricts the leg to the jumping configuration while the legs are applying a force to the ground. This reduces the possibility of a premature configuration change while in the jump phase.

### **Coast Phase**

The coast phase is responsible for the passive transition from the jumping configuration to the gliding configuration, as seen in Fig. 2.6. During the coast phase the wings are fully extended but they are beside the body parallel to the flow. As the robot leaves the ground a small amount of energy remains in the main power springs. This energy is used to tension the airfoils and therefore reduce flutter which decreases drag on the robot during the coast phase. This configuration also provides stability to the coast phase by generating a restoring moment to any rotations of the body, resulting in stabilization about the velocity vector of the robot. The shoulder, Joint 5, has two competing torques acting on it throughout the locomotion process; one created by force on

the foot and a second by a small elastic element which acts in opposition. During the coasting and gliding phases, when the foot force is zero, the total torque switches direction and it biases the stable state of the legs to the gliding configuration. Once the robot reaches the apex of the jump trajectory and the vertical velocity vector switches direction the combination of the torque at Joint 5 and increasing drag on the underside of the airfoils results in the transition to the gliding phase.

### **Glide Phase**

During the glide phase, as seen in Fig. 2.6, the four-bar legs are held at an elevated angle above horizontal to increase the lateral stability [145]. The four-bar joints also allow more flexibility in the out-of-plane direction, discussed further in the following chapter, further increasing stability by reducing the sensitivity of the wings to oscillations in airflow. The glide phase also reduces the kinetic energy of the robot before it contacts the ground resulting in lower required strength and therefore weight which, due to the high level of coupling, results in performance improvements for both modes.

## **2.4 Locomotion Mode Coupling**

The use of multiple locomotion modes inherently causes interactions between the modes which will affect the overall performance of the system. This is because the performance of each mode becomes coupled to the others. The combination of locomotion modes always results in some degree of performance coupling thereby increasing the complexity of the design process as changes to one mode will affect the other. Therefore, it is important to understand the types of coupling that exist and how they relate to the development of the system. The coupling can be broken up into three coupling parameters: inertial, energy, and structural.

1. The **inertial coupling parameter (ICP)** deals with the effect of added mass on the performance of the other modes. This coupling parameter always affects both modes as changes

to the mass of either mode affects the inertia of the entire system. This parameter tends to reduce the mobility of the system as increasing inertia increases the systems resistance to changes in its state of motion; the acceleration magnitudes are related to the mass as follows

$$\begin{aligned}\ddot{x} &\propto \frac{\sum F}{m} \implies (m \uparrow = \ddot{x} \downarrow) \\ \ddot{\theta} &\propto \frac{\sum M}{I} \implies (I \uparrow = \ddot{\theta} \downarrow)\end{aligned}\tag{2.1}$$

where  $x$  is a linear direction with  $F$  as a linear force and  $m$  is the mass. In the angular direction  $\theta$ ,  $M$  is an applied moment, and  $I$  is the moment of inertia.

2. The **energy coupling parameter (ECP)** captures the affect of modifications to the actuation, energy, and energy storage systems on the performance of the other modes. However, unlike the ICP, the ECP may be positive, negative, or zero indicating that the modifications increase, decrease, or have no effect on the energy of the other mode.
  
3. The **structural coupling parameter (SCP)** includes the effect that the structural modifications or non-shared structure of each mode has on the performance of other modes. This parameter is designed to catch all remaining variations in performance and should be determined through experimentation so as to ensure all relevant dynamics are captured. Just as the ECP can be positive, negative, or zero so to can the SCP.

As integration is most importantly a method for preserving the performance through the sharing of components between locomotion modes, integration tends to minimize the inertial coupling parameter (ICP). However the ECP and SCP are high dependent on the integration strategy implemented and, having the potential to be positive, negative, or zero, should be further analyzed for their role in the performance of the overall system.

Since integration already reduces the ICP, further mass reduction is difficult. Therefore, to isolate the ECP and SCP we assume the mass and its distribution remains constant or within negligible limits, thus the inertial coupling parameter (ICP) remains constant. Subsequently, since both the energy (ECP) and structural (SCP) coupling parameters have the potential to be zero, there may exist regions in the design space of the robot where the modes can be separated and their performance addressed independently. However, since the ECP and SCP can also be positive, the combination of the locomotion mode can create performance greater than the sum of the parts. Finally, these parameters can be considered at several levels depending on the detail required. Applied at the component level during development, they can highlight regions as discussed above however; applied at the full system level, they can be used to determine where the major changes in performance are coming from and where further performance gains may be achieved (discussed in Section 2.8). The use of the coupling parameters will be illustrated further in the following subsections which discuss some of the major coupling within the MultiMo-Bat.

### **2.4.1 MultiMo-Bat Coupling**

Jumping being the primary locomotion mode provides the initial kinetic and potential energy for the gliding mode. This integration relationship results in significant energy coupling between the jumping and gliding locomotion modes in relation to the energy state of the system at the transition from jumping to gliding. This dictates that changes to the jumping performance inherently cause changes in the gliding performance. This is an example of indirect coupling as it does not affect the mode during operation. Therefore, preservation of the jumping mode performance should be strongly considered during the development of the integrated gliding mode.

The integration level of the jumping and gliding modes is similar to that of the vampire bat, where the jumping structure will be used in conjunction with additional components to generate the gliding locomotion mode. Therefore, the jumping structure should accommodate the necessary components required for the gliding mode without a significant reduction in jumping performance. This results in potentially high structural coupling between the modes, however,

because there are components that are not utilized by both modes, there must exist uncoupled or minimally coupled regions of the design space, such as:

### **Four-bar Leg**

The coupling of the four-bar leg is examined as it is the primary structure of both modes and has a significant effect over their performance. This can be broken into three subcategories: main power springs, four-bar leg links, and mechanism dynamics.

The main power springs, mounted to the knee joints, have a significant effect over the jumping and, indirectly, over the gliding performance, therefore it is desirable to increase their stored energy. Once gliding is initiated the spring size and configuration results in little effect over the gliding performance; therefore, assuming this remains constant, the ECP and SCP of the gliding mode remain zero. Assuming an optimal spring design, discussed in the Section 2.5.4, any increase in the ICP will be compensated for by increases in energy storage. Therefore, the energy storage capacity of the main power springs, within the assumptions, can be enhanced independent of the gliding locomotion mode.

The link lengths of the four-bar legs have a significant effect on the gliding performance as they constrain the wing size; increasing the length allows for a larger supported wing span. However, longer legs, results in higher leg inertia and lower lift-off velocities if the energy is held constant. Therefore, assuming the energy stored is increased with leg length to compensate for the added inertia the link lengths are uncoupled from the jumping mode allowing for adjustment to suit the needs of the gliding mode; discussed further in Section 2.5.2.

Finally, the system dynamics (Sections 2.5.1 and 2.5.2) results in a maximum leg angle of approximately 60 degrees before the leg angle at lift-off diverges from the initial leg angle required to mount the main power springs (spring free length angle). This divergence represents energy which can not be used for jumping as the system will have left the ground before it can be delivered. However, this is therefore an uncoupled region where the energy stored above 60 degrees can be used for the gliding locomotion mode.

## **Wing Membranes**

The wing membranes are an integral part of the gliding locomotion mode; however they have the potential to significantly degrade the performance of the jumping mode. To uncouple the design of the wing membranes, the following properties must be upheld: added mass remains relatively constant, main power springs are unaffected, collapsed airfoil shape remains relatively constant, and extended airfoils are parallel to the flow. These assumptions result in a relatively constant ICP and negligible direct ECP and SCP. This region encompasses a wide range of airfoil shapes and sizes allowing for enhancement of the gliding mode's performance, independent of the jumping mode. The wing membranes held parallel to the flow creates an effective tail and thus increases coast phase stability, which in turn enhances the robustness of the passive transition between jumping and gliding. This is a good example of a positive component level SCP, which benefits both modes.

## **Internal Energy Storage Mechanism**

Since the internal energy storage mechanism exists within the body structure they will not have any effect on the ECP or SCP of the gliding mode resulting in zero values. Therefore, the only constraint on the internal components is the allowable variation in the ICP which should be minimized while maximizing the energy storage capability of the jumping mode.

## **2.5 Jumping Mode**

The design concept of the MultiMo-Bat relies heavily on the performance of the primary mode, jumping, to supply the needed energy for gliding. Therefore, within the confines of the integrated design strategy, the jumping dynamics, four-bar leg design, joint design, and energy storage mechanisms will be examined further to elucidate trends and enhance performance of the jumping mode.

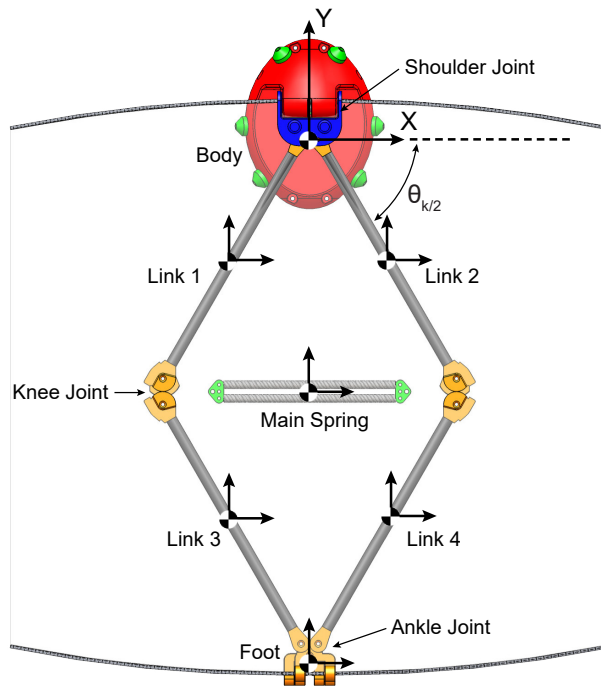


Figure 2.7: The masses considered for the single DOF and 6 DOF models are shown along with the leg angle used for the simulations.

## 2.5.1 Jumping Dynamic Model

To develop the jumping locomotion mode the underlying dynamics are derived to explore any mechanism specific traits important for development. The most fundamental question is whether the four-bar leg remains in contact with the substrate long enough to achieve the desired jumping performance. A single degree-of-freedom (DOF) model of the complete system allows for further analysis and refinement of the jumping phase of operation.

### Single Degree-of-Freedom Model

The single DOF model contains all components of the four-bar, spring, and body, each modeled as separate components contributing to the overall system dynamics; as seen in Fig. 2.7. This model assumes the system only moves in the  $z$ -direction however; this assumption does not significantly reduce the applicability of the resulting dynamics to the real system, as the four-bar leg generally restricts the motion to the  $z$ -direction. The kinetic,  $T_{(B,S,F)}$ , and potential,  $V_{(S,A)}$ ,

energies

$$T_{(B,S,F)} = \left( \frac{1}{2} M (\vec{v} \cdot \vec{v}) \right), V_{(S,A)} = \left( \frac{1}{2} k (\vec{\delta} \cdot \vec{\delta}) \right). \quad (2.2)$$

of the body  $M_B$ , two power springs  $M_S$  and  $k_S$ , two absorbing springs  $k_A$ , and two feet  $M_F$  are considered first. Next, the kinetic energy of the legs both in translation and rotation can be written as

$$T_{LTrans.} = \left( \frac{1}{2} m_L \sum_{i=1}^4 (\vec{v}_i \cdot \vec{v}_i) \right), T_{LRot.} = \left( \frac{1}{2} I_L \sum_{i=1}^4 (\vec{\omega}_i \cdot \vec{\omega}_i) \right) \quad (2.3)$$

respectively; where  $m_L$  and  $I_L$  are the leg mass and moment of inertia. The linear velocity vector  $\vec{v}$  and the angular velocity vector  $\vec{\omega}$  are defined at the COM of their respective components.

Once the inertial effects are accounted for it is necessary to fully develop the dynamics by considering the area effects. The area effects should be considered to understand their contribution to the overall performance and therefore the significance of specific system parameters. The force on the body due to air drag is found by using the standard drag model

$$F_{DB} = \left( \frac{1}{2} C_D \rho A_{EB} v_B^2 \right) \quad (2.4)$$

where  $C_D$ ,  $\rho$ , and  $A_E$  are the drag coefficient, the density of air, and the effective area respectively. The effective area  $A_E$  is computed as the area of the body projected on the plane normal to the direction of motion. The drag contribution of the legs

$$\begin{aligned} F_{DLTrans} &= \left( \frac{1}{2} C_D \rho \sum_{i=1}^4 A_{EL} v_i^2 \right), \\ F_{DLRot} &= \left( \frac{1}{2} C_D \rho \sum_{i=1}^4 \int_0^L A_{EL} v_i^2 dx \right) \end{aligned} \quad (2.5)$$

requires the consideration of both their translational  $F_{DLTrans}$  and rotational  $F_{DLRot}$  velocities. The effective area in the translational component is a function of the leg angle and the velocity vector and the rotational component is a function of both the position on the leg and the angular velocity.

This results in the equation of motion of the system,

$$\begin{aligned}
& \left[ (2M_B + M_S + 5m_L) \cot \theta_{k/2} + m_L \tan \theta_{k/2} + \left( \frac{4I_L}{L^2 \cos \theta_{k/2} \sin \theta_{k/2}} \right) \right] \ddot{\theta}_{k/2} \\
& - [2M_B + M_S + 4m_L] \dot{\theta}_{k/2}^2 \\
& - \left[ \sum_{i=1}^2 k_{k/2i} \left( 2 - \frac{x(0)_{k/2i}}{L \cos \theta_{k/2}} \right) + 2k_A \left( 2l^2 - \frac{lx(0)_A}{L \cos \theta_{k/2}} \right) \right] \\
& = \left[ \frac{1}{2L^2 \cos \theta_{k/2} \sin \theta_{k/2}} \right] Q_k
\end{aligned} \tag{2.6}$$

where  $\theta_{k/2}$  is the leg angle that is measured from compression (0 degrees) to extension (90 degrees), and the masses of the body, springs, and legs are represented by  $M_B$ ,  $M_S$ , and  $M_L$ , respectively. The leg length and moment of inertia are represented by  $L$  and  $I_L$ , respectively; full compression of the legs results in an angle,  $\theta_{k/2}$ , of approximately 5 degrees for maximum jumping energy. Finally, the main power springs and absorbing springs are represented by their spring constants,  $k_{k/2i}$  and  $k_A$ , and free lengths,  $x(0)_{k/2i}$  and  $x(0)_A$ , respectively. The non-conservative forces are represented by  $Q_k$  which includes the form drag of all the components; however, due to the difficulty in modeling all the non-conservative forces, friction has been omitted from the model. An approximation has been created based on material properties and forces between the ankle joint components - this is the only joint in the four-bar mechanism that exhibits sliding between the joint surfaces - resulting in a contribution on the order of 0.01 m/s to the lift-off velocity. All the joints in the four-bar mechanism experience friction, due to the connecting structures, as well as the cable and components of the internal energy storage mechanism however, explicit calculation of these values is difficult to achieve accurately.

Solving the equation of motion numerically produces the jump profile shown in Fig. 2.8, where the body velocity is related to  $\theta_{k/2}$  by  $v_B = 2L\dot{\theta}_{k/2} \sin(\theta_{k/2})$ . The body velocity and acceleration represent only the body structure which, due to conservation of momentum, results in a lower lift-off velocity as this value includes the mass of the entire system. Lift-off of the system occurs when the body acceleration becomes negative which indicates that the body is applying tension to the ground-foot interface. The acceleration is also shown to be positive

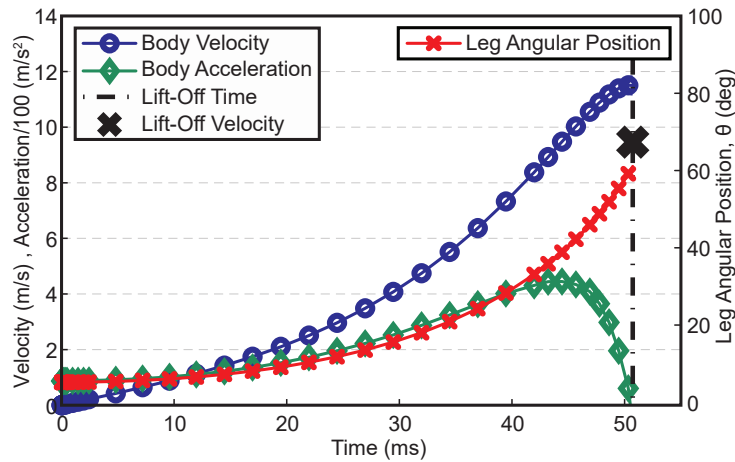


Figure 2.8: Dynamic simulation of the leg showing lift-off time and velocity in relation to body and leg states for the MultiMo-Bat. Leg position is shown on the right axis. Robot parameters  $M_B = 78.08$  g,  $M_S = 13.12$  g,  $M_F = 1.7$  g,  $M_L = 2.63$  g,  $L = 135.8$  mm,  $I_L = 40$  g cm<sup>2</sup>,  $k_{k/2,2} = 291.2$  N/m,  $x(0)_{k/2,2} = 123.9$  mm.

and smooth over the leg angle interval of 0 to approximately 60 degrees. Therefore, to increase efficiency, the main power springs should transfer all potential energy before this angular position is reached as the legs will no longer be in contact with the ground. However, small amounts of energy stored above 60 degrees can be used for other purposes and/or locomotion modes.

### Massless Components

To explore the dynamic relationship between the component masses and the total system mass, the simplified 1-DOF model consists of only the body, while all other components are assumed massless and the non-conservative forces are neglected. The simplified model shows behavior very similar to the multi-body 1-DOF simulation, however, with a shallowing of the velocity curve and a decrease in the lift-off time (Fig.F 2.9). Analysis of all the factors shows that the massless component assumption affects the shape of the velocity curve and the lift-off time, without significantly affecting the lift-off velocity. The inertia of the leg members stretches out the velocity curve however, since no energy is dissipated, the lift-off velocity should remain the same. The fiction however, only has a significant effect on the lift-off velocity and to a less extent the lift-off time. Finally, the drag component contributes very little to the overall system

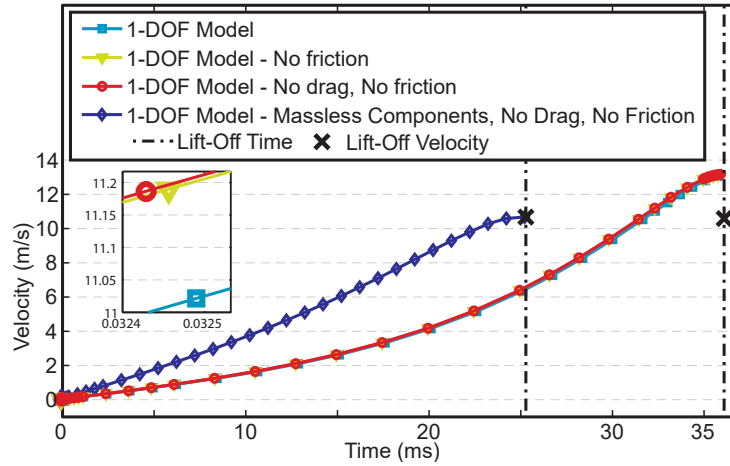


Figure 2.9: Showing the simulated comparison of the multi-body single DOF (1-DOF) and simplified 1-DOF velocity curves. The breakout section shows the difference between the multi-body 1-DOF models.

dynamics.

## Results and Discussion

The simulation was then evaluated by experimental trials of an initial proof-of-concept robot (Appendix A), yielding lift-off velocities of approximately 1.3 m/s slower than the simulation. The difference is therefore caused by the unmodeled friction in the cable system, joint connecting structures, and variability in the energy storage. However, the model provides sufficient detail to analyze the dynamic characteristics of the four-bar leg during jumping.

### 2.5.2 Four-bar Leg Dynamics

The second subsystem, the four-bar leg (Fig. 2.10a), is integral to both modes and is responsible, in the context of energy storage, for the mounting of the main power springs as well as the delivery of the jumping force to the ground. A sensitivity analysis of the multi-body single DOF model, equation 2.6, parameters yields important mechanism specific scaling relationships. The two major parameters of the four-bar dynamics are the length of the leg links and the free length of the main power springs.

To determine the dynamic affect of the main power spring's free length to the jumping mode,

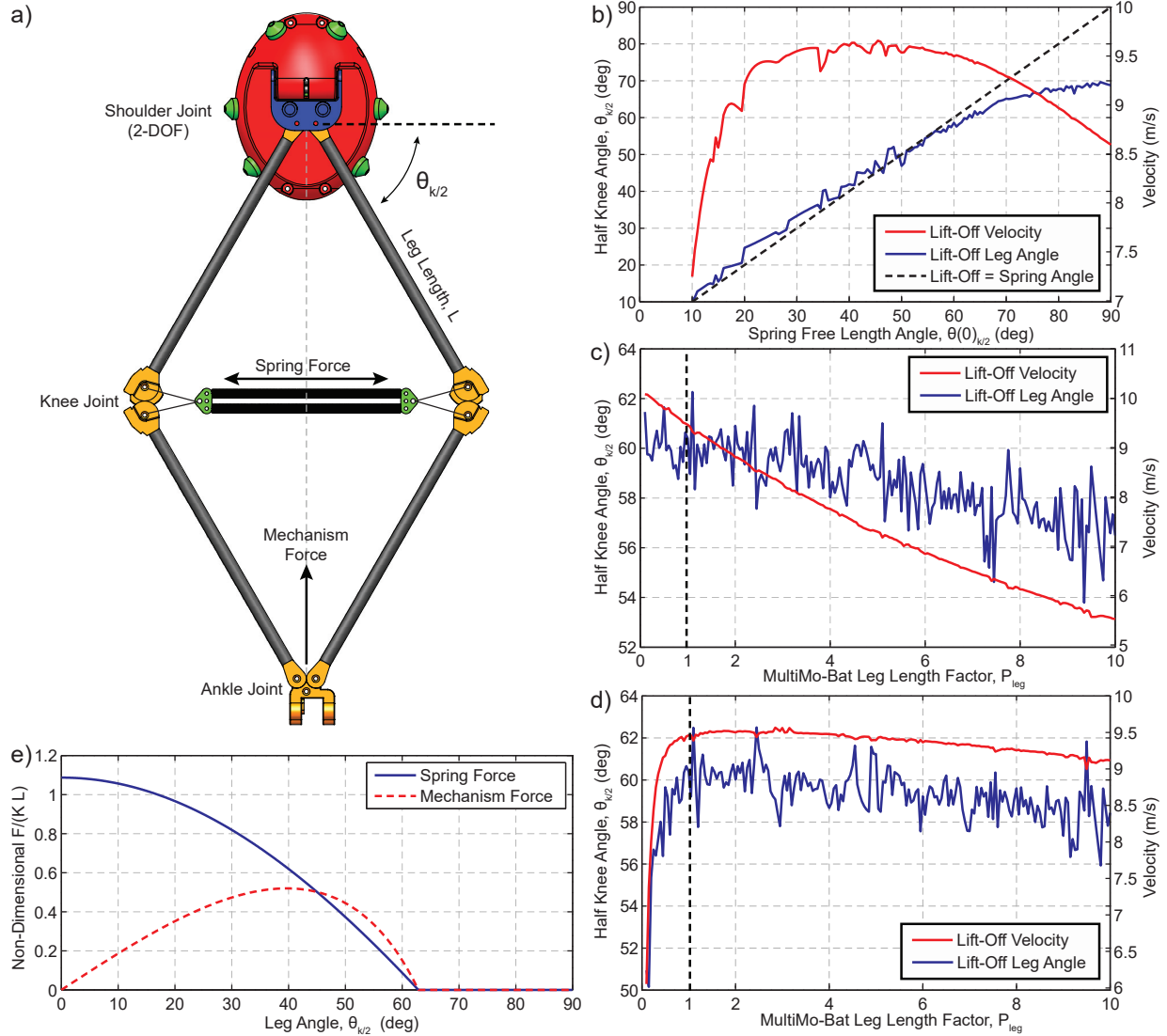


Figure 2.10: **a)** The MultiMo-Bat's four-bar leg design with an initial leg link length of 135.8 mm. **b)** The leg angle and robot velocity at lift-off are numerically calculated for spring free length angles of  $\theta(0)_{k/2_i} \in [0, 90]$  degrees. **c)** The leg angle and robot velocity at lift-off are numerically calculated for leg length factors of  $P_{leg} \in [0.1, 10.0]$  of the MultiMo-Bat. The stored energy and spring free length angle are held constant. **d)** The leg angle and robot velocity at lift-off are numerically calculated for leg length factors of  $P_{leg} \in [0.1, 10.0]$  of the MultiMo-Bat. The stored energy, spring free length angle, leg mass, and leg inertia are held constant. **e)** The mechanical advantage of the mechanism shown in dimensionless form, where the forces are shown in (a).

the stored energy in the springs and the leg link lengths are held constant while the spring free length is varied, as seen in Fig. 2.10b. The free length of the main power springs can be calculated as  $x(0)_{k/2_i} = 2L \cos(\theta(0)_{k/2_i})$  where  $\theta(0)_{k/2_i}$  is the angle at which the spring begins tensioning.

This is a convenient representation of the spring length as they must fit within the four-bar; therefore, the possible free lengths are bounded by  $\theta(0)_{k/2_i} \in [0, 90]$  degrees. The optimal value is found to be 45 degrees however the lift-off velocities are relatively constant over  $\theta(0)_{k/2_i} \in [30, 55]$  degrees. This allows for a larger extended length of the four-bar which, due to the integration strategy, benefits the gliding locomotion mode as the span-wise length of the wing is dependent on the extended length of the four-bar leg. After the 45 degree position, the drop off in initial velocity is due to premature lift-off of the system resulting in a portion of the energy stored being released after the system has left the ground. Finally, the dynamics of the mechanism limit the maximum achievable lift-off angle to approximately 70 degrees.

To determine the dynamic affect of the length,  $L$ , of the leg links, the stored energy and the free length angle of the springs are held constant while the leg link length is varied, as seen in Fig. 2.10c. For this analysis the mass and rotational inertia of the legs is a function of the link length. A shorter link length results in a significant reduction in link's rotational inertia,  $I_L = \frac{m_L L^2}{12}$ , which from the dynamic behavior favors shorter link lengths to increase initial velocity given constant potential energy. To isolate the length property, the analysis is then conducted with the mass and rotational inertia of the leg links held constant. As seen in Fig. 2.10d, the mechanism dynamics still play a role as the initial velocity varies over the range but far less significantly than the inertial effects of the leg links. Therefore, the best performance is achieved by minimizing the leg link's mass and rotational inertia.

The four-bar parameters selected for the MultiMo-Bat are a leg link length of  $L = 135.8$  mm and a spring free length angle  $\theta(0)_{k/2_i}$  of 62.9 degrees. The spring free length angle was first selected as it resulted in a minor drop in the initial lift-off velocity while providing a large mounting length for the wing membrane. Since lift-off for these parameters occurs at approximately 60 degrees, the additional few degrees of stored energy can be reserved for tensioning the wing. The selected link length creates a wing span of over 254 mm.

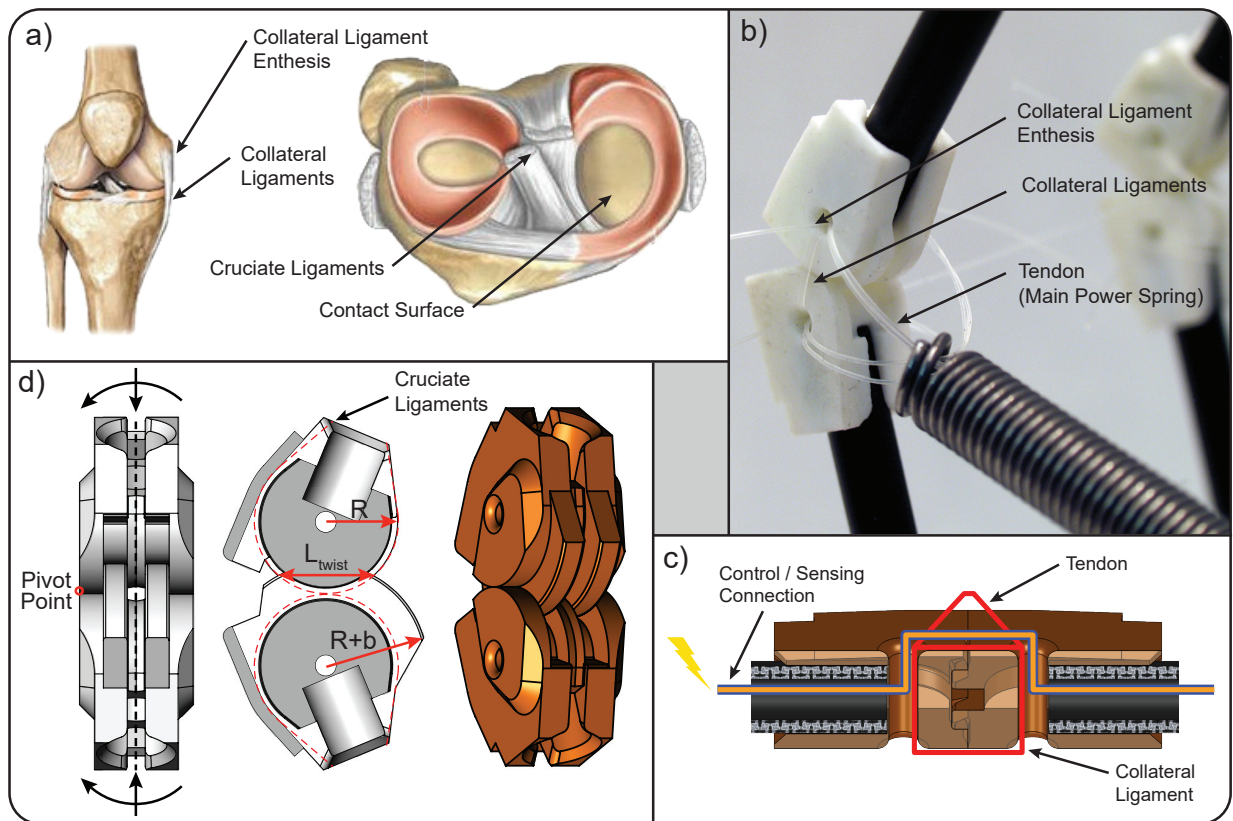


Figure 2.11: **a)** The knee joint is inspired by the human knee. **b)** The joints have high strength, low mass (1.1 g), and high twist resistance. **c)** The joints can support the routing of sensors wires and attachment cables. **d)** Second generation joint (1.3 g). Joint showing the pivot point and forces during out-of-plane deflections and the twist resistance features.

### 2.5.3 Biologically Inspired Joint Design

To physically realize the four-bar leg, a joint is necessary which is capable of withstanding and transmitting high compressive loads in the plane of the four-bar. This requires a very stiff in-plane structure while allowing for out-of-plane flexibility which is beneficial during the gliding locomotion mode. The out-of-plane flexibility can reduce the sensitivity of the wings to oscillations in airflow thus creating a more stable platform. It also can be beneficial during landing or collisions with other objects while in the gliding phase as it can absorb energy reducing the impulse on the system and therefore reducing the possibility of damage to the robot.

The joint design is inspired by the morphology of the mammalian knee or more specifically the human knee, Fig. 2.11a, as this joint is well suited for transmitting high compressive loads.

However, the structures which transmit compressive loads are separate from those which transmit tension and out-of-plane torsional loads. Compressive loads are transmitted through the major bones of the knee, the femur and tibia, which meet at roughly a cylinder-cylinder type contact over a large percentage of the width of the knee. This creates a very stiff structure with the load distributed over a large area, which can efficiently transfer compressive loads with low contact stress. The tension and out-of-plane torsional loads are transmitted through ligaments, primarily the medial and lateral collateral ligaments. This allows for independent control over the stiffness of the joint as it relates to the different loading conditions.

The two components of the joint meet with cylinder-cylinder contact at an equal radius from their respective centers, as seen in Fig. 2.11b. The contact length is between 42% and 84% of the joint width, depending on the load, which reduces the stress over the interface. The forces are also in direct opposition further enhancing the strength. The joints are designed to not only withstand high compressive forces, but also to restrict the compliance of the structure in and out-of-plane when the legs are under load while still allowing flexibility in the out-of-plane directions as the load is reduced. This is achieved by the off center pivot point, as seen in Figure 2.11d, of the joint during out-of-plane deflection resulting in increased resistive torque with increased compressive load. Therefore, during the jumping phase, the joint provides extra resistance to out-of-plane deflections; however, during gliding phase, the compressive load is zero resulting in lower overall joint stiffness.

A cable is wrapped through the two connection holes, as seen in Fig. 2.11c, which holds the two joint components together. These points are at the rotational center, resulting in no change in length during joint rotation. These holes are also used for mounting the main power springs and therefore must withstand significant loads. The edge of the connection hole is tangent to the face of the leg link resulting in a very low rotational moment on the carbon fiber leg tube (Goodwinds, XL Breeze, O.D. 0.198in). This coupled with the molded polyurethane joint helps reduce stress concentrations at the leg-joint interface increasing robustness of the overall structure.

Finally, twisting of the leg structure is undesirable in all phases of operation therefore, twist ridges are integrated into the design to eliminate this possibility. The moment arm length created by the overlapping ridges determines the twist resistance and can be calculated as

$$L_{twist} = R \sin \left( \cos^{-1} \left( 1 - \frac{2Rb + b^2}{4R^2} \right) \right) \quad (2.7)$$

where  $R$  is the joint contact radius and  $b$  is the twist ridge height (Fig. 2.11d). Also, a longer length results in lower stress at the contact points which is beneficial for polymer based components.

The design also allows for several other unique features. First, the joints are designed for direct cable base sliding restriction or actuation. Just as the posterior and anterior cruciate ligaments in the knee restrict sliding of the joint in the plane of the leg, cables can be routed in a similar fashion to achieve the same effect, as seen in Fig. 2.11d. Actuation can then be achieved by applying a force to these cables. Second, due to the position of the connection hole and the open end of the carbon fiber leg tube, a wire can be run within the entire structure, protecting it from the environment, allowing for the integration of sensors and/or actuators along the four-bar leg and wing. Finally, the joint is designed to be manufactured by soft molding, discussed in the Appendix E, or 3D printing which reduces the cost of manufacturing.

## 2.5.4 Energy Storage Mechanism

The most challenging components in miniature robotic platforms are the actuation and energy systems because of their size, weight, power transmission, and performance characteristics. These issues tend to significantly reduce the overall robot performance. The MultiMo-Bat has an even more challenging configuration due to its insect inspired jumping behavior, known as a catapult jump. It must not only have a high power actuation system but also a high energy storage system and rapid release mechanism. Jumping and gliding modes have high inertial coupling (ICP) because increasing mass significantly affects the performance of both modes. Therefore, to preserve performance, it is important for the components of the energy storage mechanism

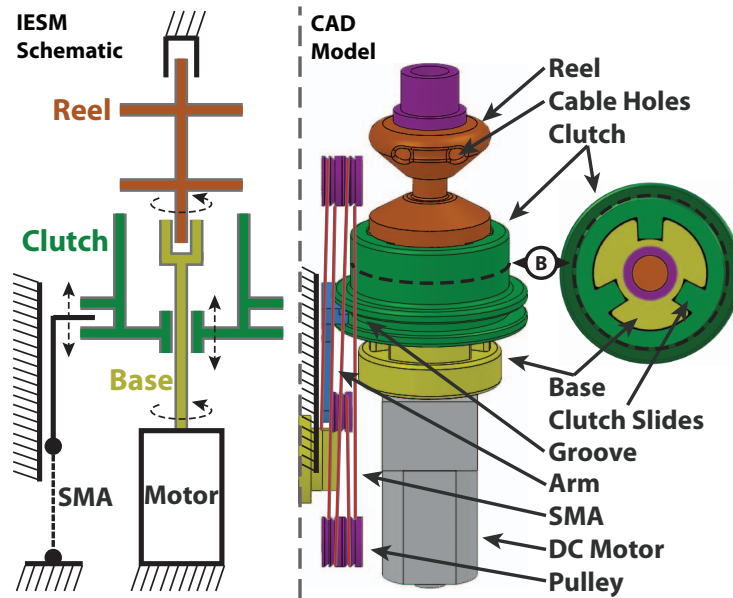


Figure 2.12: The internal energy storage mechanism (IESM) is shown in schematic form to illustrate the joints and the mounting/fixed points of the mechanism. A CAD model of the mechanism is shown with the components labeled; which includes the SMA mounting pulleys used for extending the actuator's resulting stroke length. Cross-section **B** shows the clutch slides.

be lightweight and small. To increase mobility, the stored energy should be capable of being actively released at any point in the energy storage phase. This provides not only the possibility for control over the amount of energy stored but also precise control over when it is released. The energy storage mechanism of the MultiMo-Bat can be separated into and discussed as three distinct subsystems. First, the internal mechanism (Fig. 2.5) is responsible for supplying the input energy and force necessary to compress the legs. The second subsystem is the four-bar leg which provides the mounting and support for the main power springs. The last subsystem is the main power springs themselves, which are responsible for storing the jumping energy of the system.

### Internal Energy Storage Mechanism

The internal mechanism, as seen in Fig. 2.12 and integrated into the system in Fig. 2.5, has four main components: the base, reel, clutch, and actuator. The base attaches directly to a highly geared 298:1 DC motor (Solarbotics GM14a - Previous Edition) which can generate 0.317 Nm of

torque at 6 V. The connections of the base, clutch, and reel are illustrated in Fig. 2.12. Integrated into the base structure are slides which allow the clutch component to slide along the axis of the motor while constraining rotation allowing the torque of the motor to be transferred to the clutch, as seen in cross-section **B** of Fig. 2.12. The clutch component, in addition to the slides, also has a circular groove around the external surface in which the actuator arm rests. This groove allows the actuator to remain stationary while the rest of the mechanism rotates, facilitating electrical connection and actuator mounting. The actuator is composed of the arm, which connects it to the clutch, the nickel titanium shape memory alloy (SMA) wire, which produces the motion, and pulleys used to extend the SMA length. The SMA (DynaAlloy, Flexinol) has a diameter of 203  $\mu\text{m}$ , a transition temperature of 70°C, and a maximum strain of 5% producing approximately 11.5 N of force to disengage the clutch. The arm is integrated into the overall design such that it is constrained to only a single translational DOF along the  $z$ -axis. The bottom of the arm has a Polytetrafluoroethylene (PTFE - Teflon) pulley which acts as the mounting point for the SMA. The remaining pulley mounts are integrated into the body of the robot. The pulleys are used to extend the length of the SMA to achieve the desired actuator stroke of 4 mm. Because of variation in the SMA characteristics and inconsistencies in the manufacturing process, a safety factor of around 2 is necessary to ensure the desired stroke is achieved. This results in a minimum SMA length of 160 mm which is approximately twice the length of the largest body dimension. To withstand the SMA transition temperature and maximize performance of the actuator, PTFE was chosen for its high operating temperature and low coefficient of friction. The final component is the reel which is responsible for winding up the leg compression cable and increasing the force produced by the motor. The reel mounting can be seen in Fig. 2.12. When engaged, the clutch slides fit into the slides of the reel linking the two components together; on release, the clutch moves down and the reel is decoupled and allowed to free spin releasing the stored energy. The two cable holes at the top (Fig. 2.12) allow the cable to be passed through rather than tied and consequently the final tensioning can be completed once the entire robot is assembled resulting in

accurate and symmetric initial leg tension. As multiple cables are used this feature also allows the force between cables to be equalized. The reel has a radius of 2.15 mm which further increases the cable force to approximately 147 N, assuming 6 V operation, or 73 N per leg at the output of the internal energy storage mechanism.

### **Four-bar Leg**

The four-bar leg also produces a beneficial variable mechanical advantage to the energy storage system utilized for both increasing the amount of energy stored and holding that energy until the jump is initiated, as seen in Fig. 2.10e. The additional effective mechanical advantage is equal to approximately 2, resulting in a maximum approximate force of 147 N per leg to extend the main power springs. However, the energy can be held efficiently because the mechanism force approaches zero at full extension requiring only the back driving friction of the mechanism to hold the legs in place until the jump is initiated.

### **Main Power Spring Design**

The high performance jumping mode of the MultiMo-Bat requires large energy storage springs which consequently contribute to a significant portion of the robot mass. The high inertial coupling (ICP) results in mass having a significant effect on the performance of the jumping mode and to a greater extent the gliding mode. It is therefore, necessary to understand if energy density can be maximized. Several spring materials were initially considered for the energy storage medium including metals, elastomers, and composites. Elastomers were ruled out due to their low durability and robustness especially when exposed to the elements and under sustained strains. Composite springs may be interesting for further study however the difficulty and expenses of their fabrication ruled them out for this prototype leaving helical extension spring as the feasible option. Helical extension springs are typically thought of as a torsionally loaded rod which has a constant energy density as a function of the rod diameter. However, two subtle differences between the torsional rod model and a helical spring create a situation where energy

density is variable. The first difference is with the assumption that the bulk material properties remain constant. In fact as the wire diameter decreases, the yield strength,  $S_{ys}$ , of the material increases, approaching the theoretical yield strength, because larger cross-sections have a higher probability of more significant defects. Second, the coiling of the rod into a spring increases the asymmetry of the cross-sectional stress. Therefore, we would like to find a set of equations which maximizes energy density given the application variables, which are: extension length,  $y$ , maximum mounting length,  $L_m$ , desired energy,  $E$ , and the number of springs,  $n$ .

To achieve optimal spring design two closed form equations are derived in Appendix B, from the standard spring design equations, which relate the constraints of the system to the spring parameters. First, the mean coil diameter,  $D$ , is defined by two constraining features, the spring extension,  $y$ , and the maximum mounting length of the spring,  $L_m$ , along with a reduction factor,  $\lambda = 1 \rightarrow 0$ , which reduces the free length of the spring to a percentage of the available mounting length. Therefore, eq. 2.8 can effectively bracket the possible  $D$  and  $d$  values to those within the  $D(\lambda = 1 \rightarrow 0)$  region. The region can be further reduced by increasing the lower bound of  $\lambda$ ; Fig. 2.13 shows lower bounds at  $\lambda = 0.5$  and  $\lambda = 0.75$ .

$$D_1 = \frac{d}{4} + \frac{\sqrt{C_1 + C_2 + 150d^2}}{20\sqrt{6}} + \frac{\sqrt{2C_1 - C_2 + 300d^2 + \frac{3\sqrt{3}d(173C_1 + 10^4d^2)}{10\sqrt{2}\sqrt{C_1 + C_2 + 150d^2}}}}{20\sqrt{6}} \quad (2.8)$$

$$C_1 = \frac{400GL_r d^2}{\pi S_{ys}}, \quad C_2 = \frac{10^{1/3} \left( 10^{1/3} C_3^2 + 20GL_r d^4 (200GL_r + 1257\pi S_{ys}) \right)}{\pi C_3 S_{ys}} \quad (2.9)$$

$$C_3 = \left( GL_r d^6 \left( -8(10^4)G^2 L_r^2 + 2.046(10^6)GL_r \pi S_{ys} + 6.642(10^5)\pi^2 S_{ys}^2 \right) - 3GL_r d^6 \sqrt{3\pi S_{ys}} \right. \\ \left. \sqrt{-1.66(10^{10})G^3 L_r^3 + 1.231(10^{11})G^2 L_r^2 \pi S_{ys} + 4.184(10^{10})GL_r \pi^2 S_{ys}^2 + 1.634(10^{10})\pi^3 S_{ys}^3} \right)^{1/3}$$

where  $L_r = y/(L_m \lambda)$  is the length ratio and  $G$  is the shear modulus. The mean coil diameter,  $D$ ,

is then related to the desired energy,  $E$ , and the number of spring used to store the energy,  $n$ , by

$$D_2 = \frac{-146dE + 25n\pi d^3 y S_{ys} + \sqrt{4.149(10^5)d^2 E^2 - 4.730(10^4)n\pi d^4 y E S_{ys} + 625n^2 \pi^2 d^6 y^2 S_{ys}^2}}{800E} \quad (2.10)$$

Bounding eq. 2.10 by eq. 2.8 gives the line of possible  $D$  and  $d$  values given the design parameters. If variation in the desired energy is tolerable, eq. 2.10 can be used to create a region of possible values. The region between point 3 and 4, in Fig. 2.13, shows the possible values when a  $\pm 10\%$  difference in energy is acceptable. This is useful when no standard spring sizes exist along the line of constant energy. Finally, the change in energy density, as it relates to the parameters of the system, can be calculated as

$$U = \frac{1}{4\pi^2} \left( \frac{d}{D_1} \right)^4 L_r^2 \frac{G}{\rho} \quad (2.11)$$

Equations 2.8, 2.10, and 2.11 are plotted together in Fig. 2.13 which was created using the parameters of the MultiMo-Bat. The labeled points, 1-4, highlight two critical concepts for maximizing energy density, which are the number of springs,  $n$ , and the percentage of the maximum mounting length utilized,  $\lambda$ . Point 1 is the natural starting point where the desired energy is stored with one spring which fills the entire mounting length. While still using a single spring, energy density can be improved by reducing the free length of the spring however, the mean coil diameter grows rapidly and may not be tolerable. Point 2 shows the parameters when the free length is half the mounting length. To further improve energy density, the number of springs used to store the energy can be increased. The MultiMo-Bat uses 8 springs, labeled as point 3, generating a significant increase in energy density. Point 3 yields a mean coil diameter,  $D = 2.76$  mm, and a wire diameter,  $d = 0.4$  mm, which is a standard size. To compare this analytical solution to a previously used iterative strategy, the desired energy was set to 6.35 J, a value greater than the minimum required of 6 J, which is a known optimum standard size spring for this robot. In this case both strategies produce the same spring parameters. The energy density, at point 3, is 515 J/kg. For the MultiMo-Bat, the mounting configuration of the springs restricts the outer diameter

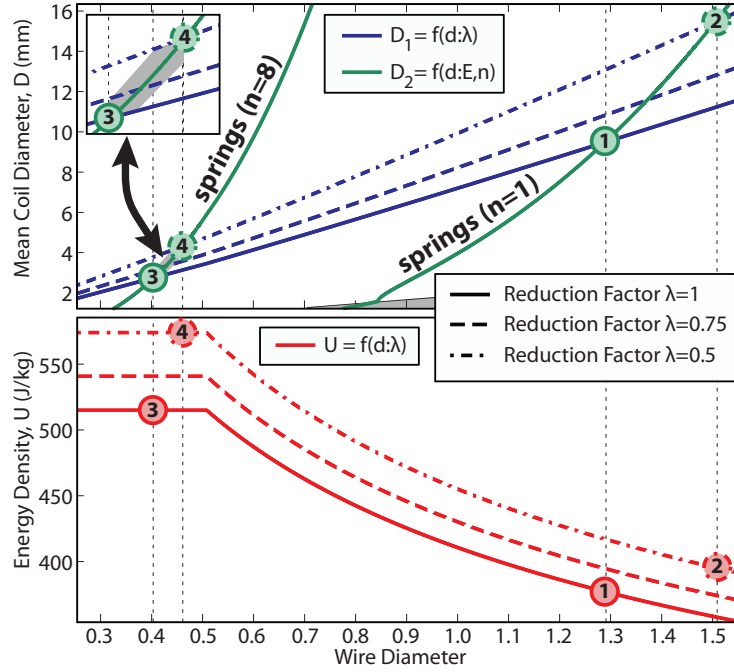


Figure 2.13: Shown is the relationship between the number of springs,  $n$ , the mean coil diameter,  $D$ , and the energy density,  $U$ , as a function of the wire diameter,  $d$ , the length ratio,  $L_r$ , and the energy,  $E$  for the MultiMo-Bat. Points 1 and 2 are using a single spring to store the energy however, while Point 1 fills 100% of the mounting length Point 2 fills only 50% but achieves an increase in energy density. The MultiMo-Bat uses 8 springs to store the jumping energy which is labeled as Point 3, further increasing energy density. Robot parameters:  $L_m = 71.1$  mm,  $y = 147.6$  mm,  $E = 6.35$  J; Material(A229) parameters:  $R = 0.7$ ,  $\xi = 1.05$ ,  $S_{ys} = 1.0119d^{-0.1833}$  GPa,  $\rho = 7.86$  g/cm<sup>3</sup>,  $G = 79.3$  GPa; Defined range of  $d$  in eq. B.1 is 0.51 – 15.88 mm.

of the coil to approximately the value at point 3. Therefore, little length reduction is possible to further improve the energy density. The shear stress equation is only defined down to 0.51 mm for material A229 therefore, the allowable shear stress is held constant for wire diameters below this value which creates the artificial flattening in the curve. Extension of the ranges would be required to determine the true value but extrapolation might give some idea of the possible improvement.

Once a  $D$  and  $d$  have been selected, within the bracketed region which satisfies the system requirements,  $\lambda$  can be calculated by using eq. B.2 solved for  $F$  and substituted into the standard spring deflection equation. Solving this equation for  $\lambda$  yields

$$\lambda = \frac{GL_r d^2 (123d^2 - 73dD - 200D^2)}{200\pi(d - D)D^3 S_{ys}} \quad (2.12)$$

The complete system is capable of storing a maximum of 6.35 J to power the jumping locomotion mode to heights of over 3 meters. This analysis highlights the benefits of increasing the number of springs, meaning it favors smaller wire diameters which increase material strength, and decreasing the percentage of the mounting length utilized, meaning it favors larger mean coil diameters to reduce stress non-uniformities in the cross-section. As compared to a more basic spring selection strategy, this guarantees that the designed spring achieves its maximum allowable energy density by accounting for the change in material properties and by ensuring that the spring reaches its maximum allowable deflection. The utilization of 8 springs by the MultiMo-Bat results in a 27% reduction in the spring mass as compared to the use of a single spring. More importantly, the reduction percentage is not constant, increasing the desired energy will increase the mass percentage reduction; for example, using the springs selected above to store twice the energy results in twice as many springs but, achieves a 36% reduction in the spring mass.

## **2.6 Gliding Mode**

The design concept of the MultiMo-Bat requires a highly integrated and completely passive gliding locomotion mode. Therefore, within the confines of the integrated design strategy, the gliding dynamics and wing design will be examined further to elucidate methods for incorporating embodied intelligence to passively adapt to the initial gliding conditions while cooperating with the jumping mode to preserve the overall performance.

### **2.6.1 Gliding Phase Dynamic Model**

To reduce the possibility of slipping and overcome tall obstacles, the jumping mode employs a vertical jump which create the most difficult initial conditions for gliding. Therefore, the goal is to design a flying wing which is able to achieve horizontal velocity from a vertical jump. Furthermore, it is advantageous to incorporate embodied intelligence into the dynamics of the wing to passively transition from jumping to the gliding state, and thus reduce the need for actuation and enhance the robustness of the mode. To this end, a 6-DOF model is presented

which can serve as a framework for predicting the gliding locomotion mode's behavior based on the aerodynamic effects, wing parameters, and initial conditions.

## 6 Degrees-of-Freedom Model

During the gliding locomotion mode the wings are locked in the gliding configuration creating a single body with distributed mass. Therefore, 6 degrees-of-freedom (DOF) can capture the entire behavior of the system. From Newtonian mechanics, the 6-DOF dynamic equations of motion can be calculated as the rate of change of the linear  $\vec{p}$  and angular  $\vec{h}$  momentum

$$\vec{p}_I = m\vec{v}_I \Rightarrow \frac{d}{dt}(\vec{p}_I) = \vec{F}_I = \frac{d}{dt}(m\vec{v}_I) \quad (2.13)$$

$$\vec{h}_I = \mathbf{I}_I\vec{\omega}_I \Rightarrow \frac{d}{dt}(\vec{h}_I) = \vec{M}_I = \frac{d}{dt}(\mathbf{I}_I\vec{\omega}_I) \quad (2.14)$$

where, in the inertial frame,  $\vec{v}_I$  and  $m$  represent the body's velocity and mass, respectively, and  $\mathbf{I}_I$  and  $\vec{\omega}_I$  represent the body's moments of inertia and the angular velocity, respectively. However, as the moments of inertia are constant in the body frame,  $\mathbf{I}_B$ , it is advantageous to write the equations of motion in the body frame instead of the inertial frame. Accounting for the observation differences and rotation of the body frame through the use of the ZYX-Euler angles the equations of motion can be written as

$$\dot{\vec{v}}_B = \frac{1}{m}\vec{F}_B + \mathbf{H}_I^B g_I - \vec{\omega}_B \times \vec{v}_B \quad (2.15)$$

$$\dot{\vec{\omega}}_B = \mathbf{I}_B^{-1}(\vec{M}_B - \vec{\omega}_B \times \mathbf{I}_B\vec{\omega}_B) \quad (2.16)$$

where,  $\vec{v}_B$  and  $\vec{\omega}_B$  are the robot velocity and angular velocity in the body frame, respectively. The aerodynamic body forces,  $\vec{F}_B$ , and moments,  $\vec{M}_B$ , are represented as,

$$\vec{F}_B = \frac{1}{2}\rho V^2 S \begin{bmatrix} C_X \\ C_Y \\ C_Z \end{bmatrix}_B \quad (2.17)$$

$$\vec{M}_B = \frac{1}{2}\rho V^2 S \bar{c} \begin{bmatrix} C_l \\ C_m \\ C_n \end{bmatrix}_B \quad (2.18)$$

where the air density,  $\rho$ , reference velocity,  $V$ , and reference wing area,  $S$ , define the body frame lift  $C_Z$ , drag  $C_X$ , side-slip  $C_Y$ , roll moment  $C_l$ , pitch moment  $C_m$ , and yaw moment  $C_n$ . The rotation matrix,  $\mathbf{H}_I^B$ , rotates vectors in the inertial frame to the body frame. However, the goal is to determine the motion of the system in the world (inertial) frame therefore, two variable transformations required are included

$$\vec{v}_I = \mathbf{H}_I^B \vec{v}_B \quad (2.19)$$

$$\vec{\omega}_{Euler} = \mathbf{H}_B^{Euler} \vec{\omega}_B \quad (2.20)$$

where,  $\vec{v}_I$  represents the body velocity of the inertial frame and  $\vec{\omega}_{Euler}$  represents the angular velocity in the frames of the Euler angles. The rotation matrix,  $\mathbf{H}_B^{Euler}$ , rotates vectors in the body frame to the Euler angle frames.

This 6-DOF model accounts for the full dynamics of the system, where the aerodynamic forces and moments provide the possibility to encode mechanical intelligence into the gliding locomotion mode. In particular, to passively transition from a vertical jump to gliding flight, focus is placed on the pitching moment characteristics. However, the aerodynamic coefficients are highly dependent on the shape, angle-of-attack (AoA), and flow regime of the airfoils. Therefore, the coefficients are best determined using computational fluid dynamics.

### **Aerodynamics Coefficient Calculation**

Calculating the aerodynamic coefficients begins with the selection of the airfoil shape, as this is the dominant aerodynamic structure on the MultiMo-Bat. A computational fluid dynamics solver is then used to determine the pressure distribution over the surface of the airfoil for all angles-of-attack ( $\text{AoA} \in [-180, 180]$  deg). In particular, because the airfoils transition between the flying and stalled regime, a higher point density is used near the transition  $\text{AoA} \in [5, 15]$  deg. From the pressure distribution, the aerodynamic coefficient for lift  $C_L$ , drag  $C_D$ , and pitching moment  $C_m$  are calculated in the velocity frame at the assumed aerodynamic center of the wing, 25% of the

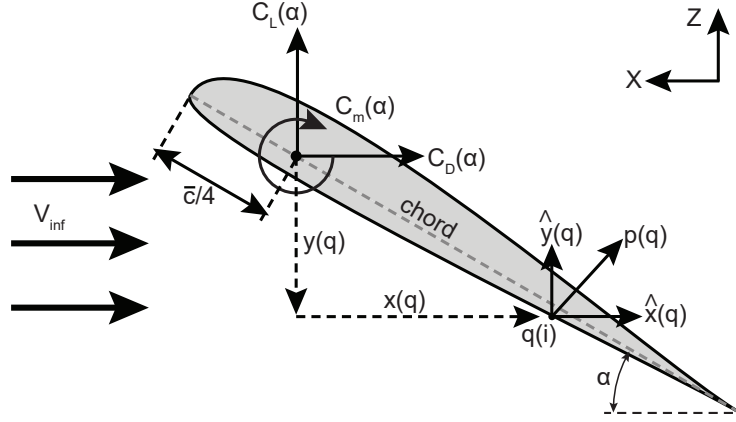


Figure 2.14: Diagram of the airfoil model where the parameters for calculating the aerodynamic coefficients are presented. The surface normals point into the airfoil body and are used to determine the direction of the pressure force.

chord length measured from the leading edge, through rearrangement of the drag equations 2.17 and 2.18 as

$$\begin{bmatrix} C_L \\ C_D \end{bmatrix} = \frac{1}{\frac{1}{2}\rho V^2 \bar{c}} \int_q p(q) \begin{bmatrix} \hat{z}(q) \\ \hat{x}(q) \end{bmatrix} dq \quad (2.21)$$

$$C_m = -\frac{1}{\frac{1}{2}\rho V^2 \bar{c}^2} \int_q p(q) \hat{z}(q) x(q) - p(q) \hat{x}(q) z(q) dq \quad (2.22)$$

where,  $\rho = 1.2041 \text{ kg/m}^3$  is the density of air at sea level and  $20^\circ\text{C}$ ,  $V$  is the magnitude of the body velocity,  $\bar{c}$  is the mean aerodynamic chord length of the airfoil,  $p$  is the absolute surface pressure,  $(\hat{x}, \hat{z})$  is the surface normal,  $(x, z)$  is the position measured from the quarter chord  $\bar{c}/4$ , and  $q$  is the point along the airfoil perimeter as seen in Fig. 2.14. Then the center-of-pressure (CP), the point at which the aerodynamic forces produce zero moment, can be calculated as

$$\begin{bmatrix} x_{cp} \\ z_{cp} \end{bmatrix} = \frac{\int_q p(q) \begin{bmatrix} \hat{z}(q) \\ \hat{x}(q) \end{bmatrix} \begin{bmatrix} x(q) \\ z(q) \end{bmatrix} dq}{\int_q p(q) \begin{bmatrix} \hat{z}(q) \\ \hat{x}(q) \end{bmatrix} dq} \quad (2.23)$$

Typically, the forces and moments on the wing are considered around the aerodynamic center however, due to the high AoAs caused by the passive transition between jumping and gliding, the CP is necessarily calculated to understand the effect of its relative position in relation to the positioning of the center-of-mass (COM).

## **Aerodynamics Coefficients - Flat Plate Airfoil**

The flat plate airfoil provides a lower bound for the performance of the MultiMo-Bat and allows for comparison, in the future, to more complex airfoils. The coefficient calculation begins with computational fluid dynamics (CFD), employing the full Navier Stokes Equations and a Turbulence model (Comsol), to calculate both the pressure and velocity distribution over the surface of the airfoil. The CFD analysis produces the plots shown in Figure C.1 and C.2 which represent the velocity and pressure distribution. At the AoA of 6 degrees the divergence of the wake is seen indicating the transition to turbulent flow or airfoil stall. At the AoA of 45 degrees the upper side of the airfoil has nearly zero velocity resulting in an equal pressure distribution over the upper surface. This asymmetry of the center-of-pressure is then a result of the asymmetry in the under surface pressure distribution. The pressure distribution over the surface of the airfoil is presented in Figure 2.15 where the (green) indicates negative pressure relative to atmospheric pressure and (red) indicates positive relative pressure. Through integration of the surface pressure over the airfoil, Fig. 2.16a, the total force vector is calculated. Using equations 2.21 and 2.22 the lift  $C_L$ , drag  $C_D$ , and pitching moment  $C_m$  coefficients are plotted, as seen in Fig. 2.16b with the lift-to-drag ratio presented in Fig. 2.16c and the center-of-pressure along the chord in Fig. 2.16d. Table 2.2 compiles the aerodynamic parameters necessary for the 6-DOF simulation of the MultiMo-Bat using flat plate airfoils.

## **Results and Discussion**

Figure 2.16c shows that the position of the center-of-pressure (CP), along the chord of the airfoil, is a function of the angle-of-attack (AoA). At an AoA=90 deg the CP, measured along the chord from the leading edge, is at the 50% position however, as the airfoil comes out of the stall at approximately AoA=6 deg, the CP moves to the 32.3% position with a maximum possible shift of 24.5% at AoA=3 deg. This is important because the wings are deployed parallel to the ground therefore, as the robot begins to fall, they will initially see flow normal to the airfoil however, for directional gliding it is necessary that the AoA be less than 90 degrees. The passive transition to

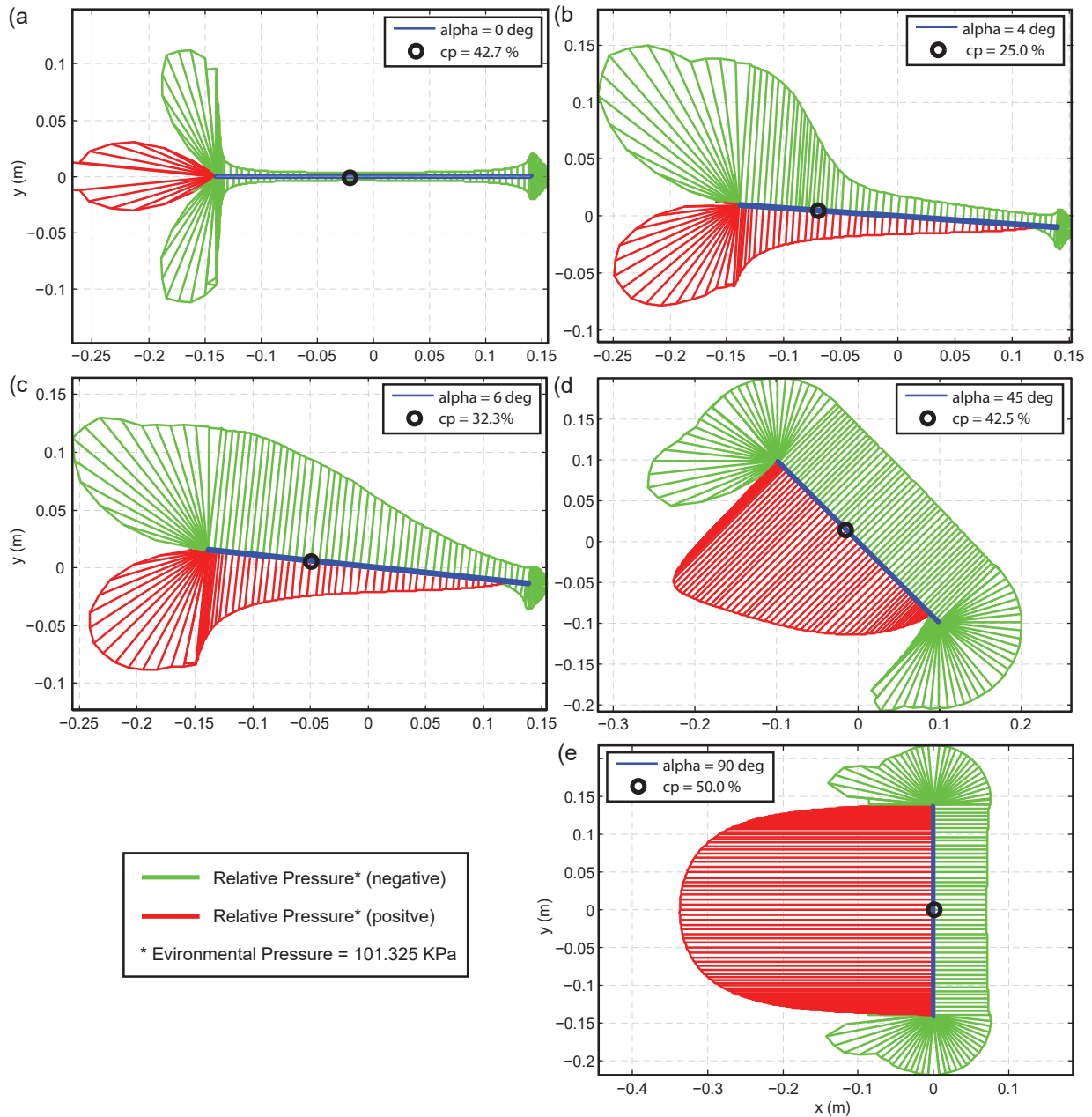


Figure 2.15: Relative pressure distribution around a flat plate airfoil. **a)**  $\alpha=0$  degree angle-of-attack (AoA), **b)**  $\alpha=4$  degree AoA and the center-of-pressure (CP) at the 25% chord position **c)**  $\alpha=6$  degree AoA and CP shifted from the 25% position, **d)**  $\alpha=45$  degree AoA and stalled regime, and **e)**  $\alpha=90$  degree.

Table 2.2: Flat Plate Airfoil Coefficients at Angle-of-Attack (AoA)

AoA ( $\alpha$ ) (deg)	Properties*				
	CL	CD	Cm	cp( $\bar{c}$ ) <sup>†</sup> (chord %)	cp(t) <sup>‡</sup> (mm)
0	0.0000	-0.0035	-0.0001	42.7	-0.83
1	0.1108	-0.0049	-0.0001	24.9	-0.61
2	0.2232	-0.0100	-0.0007	24.7	-0.16
3	0.3361	-0.0184	-0.0018	24.5	-0.07
4	0.4570	-0.0325	0.0000	25.0	0.22
5	0.5893	-0.0515	0.0163	27.8	0.34
6	0.6971	-0.0735	0.0515	32.3	0.40
7	0.7351	-0.0915	0.0748	35.1	0.33
8	0.7552	-0.1079	0.0857	36.2	0.21
9	0.7581	-0.1228	0.0949	37.4	0.13
10	0.7677	-0.1385	0.1006	37.9	0.00
11	0.7769	-0.1545	0.1046	38.2	-0.10
12	0.7890	-0.1713	0.1080	38.4	-0.21
13	0.8027	-0.1889	0.1112	38.5	-0.31
14	0.8130	-0.2062	0.1139	38.6	-0.42
15	0.8278	-0.2251	0.1166	38.6	-0.55
20	0.9133	-0.3345	0.1331	38.7	-0.94
25	1.0077	-0.4705	0.1564	39.1	-1.21
30	1.1072	-0.6387	0.1890	39.8	-1.35
35	1.1952	-0.8359	0.2281	40.6	-1.42
40	1.2656	-1.0609	0.2733	41.5	-1.45
45	1.3083	-1.3058	0.3228	42.5	-1.53
50	1.3159	-1.5657	0.3755	43.4	-1.53
55	1.2845	-1.8318	0.4309	44.3	-1.53
60	1.2088	-2.0912	0.4859	45.1	-1.54
65	1.0887	-2.3316	0.5387	45.9	-1.56
70	0.9307	-2.5538	0.5925	46.8	-1.55
75	0.7337	-2.7341	0.6401	47.6	-1.55
80	0.5072	-2.8708	0.6826	48.4	-1.55
85	0.2596	-2.9557	0.7186	49.2	-1.54
90	0.0000	-2.9841	0.7460	50.0	1.32

\* right handed axes with +X right, +Z up.

†Center-of-pressure measured as percent of chord length (chord %) from the leading edge of the airfoil in the body frame (chord = 279 mm).

‡Center-of-pressure measured perpendicular to chord in the body frame.

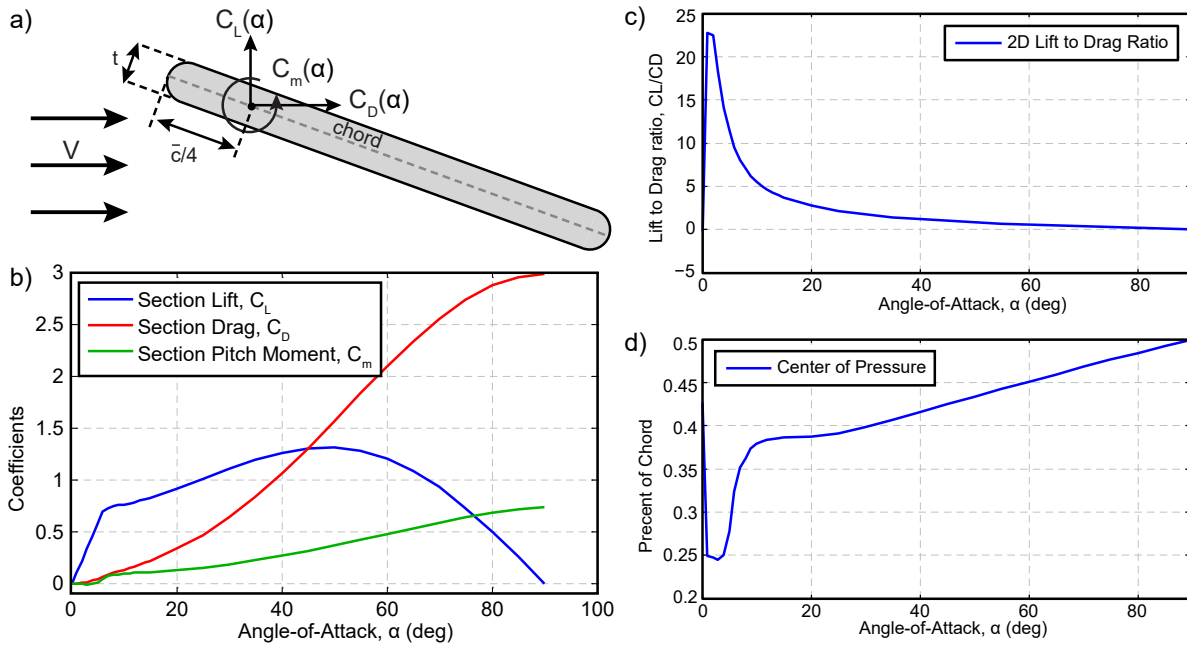


Figure 2.16: **a)** Diagram of the flat plate airfoil where,  $t = 3$  mm and  $c = 279$  mm. **b)** Flat plate lift, drag, and pitching moment coefficients. The coefficients are calculated from Comsol CFD data of the pressure distribution around the airfoil at angles-of-attack (AoA) of: 0, 1, 2, 3, 4, 5, 6, 7, 8, 9, 10, 11, 12, 13, 14, 15, 20, 25, 30, 35, 40, 45, 50, 55, 60, 65, 70, 75, 80, 85, and 90 degrees. **c)** The center-of-pressure (CP) moves along the chord axis of the airfoil starting from around the quarter chord position during flying and shifting toward the half chord position as the airfoil stalls. At an AoA of 90 degrees the CP reaches half chord position. **d)** Flat plate lift to drag ratio is shown as a function of the angle-of-attack (AoA).

gliding can then be achieved by positioning the COM of the robot between the extremes of the CPs, as illustrated in Fig. 2.17. Therefore, as the robot drops the airfoils are initially rotated into the flow, by the nose down pitching moment, as they come out of the stall, and the CP moves forward, the resulting nose up pitching moment slows the rotation and the system stabilizes around some non-steady directional glide trajectory.

With the passive transition from a vertical jump to a horizontal glide now possible, the simulation is used to explore the overall behavior. Figure 2.18 presents the simulated result for the MultiMo-Bat presented in Fig. 3.12, where the initial pitch angle is set to 2, 20, and 40 degrees and the insets show the pitch angle of the body. The pitch angles of the 3 trials, demonstrates the non-steady state nature of this gliding behavior where the pitch angle varies continuously

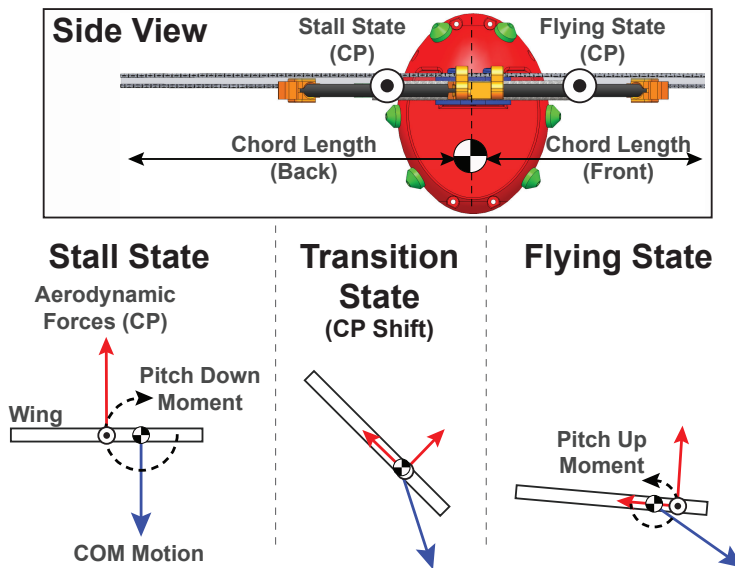


Figure 2.17: The robot can passively reorient through the positioning of the center of mass (COM) and the center-of-pressure (CP) such that during the stalled state a pitch down moment is generated and once the wings come out of the stall, the CP shifts generating and pitch up moment. The boundaries of the CP are the 50% chord position for stall to the 24.5% chord position for flying.

throughout the glide; stable gliding would result in constant pitch angles. As aerodynamic forces are non-conservative, the trend shows increased performance with a reduction in the pitching velocity which is achieved by minimizing the initial pitch down reorientation phase; compare the 20 deg trial, Fig. 2.18b, with significant pitch down during the initial acceleration phase whereas the 40 deg trial, Fig. 2.18c, shows only minor increases.

The simulation also allows for exploration of the combination of jumping and gliding locomotion. In addition to jumping vertically, a later generation MultiMo-Bat, Fig. 4.5, is capable of jumping at angles. The simulation shows significant increase in the gliding performance as the jumping angle is reduced from 90 deg. This is due to the orientation and kinetic energy created during the jump, being carried through the coast phase to the gliding phase, allowing for quicker reorientation and reduced initial acceleration period to achieve the dynamic characteristics necessary for gliding. The challenge then becomes creating an airfoil within the integration strategy, which requires highly collapsible wings, to take advantage of this dynamic behavior.

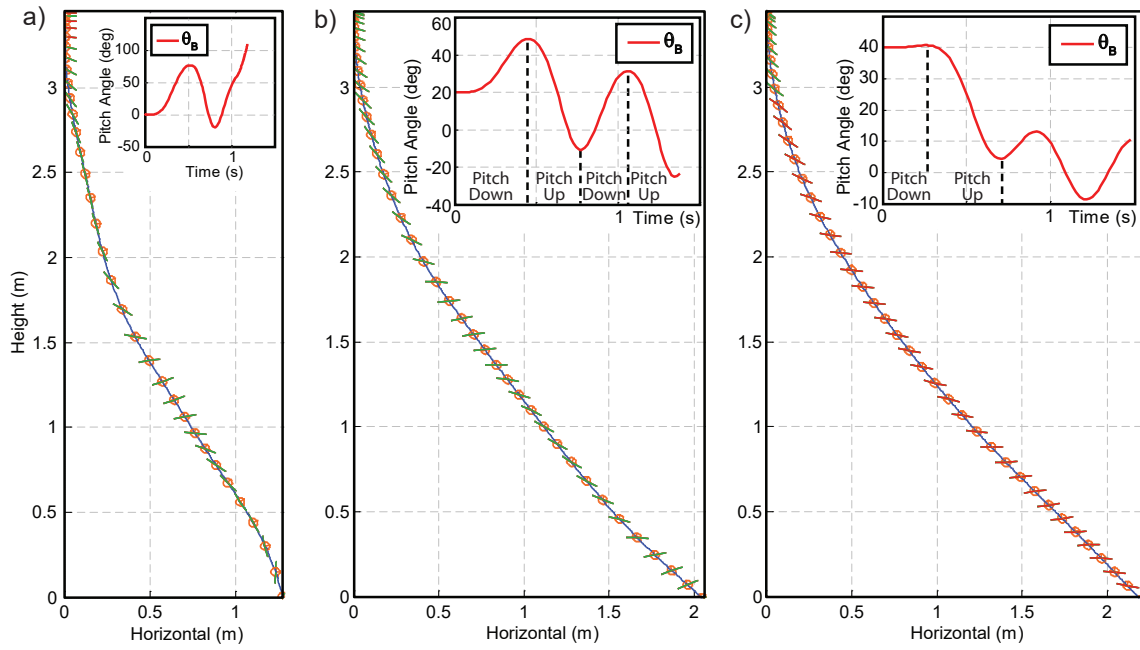


Figure 2.18: Simulated gliding behavior for a center-of-mass at 42.5% of the chord and initial conditions of height 3.45 m and pitch down angles **a)** 2 degrees, **b)** 20 degrees, and **c)** 40 degrees. **Note:** Parameters from later generation MultiMo-Bat, Fig. 3.12.

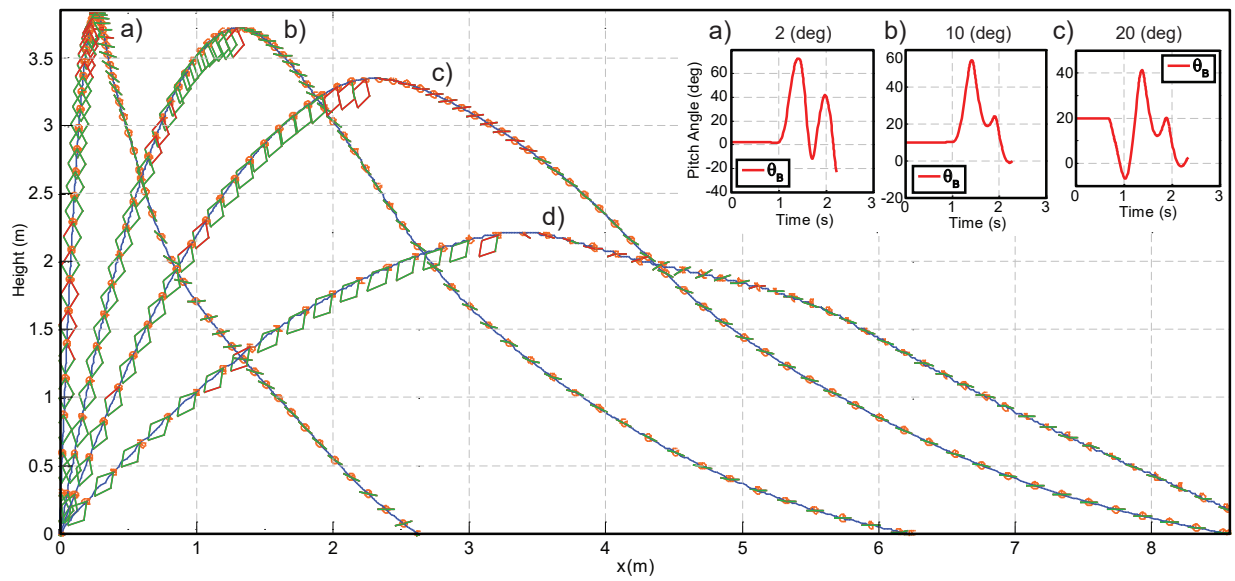


Figure 2.19: Simulated jumping and gliding behavior for initial conditions of velocity 8.677 m/s and jumping angles **a)** 2 degrees, **b)** 10 degrees, **c)** 20 degrees, and **d)** 40 degrees. **Note:** Parameters from later generation MultiMo-Bat, Fig. 3.12.

## 2.6.2 Wing Design

The wings of bats are made of skin and are therefore similar to soft elastic materials. This property allows the wing membranes of bats to not only change shape but also the surface area-to-volume ratio, facilitating membrane collapse. Collapsing the membranes reduces their effect on the performance of the jumping mode. However, engineered elastomers have high mass and very low durability and robustness especially when exposed to the elements and under sustained strain. Therefore, various other materials were considered for the wing membranes. To achieve high durability and low mass, coated ripstop nylon (Goodwinds, 0.75 oz) was chosen for its high strength-to-weight ratio. This material has a ripstop weave to reduce the propagation of tears, can withstand ultra violet exposure, and has a coating that reduces water absorption. This material however does not stretch, thus it can be deformed but it is not possible to use stored energy in the membrane to facilitate collapse. Utilizing this material therefore creates two significant challenges over an elastomer for the wing membranes of the robot.

The first challenge is due to the static behavior of the material requiring that the membranes must be able to collapse in a way that does not interfere with the jumping locomotion mode. To achieve this, the wing membranes are mounted to the exterior of the leg structure and designed to be longer in the chord-wise direction than the leg structure when fully compressed (Fig. 2.20). Based on the standard buckling theory of a beam, with two pin joints and no other constraints, mode 1 is the lowest energy state and therefore is the stable configuration the membranes will adopt as the legs are compressed however; it could be in either the internal or external direction. If it were to buckle inward it could potentially interfere with any one of the leg components resulting in reduced performance or structural failures. Ensuring the chord-wise length of the leg structure is always less than the membrane creates a restricting feature on the inside which ensures the stable mode 1 buckling state is in the external direction, as can be seen in A-C of Fig. 2.4.

The next challenge is due to the integrated locomotion design concept. The goal is to add

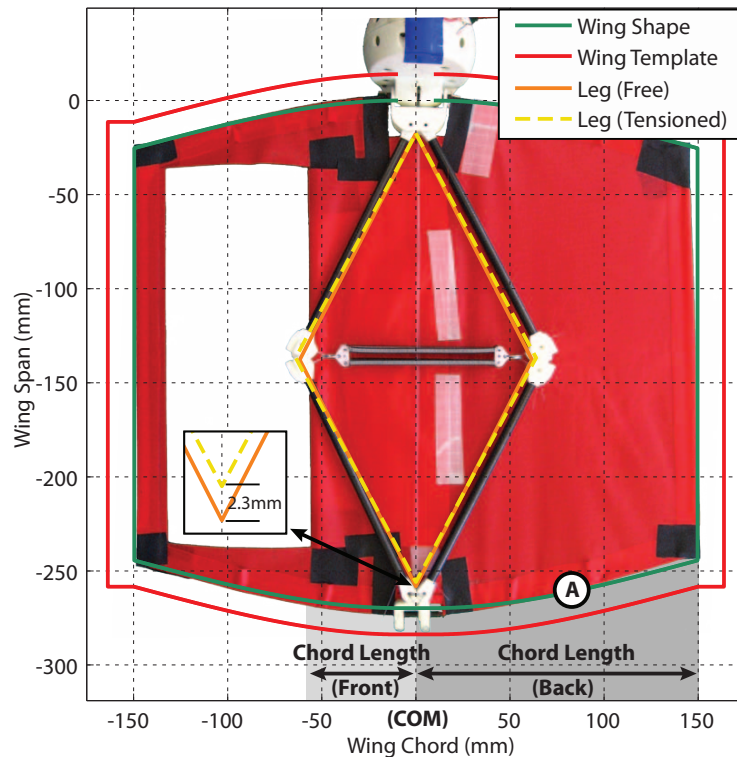


Figure 2.20: The wing shape generated by the desired tension profile is shown along with the cut profile for construction. Superimposed on the graph is the manufactured wing to show the wing configuration and position of the center of mass. The opening in the wing is used for rapid testing of various center of mass (COM) positions whereas the final wing should be constructed asymmetrically.

the gliding locomotion mode without significantly reducing the performance of the jumping mode. This requires that it does not affect the jumping energy delivered to the ground, does not produce significant additional drag during the coast phase of the jump, and requires minimal addition of mass. The vampire bat uses the major bones of the leg as attachment points for the membrane, and tension is controlled through the configuration of these components. This idea will be employed in the robot design to achieve similar results. The wing membrane is attached to both the shoulder joint and the foot of the robot, passively collapsing the membrane when the leg is compressed. Extension of the leg creates tension on the membrane; however, as this is not controlled, tensioning is achieved through the utilization of a small amount of energy retained in the main power springs. The membranes are mounted to 1.53 mm diameter pultruded carbon

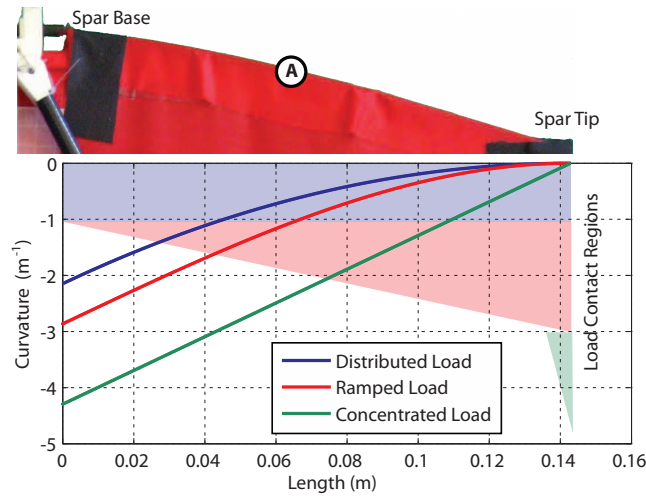


Figure 2.21: The second spatial derivative of the beam shape (curvature) provides an understanding of the amount of error which can be tolerated in the manufacturing process. Shown are the three loading conditions utilized for this system with normalized reaction forces to show the variation over the contact regions. The label (A) shows the position of this spar in Fig. 2.20.

fiber spars (Goodwinds). This creates a unique wing design in that it has no support in the span-wise direction allowing it to be highly deformable. However, without the leeway provided by the stretch associated with elastomers, the challenge is to produce the desired tension over the entire membrane.

To achieve the desired tension profile along the chord-wise axis, the carbon fiber spars are used as distributed springs. Assuming the spar can be modeled as an Euler-Bernoulli beam the deflections can be easily determine for several different types of loading conditions such as, concentrated tip loading, ramped loading, and equally distributed loading as well as many other variations. This assumption also allows the use of the superposition principle which permits the simple addition of the effects of individual loading conditions to determine the total deflected shape. As the accuracy of the shape is very important, deflection values were obtained experimentally and used as a fitting parameter to adjust the elastic modulus of the material. Theoretically, this now allows for any tension profile, in the chord-wise direction, to be generated. The challenge comes in manufacturing the wing membranes with the required shape.

To facilitate manufacturing of the airfoil, it is advantageous to consider the magnitude of

the second spatial derivative of the shape, the curvature, at the contact points of each loading condition. The greater the magnitude of this value, the more manufacturing error can be tolerated without reversing the loading condition on regions of the airfoil, such as going from a desired tension to slacking of the airfoil. As can be seen in Fig. 2.21, the concentrated load at the tip creates the highest curvature over the region nearest the leading or trailing edge and should therefore be incorporated into the design to ensure edge tensioning. The ramped load with the peak at the tip causes the largest curvature variation over the region of contact and therefore, should be included to bias the load profile of the wing into tension and reduce the possibility of slacking. Finally, the distributed load should be included to generate a minimum desired tension. Also, to ensure that the least amount of energy possible is removed from the jumping mode, to achieve the desired tension profile, the tension at the base of the spar should not exceed the desired tension. Because of the rigid nature of the membrane material, any additional tension at the spar base will not contribute to the tension profile over the spars but will remove that energy from the jumping mode. As discussed previously, the energy to tension the MultiMo-Bat's airfoils is actually stored above the leg angle where the robot leaves the ground during jumping resulting in no loss in jumping energy.

The design strategy for the wings is to first select a desired reaction force or leg deflection at the fixed point of the beam, then simply change the weights on particular loading conditions while maintaining the same reaction force. The current prototype uses all three loading conditions for the benefits discussed previously. They consist of a 0.7 N concentrated tip load, 3.5 N/m ramped load, and 1 N/m distributed load; the total reaction force is 1.09 N with the loads breaking down as follows: 0.7 N, 0.25 N, and 0.143 N, respectively. This results in a total leg extension change of approximately 2.3 mm; this small difference is due to both the high performance jumping mode springs and the mechanical advantage profile generated by the four-bar leg. Then from the beam shape the complete wing shape can be generate and printed out at full scale for use as a manufacturing template, as seen in Fig. 2.20.

## 2.7 Prototype and Experiments

To verify the performance and feasibility of the integrated design strategy, a prototype was constructed and tested (Fig. 2.2). As previously stated, integrating locomotion modes has the potential to significantly reduce the negative effects associated with the additional modes however, this may not entirely remove all effects. Therefore, it is necessary to quantify the effect that each mode has on the other to determine how well the integration was achieved. The primary mode of the MultiMo-Bat is the jumping mode with a highly integrated gliding mode resulting in a bias toward jumping performance. Therefore, jumping experiments were conducted to determine both the performance with and without the additional wing structure. Gliding experiments were then conducted to determine the best chord-wise position of the COM as well as the effect of passive vs. active wing deployment to the overall gliding performance.

### 2.7.1 Jumping Performance

The jumping performance of the MultiMo-Bat is a function of the energy stored in the main power springs, the release mechanism, and the configuration of the robot. Therefore, to test the integration performance of the robot, six robot configurations, seen in Table 2.3, were tested with the energy stored and the release mechanism held constant. Jumping experiments were conducted with robot configurations which included: with the wing structure, without the wing structure, and with a variety of wing deployment assist springs. The deployment assist springs are used to bias the robot configuration into the gliding state by generating a torque about the shoulder joint. The experiments with and without the wing structure were conducted to determine the major changes in performance associated with the addition of the gliding mode whereas the experiments with varied wing deployment assist springs were conducted to determine the effect of the passive wing deployment strategy.

The overall jumping performance of each test was recorded using a high speed camera (pco.dimax) at frame rates between 400 and 2000 fps depending on the desired motion reso-

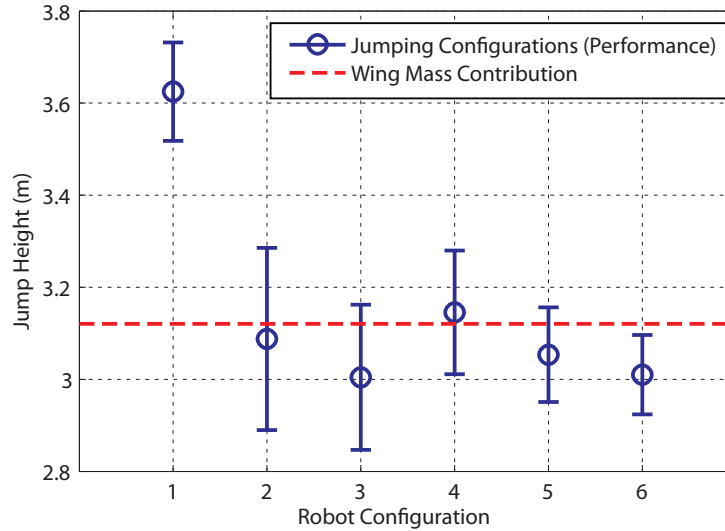


Figure 2.22: The jumping performance for the no wing configuration (1) is shown along with the winged configurations (2-6) to show the change in performance associated with the addition of the gliding mode. See Table 2.3 for configuration details. The jumping and gliding robot performance is coupled in both mass and structure; however, the mass contribution is shown to illustrate how the integration strategy minimizes the mass contribution and has minimal structural contribution. The wing mass contribution line shows the loss in jumping performance associated with only the added mass of the additional wing structure which shows other energy losses are minimal (minimum 10 samples tested per configuration).

Table 2.3: Prototype Experimental Jumping Configurations

Robot Config.	Properties			Mass (g)
	Wing Membranes (Chord %)	Deployment Assist Springs (mN.m)		
<b>1</b>	N/A	N/A		99.5
<b>2</b>	50	7.2		115.6
<b>3</b>	50	14.3		115.6
<b>4</b>	50	23.8		115.6
<b>5</b>	29.4	26.0		115.6
<b>6</b>	27.3	35.8		115.6

lution. The experiments are analyzed for both the maximum height achieved as well as the overall system behavior during the ascent phase of the jump. The maximum height achieved by the system provides an understanding of the overall power and drag of the particular system

configuration and the behavior during the ascent phase can show coast phase stability of the system. For the jumping experiments, both the energy storage and release was achieved by on-board mechanisms however, the power and signal to operate the system was supplied off-board. Once the jump is triggered the power tether falls away so as to not affect the jumping performance. For the configuration 1 tests, which have the wing structure removed, the robot, seen in Fig. 2.23 with the associated data in Fig. 2.22, was able to achieve jumping heights of  $3.63 \pm 0.11$  m. Configurations 2-6 of the MultiMo-Bat require the addition of 16.1 g, shown in Table 2.3, which is comprised of the wing membrane and support spars, to achieve the second locomotion strategy, gliding. However, with the addition of the second locomotion strategy the robot was still able to achieve a maximum jumping height of  $3.15 \pm 0.13$  m; a reduction of just 13.2% for the full jumping and gliding robot.

The variability found in the experimental results has several potential causes and should be considered for completeness. The major source of variation introduced into the results is the energy storage mechanism for the jumping mode. Since the legs do not have a fixed stop the extension length of the springs can be inconsistent between runs resulting in around  $\pm 1.5\%$  of possible variation in the energy stored. The cable used to compress the legs is wrapped around the reel and possible differences in the unraveling of this cable may result in changes to the performance. The coast phase behavior can also cause changes in performance; however, with the addition of the gliding locomotion mode the coast phase stability is improved. The large airfoils produce a restoring moment to any disturbances creating a more stable system and potentially reducing losses associated with undesirable body and leg motions which can be seen in the jumping only system. Finally, the jumping direction can have a small bias to either the forward or backward direction due to the cable attachment on the legs which affects the experimental results; for the following jumping and gliding trials, the bias was set in the forward direction.

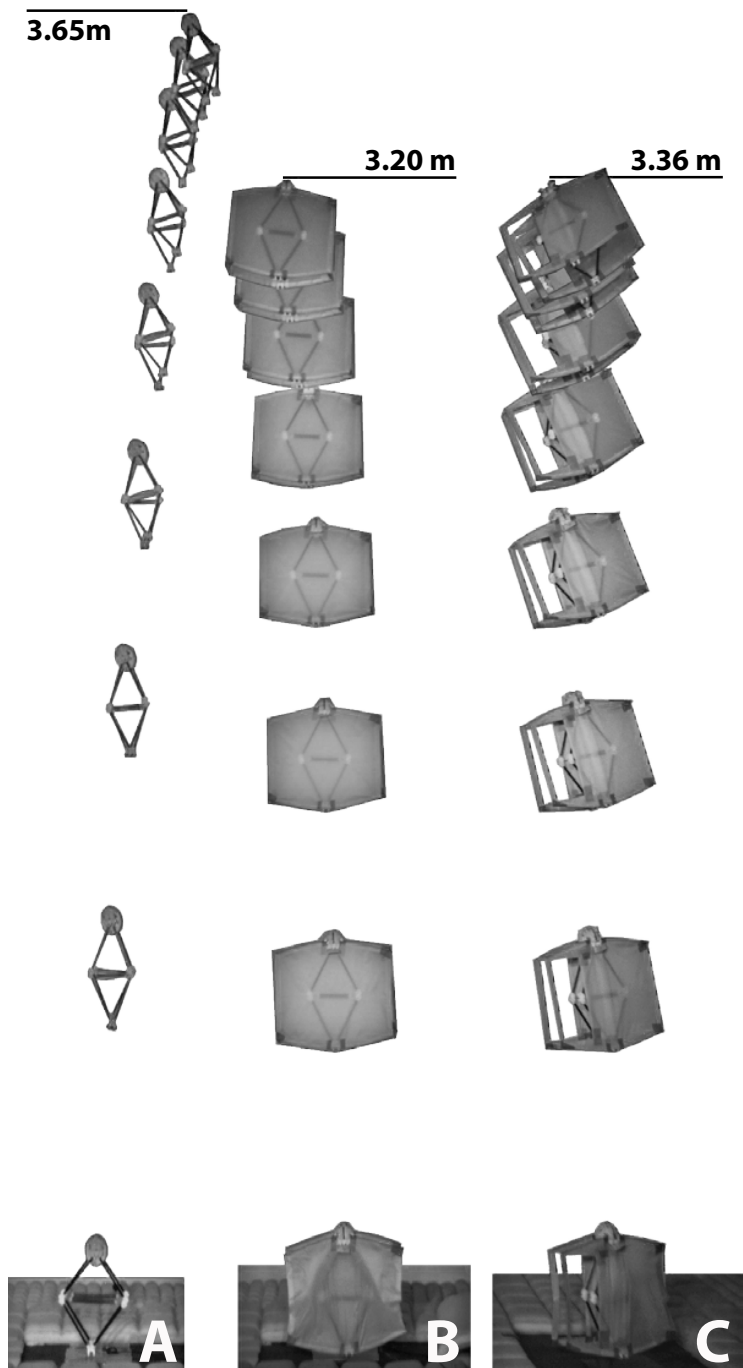


Figure 2.23: Shown are individual video snapshots of three jumping configurations which encompass the total variation in the jumping experiments. A) Configuration 1, which has the wing structure removed. B) Configuration 2, which has symmetric airfoils and no wing deployment assist springs. C) Configuration 6, which has asymmetric airfoils and strong wing deployment assist springs. The interval between snapshots is 100 ms.

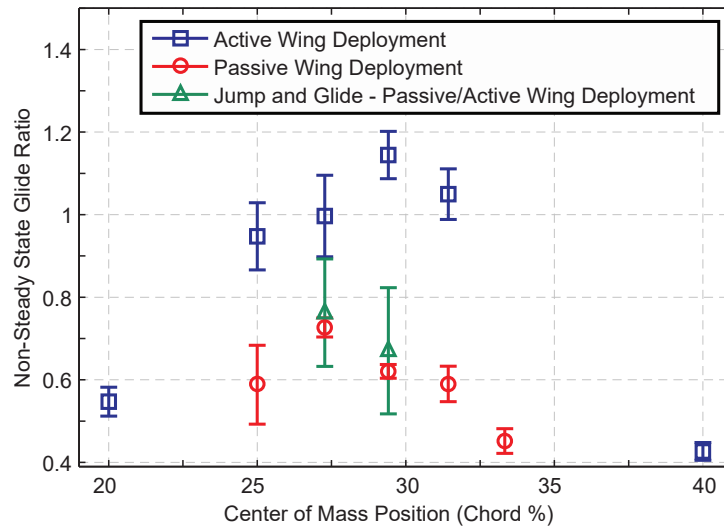


Figure 2.24: The initial wing state of the system for the 'Active Wing Deployment' tests is the gliding configuration whereas the initial state for the 'Passive Wing Deployment' tests is the jumping configuration. These two states are the extremes of the possible initial configurations of the system at the top of the jump. The jumping and gliding system with passively deployed wings has performance bracketed by these two extremes showing that the wings begin to deploy before the apex of the jump is reached (minimum 10 samples tested per configuration).

## 2.7.2 Gliding Performance

The gliding performance of the MultiMo-Bat is a function of several parameters which include the COM position in relation to the wing chord, the wing deployment type, the orientation at deployment, and the height. To analyze the effect of these parameters three sets of experiments were conducted which include active wing deployment, passive wing deployment, and full robot tests. It is important to note that the active wing deployment tests only simulate active deployment by beginning the tests with the wings manually deployed. Determining the best position for the COM of the robot in relation to the wing chord was achieved through testing of various COM positions; the COM position is measured as a percentage of the wing chord length in front of the COM divided by the total chord length as seen in Fig. 2.20. To achieve the COM shifting behavior and facilitate testing of multiple positions an opening was cut into a symmetric airfoil; for the final design the airfoil should be designed asymmetrically. The opening allows for the COM to be positioned between the half chord position and just in front of the quarter chord po-

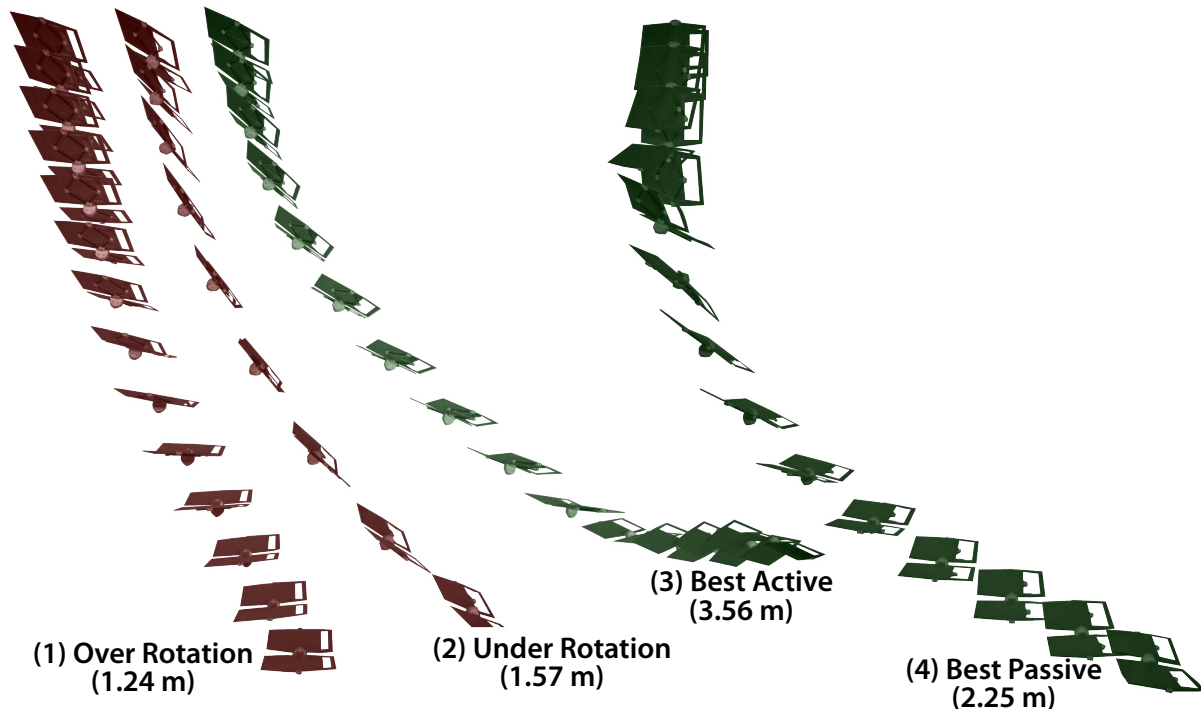


Figure 2.25: Video snapshots from individual runs of the wing deployment experiments, with the COM position at chord percents from 20% to 40%. Runs (1) and (2) show the two extremes of the behavior; (1) shows over-rotation (40.0%) and (2) shows under-rotation (20.0%), both resulting in poor performance. Runs (3) and (4) show the behavior of the robot at the particular chord percent which results in the best performance for both actively (29.4%) and passively (27.3%) deployed wings, respectively. The interval between snapshots is 100 ms.

sition which encompasses the extremes of the possible positions of the center of pressure (COP). It is important to understand that this is not steady state gliding, as discussed previously, which is why the initial height will play a role in the gliding performance. Therefore, the maximum jumping height of the system was determined and the glide tests were conducted from a similar height to characterize the maximum gliding performance. The final parameter, orientation at deployment, will be discussed in the full system tests in the following section.

In the initial tests, the active and passive wing deployment experiments were conducted by dropping the robot from the approximate maximum jumping height (3.03 m) with the initial configuration of the wings set to the jumping configuration to simulate passive deployment and the gliding configuration to simulate active deployment. The COM position was varied from 20%

to 40% of the chord, measured from the leading edge, over six steps with four points grouped around the maximums. This range ensured that tests were conducted with the COM in front of and behind the center of pressure - ideally for a flat plate at steady state gliding the position should be 25%. As the behavior of the system is unsteady, the trajectory is much more of a stair step shape with a very steep initial drop, where the system reorients to the flow and increases velocity, which flattens out and ends with the wings over-rotating and reentering a stalled state. To maximize the glide performance of this trajectory, the stall at the bottom of the trajectory should be achieved just above the ground to maximize the horizontal distance traveled as well as using the stall to remove energy from the system just before landing. The active deployment configuration will achieve lower velocities over the gliding range as the deployed airfoils create significant drag. However, the passive configuration initially drops with the wings beside the body, parallel to the flow. Thus upon opening they will experience higher initial velocity before stabilizing to the velocity of the active deployment configuration. This higher initial velocity and thus higher force requires a shorter moment arm to avoid premature over-rotation and this is what we see in the experimental results in Fig. 2.24. Illustrated in Fig. 2.17 as the distance between the COM and flying COP, the pitch up moment arm is larger for larger chord percentages and the maximum glide performance for the active deployment tests occurs at a higher chord percentage than the passive deployment tests. The glide performance is measured by the glide ratio, defined as the horizontal distance traveled divided by the maximum height of the robot. Experiments were conducted at 20% for the passive deployment configuration but were ceased before 10 runs due to potential damage to the robot as it dropped nearly straight into the ground. The best performance achieved, seen in Fig. 2.24, was a glide ratio of  $1.14 \pm 0.06$  at 29.4% of the chord, for the active configuration, and a glide ratio of  $0.73 \pm 0.02$  at 27.3% of the chord, for the passive configuration. The jumping and gliding robot should therefore have performance within this range.

### 2.7.3 Robot Performance

The MultiMo-Bat prototype has a combination of both passive and, to some degree, active wing deployment mechanisms. Small springs bias the wings into the jumping configuration. As the robot reaches the top of the jump the wings begin to deploy before the velocity vector of the robot switches directions. As the robot begins to fall and the velocity increases, the drag on the underside of the wings completes the deployment and the system begins the gliding phase of operation. To test the last parameter, the effect of the orientation of the robot on the wing deployment and gliding behavior, the complete system was used and underwent a complete locomotion cycle, shown in Fig. 2.26. Starting from the ground, the system jumped up to the drop height, the wings were deployed, and the glide measured. By allowing the system to reach the drop height, through the jumping and coasting phases, the initial orientation of the robot, at wing deployment, would be varied by an amount equal to the variation of the system itself therefore ensuring validity of the experiments. Each run was captured using a high speed camera (pco.dimax), at 1279 fps, this allowed the jumping height of each run to be measured to ensure accuracy of the calculated glide ratio. The full system was tested at the COM positions which exhibited the best performance for the two gliding tests. The MultiMo-Bat achieved a jump height of  $3.01 \pm 0.09$  m with a glide ratio of  $0.76 \pm 0.13$  at a COM position of 27.3% of the chord and a jump height of  $3.05 \pm 0.10$  m with a glide ratio of  $0.67 \pm 0.15$  at a COM position of 29.4% of the chord, shown in Figs. 2.22 and 2.24.

Overall the active wing deployment demonstrated much better glide performance because the airfoil reorients quicker resulting in more time spent moving horizontally whereas the passive wing deployment drops straight down initially before the wings deploy and reorient. As stated previously, the full system has springs that assist the wing deployment allowing them to open before the robot begins to fall. However, the full system experiments show close alignment to the passive wing deployment behavior as seen in Fig. 2.24. There is a slight increase in the glide ratio which is due to the tendency of the robot to jump slightly forward resulting in an increase

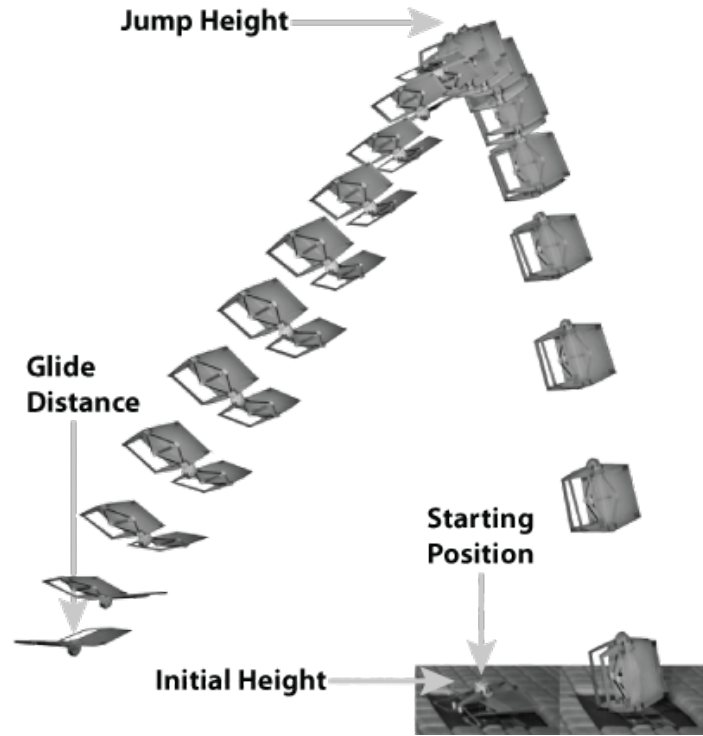


Figure 2.26: Video snapshots of a typical experimental run of the MultiMo-Bat with the measurement points labeled. The interval between snapshots is 100 ms.

in the effective glide ratio. Therefore, the deployment assist springs do not improve the gliding performance however; without these springs any variation from vertical alignment of the robot at the top of the jump would cause the wings to not deploy and the robot to flip upside down and fall. This stability can be thought of in terms of a support polygon where the opposing force is the drag; if the gravity vector penetrates the wing membrane the system is unstable. The bias these springs cause results in an increase in the support polygons size and therefore more tolerance to misalignment of the robot and a greater probability of successful wing deployment. Finally, there is one more consideration that should be taken into account. These airfoils stabilize the system about the velocity vector. Therefore any airflow in the environment will cause the robot to orient in the direction of the effective velocity of the robot plus the airflow. This effect can further complicate passive wing deployment. Therefore, to increase the deployment reliability, further designs should include an active wing deployment mechanism.

These experiments also show that the off-center mounting of the airfoils causes significant out-of-plane torque as the legs reach maximum extension as seen in the bowing in Fig. 2.4. The biologically inspired knee joints, discussed in [159], have been specifically designed to compensate for this effect. However, adding some compliance to the airfoil could also be beneficial in reducing this effect.

## 2.8 Integrated Locomotion Metrics

These locomotion strategies are coupled in three distinct ways: inertial (ICP), energy (ECP), and structural (SCP). A quantitative method for identifying and comparing their contribution can significantly inform further robot design and development however, as of yet, none have been presented. As inertial coupling is the only unavoidable type, and is minimized through the integrated design approach, it would be beneficial to have a measure of the level of integration between the modes or the amount of sharing achieved by the system (Mass Integration Metric). Energy as well as structural coupling may or may not exist at all. Therefore, to understand the effects of each coupling type, it is necessary to evaluate the overall cost, incurred by the system, for the second locomotion mode (Performance Integration Metric).

These metrics however, are not intended to guarantee good locomotion performance, instead they are design tools which characterizes specific traits about the particular design; therefore, these metrics have no optimal values. These metrics can indicate further design directions and provide an initial framework for comparing not only other similar integrated systems but also their biological counterparts. While overall locomotion mode performance should still employ the standard mode specific performance metrics for characterization and comparison.

Table 2.4: Robot Metrics

Integration Metrics	Robot Configurations	
	5	6
<b>Mass, <math>I_{mass}</math></b>	<b>1.69</b>	<b>1.69</b>
<b>Performance, <math>I_{perf}</math> (Jumping)</b>	<b>-18.7±4.5%</b>	<b>-20.4±4.1%</b>
Inertial (ICP)	-16.2%	-16.2%
Energy (ECP)	0	0
Structural (SCP)	-2.5±4.5%	-4.2±4.1%

### 2.8.1 Mass Integration Metric

The mass integration metric,  $I_{mass}$ , is a measure of the percent of the total integrated robot mass required to combine the modes without any integration between them and is given as

$$I_{mass} = \frac{1}{m_{sys}} \sum_{i=1}^{n_m} m_{ind} \implies \frac{99.5_{jumping} + 96.1_{gliding}}{115.6_{sys}} = 1.69 \quad (2.24)$$

where  $I_{mass}$  has possible values of 1 to the number of modes,  $n_m$ , which can be exhibited by a particular robot. One means no integration and  $n_m$  means complete integration between modes. Also,  $m_{ind}$  is the mass associated with the components necessary for a specific mode and  $m_{sys}$  is the total integrated robot mass. As this metric is intended to provide insight into the amount of mass shared between modes, even though design decisions may be different for specific independent modes, the modes should not be redesigned to determine the specific mode masses. Further insight may be attained through assigning percentages to the masses of components used by each mode however, as this is non-deterministic, it cannot be used for comparison. It is also important to note that this metric does not quantify the quality of the integration strategy.

The MultiMo-Bat requires an additional 16.1 g or just 14% of the system mass to achieve the second locomotion strategy, gliding. However, to evaluate the mass integration metric the two modes must be considered separately. The jumping locomotion mode does not require the wing structure to operate therefore it utilizes 99.5 g of the total 115.6 g robot mass. The gliding mode does not require the use of the internal energy storage mechanism and therefore utilizes 96.1 g.

This results in an integration measure of 1.69 at  $n=2$  meaning that 69% of the system mass is utilized by both modes or another way to think about it is that the robot is 41% lighter than it would be without integration. This significant reduction in system mass results in the possibility of preserving a significant portion of the performance of the jumping mode; assuming the effects of the other two coupling types are minor as well.

## 2.8.2 Performance Integration Metric

The performance integration metric,  $I_{perf}$ , is a measure of the change in energy per unit mass, to a particular mode, due to the existence of the other locomotion strategies; it provides an overall understanding of the cost of the additional modes. This is achieved by measuring the energy state at the end of the locomotion cycle, of a particular locomotion strategy, both within the full system and with the unnecessary components removed. The energy state for the jumping locomotion mode is the sum of the kinetic and potential energies at the apex of the jump trajectory, assuming flat ground, and is calculated as

$$I_{perf} = 1 - \frac{\frac{1}{m_{ind}}(KE + PE)_{ind}}{\frac{1}{m_{sys}}(KE + PE)_{sys}} \implies 1 - \frac{g(3.62 \pm 0.11)}{g(3.05 \pm 0.10)} = -18.7 \pm 4.5\% \quad (2.25)$$

where  $(KE + PE)_{ind}$  is the total energy of the independent mode and  $(KE + PE)_{sys}$  is the total energy of the full system. It is then possible, with further analysis, to attain an understanding of the contribution of each coupling type which can facilitate further development.

The performance integration metric for the jumping locomotion mode, of the MultiMo-Bat, is determined by comparing the overall jumping performance of configuration 1, jumping mode only, to that of the MultiMo-Bat configurations 5 and 6 (Table 2.3). This yields a performance integration value of  $-18.7 \pm 4.5\%$  and  $-20.4 \pm 4.1\%$  for configurations 5 and 6, respectively. The loss of only one fifth of the performance is significant because of the difficulty in combining these two modes in a single system with on-board actuation. To determine the quantitative effect of each coupling parameter, the possible effects of each, as they relate to this specific system, must be considered. The gliding locomotion mode does not affect the actuation and energy coupling

of the system and therefore, its contribution is zero, leaving just inertial and structural coupling. The contribution of the mass can be calculated as

$$m_1gh_1 + 0.5m_1v_1^2 + F_{D_1} = m_2gh_2 + 0.5m_2v_2^2 + F_{D_2}$$

$$1 - m_1/m_2 = 1 - (gh_2 + 0.5v_2^2)/(gh_1 + 0.5v_1^2) \quad (2.26)$$

where  $m_i gh_i$  is the height potential energy and  $F_{D_i}$  is the non-conservative energies for both the full system,  $i = 1$ , and the separated jumping mode,  $i = 2$ . Setting the drag to be equal in both configurations,  $F_{D_1} = F_{D_2}$ , yields the latter relationship, in eq. 2.26, which provides the contribution associated with the mass, resulting in a 16.2% loss in jumping mode performance. Then, relaxing the  $F_{D_1} = F_{D_2}$  constraint, the structural coupling, of the airfoils, therefore accounts for the remaining minor losses in performance of only a few percent, which can be seen in Table 2.4.

## 2.9 Robot Scaling

The comparative size and diversity of obstacles in the environment to miniature biological organisms (approximately 1 to 100s of grams) has produced a wide variety of integrated locomotion strategies. However, within this range, the scaling of the organism as well as a robot may yield performance benefits.

The scaling relationships can be separated into several categories: general properties, energy storage, forces, and actuators, which elucidate the overall scaling potential of the MultiMo-Bat within the high Reynolds number dynamic regime in which it exists. The symbols after the length scale,  $S$ , indicate a preference to scaling down,  $(-)$ , up,  $(+)$ , situation dependent,  $(\pm)$ , and non-scaling values,  $(c)$ . All scaling relationships assume isometric scaling where dimensional proportionality is maintained.

The general properties, Table 2.5, for which the scaling relationships are presented are those which affect the dynamics and structural integrity. The major contributors to the dynamics are

Table 2.5: Scaling: General Properties

Properties	Details	Equation	Scaling *
Mass <sup>†</sup>	Translational	$m = LWH\rho$	$S^3(-)$
Moment of Inertia	Rotational	$J \propto mL^2$	$S^5(-)$
Volume		$V = LWH$	$S^3(-)$
Surface Area		$A = LW$	$S^2(\pm)$
Surface Area/Volume		$S/V = A/V$	$S^{-1}(\pm)$
Stiffness	Second moment of area.	$I = \int_A y^2 dA$	$S^4(+)$
<b>Beam Stiffness</b>	Euler-Bernoulli beam		
Beam Deflection	Concentrated tip loads.	$\delta_1 = \frac{PL^3}{3EI}$	$P_{const} \Rightarrow S^{-1}(+)$ $P_{mass} \Rightarrow S^2(-)$ $P_{spring} \Rightarrow S^1(-)$
	Distributed load beam mass.	$\delta_2 = \frac{mL^3}{8EI}$	$S^2(-)$

\* Scaling Relationship (S=length scaling).

† where the length,  $L$ , width,  $W$ , height,  $H$ , and density,  $\rho$ , define the mass.

Table 2.6: Scaling: Forces

Force	Details	Equation	Scaling *
Spring Force	Helical spring	$F_S = \frac{1}{2}Kx$	$S^2(+)$
		$K = \frac{d^4G}{8D^3N_a}$	$S^1$
Friction Force		$F_f = \mu N + \tau A$ $N \propto m$	$S^3 + S^2(-)$
Aerodynamic Force	Lift	$F_L = \frac{1}{2}C_L\rho Av^2 \propto A$	$S^2(+)$
	Drag	$F_D = \frac{1}{2}C_D\rho Av^2 \propto A$	$S^2(-)$

\* Scaling Relationship (S=length scaling).

the translational  $S^3$  and rotational  $S^5$  inertias and the projected drag areas which relate to accelerations and velocities and thus the overall locomotion mode performance of the robot. The structural integrity is related to the stiffness of the components as compared to the robot mass which affects their deflection,  $S^2$ . The general properties point towards a down scaling as beneficial, in particular because reducing inertia reduces impact forces and thereby damage to the robot.

Table 2.7: Scaling: Energy Storage

Component	Details	Equation	Scaling *
Spring		$E_S = \frac{1}{2}Kx^2$	$S^3(+)$
Battery	Volume dependent.	$E_B \propto V$	$S^3(+)$
Capacitor <sup>†</sup>	Parallel plate capacitor model.	$E_C = \frac{1}{2}CV_c^2 = \frac{1}{2}\epsilon AdU_d^2$ $V_c = \frac{Qd}{\epsilon A} \therefore C = \frac{\epsilon A}{d}, V_c = U_d d$	$S^3(+)$

\* Scaling Relationship (S=length scaling).

<sup>†</sup>where the capacitor voltage,  $V_c$ , capacitance,  $C$ , total charge,  $Q$ , dielectric permittivity,  $\epsilon$ , dielectric strength,  $U_d$ , plate area,  $A$ , and gap,  $d$ , define the energy storage capacity.

The forces, Table 2.6, for which the scaling relationships are presented are those which are dominant in the MultiMo-Bat or miniature robots in general. Both the spring force,  $S^2$ , which relates to jumping, and the lift force,  $S^2$ , which relates to gliding, tend to increase the performance, whereas the friction,  $S^3$ , and drag forces,  $S^2$ , tend to reduce it. The energy storage devices, Table 2.7, present equal scaling amongst the different devices and therefore can be chosen to meet the needs of the energy application and availability. The preferred scaling direction of the forces and energy storage devices is more ambiguous as they must typically act against the inertias of the robot.

The actuators, Table 2.8, for which the scaling relationships are presented are those which are used in the MultiMo-Bat and many other miniature robots. Both actuators show the standard scaling behavior where scaling up increase forces and torque whereas scaling down increases speed. The preferred scaling direction of the actuators is therefore dependent on the requirements of the mechanisms and the actuation characteristics of the degree-of-freedom.

The robot characteristics, Table 2.9, for which the scaling relationships are presented, are those from both the locomotion mode performance and components perspectives. The primary relationships, spring energy density,  $S^0$ , and lift-to-drag ratio,  $S^0$ , scale in direct proportion, resulting in no difference between size scales and therefore no means to increase performance. However in concert with Section 2.5.2, the leg inertia,  $S^5$ , does exceed the spring,  $S^3$ , and mo-

Table 2.8: Scaling: Actuators

Actuator Properties	Details	Equation	Scaling *
<b>Electric Motor</b>			
Force <sup>†</sup>	Lorentz Force	$F_{em} = qE + qv_p \times B$	$S^2 + S^3(+)$
Torque		$T_{em} = F_{em}d$	$S^3 + S^4(+)$
	Experimental	General Motors $\propto m^1$	$S^3$ [37]
	Experimental	Maxon Motors $\propto m^{1.27}$	$S^{4.0}$ [37]
Stroke	Rotational	Continuous	$S^0(c)$
Speed		$\propto T_{em}/J$	$S^{-1} \rightarrow S^{-2}(-)$
<b>Shape Memory Alloy</b>			
Force		$F_{SMA} = \sigma_{SMA}A$	$S^2(+)$
Stroke	Linear	$L_{SMA} = 0.05L$	$S^1(+)$
Speed	Thermal energy dissipation limited.	$\propto S/V$	$S^{-1}(-)$

\* Scaling Relationship (S=length scaling).

†where the charge on the particle,  $q$ , electric field,  $E$ , particle velocity,  $v_p$ , and magnetic field,  $B$ , define the particle force.

Table 2.9: Scaling: MultiMo-Bat

Properties	Details	Equation	Scaling *
<b>Jumping</b>			
Spring Energy/Mass	Jump Height (Stored Energy)	$E_S/m$	$S^0(c)$
Motor Energy/Mass		$F_{em}x/m$	$S^0 \rightarrow S^1(+)$
Spring Torque/Leg Inertia	Rotational	$\ddot{\theta} \propto F_S L/J$	$S^{-1} \rightarrow S^{-2}(-)$
<b>Gliding</b>			
Airfoil Lift/Drag		$F_L/F_D$	$S^0(c)$
<b>Structures</b>			
Stiffness	Deflection (Robot mass)	$\delta_1$	$S^2(-)$
	Deflection (Component mass)	$\delta_2$	$S^2(-)$
<b>Actuators</b>			
Motor Torque/Mass		$T_{em}/m$	$S^0 \rightarrow S^1(+)$
SMA Force/Mass		$F_{SMA}/m$	$S^{-1}(-)$
SMA Speed		$\propto S/V$	$S^{-1}(-)$
<b>Energy Storage</b>			
Energy Storage/Mass	Battery and Capacitor	$E_{B,cap}/m$	$S^0(c)$

\* Scaling Relationship (S=length scaling).

tor,  $S^4$ , torque thus preferring a reduction in scale. Whereas the component scaling perspective presents a clear preference towards reducing the scale which also significantly reduces the inertia and, as discussed previously, the potential impact damage.

Since the primary scaling relationships show very little difference between scales, a simple isometric scaling is not sufficient to significantly improve the performance. Instead, as with biological systems [156], robots too, within the framework of the coupling parameters (Section 2.4), must exploit allometric scaling to enhance performance.

## 2.10 Discussion

The MultiMo-Bat is able to preserve over 80% of the jumping mode performance which is quite significant because of the conflicting requirements of these two locomotion strategies. Jumping locomotion requires high energy per unit mass, high stiffness, and low drag to achieve high performance while high performance gliding requires large airfoils which could create very high drag during the jumping phase as well as significantly increase the mass of the system. With all of the conflicting requirements, the system lost only 20% of its jumping mode performance and 16% of that was due to the additional mass (16.1 g) of the gliding structure. This results in a minor 4% contribution from the structural coupling between the modes. This demonstrates that there exists a very high cooperation between modes and each is able to reconfigure itself to cause almost no negative structural effect on the other. The locomotion modes are also highly integrated; sharing nearly 70% of the total system mass meaning that, of the 83.1% of the system mass necessary for the gliding mode, only a small amount, 16.8%, of it must be added to the system. Consequently, the integration strategy abstracted from the vampire bat and employed in the design of the MultiMo-Bat is successful in creating a high performance electrically power jumping and gliding robot. Shown in Table 2.10, the MultiMo-Bat has the second highest absolute jumping height even with the addition of the gliding mode. More importantly, normalizing the vertical and horizontal distances traveled by the largest dimension of the system, during the

Table 2.10: Current High Performance Jumping Robots

Robots	Jump Height (cm)	Dist. Horiz. (cm)	Norm Jump Height	Norm Dist. Horiz.	Jump Length Max (cm)	Mass (g)	Actuation	Mass Integration Metric	
<i>JUMPING</i>									
Energetic Silicon Flea	[30]	0	11.4	0	0.7	0.3	Combustion SMA		
7g Jumper	[100]	64	21.3	23.3	3	1.1	DC Motor		
7g Self-Righting Steering	[82]	138	27.6	15.8	5	6.98	DC Motor		
Buckling Robot	[83]	76	6.3	5.3	12	9.8	DC Motor		
MSU Jumper 1	[84]	62	3.4	2.6	18	14.3	DC Motor		
MSU Jumper 2	[162]	1.5	0.1	8.6	11	18	DC Motor		
Rescue Robot	[175]	55	6.9	unkn	8	20.4	DC Motor		
Sand Flea	[176]	87	10.9	11.3	8	23.5	DC Motor		
	[149]	80	3.5	unkn	23	2300	Pneumatic		
	[18]	800	17.5	unkn	45.7	4990	Combustion		
<i>JUMPING AND GLIDING</i>									
7g Jump Glider	[81]	12	0.2	0.6	49	16.5	DC Motor	1.06	
Jump Glider	[39]	125	1.8	7.1	70	30	Off-board	1.0	
Glumper	[7]	130	1.3	2	100	700	DC Motor	1.56	
Common Vampire Bat	[129]	29	3.6	unkn	8	23	Muscles	>1.69	
<b>MultiMo-Bat</b>	<b>[presented here]</b>	<b>305</b>	<b>232</b>	<b>9.8</b>	<b>7.5</b>	<b>31</b>	<b>115.6</b>	<b>DC Motor</b>	<b>1.69</b>

\* The vertical and horizontal jumping distances are normalized by the largest system dimension during the jumping phase.

\* The values for the mass integration metric are approximated for other system.

jumping phase, demonstrates that the performance of the integrated jumping mode is comparable to existing jumping systems and surpasses that of current jumping and gliding systems. This provides good evidence for proposing integration as a possible method for improving miniature robot mobility.

To further improve the performance, an analysis of the coupling parameters can indicate where the biggest improvements can be achieved. In this case the primary loss is due to the inertial coupling, which is the only unavoidable parameter, with the majority of that contained within the membranes themselves. Therefore, the largest improvement in performance would be achieved by the addition of lighter membranes.

## **2.11 Chapter Summary**

An integrated strategy, abstracted from a biological system, for the combination of jumping and gliding locomotion modes has been presented which achieves high performance at a high level of integration. This is achieved through an understanding of the two key underlying concepts of integrated design strategies. The sharing of similar structures can preserve performance through decreasing the size and weight and increasing the structural cooperation. Maximization of individual mode performance is achieved, within the integrated framework, through the utilization of regions of the design which are uncoupled from the other locomotion modes. The MultiMo-Bat, with a mass of only 115.6 grams, is shown to preserve over 80% of its independent jumping mode performance due to the integration strategy of the gliding mode. The MultiMo-Bat overcomes one of the most significant challenges to the maximization of individual mode performance as it has all actuation components on-board. These high energy actuation components can exert forces of nearly 300 N, from a device which has a mass of only 19.5 grams, to power the jumping locomotion mode to heights greater than 3 meters. It also uses airfoils with no span-wise support and unique distributed springs to generate specific airfoil tension profiles to increase gliding performance while minimizing their effect on the jumping performance. The full system achieved a

maximum glide ratio of almost 0.9 and the active wing deployment experiments achieved glide ratios of around 1.2. Most importantly, within the integrated framework, significant mechanical intelligence has been encoded into the system which allows the MultiMo-Bat to passively reconfigure components, both necessary and not, for the active mode and passively transition between jumping and gliding locomotion, thus freeing up robot controllers to focus on higher level tasks.

## Chapter 3

# MultiMo-Bat: Tailored Magnetic Springs for Detwinning of Shape Memory Alloy-Actuated Mechanisms in Miniature Robots

### 3.1 Introduction

One consequence of integrating locomotion modes is that it minimizes the need for actuators, but does not remove it. Therefore, the method by which these modes are actuated can significantly alter the mobility enhancement gained from the added mode. Thus posing a particular question, how best are degrees-of-freedom (DOFs) and particularly actuated ones added. The possible solutions to this problem are highly dependent on the size scale of the robotic system. Whereas large scale robots can better tolerate the addition of electromagnetic (EM) actuators, miniature robots cannot, due to the EM actuator's size, weight, and actuation characteristics. Instead, miniature robots rely more and more on smart material based actuation strategies. These smart material actuators include: shape memory alloy (SMA) actuators, dielectric elastomer actuators (DEA), ionic polymer-metal composites (IPMC) actuators, and recently buckling elastomeric beam actuators [164] and coiled polymer muscles [53]. However, they too have deficiencies which limit their applicability. Common deficiencies of smart material actuators are unidirectional actuation, force drop-off at the ends of their stroke, and, for thermal based actuation, low

efficiency. A tailored magnetic spring could be designed to increase the work output by providing the minimum necessary return force, increase the stroke by increasing the force at the extremes of actuation, and increase the efficiency by providing a holding force so the actuator can be turned off while adding application specific functionalities. However, the design flexibility of traditional springs limits their ability to satisfy these requirements. We propose a methodology for tailoring custom magnetic springs, based on sets of permanent magnets, to the characteristics of SMA actuators and the desired functions of the mechanism, thereby facilitating inclusion of these mechanisms into the jumping-gliding robot, MultiMo-Bat (Fig 3.1) [159, 160], as well as more miniature robots in general.

Permanent magnets have found their way into a wide variety of applications from magnetic bearings [9, 65, 104, 146, 167], latches [11], springs [106, 122], motors [131, 144], and levitation systems [26] to vibrational energy harvesting [8, 20, 125, 165, 171] and many other fields as well. Using magnets to impart forces has several advantages over other principles including: non-contact force, no material fatigue, and unique force-displacement relationships [34]. This widespread use of magnets has resulted in many works over the decades to understand the fields produced and the forces and torques exerted for cylindrical [1, 130, 151], cylindrical arrays [152], cuboidal [1, 3], ring [117, 118], thin coils [33], and arbitrary [36] geometries. Design of these types of systems generally begins with preset or preconceived magnet configurations and/or geometries with known behaviors. These preconceptions about configuration and/or geometry tend to limit the applicability and flexibility of the resulting solution. Here, the design problem is approached without these restrictions. This chapter proposes a methodology to determine a magnet configuration which will produce a desired magnetic force-displacement relationship or tailored magnetic spring to suit any application.

These tailored magnetic springs do have several differences from traditional springs, as seen in Fig. 3.2. Instead of mounting between opposing surfaces, the magnets used to create the force-displacement relationship are embedded into the surfaces of the mechanism. The scaling

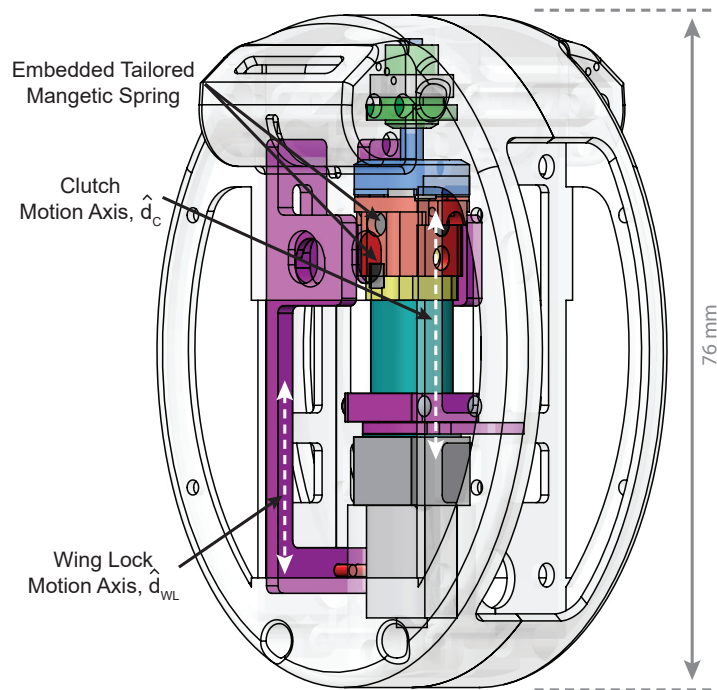


Figure 3.1: CAD model of the MultiMo-Bat with the shape memory alloy-actuated energy storage and wing locking mechanisms; both of which contain a tailored magnetic spring. The energy storage mechanism requires six sets of magnets to produce the desired force while the wing locking mechanism requires only four.

relationship of magnetic force also differs from traditional springs. Depending on the position and the geometry of magnetic object, the scaling relationship can change however, a good approximation comes from Biot-Savart's law - fully compliant with Maxwell's equations - where the magnetic field scales with  $B \propto L^{-2}$ , assuming only the distance from the object scales [154]. Therefore, magnetic force scales with  $F \propto L^{-3}$  and the magnetic force gradient with  $F' \propto L^{-4}$ . Thus significant variation in force is possible, albeit over relatively short distances; perfect for typical SMA actuators used in miniature robots. In practice several millimeters and below is a good range. However, theoretically any well-defined function of force vs. displacement can be created to satisfy the needs of a miniature robot mechanism or smart material actuator. Combined with traditional springs, these tailored magnetic springs can add functionality to a broad range of applications.

Despite the current challenges, SMA actuators have been implemented on many robotic plat-

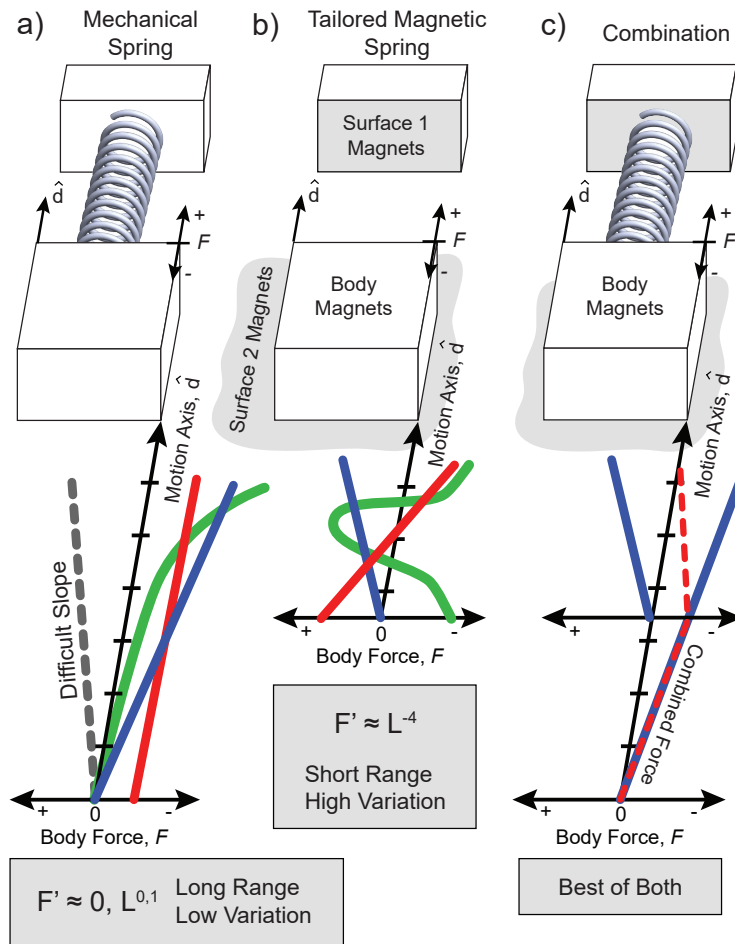


Figure 3.2: **a)** Mechanical springs are typically mounted between opposing surfaces and create force-displacement relationships which tend to resist the motion (negative slope). For linear and non-linear springs the scaling of the change in force,  $F'$ , favors a longer displacement range but with low variation. **b)** Tailored magnetic springs are embedded into surfaces which move in relation to each other; such as surface 1 and surface 2. These surfaces have opposing surfaces on the body which will also have embedded magnets. The scaling of the change in force,  $F'$ , favors a very short displacement range but with very high variation. **c)** Both mechanical and tailored magnetic spring have areas in which they are most applicable, however, the combination can take advantage of both types and add significant functionality to a spring system. **Note a,b)** The red, green, and blue lines are examples of possible force-displacement relationships for mechanical and magnetic springs, respectively. **Note c)** The example combination curve (dashed red) shows a possible tailored magnetic spring with energy storage or damping characteristics. ©[2017] IEEE

forms. As primary actuators, SMA has been implemented in crawling [88, 91, 116], walking/running [60, 80, 150], climbing [29, 54, 67, 76, 77], swimming [123, 134], and jumping [58, 78, 79, 100] robots. Shape memory alloy has also been used in soft robots [103, 132] be-

cause of its low stiffness, and medical devices [49, 59, 69, 75, 92, 97, 148] because of its small size and high force-to-weight ratio. High dimensional robotic platforms such as reconfigurable robots [98, 168, 169] and robotics hands [27, 28, 86] also make use of the miniature size to integrate large numbers of actuators. A number of groups are also exploring methods for increasing control, reliability, cycle time, and stroke of SMA actuators [25, 62, 71].

The added functionality of tailored magnetic spring paired with a smart material actuator may facilitate increased performance in a variety of miniature robotic platforms. The smallest and lightest scale of these miniature robots [79, 99, 100, 137, 172] may benefit from increased actuator work output. Whereas, miniature robots exploring enhanced mobility [12, 45, 63, 77, 82, 95, 102, 147, 178], reconfigurable robots [24], construction robots [155], and deformable robots [66], which implement EM actuators for the main energy input, may find benefit in added DOFs with low weight high function actuators. In certain cases, the intended environment itself imposes restrictions to the use of EM actuators and thus requires the use of smart materials such as soft robots [21, 90, 124, 132, 135] which must remain soft, medical robots [50, 105, 119, 166] which must fit in the in-vivo environment, swimming robots [114, 173] which must ensure electrical isolation from the fluid, and high DOF robots [28] which cannot fit sufficient quantities of EM actuators. All these systems may benefit from the added functionality afforded by a tailored magnetic spring.

The chapter is organized as follows: Section 2 begins by introducing the concept of magnetic segments and, through combination of these segments, tailored magnetic springs (TMS), and Section 3 discusses how these segments can relate to the characteristics of shape memory alloy-actuated mechanisms in miniature robots. Sections 4 and 5 presents the design strategy for relatively simple TMS and the adaptability of a TMS afforded by the irreducible set, respectively. Sections 6 and 7 develop the energy storage and wing lock mechanisms, respectively. Section 8 and 9 experimentally characterize the mechanism and the performance improvement to the MultiMo-Bat, respectively. Section 10 introduces the extension of the custom complex spring

design methodology where Sections 11 and 12 present the analytical and numerical portions of the methodology, respectively. Section 13 compares and discusses the results of the methodology using different segment sets. Sections 14 and 15 present estimations of mounting space and extensions of the methodology to any interaction force and magnetic fields, respectively. Finally, Section 16 discusses the strengths of the methodology and Section 15 summarizes the chapter.

## Nomenclature

$d$	- Desired displacement.
$\hat{d}$	- <b>motion-axis</b> : Unit displacement vector.
$K$	- Total displacement or evaluation points.
$\vec{F}_i$	- <b>Force vs. displacement (f-d) function</b> : Discretized.
$\mathbf{S}_i$	- Sub-matrix of segments from $\vec{F}_i$ .
$\vec{s}_{i,j}, \vec{s}_n$	- <b>Segment</b> : Column $j$ of $\mathbf{S}_i$ or $n$ of $\mathbf{S}$ .
$a_{i,j}, a_n$	- Absolute start point of $\vec{s}_{i,j}$ or $\vec{s}_n$ .
$b_{i,j}, b_n$	- Absolute end point of $\vec{s}_{i,j}$ or $\vec{s}_n$ .
$\mathbf{S}$	- <b>Segment Set</b> : $\mathbf{S} = [\mathbf{S}_1, \mathbf{S}_2, \dots, \mathbf{S}_i]$ .
$N$	- Total number of segments, $\sum_i \sum_j 1$ .
$\vec{q}$	- <b>Solution</b> : Total segment quantity vector.
$q_{i,j}, q_n$	- Quantity of $\vec{s}_{i,j}$ or $\vec{s}_n$ .
$\mathbf{Q}$	- <b>Family of Solutions</b> : Matrix of possible solutions.
$d\vec{f}$	- The desired f-d relationship.
$c\vec{f}$	- The calculated f-d relationship of a solution $\vec{q}$ .
$m\vec{f}$	- The experimentally measured f-d relationship of a tailored magnetic spring.
$^{20}\mathbf{S}$	- Small segment set, 20 segments.
$^{3000+}\mathbf{S}$	- Large segment set, greater than 3000 segments.
<b>Magnet Set</b>	- At least one fixed magnet and one constrained magnet which is able to move along the motion-axis, $\hat{d}$ .
<b>Good Solution</b>	- A manufacturable solution with minimum magnet quantity.

## 3.2 Concept Development

To illustrate the proposed concept, we first consider the magnetic force curves,  $\vec{F}_i$ , which are produced by moving one magnet in relation to another, as seen in Fig. 3.3a; Fig. 3.3b points 1-3 present the force along the motion-axis as the magnets approach axial alignment. In general, the force between two magnets will have components in all 6-degrees-of-freedom however, with the

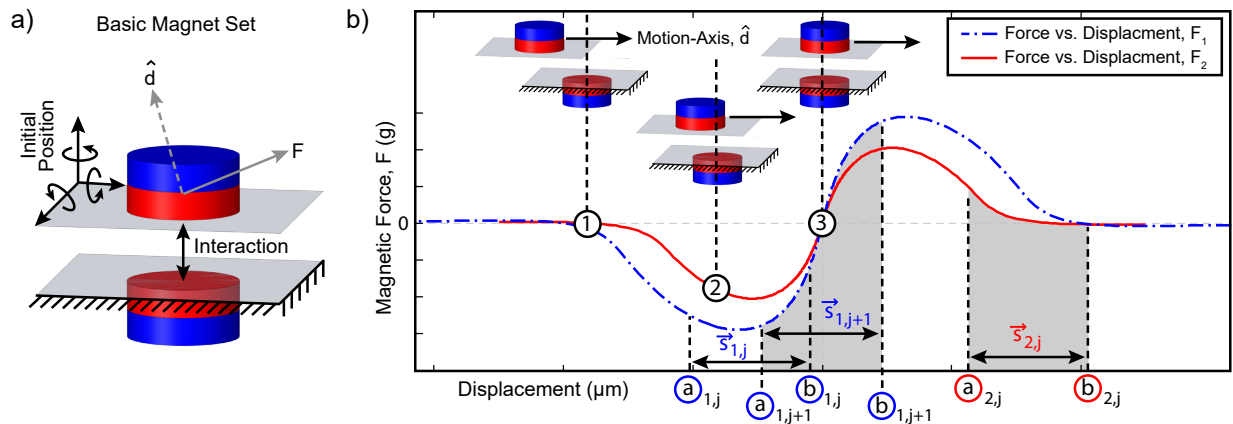


Figure 3.3: **a)** A basic magnet set contains at least one fixed magnet and one constrained magnet which is able to move along the motion-axis,  $\hat{d}$ . The initial position can be chosen arbitrarily. **b)** Two example magnetic force-displacement curves,  $\vec{F}_1$  and  $\vec{F}_2$ , are presented each with a few segments,  $\vec{s}_{i,j}$ , highlighted along with their respective start,  $a_{i,j}$ , and end,  $b_{i,j}$ , points. The difference between  $\vec{F}_1$  and  $\vec{F}_2$  is produced by varying the diameters of cylindrical magnets however, any configuration of magnets would create a unique  $\vec{F}_i$ . Due to the assumed constraints on all axes except the motion-axis, the forces presented are only those which coincides with the motion-axis direction. ©[2017] IEEE

assumption of a prismatic joint, these are limited to 1-DOF along the motion-axis. Fig. 3.4a, presents two different configurations of magnets and their respective motion,  $\hat{d}$ , and force,  $\hat{f}$ , axes; where each line corresponds to a different magnet diameter. These 2 configurations share the same origin and geometry, however the difference in the motion and force axes, leads to the difference in the resulting magnetic force-displacement curves.

We will also consider the 1-DOF translational forces,  $\vec{F}_i^*$ , produced perpendicularly to the motion-axis; as seen in Fig. 3.4b. Only configuration 2 produces a perpendicular force and these forces will be used to add additional functionalities to the tailored magnetic springs.

To generate the force curves,  $\vec{F}_i$  and  $\vec{F}_i^*$ , shown in Fig. 3.4a at distances near contact for arbitrary magnet sets, a simulation was created using a distributed amperian model (MATLAB) [52]. The simulation approximates the total force between arbitrary magnets by discretizing them into thousands of small volumes,  $d\tau$ , the smallest of which, for our purposes, are approximately  $100^3 \mu\text{m}^3$ ; as seen in Fig. 3.5, with Appendix F showing a actual distribution. Others have looked at optimizing computational time through optimal dipole [93] and minimal node [10]

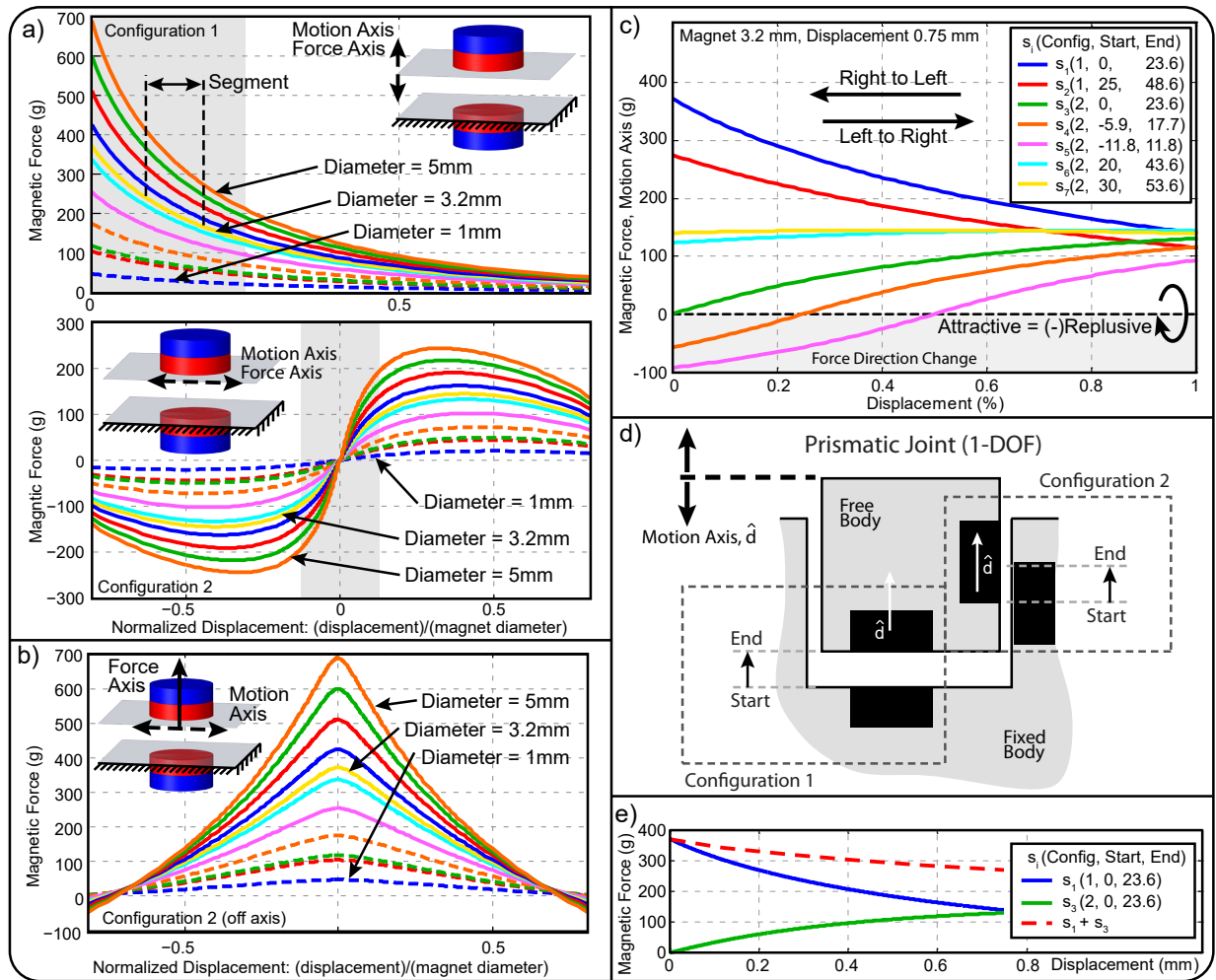


Figure 3.4: **a)** Configuration 1 - calculated magnetic force-displacement curves for axially aligned and displaced magnet sets of various diameters. Configuration 2 - calculated magnetic force-displacement curves for axially parallel and perpendicularly displaced magnet sets of various diameters. **b)** Configuration 2 - Same motion direction as configuration 2 in (a), but the force presented is now that which is normal to the surface. **Note:** The magnetic force-displacement curves,  $\vec{F}_i$  and  $\vec{F}_i^*$ , shown are for repulsive magnet sets. Magnet set diameters: 1, 1.5, 1.6, 2, 2.5, 3, 3.2, 3.5, 4, 4.5, and 5 mm from lowest to highest force respectively; all with a thickness=1.6 mm, material: NdFeB grade N52, and initial gap=50  $\mu\text{m}$ . **c)** Extracted segments for constructing tailored magnetic springs. Each segment has 4 different transformation of the forces-displacement relationship which can be used including: repulsive right-left (R-RL), repulsive left-right (R-LR), attractive right-left (A-RL), and attractive left-right (A-LR); segments shown are R-LR. **d)** A prismatic joint (1 degree-of-freedom) with mounting examples of both configuration 1 and configuration 2 magnet sets. The start and end points represent the start and end positions of the relative motion between the magnets of each configuration. **e)** The individual segments,  $\vec{s}_1$  and  $\vec{s}_3$ , are presented along with the combined force,  $\vec{s}_1 + \vec{s}_3$ , which would be exerted on the free body in (d).

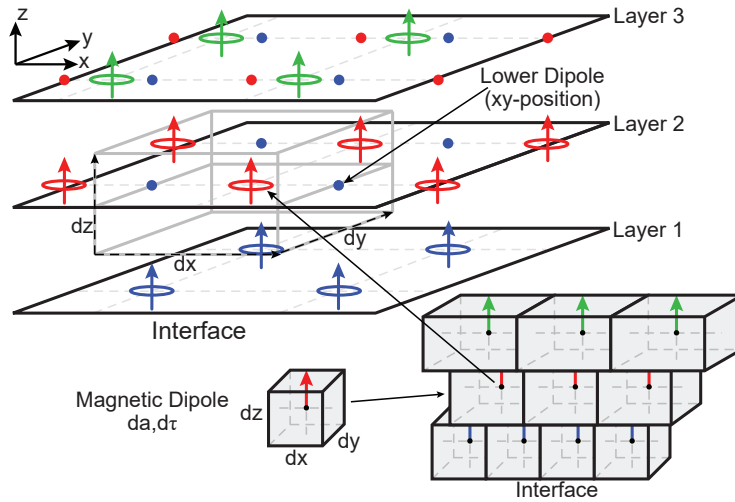


Figure 3.5: An example dipole configuration demonstrating the dipole staggering, volume of each dipole, and dipole layering in the magnet. From the interface: layer 1 (blue), layer 2 (red), and layer 3 (green). Actual example distribution shown in Appendix F. ©[2017] IEEE

configurations for particular geometries, or geometries which are well approximated by dipole fields [111], however our methodology is independent of the method or model used. So we will instead give some general design rules for these distributed dipole type models. These rules tend to reduce the number of dipoles necessary and maintain accuracy. First, the  $xy$ -area,  $da = dxdy$ , of the individual volumes should be scaled linearly with distance from the interface,  $da \propto L^1$ . This ensures the volume sizes never scale faster than the magnetic field which can scale with  $B \propto L^{-1,-2,-3}$ , depending on position and configuration. Second, in each layer of the magnet, as seen in Fig. 3.5, the dipole distribution should not be aligned; rather, using a bisection method, the dipoles of each subsequent layer should be positioned between, in the  $xy$ -plane, the dipoles of all the previous layers. This significantly reduces fictitious ripples in the net magnetic field. At the center of each volume is assumed an infinitesimal current loop (Ampère's model) with a magnetic dipole moment equal to the magnetization multiplied by the enclosed volume,  $d\tau$ . This assumption allows us to approximate the current loop as a magnetic dipole, as the distance between the loops within the separate magnets of a set is much greater than the diameter of the loop itself. This is the fringing region of the magnetic field and is therefore well captured by the dipole field approximation [52]. From the magnetic field (Appendix F eq. F.1) the 3-DOF forces

between two distant dipoles can then be calculated (Appendix F eq. F.2 [170]). Summing the forces from all dipoles in each magnet, at displacement  $k$ , dotted into the motion-axis,  $\hat{d}$ , gives the force as,

$$\vec{F}_i(k) = \left( \sum_u \sum_v g(\vec{r}_{u,v}(a_i) + \frac{k-1}{K-1}(b_i - a_i), \vec{m}_u, \vec{m}_v) \right) \hat{d} \quad (3.1)$$

where  $u$  and  $v$  are the indices of the magnetic dipoles in the two magnets,  $a_i$  is the start and  $b_i$  is the end point of  $\vec{F}_i$ ,  $\vec{r}_{u,v}(a_i)$  is the distance vector between them at the start of motion, and  $\vec{m}_u$  and  $\vec{m}_v$  are the magnetic moment vectors of the dipoles in the fixed and free magnets, respectively.

**Remark 1:** *This design methodology is independent of the method or model used to determine the forces,  $\vec{F}_i$ 's. Any discretizable method or model will suffice. The computational time is also independent of the model, and therefore it is not necessary to optimize the model for each shape.*

By selecting a configuration, magnet diameter, and motion start,  $a_{i,j}$ , and end,  $b_{i,j}$ , point (Fig. 3.3b) from Fig. 3.4a, we can extract through interpolation, from a particular magnetic force curve,  $\vec{F}_i$ , a segment,  $\vec{s}_n$ ; as seen in Fig. 3.4c where the legend presents the configuration and the relative start and end point as a percent of the magnet diameter for each segment. **Remark 2:** *All segments must have the same absolute displacement as the SMA actuator, assuming no transmission, and each segment is produced by its own independent set of magnets; the segments in Fig. 3.4c were all taken from the 3.2 mm diameter set with 750  $\mu\text{m}$  displacement. **Remark 3:** *Each segment has 4 different transformation of the force curve which can be used including: repulsive right-to-left (R-RL), repulsive left-to-right (R-LR), attractive right-to-left (A-RL), and attractive left-to-right (A-LR); the segments shown are R-LR. Flipping the polarity of the magnets to attractive, produces the negative of those presented whereas, changing the mounting position can determine whether the forces progress from left-to-right or right-to-left.**

To physically realize the segment forces, the two magnets which create the segment are embedded into the fixed and free bodies of a prismatic joint with the motion axes aligned at their relative start position. Placing stops at the start and end positions of the motion, creates a simple magnetic spring; see Fig. 3.4d for example mounting positions for both configurations.

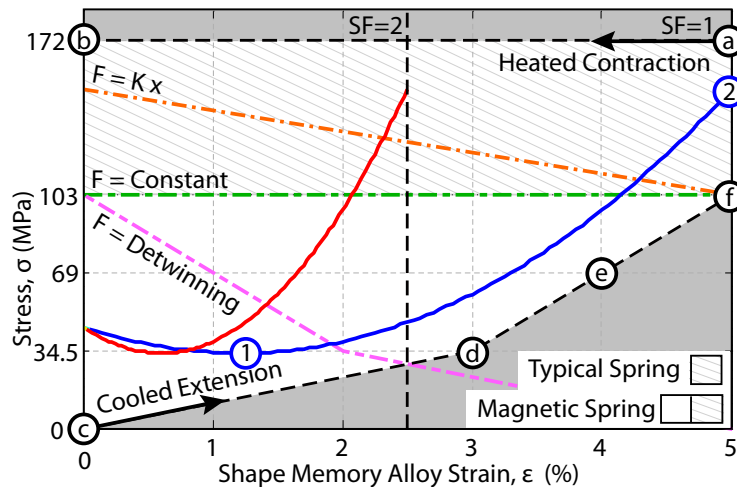


Figure 3.6: Shape memory alloy (SMA) stress-strain boundaries are shown along with mechanical (orange, linear and green, constant) and magnetic (blue, safety factor=1 and red, safety factor=2) spring examples to illustrate the detwinning stress regions for the particular spring types. Boundary values are for Nitinol (DynaAlloy Inc, Flexinol) [64]; however, this is just one example of a shape memory alloy. Upper bound (a,b) is the maximum pull stress of the SMA. Lower bound (c,d,e,f) is the stress required to recover a given amount of strain when cooled. Several beneficial detwinning stress characteristic are labeled as: 1) greater than lower boundary stress for strain recovery, 2-to-1) snapping behavior, and 2) high holding force. Magnetic springs have a potential to allow for greater actuator work than typical mechanical springs.

A good approximation of an initial median magnet diameter for a particular application can be calculated as,  $D_{magnet} = \frac{d}{0.25}$ . This comes from the behavior of the magnetic force curves themselves, where the most significant change in force occurs over displacements of approximately 25% of the magnet diameter; shown as gray regions in Fig. 3.4a. The dimensions of the MultiMo-Bat, Fig. 3.1, dictate an actuator displacement of  $d \approx 750 \mu m$  with a safety factor of 2; leading to an approximate median magnet diameter of 3 mm and a selected magnet diameter of 3.2 mm (K&J Magnetics; NdFeB, Grade N52). Fig. 3.4c presents a limited segment set but this set provides sufficient building blocks to account for many characteristics of SMA actuated mechanisms necessary for the MultiMo-Bat and miniature robots.

### 3.3 Characteristics for Shape Memory Alloy-Actuated Mechanisms

The unidirectional actuation behavior of SMA is caused by the existence of two energy minima, when the SMA is in the martensitic (cooled) state; twinned and detwinned martensite. In the absence of an applied load, SMA will cool to the twinned martensite state which, when heated, will produce nearly no strain. To be used as an actuator, the desired cooled state is detwinned martensite which, when heated above the austenitic transition temperature, 70 to 90 °C, will produce a restoring stress and strain of approximately 172 MPa and 5%, respectively [64].

Detwinning the martensite lattice is typically achieved through the use of either elastic elements or another actuator positioned to pull in the opposite direction (antagonistic actuation). Using typical elastic elements (Fig. 3.6 orange line) tends to reduce the available work output as the resistance tends to increase from the maximum necessary detwinning force (Fig. 3.6 point *f*). Whereas, antagonistic actuation preserves the maximum work output but at the cost of no holding force (Fig. 3.6 pink line). Therefore, to hold position, the actuator must remain active, which consumes significant power and is inefficient. Both tend to create increasing resistive force over the actuation stroke, thus slowing the transition between states. A tailored magnetic spring can be designed to capture the best of both elastic elements and antagonistic actuation while integrating additional features to improve the performance of a SMA actuated mechanism in a miniature robot.

#### 3.3.1 Detwinning Force

Figure 3.6 presents a basic cyclic SMA stress-strain relationship, as well as the typical region of mechanical springs (hatched region). Magnets, however, having much more variable force-displacement relationships, can better mimic the detwinning force-displacement relationship of SMAs. Using the properties of the purchased nickel-titanium alloy (DynaAlloy Inc, Flexinol) as

a base line, a function is fit to the detwinning stress relationship,  $\sigma_d$ , resulting in,

$$\sigma_d = 43250 \left(\frac{x}{L}\right)^2 - 74 \left(\frac{x}{L}\right), MPa \quad (3.2)$$

where,  $L$  is the length of the SMA and  $x \in [0, 0.05L]$ . The complete actuation cycle, points  $a$ -to- $f$ , is shown in Fig. 3.6.

Ideally, the resistive force would be zero during actuation, however, without disconnecting the detwinning element, the best option is antagonistic actuation, as it directly mimics the SMA's force-displacement relationship,  $\sigma_d$ . Comparing this to using a constant spring,  $\sigma_{cs} = 103 MPa$  (Fig. 3.6 green line), for detwinning, gives a ratio of the difference in available work as,

$$\rho_w = \frac{A_{SMA} \int_0^{0.05L} (\sigma_a - \sigma_d) dx}{A_{SMA} \int_0^{0.05L} (\sigma_a - \sigma_{cs}) dx} = 2 \quad (3.3)$$

where,  $\sigma_a = 172 MPa$  is the actuation stress and  $A_{SMA}$  is the cross-sectional area of the SMA. Suggesting that there is nearly 100% more available work output, beyond that produced by using a constant detwinning spring. In particular, segments with positive slopes can achieve this behavior, which is difficult for elastic elements, as seen in Fig. 3.6. Segments  $\vec{s}_3$  to  $\vec{s}_5$  (Fig. 3.4c) are all good examples of this type of behavior; through changing the direction to right-to-left or attractive magnets, further segments are also well suited to this behavior.

### 3.3.2 Holding Force

The inefficiency of shape memory alloys stems from their thermal based actuation and need to sustain power to sustain force; this is a major drawback of antagonistic actuation. However, if the start and/or end positions are stable, the actuator need only to activate briefly to switch the state. A high holding force at these stable points, provides further benefits as it maximizes the actuators stroke by forcing the prismatic joint to the actuation limits; Fig. 3.6 point 2 shows this behavior in a tailored magnetic spring. Segments  $\vec{s}_1$ ,  $\vec{s}_2$ , and  $\vec{s}_5$  all undergo large changes in force and are therefore good candidates for increasing the force at the start or end points of the motion.

### 3.3.3 State Transition

For many applications SMA actuators have only two states, and in certain cases it is necessary to switch between these two states quickly. Elastic elements and antagonistic actuation make this difficult as the force tends to increase with displacement, resulting in a slow progression from one state to the other (Fig. 3.6 orange and pink lines). A tailored magnetic spring may be able to instead reduce the resistive force with displacement (Fig. 3.6 blue and red lines). Therefore, once the critical force is reached, the actuator will jump between the two states; an example is shown in Fig. 3.6, where the tailored magnetic spring (blue line) will jump from point 3 to point 1. With the exception of  $\vec{s}_6$  and  $\vec{s}_7$ , all the segments in Fig. 3.4c can create this transition behavior either unidirectionally or bidirectionally. This is particularly useful for coupling devices where a slow progression may result in some intermittent contact between engagement and disengagement, causing damage or reduced performance.

### 3.3.4 Off-Axis Force and Torque Equalization

Up to this point the resulting forces in the off-axis directions and torques have not been considered. This can result in high off-axis forces and torques and thus potentially high friction between the constraining features of the prismatic joint, resulting in low efficiency. Multiplying the selected segments  $\vec{s}_n$  by an even integer gives,

$$\begin{aligned} 2\vec{s}_n &= 2\vec{s}_n \\ 4\vec{s}_n &= 4\vec{s}_n \end{aligned} \tag{3.4}$$

effectively doubling or quadrupling each segment; and therefore the magnet set used to produce it. Through symmetric placement of the resulting magnet sets, the other 2-DOF forces and 3-DOF torques can be equalized, thus reducing friction and cogging torques on the mechanism. However, this may not be a stable equilibrium requiring the prismatic joint to maintain its position.

### 3.3.5 Actuator Mounting

All components must be constrained, in some form or fashion, to part of the existing structure. Therefore, it is advantageous to create the constraints via the magnetic forces from the vary magnets used to produce the tailored magnetic spring, instead of additional features. This provides several addition benefits including: shock absorption, deterministic friction, and auto alignment. Since the device no longer relies on rigid constrains, impulses to the system will be damped by the friction of the mounting surface; lessening the forces on the mechanism itself. The friction is much more deterministic as the only interaction is with the mounting surface; rather than constraint features. Finally, since mounting requires a stable equilibrium, once a critical distance is reached the mechanism will auto align and auto assemble itself to the proper position and orientation and maintain this until the attachment force is exceeded.

To achieve this the segments,  $\vec{s}_n$ , must contain both the motion-axis and off-axis forces as,

$${}^* \vec{s}_n = \begin{bmatrix} \vec{s}_n \\ \vec{s}_n^* \end{bmatrix} \quad (3.5)$$

where,  $\vec{s}_n^*$  represent the forces in the perpendicular axis. Of the two configuration presented, only configuration 2 produces force perpendicular to the motion-axis; as seen in Fig. 3.4b. These are the forces which will be used to constrain the mechanism. The A-LR segments  $\vec{s}_6$  and  $\vec{s}_7$  both create this behavior with  $\vec{s}_6$  having higher mounting force and  $\vec{s}_7$  slightly more linear motion-axis force.

## 3.4 Tailored Magnetic Spring Design

To design a tailored magnetic spring several different segments are combined together; this is physically represented in Fig. 3.4d, where segments  $\vec{s}_1$  and  $\vec{s}_3$  are integrated into the same prismatic joint. To allow for summation via superposition however, the interaction between segments (i.e. magnet sets which create each segment) must be negligible. **Remark 4:** *This implies that each magnet set may be positioned arbitrarily on non-ferromagnetic bodies, with motion axes*

aligned, but at distances from one another in which their mutual interactions are relatively weak. The resulting net calculated magnetic force,  ${}^c\vec{f}$ , will be the sum of the forces of the individual segments; as seen in Fig. 3.4e. This provides a great deal of flexibility in mounting a tailored magnetic spring in an intended mechanism and greatly facilitates manufacturing.

Selecting the proper segments can generally be done manually from the magnetic force-displacement curves,  $\vec{F}_i$ , or from those already selected in Fig. 3.4c. Begin with the segment,  $\vec{s}_n$ , which best represents the desired force,  ${}^d\vec{f}$ , then add additional segments to tune the overall behavior. In either case, typically only a few different segments are necessary as magnetic force-displacement relationships are well suited to SMAs. However, the selection process can also be mathematically formulated as,

$$\begin{bmatrix} \vec{s}_1 & \vec{s}_2 & \vec{s}_3 & \vec{s}_4 & \vec{s}_5 & \vec{s}_6 & \vec{s}_7 \end{bmatrix} \begin{bmatrix} q_1 \\ q_2 \\ q_3 \\ q_4 \\ q_5 \\ q_6 \\ q_7 \end{bmatrix} = \begin{bmatrix} f_1 \\ f_2 \\ f_3 \\ f_4 \\ f_5 \\ f_6 \\ f_7 \\ f_8 \\ f_9 \\ f_{10} \\ f_{11} \\ f_{12} \\ f_{13} \\ f_{14} \\ f_{15} \\ f_{16} \\ f_{17} \\ f_{18} \\ f_{19} \\ f_{20} \end{bmatrix} \quad (3.6)$$

where,  ${}^d\vec{f}$  represents the known desired force and  $\vec{q}$  the unknown quantities of each segment. The segments,  $\vec{s}_1$  to  $\vec{s}_7$ , represent the segment forces in Fig. 3.4c, evaluated at 20 points along the displacement with a uniform separation of  $39.5 \mu\text{m}$ . Higher displacement resolution tends to increase the reproduction accuracy, but at the cost of potentially increasing the quantity of magnet; we recommended starting with the fewest points necessary to define the shape of the desired force,  ${}^d\vec{f}$ , and increase as needed. The solution is then a linear combination of the

columns that best represents the desired force,  ${}^d\vec{f}$  [141]. Depending on the column space of the segment matrix and rounding of the calculated quantities, the solution may not be exact, leading to a calculated force,  ${}^c\vec{f} = \mathbf{S} \text{round}(\vec{q})$ , which differs from the desired force,  ${}^d\vec{f}$ .

As the number of segments increases, so too does the complexity of the analytical solution. For detwinning SMA actuated mechanisms, the complexity can outweigh the utility at large segment sets due to the nature of this solution, which tends to produce small fractional quantities. However, this can provide a quick check of the likelihood that the desired force,  ${}^d\vec{f}$ , can be produced, given the segments selected; very large or very small quantities can indicate that different segments may be required. For very complicated tailored magnetic springs a more rigorous custom complex spring design methodology will be presented in a later section which can manage very large segment sets.

### 3.5 Irreducible Set

An irreducible set of segments is calculated as the segment quantities,  $\vec{q}$ , divided by the greatest common divisor of the quantities,  $GCD(\vec{q})$ . This produces the minimum integer quantities,  ${}^l\vec{q} = \vec{q}/GCD(\vec{q})$ , of the segments while preserving much of the force characteristics in the resulting force-displacement curve,  ${}^l\vec{f} = \mathbf{S} {}^l\vec{q}$ . Once an irreducible set is identified which exhibits useful characteristics, we can adapt it to other situations and fine tune the behavior for specific applications with several types of transformations including: force magnification, stretching, and tuning.

Magnifying the force,  ${}^l\vec{f}$ , is achieved by simply multiplying the irreducible set by a positive integer  $n \in [\mathbb{Z}]$  whereas multiplying by a negative integer both magnifies and flips the direction of the force. Monostable forces,  ${}^l\vec{f}$ , will have only a change in the magnitude while the slope will be preserved, whereas forces,  ${}^l\vec{f}$ , with multiple stable points will see increases in both magnitude and slope.

Stretching the displacement over which the force,  ${}^l\vec{f}$ , is exerted, is achieved by increasing

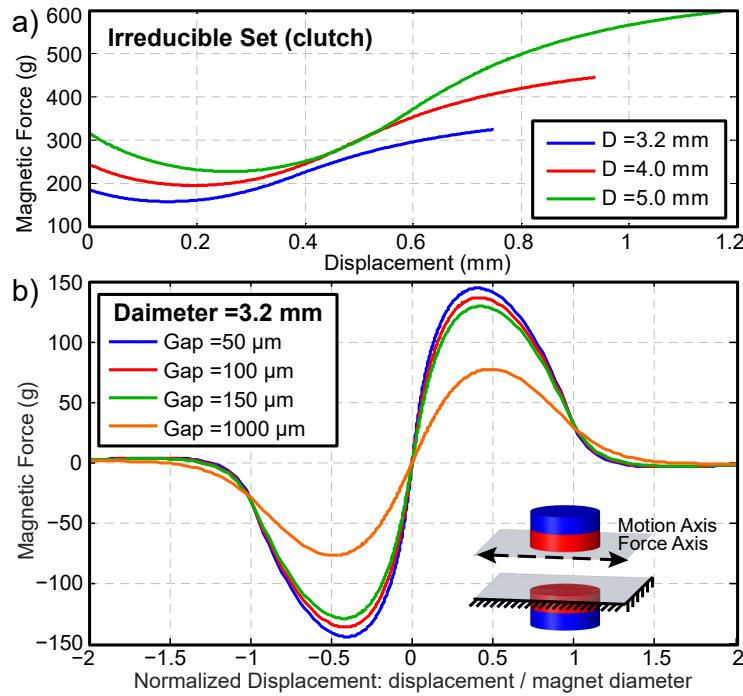


Figure 3.7: **a)** Increasing the magnet diameter in proportion to the displacement can allow traits designed for a particular displacement to be transferred to another. **b)** Varying the gap between the faces varies the force, while preserving much of the overall behavior.

the magnet diameters in direct proportion to the increase in the desired displacement; as seen in Fig. 3.7a. Compression can be achieved though decreasing the magnet diameters and displacement. This procedure adds significant flexibility to the irreducible set, as it transfers much of the force characteristics to different displacements; although, both slope and magnitude will be modified.

Tuning the characteristic of the force,  ${}^I\vec{f}$ , is accomplished in several ways including changing the initial gap, thickness, and magnetization, of the magnet sets. The magnetic forces,  $\vec{F}_i$  and  $\vec{F}_i^*$ , presented in Fig. 3.4a,b represent the maximum achievable forces which occur at contact (coating thickness  $\approx 50 \mu m$ ) for 1.6 mm thick, NdFeB Grade N52 magnets. Increasing the initial gap (Fig. 3.7b), decreasing the thickness, and decreasing the magnetization all result in a decrease in the magnitude of the force,  ${}^I\vec{f}$ ; increasing the force can be achieved through increasing the thickness.

While both stretching and tuning require a recalculation of the magnetic force curves,  $\vec{F}_i$  and

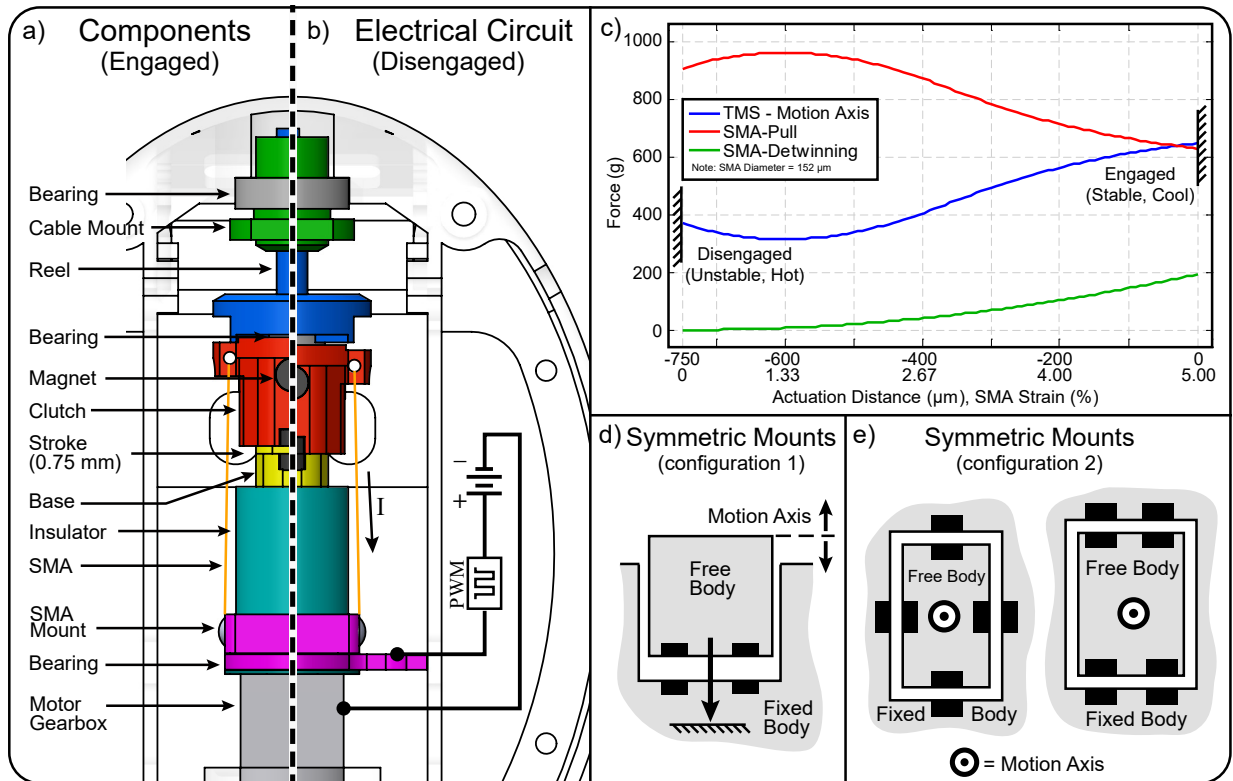


Figure 3.8: **a)** The components of the actuator are labeled in the engaged state; load bearing components are aluminum (6061-T6). **b)** The electrical connections are shown in the disengaged state. **c)** The force-displacement curve of the tailored magnetic spring along the motion-axis direction. Note: figure is for 5 % strain, whereas robot uses 2.9 %. **d)** 2D representation of a stable mount for the configuration 1 magnet sets. **e)** 2D representation of two possible stable mounts for the configuration 2 magnet sets.

$\vec{F}_i^*$ , for exact determination of the force,  ${}^I\vec{f}$ , magnification does not. Therefore, magnification, especially for monostable forces, can be used to create desired symmetries after the force is calculated, to balance off-axis forces and torques. This greatly facilitates design as it removes the need to consider symmetry during the design process.

### 3.6 Energy Storage Mechanism Design

The jumping locomotion mode of the MultiMo-Bat is initially powered by an energy storage mechanism (ESM) that was developed previously [160]. However, as this system was not fully self-contained, its reliability and robustness suffered. Employing a tailored magnetic spring, a

new ESM is developed which can produce a maximum of  $348\text{ N}$  at  $6\text{ V}$  to extend the main power springs at a mass of under  $22\text{ g}$ ; which includes the highly geared 298:1 DC motor (Solarbotics GM14a). As before, to vary the jumping performance and improve mobility, the stored energy is actively released via an SMA actuated clutch; as seen in Fig. 3.8a,b. Robustness and reliability are ensured with a safety factor of 2 applied to the SMA length which, given the available mounting distance, results in a total stroke of  $750\text{ }\mu\text{m}$  and an interlocking distance of  $500\text{ }\mu\text{m}$ . A prismatic joint constrains the motion of the device, so focus is placed on tailoring the magnetic spring to the desired characteristics.

### 3.6.1 Desired Characteristics and Tailored Magnetic Spring

The desired characteristic for detwinning the SMA actuated clutch are those of Sections 3.3.1-4. Characteristic 3.3.1 must be satisfied to achieve repeated actuation however, this should be tailored to the detwinning stress-strain relationship to maximize the work output of the actuator. Characteristic 3.3.2 must be included because of the  $500\text{ }\mu\text{m}$  engagement distance; the high holding force reduces the chance of premature disengagement. Characteristic 3.3.3 allows the clutch to jump between engagement and disengagement, avoiding any undesirable contact between the reel and clutch during the energy release process; and characteristic 3.3.4 ensures maximum efficiency through minimization of friction. Traditional elastic elements could be used to achieve characteristic 3.3.2 and 3.3.4, however, 3.3.1 and 3.3.3 are much more difficult.

Permanent magnets mounted between the reel and clutch, configured to attract each other (A-RL segment  $\vec{s}_1$ , Figure 3.4c), would generate the desired characteristics. However, during the energy release process, the reel spins rapidly and the clutch remain stationary. This creates a significant torque ripple which is transmitted to the reel and reduces the jumping performance. Instead, the tailored magnetic spring must be mounted on components which always revolve together; in this case that is the clutch and base components. However, a more complicated magnet configuration is necessary to achieve the desired characteristics using these components.

Figure 3.8c presents the calculated force,  ${}^c\vec{f}$ , for a safety factor of one, where the irreducible

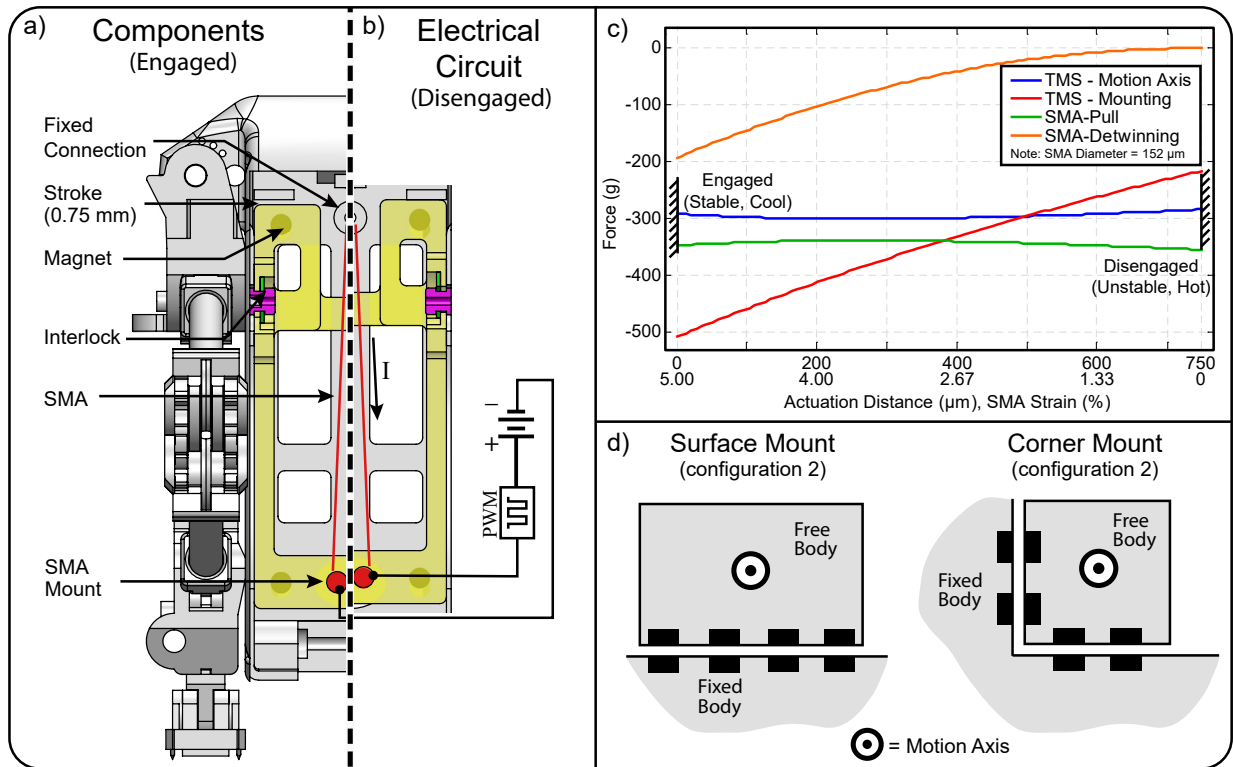


Figure 3.9: **a)** The components of the actuator are labeled in the engaged state. **b)** The electrical connections are shown in the disengaged state. **c)** The force-displacement curve of the tailored magnetic spring for both the motion-axis and off-axis directions. Note: figure is for 5 % strain, whereas robot uses 1.4 %. **d)** 2D representation of two possible stable mounts for the configuration 2 magnet sets. These allow the actuator to be mounted to either a surface or corner.

set is listed in Table 3.1. In this case, two of these sets are required to produce the necessary force magnitude and symmetry for this particular application. The tailored magnetic spring has sufficient force for detwinning the SMA ( $\epsilon = 2.9\%$ ), high holding force when engaged, and snapping behavior, which satisfies all three requirements. Figure 3.8d presents possible mounting positions for the configuration 1 magnet sets which balance the off-axis forces and torques, and Fig. 3.8e presents two possible balanced mounting positions for the configuration 2 magnet sets; the first of which is employed in the clutch design for its four-fold symmetry.

Table 3.1: Clutch Tailored Magnetic Spring - Irreducible Set

Magnet Config.	Qty	Magnet Parameters *		
		Diameter (mm)	Thickness (mm)	Start , End (% Diameter)
1 (R)	1	3.2	1.6	0 , 23.6
2 (R)	2	3.2	1.6	-11.8 , 11.8

(R) = Repulsive, (A) = Attractive.

\* Material is NdFeB grade N52 (K&J Magnetics)

### 3.6.2 Driving Circuit

The fully self-contained ESM requires the SMA actuator to rotate continuously, necessitating a floating power connection. To achieve this, the materials for the components are selected for not only their mechanical but also their magnetic and electrical properties; the configuration of the components creates the circuits.

The driving circuit for the SMA actuator utilizes the metal transmission (negative) and the lower bearing (positive) as the fixed points for the electrical connections, as seen in Fig. 3.8b. Therefore, the electrical connections remain stationary thereby facilitating connection. The current flows through the components in the following order: lower bearing, SMA mount, SMA, clutch, base, motor shaft, and transmission housing.

## 3.7 Wing Lock Design

The MultiMo-Bat [160] was initially designed to transition to flight passively however, this reduces the robustness of the locomotion cycle as disturbances in the air can result in a failure to deploy the wings. This strategy also restricts the ability of the robot to jump at an angle, which could reduce the cost of transport while traveling over terrain with relatively low obstacles. To improve the mobility and robustness of the MultiMo-Bat an active wing deployment mechanism is developed. This is achieved by storing energy in elastic elements in the shoulder joints of the robot as the jumping energy is being stored. However, to ensure deterministic deployment, a

wing lock is designed which is actuated by a SMA actuator; as seen in Fig 3.9a,b. The wing locking device weighs 3.0 g and produces a disengagement force of approximately 350 g over a stroke length of 750  $\mu m$  and an engagement distance of 500  $\mu m$ .

### 3.7.1 Desired Characteristics and Tailored Magnetic Spring

The desired characteristic for detwinning the SMA actuated wing lock are the same as those for the SMA actuated clutch, Sections 3.3.1-4, but with one addition, Section 3.3.5. Constraining the device to a surface requires an attractive force, thus the A-LR transformation of the segments and the negative of the magnetic force curves in Fig. 3.4c,d, respectively. This feature comes with an added level of design difficulty as both axes are considered simultaneously.

Figure 3.9c presents the calculated force,  ${}^c\vec{f}$ , where the irreducible set is listed in Table 3.2. In this case 4 of these sets are required to produce the necessary force magnitude and symmetry for this particular application. The first four characteristics are again achieved however the snapping behavior is less pronounced as the force difference is mainly due to the transition from static to kinetic friction. However, this tailored magnetic spring does produce between 216 g and 510 g of attachment force, for the 3.0 g mechanism, allowing it to auto align and self assemble without the need for mounting features. Figure 3.9d presents two possible mounting positions for the configuration 2 magnet sets which allow the device to be constrained to either a surface or corner; the wing lock employs the single surface mounting configuration.

Table 3.2: Wing Lock Tailored Magnetic Spring - Irreducible Set

Magnet Config.	Qty	Magnet Parameters *		
		Diameter (mm)	Thickness (mm)	Start , End (% Diameter)
2 (A)	1	3.2	0.8	20 , 43.6

(R) = Repulsive, (A) = Attractive.

\* Material is NdFeB grade N52 (K&J Magnetics)

## **3.8 Experimental Characterization**

### **3.8.1 Materials and Methods**

The experimental setup for characterizing a tailored magnetic spring, consists of a precision motorized stage (Newport MFA-CC) and a load cell (1000 gram, Transducer Techniques) both connected to a computer to simultaneously drive the stage and read the load cell; example setup, Fig. 3.10a. The load cell is mounted to the stage and positioned to move along the motion-axis.

The experiential procedure begins at either the start or end position of the stroke. A stage velocity, displacement, and a force measurement rate must be specified before proceeding through the stroke. However, to extract the magnetic force, the measurements must be recorded for both motion directions; start-to-end and end-to-start. Therefore, at the end of the stroke, the process is reversed, obtaining force measurements from both directions of motion.

The measured force will include both a magnetic and a frictional force component. The magnetic part is then extracted through an understanding of the frictional force directions, as seen in Fig. 3.11. During disengagement the frictional and magnetic forces are pointing in the same direction, increasing the measured force, whereas, during engagement, the frictional force opposes the magnetic force, decreasing the measured force; example Fig. 3.10c. A free body diagram of this procedure then shows that, the magnetic force component is the average of the force measured in both directions.

### **3.8.2 Results**

To validate the concept and examine the manufacturing feasibility of these tailored magnetic springs, the SMA actuated energy storage mechanism, being more complicated and the magnets closer together, was experimentally characterized.

The manufactured clutch has two stable orientations around the motion-axis of the assembly. This is due to the manufacturing tolerances of the base and clutch components; the angular difference between the two states is approximately 2 degrees. In this case state 1 produces the

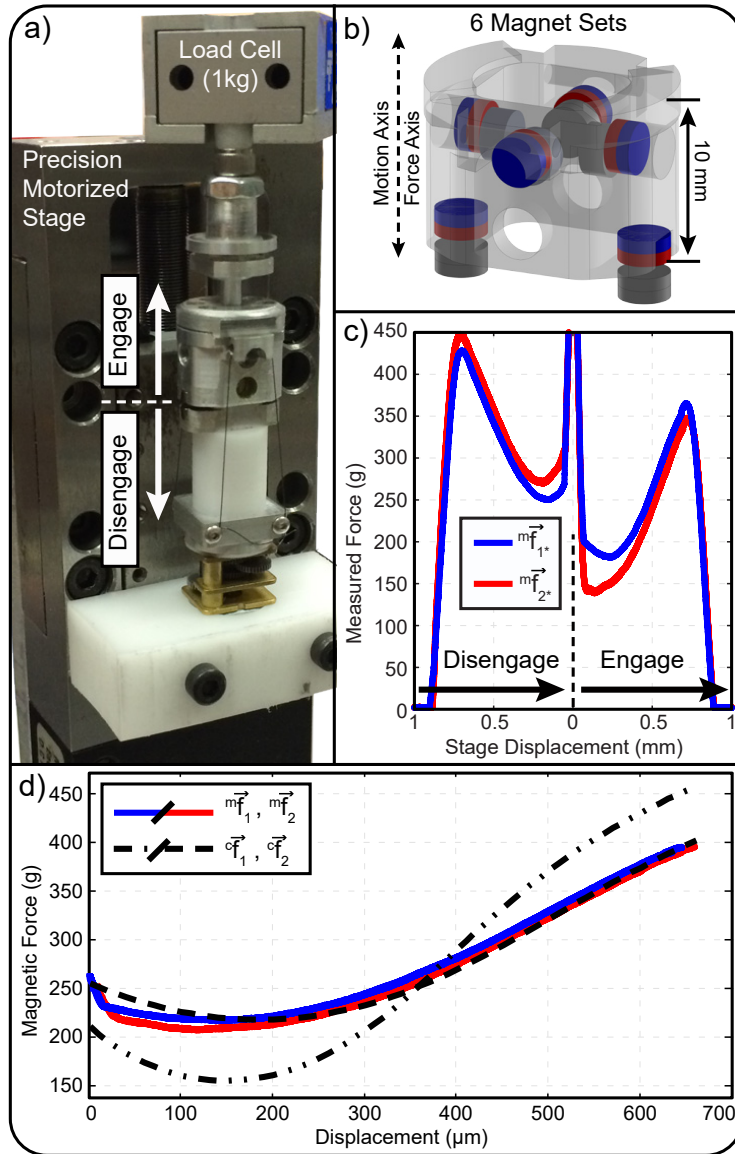


Figure 3.10: **a)** The experimental setup consists of a precision motorized stage and load cell oriented vertically which are both connected to a computer to simultaneously measure and drive these components. **b)** The magnet configuration, of the tailored magnetic spring, for the energy storage mechanism; fixed body magnets (gray) and the free body magnets (red/blue). **c)** The measured bidirectional force of the SMA clutch mechanism. Manufacturing tolerances result in two stable states; state 1 has better magnet alignment than state 2. **d)** The experimental measured and designed tailored magnetic springs are shown for comparison. For completeness the two stable positions (state 1,  $m\vec{f}_{1^*}$ , and state 2,  $m\vec{f}_{2^*}$ ) of the manufactured clutch were tested and show similar results. The initial  $c\vec{f}_{1^*}$  assumes an ideal magnet configuration; whereas the tolerance adjusted  $c\vec{f}_{2^*}$  used the tolerances of the manufactured magnet configuration and shows better agreement. For comparison of the shape of the tailored magnetic spring, the initial  $c\vec{f}_{1^*}$  and tolerance adjusted  $c\vec{f}_{2^*}$  are shifted down 160 and 120 grams, respectively. Each state was tested 10 times with the data presented here unfiltered.

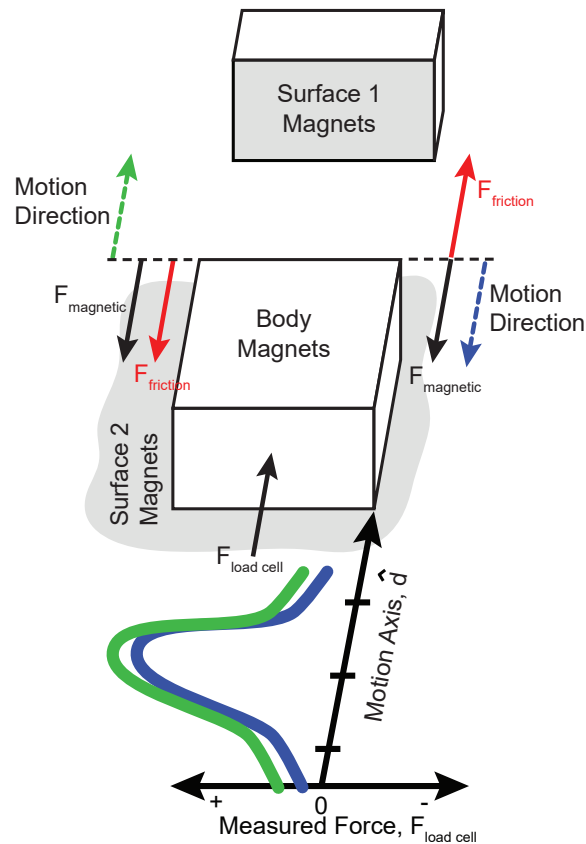


Figure 3.11: Isolating the magnetic force from the measured force where the measured values will be higher when the magnetic and frictional forces act in the same direction and lower when they oppose each other.

best alignment of the magnets and should result in slightly higher magnetic force than state 2.

The experimental procedure begins by first manually setting the clutch to the state to be tested; both states will be tested as the operational state may be either one. The load cell begins out of contact with the assembly and the automated testing procedure is initiated. The procedure begins by depressing the clutch (disengagement), and motion ceases after contact is reached, which is determined by a load threshold; contact occurs at the  $0 \text{ mm}$  position shown in Fig. 3.10c. The stage then holds position for one second before reversing the procedure and allowing the clutch to extend (engagement) back through its stroke. The load cell and stage position values are recorded at approximately  $1000 \text{ Hz}$  with the stage velocity is set at  $5 \mu\text{m}/\text{s}$ . The raw experimental data from both states can be seen in Fig. 3.10c; each state is tested 10 times.

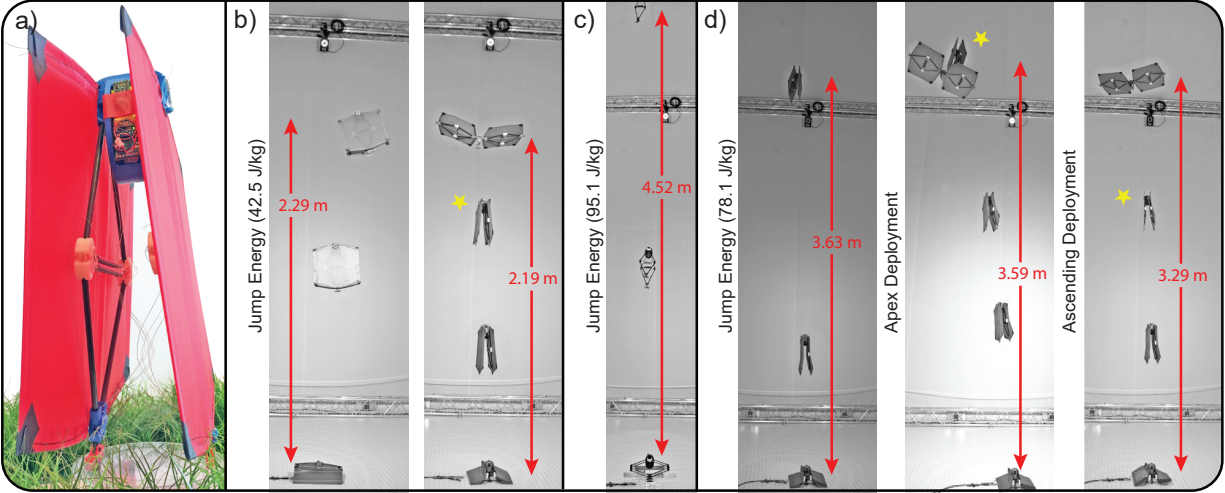


Figure 3.12: **a)** MultiMo-Bat, integrated jumping and gliding locomotion with tailored magnetic spring components for active clutch release and active wing deployment. **b)** Jumping trials both with and without active wing deployment at an energy density of  $42.5 \text{ J/kg}$  where the star (yellow) marks the initiation of the wing deployment. **c)** Jumping trial with the wings and controller removed at an energy density of  $95.1 \text{ J/kg}$ . **d)** Jumping trials both with and without wing deployment at an energy density of  $78.1 \text{ J/kg}$ . Two wing deployment timings are examined: apex and ascending where the star (yellow) marks the initiation of the wing deployment. **NOTE:** Motion capture system (Vicon, Vantage) was used for positional data. Heights are measured relative to start position; for height above ground add approximately  $76 \text{ mm}$ .

The two calculated forces,  ${}^c\vec{f}_1$  and  ${}^c\vec{f}_2$ , present the ideal magnet configuration and one adjusted for the manufacturing tolerances of the mechanism, respectively; as seen in Fig. 3.10d. The calculated forces,  ${}^c\vec{f}_1$  and  ${}^c\vec{f}_2$ , are shifted down to the measured forces,  ${}^m\vec{f}_1$  and  ${}^m\vec{f}_2$ , by 160 g and 120 g, respectively. This offset is most likely due to variation in the magnetization of the purchased magnets, unaccounted for manufacturing tolerances, misalignment, and small interactions between the magnet sets themselves; for example Grade N42 would nearly align  ${}^c\vec{f}_2$  with the measured forces. However, both the measured forces,  ${}^m\vec{f}_1$  and  ${}^m\vec{f}_2$ , show good agreement with each other as well as to  ${}^c\vec{f}_2$ .

### 3.9 MultiMo-Bat: Results and Discussion

The mounting flexibility afforded by the use of a tailored magnetic spring requires only that the surface area necessary for mounting the magnet sets be available, whereas the remaining majority

of the mechanism can be developed independently. Figure 3.12a presents the MultiMo-Bat with both the energy storage mechanism and wing lock mounted within; where the self contained ESM uses surface areas between its constituent components and the wing lock uses its mounting surface to embed the magnet sets, which make up their tailored magnetic springs.

The developed energy storage mechanism was tested to a maximum load of  $98.3\text{ N}$  (Appendix Appendix G) where, excluding friction within the mechanisms, the robot requires a maximum of  $83.7\text{ N}$  to store the  $12.7\text{ J}$  of energy for the jumping locomotion. This allows for twice the energy and force of the previous robot [160]. Figure 3.12b presents the initial trials, which were conducted at the same energy level as the previous robot ( $54.9\text{ J/kg}$ ) albeit at a lower energy density of  $42.5\text{ J/kg}$  due to the added on-board locomotion controller, resulting in jumping heights of approximately  $2.2\text{ m}$ . Increasing the jumping energy to  $12.7\text{ J}$  allows the MultiMo-Bat with the wings and controller removed ( $95.1\text{ J/kg}$ ) to reach heights greater than  $4.5\text{ m}$ , Fig 3.12c. The complete robot, Fig 3.12d, reaches heights of  $3.45 \pm 0.07\text{ m}$  as compared to the previous robot at  $3.03 \pm 0.09\text{ m}$  ( $t(16)=12.9, p<0.001$ ). The added energy allows the newest MultiMo-Bat to not only carry a full controller for sensing jumps and actively deploying the wings but reach new heights while doing so.

The robot controller, using an IMU, calculates the magnitude of the body acceleration to detect the initiation of the jump and begin the wing deployment. However, the relatively slow thermal based actuation of SMA coupled with the limited power source,  $3.7\text{ V}$ ,  $200\text{ mAh}$ ,  $1\text{C}$  discharge current, polymer lithium ion battery (Sonstige), results in an actuation time of  $385 \pm 16\text{ ms}$  which is not sufficient for the locomotion characteristics of MultiMo-Bat. Therefore, to increase the actuation speed, the SMA is preheated to just below the phase transition temperature before the jump is initiated. In this way, the total time reduces to  $232 \pm 12\text{ ms}$  ( $t(7)=17.2, p<0.001$ ) to sense the jump and begin the wing deployment. The wings are then able to be deployed during the ascending, apex, or descending periods of the MultiMo-Bat's coast phase; the apex of which is reached at approximately  $750\text{ ms}$ . Figure 3.12d presents trails with

no, apex, and ascending wing deployment, where the stars indicate the start of the deployment. Maximum jumping heights are achieved when the wings are deployed at or after the apex whereas ascending deployment tends to produce more stable trajectories and deployments, albeit at the cost of lower jumping performance.

### 3.10 Custom Complex Spring Design Methodology

The segments,  $\vec{s}_n$ , presented in Fig. 3.4c, are but a few of the infinitely many possible segments which can be created and used to construct tailored magnetic springs. **Remark 5:** *The magnetic force-displacement relationships,  $\vec{F}$ , are a function of the motion-axis, which can be chosen arbitrarily in any direction assuming no collision, and several parameters including: magnetic moment, 6-DOF position and orientation in relation to each other, and geometry of the magnets.* This allows for extreme variability in the initial force-displacement relationships,  $\vec{F}s$ , and thus the extracted segments,  $\vec{s}_n$ , however, the full power of the two configurations selected has not yet been realized.

To realize the full power of the selected configurations, first the total displacements must be extended to encompass the entire region of non-negligible forces. Figure 3.13 presents the regions for the two selected configurations as approximately 1.5 and  $\pm 1.5$  magnet diameters for configuration 1 and 2, respectively; these are extended force-displacement relationships of the configurations presented in Fig. 3.4a. These extended force-displacement relationships then form the basis from which the extended segment sets are selected. However, a number of new challenges arise as the number of segments increases. The following sections will develop a methodology which manages large segment sets to create any well-defined function of force vs. displacement; meaning any function in which each displacement has only a single desired force.

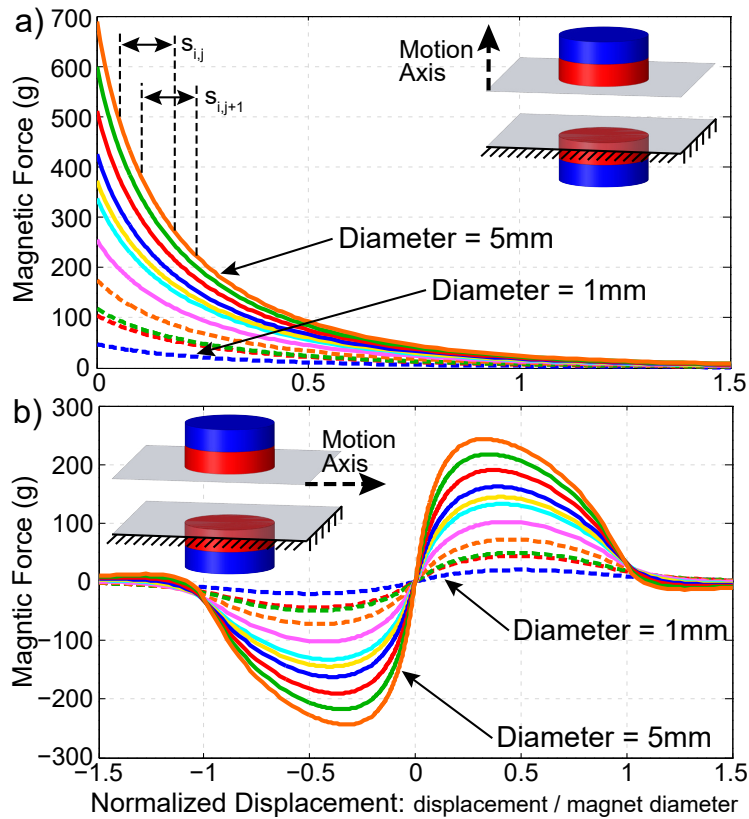


Figure 3.13: The  $\vec{F}$  shown are for magnets configured to repel each other. Magnet set diameters: 1, 1.5, 1.6, 2, 2.5, 3, 3.2, 3.5, 4, 4.5, and 5 mm from lowest to highest force, respectively; all with a thickness of 1.6 mm and an initial gap of 50  $\mu\text{m}$ . The arrows on the inset magnet set shows both the direction of force and motion. **a)** Simulated  $\vec{F}$  for axially aligned and displaced magnet sets. **b)** Simulated  $\vec{F}$  for axially parallel and perpendicularly displaced magnet sets. ©[2017] IEEE

## Methodology Steps

Each step will be discussed in detail in the following sections, however, the general steps are as follows:

1. Determine desired force-displacement relationship,  $d\vec{f}$ .
2. Select magnet diameters,  $D$  (suggest,  $D = 4d$ ).
3. Select configurations (example configurations 1,2).
4. Calculate or experimentally determine the  $\vec{F}$ 's.
5. Subdivide the  $\vec{F}$ 's into  $N$  segments and construct  $\mathbf{S}$ .

6. Select the number of evaluation points,  $k$ , and the dimensionality reduction percents,  $P_\lambda$  (see text for the definition and ranges used).
7. Solve for initial analytical solution,  $\vec{q}$ , for a given,  $k$  and  $P_\lambda$ .
8. Save solution,  $\vec{q}$ .
9. Filter  $\mathbf{S}$  to remove some of the segments.
10. Resolve for  $\vec{q}$  via the analytical solution.
11. Save solution,  $\vec{q}$ .
12. Repeat steps 9-11 until  $\mathbf{S}$  has no remaining segments.
13. Select another  $k$  and  $P_\lambda$  and repeat steps 7-12.
14. Create optimization seed population, from solutions in steps 8,11.
15. Run numerical refinement.
16. Save best solutions,  $\vec{q}$ .
17. Solutions from steps 8,11,16 are all possible tailored magnetic springs.

### 3.11 Analytical Design

To develop the analytical solution we begin by expressing eq. (3.6) in general form as,  $\mathbf{S}\vec{q} = {}^d\vec{f}$ , or expanded as,

$$\mathbf{S} \quad \vec{q} = {}^d\vec{f}$$

$$[[\mathbf{s}_1] [\mathbf{s}_2] \cdots [\mathbf{s}_n]] \begin{bmatrix} q_1 \\ q_2 \\ \vdots \\ q_n \end{bmatrix} = \begin{bmatrix} f_1 \\ f_2 \\ \vdots \\ f_k \end{bmatrix} \quad (3.7)$$

$$\vec{s}_n = [s_1 \quad s_2 \quad \cdots \quad s_k]^T \quad (3.8)$$

where as before, the segment quantities,  $\vec{q}$ , are *unknown* and the desired force,  ${}^d\vec{f}$ , and segment set,  $\mathbf{S}$ , are *known* and specified by the designer; both  ${}^d\vec{f}$  and  $\mathbf{S}$  have units of force while  $\vec{q}$  is

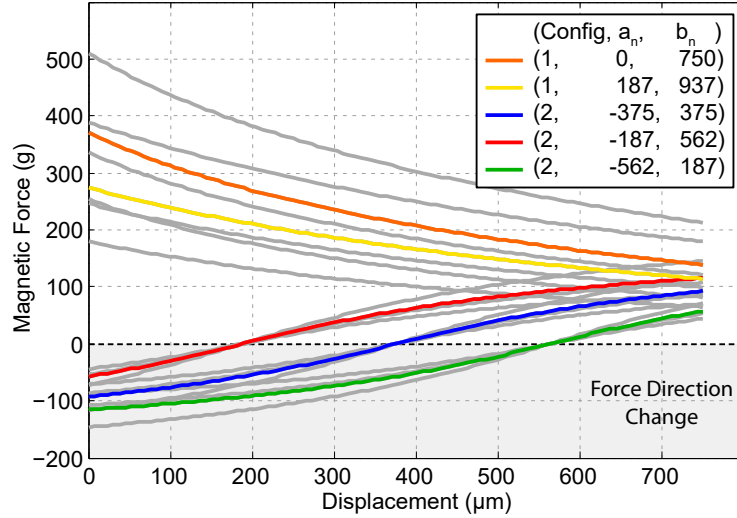


Figure 3.14: Small segment set, which encompass 5 parameter sets (magnet configuration, start point, end point) and 4 different magnet diameters (2.5,3,3.2,4 mm) are shown to illustrate a simple collection of segments which can be used to create a tailored magnetic spring. Those in color represent the segments taken from the 3.2 mm diameter magnet set. The start,  $a_n$ , and end,  $b_n$ , points are given in micrometers and represent the positions from which the segments were taken from the  $\vec{F}$ 's. From each magnet diameter, three segments were taken which have positive slope, a very difficult thing for traditional springs to achieve. ©[2017] IEEE

unit-less. As the segments will now be considered as sets, the indices  $i, j$  will now be replaced with  $n$ , where the total is  $n = \sum_i \sum_j 1$ . The problem then becomes finding the linear combination of the columns,  $\vec{q}$ , which best reproduces the desired force,  ${}^d\vec{f}$  [141]. Keeping in mind that all segments need not be used (i.e.  $q_n = 0$ ), allowing the methodology to be universal as the segment set,  $\mathbf{S}$ , can contain more segments than is necessary for a particular,  ${}^d\vec{f}$ . The key challenges are in understanding the behavior of the solution and using it to find *good* solutions which are manufacturable at a minimum magnet quantity.

The desired force-displacement relationship,  ${}^d\vec{f}$ , for the tailored magnetic spring is simply a vector of forces at particular displacement points. For a well-defined function, each displacement point must have only a single desired force. However, **Remark 6:** *this methodology can design a tailored magnetic spring for any well-defined function so this vector can be arbitrary and is therefore, completely up to the designer to specify.*

The segment quantities,  $\vec{q}$ , are the solution to the problem, however, this solution is depen-

dent on the segment matrix,  $\mathbf{S}$ . One difficulty is in interpreting the meaning of a negative quantity ( $q_n < 0$ ) of a physical object. In this case however, the segment transformations discussed previously offer an easy interpretation; a negative quantity simply flips the magnet set between attractive and repulsive.

The segment set,  $\mathbf{S}$ , contains all segments which can be used to construct the desired force-displacement relationship,  ${}^d\vec{f}$ , for the tailored magnetic spring. The only requirement is each segment must have the same relative displacement,  $|b_n - a_n|$ , and resolution,  $k$ , as the desired force vector,  ${}^d\vec{f}$ . The segments, which make up  $\mathbf{S}$ , can be deterministically chosen by the designer for desirable characteristics or arbitrarily selected through a generalized process. The complexity of the problem will increase with the number of segments, however, so too does the adaptability and power of the segment set,  $\mathbf{S}$ .

The generalized selection process consists of simply subdividing the complete 22  $\vec{F}$ 's in Fig. 3.4a into over 3000 different segments,  $\vec{s}_n$ , creating the  ${}^{3000+}\mathbf{S}$  segment set; where  $\vec{s}_n$  overlaps  $\vec{s}_{n+1}$  by 90%, due to sequential nature of the segment creation.

To demonstrate the difference between different segment sets, a deterministic set of 20 segments,  ${}^{20}\mathbf{S}$  is also created; shown in Fig. 3.14 and Appendix H. These two segment sets each have their own strengths and weaknesses,  ${}^{20}\mathbf{S}$  is easier to work with, as the matrix is more manageable, whereas  ${}^{3000+}\mathbf{S}$  is significantly more powerful and able create much more complex tailored magnetic springs.

### 3.11.1 Solution

The solution takes the form,  $\vec{q} = \mathbf{S}^+ {}^d\vec{f}$ ; an example  ${}^d\vec{f}$  is shown in Appendix H. The pseudoinverse,  $\mathbf{S}^+$ , is obtained by way of the Moore-Penrose pseudoinverse which uses the singular value decomposition of  $\mathbf{S}$ . A reduction in dimensionality can be preformed at this stage by removing a percentage,  $P_\lambda$ , of the higher order singular values - the singular values represent the fundamental mode shapes of the segments. This smooths the segments and tends to reduce the calculated quantities,  $\vec{q}$ , at the cost of additional error. However, the reduction in quantity can be much

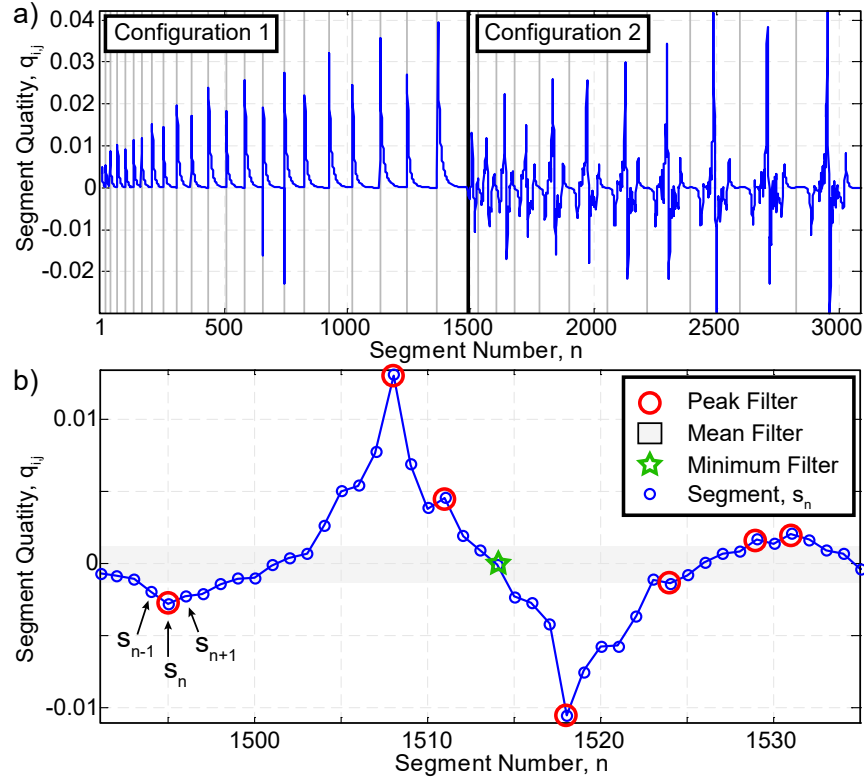


Figure 3.15: **a)** Initial analytical solution  $\vec{q}$ , using  $S_{3000+}$ , for the 'monostable' tailored magnetic spring - discussed later. However, this solution is not manufacturable due to the fractional magnet quantities. To condense these quantities,  $\mathbf{S}$  is filtered, removing some of the segments, and the problem resolved. This process is repeated until  $\mathbf{S}$  has only a single segment remaining. Vertical gray lines denote different  $\vec{F}_i$ 's. **b)** Three different filters are used including: peak filter, mean filter, and minimum filter. The peak filter removes all segments which are not local maxima or minima, the mean filter removes all segments with quantities below the mean, and the minimum filter removes the segment with the lowest quantity; as defined in Table 3.3. ©[2017] IEEE

more significant than the added error. In the following section we will analyze the behavior of the analytical solution to elucidate properties which can be used to help generate *good* solutions.

### 3.11.2 Solution Behavior

If  $d\vec{f}$  is within the column space of  $\mathbf{S}$  ( $d\vec{f} \in C(\mathbf{S})$ ) the solution  $\vec{q}$  will be exact, whereas if it is not ( $d\vec{f} \notin C(\mathbf{S})$ ) then the solution will be the least-squares approximation. In either case, the Moore-Penrose pseudoinverse produces the minimum magnet quantity solution, as it will contain nothing from the nullspace of  $\mathbf{S}$  ( $\vec{q} \notin N(\mathbf{S})$ ). However,  $\mathbf{S}$  tends to have both highly dependent

rows and columns which creates difficulty in manufacturing the solution. This is because the solution will use not only the segments which best fit  ${}^d\vec{f}$ , but also all those dependent segments as well, requiring an excess of segments. This also tends to produce many small fractional quantities which must be rounded to the nearest whole magnet for manufacturing; an example  $\vec{q}$  for  ${}^{3000+}\mathbf{S}$  is shown in Fig. 3.15a and an example  $\vec{q}$  for  ${}^{20}\mathbf{S}$  is shown in Appendix H. This rounding can significantly alter the calculated force,  ${}^c\vec{f} = \mathbf{S} \text{ round}(\vec{q})$ , resulting in a solution which is mathematically feasible but not necessarily a *good* solution for manufacturing.

The challenge then becomes filtering the segment set,  $\mathbf{S}$ , to those segments which create the desired force,  ${}^d\vec{f}$ , with the fewest integer quantity segments. The most intuitive option would be to simply remove the dependent columns. However, as there is a huge number of bases which describe the column space of  $\mathbf{S}$ , there is no way to know whether the chosen one will produce a *good* solution; as many bases tend to produce solutions which require an excessive quantity of magnets. Instead a good first step is to *peak* filter the segment set, removing those which are not local maxima or minima within the solution,  $\vec{q}$ . Since the segments of  ${}^{3000+}\mathbf{S}$  overlap their neighbors by up to 90%, which causes the solution to broadly distribute small fractional quantities over large numbers of segments, the *peak* filter removes these highly dependent neighbors and focuses the solution to the segments with highest quantities within their local neighborhood; as seen in Figure 3.15b, red circles indicate the remaining segments. The problem is again solved however, this second filtering cannot use the *peak* filtering technique, as the column dependence is no longer known; this is also true for the initial filtering of  ${}^{20}\mathbf{S}$ . Instead,  ${}^{3000+}\mathbf{S}$  and  ${}^{20}\mathbf{S}$  are *mean* filtered, removing all segments which have absolute quantities below the mean; as seen in Figure 3.15b, segments within the gray bar are removed. Finally, when only a few segments remain, the segment with the lowest quantity is removed, *minimum* filtering; as seen in Figure 3.15b, green star indicates the removed segment. Table 3.3 presents the specific filter equations. These filtering steps tends to not only reduce the total quantity of magnets in the solution, but also the effect of fractional quantities during rounding. Repeating this process several times can dramat-

ically enhance this effect while creating a family of solutions,  $Q$ , since each step will produce a possible solution.

Table 3.3: **S** Filters: Mathematical description

Name	<b>S</b> Criteria	Filter *
Peak	Initial, General	$q_{n-1} \leq q_n \leq q_{n+1}$
	Selection	$q_{n-1} \geq q_n \geq q_{n+1}$
Mean	$N > 25$	$ q_n  < \frac{1}{N} \sum  q_n $
Minimum	$N \leq 25$	$q_n = \min\{ \vec{q} \}$

\* Filters determine which segments are removed.

Through variation of the dimensionality reduction percent,  $P_\lambda = \{1.0, 0.75, 0.5, 0.4\}$ , and evaluation points,  $k = \{20, 30, 40, 60, 80, 100, 500, 1000, 4000\}$ , a family of several hundred possible solutions,  $Q$ , can be generated; see Appendix H for an example. These can be rounded and sorted by their fitness - discussed in the following section - which can yield an acceptable solution without progressing to the numerical refinement step.

### 3.12 Numerical Refinement of the Analytical Solutions

The design space of  $^{3000+}\mathbf{S}$  has extremely high dimensionality with greater than 3000 variables (segments) accompanied by values (quantities) up to  $\pm 100$  or more, significant local minima, and regions of relatively low gradient due to the high similarity between segments, all of which can cause problems for many optimization algorithms. Any optimization technique is possible, although, a genetic algorithm based approach is the best suited for this type of design space.

The genetic algorithm is setup with the chromosome equal to the segment quantities,  $\vec{q}$ . The initial population is composed of two parts, the family of analytical solutions and randomly generated solutions. The family of analytical solutions is used to increase the chance of convergence and decrease the computation time. The remaining variables in the optimization are the selection, crossover, mutation, and cost functions.

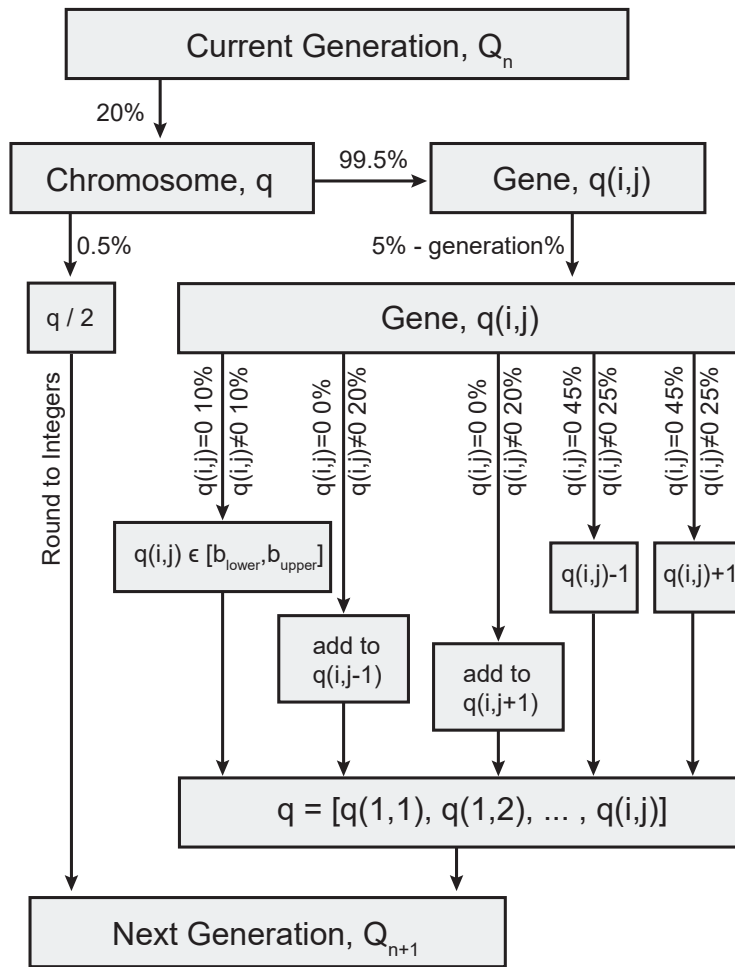


Figure 3.16: Mutation algorithm developed around the characteristics of the custom complex spring design methodology. The next generation is composed of individuals created by both crossover (80%) and mutation (20%). ©[2017] IEEE

### Selection Function

The selection function uses a standard tournament approach with four individuals randomly selected. The best two are then sent to the crossover function.

### Crossover Function

The crossover function uses a standard scattered approach, where each gene in the chromosome is treated separately. The corresponding gene in the child is selected randomly from one of the parents.

## Mutation Function

The mutation function which creates 20% of the next generation, however, benefits from a non-standard approach. Presented in Fig. 3.16, the developed mutation function accounts for three characteristics of the custom complex spring design problem including: integer values, cancellation, and similar neighbors. Integer values are simply ensured by restricting the gene mutations to addition, subtraction, or replacement by integer values. Cancellation, where some segments are nearly canceled out by others, occurs because of the similarity between segments and the analytical solution behavior. To check for this, there is a small chance that the entire chromosome will be divided by 2 and rounded to the nearest integer. Since the cost function - discussed later - includes the total quantity, the fitness of these individuals will be improved and propagated. Finally, since the neighboring segments in  $\mathbf{S}$  can overlap by up to 90%, shifting the quantity of a particular segment to one of its neighbors can help fine tune the solution and condense the number of different segments ultimately required. The probabilities of each step are presented in Fig. 3.16.

## Cost Function

The cost function is composed of four terms which are broken up into three categories: average error, maximum error, and manufacturing constraints. The average error terms are the root-mean-squared error (RMSE) in the position and slope of the calculated forces,  ${}^c\vec{f} = \mathbf{S}\vec{q}$ . The maximum error term is the maximum error between the desired,  ${}^d\vec{f}$ , and the calculated,  ${}^c\vec{f}$ , forces. This term is added to encourage the solution to reach the peaks and valleys of  ${}^d\vec{f}$ . Lastly, the major manufacturing constraint, is the total number of magnets required to generate the tailored magnetic spring. Multiplied by appropriate weights, these form the cost function as

follows,

$$\begin{aligned}
C_{GA} = & w_1 \cdot \sqrt{\frac{1}{K} \sum_k \left( {}^d f_k - {}^c f_k \right)^2} + w_2 \cdot \sqrt{\frac{1}{K} \sum_k \left( {}^d f'_k - {}^c f'_k \right)^2} \\
& + w_3 \cdot \frac{\max\{|{}^d \vec{f} - {}^c \vec{f}|\}}{\max\{|{}^d \vec{f}|\}} + w_4 \cdot \sum_n |q_n|
\end{aligned} \tag{3.9}$$

where,  ${}^d f_k$  and  ${}^c f_k$  are the forces and  ${}^d f'_k$  and  ${}^c f'_k$  are the derivatives of the forces at point  $k$ . The associated weights,  $w_{1 \rightarrow 4}$ , are modified according to the application and error tolerances; however, simply varying orders of magnitude between them is sufficient to produce *good* solutions.

### 3.13 Methodology Results and Discussion

To demonstrate the capabilities of the proposed methodology a number of different tailored magnetic springs were designed, where the results using  ${}^{20}\mathbf{S}$  are presented in Fig. 3.17a,b,e and the results using  ${}^{3000+}\mathbf{S}$  are presented in Fig. 3.17f-i.

The analytical solutions will always suffer from additional rounding error. The effect of which can be seen in Fig. 3.17 where  ${}^c \vec{f}_F$  and  ${}^c \vec{f}_E$  represent the best fitness and lowest RMSE solutions, respectively. The former demonstrates the manufacturable solution whereas the latter illustrates the solution's accuracy in reproducing the desired force,  ${}^d \vec{f}$ . To eliminate the rounding error, the analytical solutions are numerically refined. The results of which can be seen in Fig. 3.17, where the refined solutions,  ${}^c \vec{f}_R$ , have equal to or better fitness than that of the best analytical solutions.

Using  ${}^{20}\mathbf{S}$ , two tailored magnetic springs are presented in Fig. 3.17a,b which may have more practical applications for ON-OFF controlled actuators, such as shape memory alloy based mechanisms. These can be produced with relatively few magnet sets and exhibit both high holding force and snapping behavior in a bistable, Fig. 3.17a,c, and a monostable, Fig. 3.17b,d, configuration. Similar behavior would be very hard to achieve with traditional springs.

To compare the flexibility afforded by using either  ${}^{20}\mathbf{S}$  or  ${}^{3000+}\mathbf{S}$ , a more complex sine wave shaped tailored magnetic spring was designed using both sets; as seen in Fig. 3.17e,f. In both

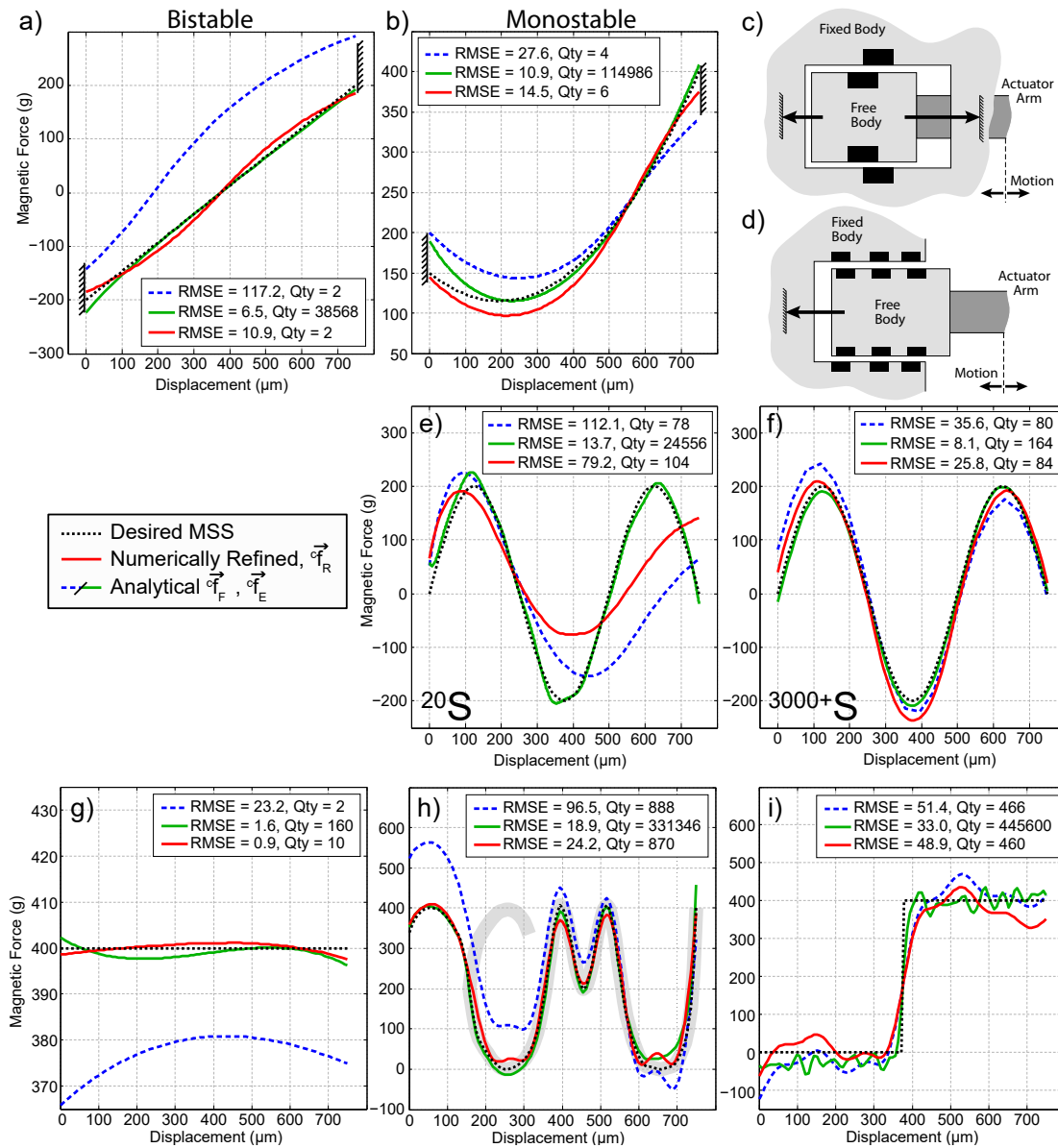


Figure 3.17: Each graph compares three solutions to the design of a particular tailored magnetic spring: analytical best fitness,  ${}^c\vec{f}_F$ , analytical lowest root-mean-squared error (RMSE),  ${}^c\vec{f}_E$ , and the numerical best fitness,  ${}^c\vec{f}_R$ . The RMSE and magnet quantity are presented to highlight the relative difficulty of the solutions, given the selected  $\vec{F}$ s. **a,b)** Two practical tailored magnetic springs which can be easily achieved using magnets: bistable and monostable, respectively. **c,d)** 2D representations of possible mounting configurations for the magnet sets of the numerically refine force  ${}^c\vec{f}_R$  selected for the bistable and monostable tailored magnetic springs, respectively. **e)** sine wave designed with the small segment set,  ${}^{20}\mathbf{S}$ . **f)** sine wave designed with the large segment set,  ${}^{3000+}\mathbf{S}$ . **g)** constant force designed with the large segment set,  ${}^{3000+}\mathbf{S}$ . **h)** ‘CMU’ designed with the large segment set,  ${}^{3000+}\mathbf{S}$ . **i)** step force designed with the large segment set,  ${}^{3000+}\mathbf{S}$ . **e,f)** presents the results of using both the small and large segment sets to design the same tailored magnetic spring whereas **g,h,i)** present a range of tailored magnetic springs with varying slopes and curvatures to demonstrate the design variability. ©[2017] IEEE

cases the methodology found a solution which creates the desired force  ${}^d\vec{f}$ , however,  ${}^{20}\mathbf{S}$  does so with 24,556 magnet sets whereas  ${}^{3000+}\mathbf{S}$  is able to achieve nearly the same result at 84 magnet sets. This illustrates an important characteristic of this methodology, **Remark 7:** *The quantity of magnets or the relative difficulty in producing a particular  ${}^d\vec{f}$  is a function of the similarity between the segments and  ${}^d\vec{f}$ ; not the  ${}^d\vec{f}$  alone. The similarity is inversely related to magnet quantity (i.e. higher similarity equals fewer quantity).* Practically, both of these would be difficult to manufacture. Therefore, other magnet configurations may need to be considered to further reduce the magnet quantity. In this case emphasis was placed on symmetry and ease of integration into existing mechanisms which lead to the selection of cylindrical magnets displaced either parallelly or perpendicularly from their faces.

To demonstrate the power of this methodology, the large segment matrix,  ${}^{3000+}\mathbf{S}$ , is used to compute four different tailored magnetic springs including: constant force, sine wave, ‘CMU’, and stepped force, all over a displacement of 750  $\mu\text{m}$  and force amplitudes of 400 g; as seen in Fig. 3.17f-i. These particular  ${}^d\vec{f}$ 's are selected for their differing slopes and curvatures which represent a wide range of possible solutions. The constant force and sine wave in Fig. 3.17f,g are reproduced with relative ease as both the root-mean-squared error (RMSE) and magnet quantity are low, whereas Fig. 3.17h,i are more difficult, requiring hundreds of magnets. The large quantities required to produce the, sine wave, ‘CMU’, and step desired forces,  ${}^d\vec{f}$ 's, demonstrates a need for additional segments which can better represent these shapes.

### 3.14 Manufacturing Feasibility

In order to determine the manufacturing feasibility of a tailored magnetic spring, its necessary to understand how the magnet quantity relates to the required surface area,  $A_{surf}$ , for integration.

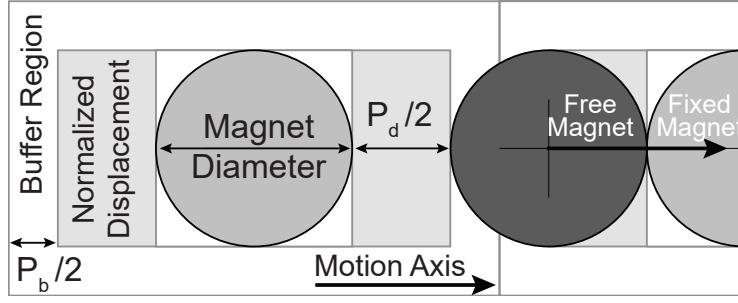


Figure 3.18: Mounting surface area: Each magnet will occupy a region larger than its own dimensions. The total surface area will be a function of the maximum normalized displacement, from alignment, that a magnet can travel,  $P_d$ , and a buffer region,  $P_b$ , which reduces interactions between magnet sets. Equation 3.10 takes into count both of these parameters to calculate the estimated total surface area. ©[2017] IEEE

Table 3.4: Estimated Areas of the Optimized Solutions

Figure	Qty	Estimated Surface Area, $mm^2$		
		$P_d = 1$ $P_b = 0.5$	$P_d = 1$ $P_b = 0$	$P_d = 0$ $P_b = 0$
3.17.a	2	68	36	18
3.17.b	6	203	108	54
3.17.g	10	338	180	90
3.17.f	84	2835	1512	756
3.17.e	104	3510	1872	936
3.17.i	460	15525	8280	4140
3.17.h	870	29363	15660	7830

Using the scenario presented in fig. 3.18, we derived an estimation of the surface area required,

$$l_{\hat{d}} \approx \frac{d}{P_s}$$

$$A_{surf} \approx (l_{\hat{d}} \cdot l_{off})(1 + P_d + P_b)(1 + P_b) \sum_n |q_n| \quad (3.10)$$

where,  $l_{\hat{d}}$  and  $l_{off}$  are the approximate average magnet size in the motion-axis and off-axis directions, respectively; for cylindrical magnets  $l_{off} = l_{\hat{d}}$ . The percentage,  $P_s$ , is used to determine the median magnet diameter; in this case 25% was used to ensure significant change in force over each segment. The major assumption, and reason for the approximation, is that all the magnet diameters are assumed to be equal to the median magnet diameter. The two additional

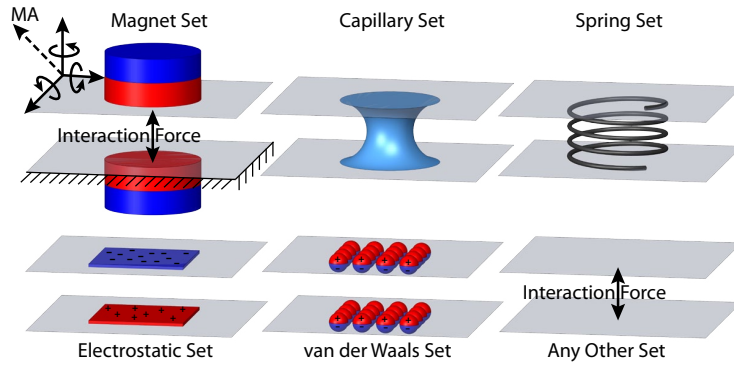


Figure 3.19: In the same way as the *magnet set* was defined previously, so too can other interaction sets be defined. Shown are several different examples of basic possible interaction sets. ©[2017] IEEE

percentages of the magnet diameter are the maximum possible normalized displacement,  $P_d$ , and a buffer region,  $P_b$ , to reduce interaction between magnet sets; these can range from  $\{P_d|0 : 1\}$  and  $\{P_b|0 : 1\}$ , respectively. Table 3.4 presents three different magnet spacings including: one half the magnet diameter spacing ( $P_d = 1, P_b = 0.5$ ), minimum spacing ( $P_d = 1, P_b = 0$ ), and magnet surface area only ( $P_d = 0, P_b = 0$ ).

Rearrangement of eq. 3.10 can also yield a method for estimating the maximum number of magnet sets,  $\sum_n |q_n|$ , which could be mounted within an existing system. In this case,  $A_{surf}$  represents the surface area available to mount a tailored magnetic spring. This quick estimation can help determine whether a tailored magnetic spring would be applicable for a given mechanism.

### 3.15 Extensions of the Methodology

#### 3.15.1 Additional Interaction Types

The analytical design strategy can also be extended to interactions other than magnetic,

$$multi\mathbf{S} = \left[ \begin{array}{c} \left[ \begin{array}{c} \text{Magnetic} \\ \text{Mechanical Spring} \\ \text{Electrostatic} \\ \text{Capillary} \\ \text{van der Waals} \\ \dots \\ \text{Other Forces} \end{array} \right] \end{array} \right] \quad (3.11)$$

In fact, any interaction which can be described by a force-displacement curve can be included in the formation of  $\mathbf{S}$ ; as shown in Fig. 3.19 and eq. 3.11. This in turn allows the custom complex spring design methodology to utilize whatever category or combination of forces which best fit. The challenge comes in using force-displacement relationships which cannot produce the negative of the force,  $\vec{F}_i$ , by simply switching ‘polarity’, as in the magnetic case, such as mechanical springs, van der Waals forces, and capillary forces. Remember that previously, the calculated solution,  $\vec{q}$ , had nothing in the nullspace of  $\mathbf{S}$ ; however, including the nullspace now allows for modification of the quantities according to the characteristics of each interaction type. The calculated solution,  $\vec{q}^*$ , now has two parts,

$$\vec{q}^* = \vec{q} + N(\mathbf{S})_{n \times n - \text{rank}(\mathbf{S})} \begin{bmatrix} q_1^* & q_2^* & \cdots & q_{n - \text{rank}(\mathbf{S})}^* \end{bmatrix}_{Free}^T \quad (3.12)$$

where  $\vec{q}_{Free}^*$  contains the quantities of the dependent variables; these quantities can be modified freely as they are independent and arbitrary. Therefore, within the limits of the nullspace of  $\mathbf{S}$ , quantities can be shifted to account for certain segment properties. However, because of rounding this may change the relative error of the calculated force,  ${}^c \vec{f}$ .

### 3.15.2 Multidimensional Magnetic Field Design

To design magnetic fields instead of magnetic forces the segment matrix must contain the resulting magnetic fields produced by fixed permanent magnets at specific positions,  $\vec{r}_i$ , and orientations with respect to the center of the desired area or volume, as seen in Fig 3.20. The segment matrix,  ${}^{field} \mathbf{S}$ , contains the field, over the desired space, of each magnet organized into a column as,

$${}^{field} \mathbf{S} = \begin{bmatrix} \left[ \begin{array}{c} \text{2D,3D Magnet 1 Field} \end{array} \right] & \left[ \begin{array}{c} \text{2D,3D Magnet 2 Field} \end{array} \right] & \left[ \begin{array}{c} \text{2D,3D Magnet 3 Field} \end{array} \right] & \cdots & \left[ \begin{array}{c} \text{2D,3D Magnet i Field} \end{array} \right] \end{bmatrix} \quad (3.13)$$

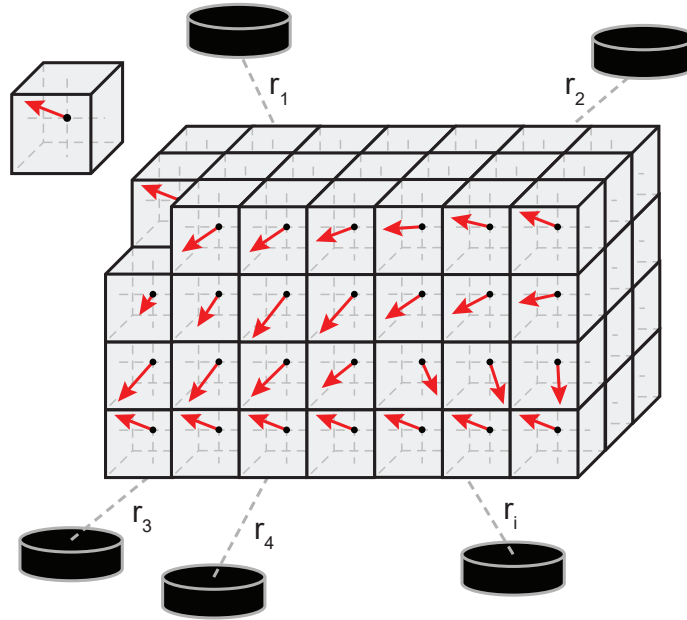


Figure 3.20: Fixed permanent magnets generate constant magnetic fields over 2-dimensional areas or 3-dimensional volumes which can be included in the formation of the segment matrix by discretizing the aforementioned spaces. Red arrows represent magnetic field direction and magnitude. ©[2017] IEEE

where each voxel has the included  $x,y,z$ -axis fields,  $s_n = [x_1, y_2, z_1, x_2, y_2, z_2, \dots, x_i, y_i, z_i]^T$ , in column form. The calculated quantities,  $\vec{q}$ , can now represent either the magnetic material volume, for single dipole approximated magnets, or magnetization strength, for distributed dipole magnets, depending on the problem formation. The desired field,  $^{field}\vec{f}$ , is a column vector of the desired  $x,y,z$ -axis fields configured in the same manner as the segments. The custom complex spring design methodology is then just as applicable, however, as there is no dependence between neighboring segments, the initial peak filtering is not possible. The multidimensional nature now increases the complexity even more, however, as before the complexity is a function of the characteristics of the magnets used to create the desired shape and is a topic of future work.

## 3.16 Adaptability of the Methodology

### 3.16.1 Scaling

A tailored magnetic spring is particularly beneficial in situations where significant changes in force are required over relatively short distances. The inspiration for this work required a force differential of 100s of grams over a displacement of  $750 \mu m$ . However, the displacement of a tailored magnetic spring can be chosen to suit any application from micron scale motions in microelectromechanical systems (MEMS) to millimeters scale motions in miniature robots to centimeter scale motions when combined with traditional springs and theoretically even larger. Scaling the size of the magnet sets, used to create the segments, with the desired displacement is helpful in reducing the quantity of magnets required but not necessary for the solution. The most important concept to remember is that, the relative difficulty of achieving a particular desired force,  ${}^d\vec{f}$ , is a function of the similarity between the desired force,  ${}^d\vec{f}$ , and the segments selected. If the initially chosen  $\vec{F}_i$ 's do not result in a feasible solution, consider creating more complex magnet sets (different shapes, motion axes, assemblies, etc.) with greater variation in their individual  $\vec{F}$ 's. This can result in significant differences in the quantities of the magnet sets required to create a particular tailored magnetic spring.

### 3.16.2 Segment Set

The strength of this custom complex spring design methodology is in the model independence and flexibility with which the segment set,  $\mathbf{S}$ , is created. There are only two requirements that must be upheld: the superposition principle holds and the interaction between segments is negligible, and the segments themselves are constant. This produces almost no limitations to the inclusion of interaction forces in  $\mathbf{S}$ , anything from different configurations and/or shapes of a pair of magnets to assemblies and to interactions between magnets and ferromagnetic materials to even other possible type of interactions can be easily included. As long as the discretized force-displacement curves can be determined, this methodology can use them to create a desired

force,  ${}^d\vec{f}$ .

To avoid excessive recalculation and improve computation efficiency, the segments need not be directly calculated each time. Instead, high resolution  $\vec{F}$ 's, over the entire range in which forces interact strongly ( $\approx 1.5$  times the magnet diameter), are precalculated and saved to create a library of  $\vec{F}$ 's. The segments are then calculated via interpolation of these high resolution  $\vec{F}$ 's from  $a_n$  to  $b_n$  at the same relative displacement points,  $k$ , as the desired force,  ${}^d\vec{f}$ . **Remark 8:** *Therefore, once calculated, the  $\vec{F}$ 's never need to be calculated again; more importantly, this allows for experimentally measured or computationally expensive  $\vec{F}$ 's to be utilized as well.*

### 3.17 Chapter Summary

In this chapter, we presented a design methodology for customizing magnetic springs to the characteristics of SMA actuators as well as to any well-defined function of force vs. displacement to suit any application and demonstrated the performance improvement to MultiMo-Bat. The non-contact force and no material fatigue characteristics of permanent magnets makes them a robust and reliable spring. The variability of the irreducible set creates a flexible design framework from which to adapt previously developed tailored magnetic spring to new applications. However, this design methodology is not limited to shape memory alloy and could adapt magnetic springs to any smart actuator or joint at any scale, accommodating the specific characteristics while adding additional features; and possibly improving the performance of all actuation systems in miniature robots.

Only a hand full of magnet sets were used to create the mechanisms, thus facilitating the manufacturing of the energy storage and wing lock devices. However, with the advent of printable magnets in recent years, even the difficulty of fabricating these tailored magnetic springs is decreasing. In the future, as the 3D printing of magnets improves, it's conceivable that tailored magnetic springs with even thousands of magnets may be easily manufactured; the limit being only the available space to position them.

Even though the focus of this chapter has been the design of magnetic springs for SMA, this concept can be extended to any application which requires a specific force-displacement relationship and any type of force or combination of forces. The segments used to design the tailored magnetic springs could just as easily represent the force-displacement relationships of mechanical springs, capillary bridges, electrostatic interactions, or any other interaction which can be described by a fixed force-displacement relationship. This design methodology is not just a magnetic spring design methodology but a universal design methodology, requiring only that the segments be sufficiently independent.

# Chapter 4

## MultiMo-Bat: multi-Surface Locust Inspired Passively-adaptable (SLIP) Foot

### 4.1 Introduction

Dynamic locomotion in unstructured terrestrial environments necessitates a closer look at how animals interact with the surfaces around them. Just as humans have developed shoes for ice, grass, wood, rock, track, slip, and stick, animals have developed similar strategies; however, as they cannot change their shoes, their feet must be multi-functional. To continue pushing the limits of terrestrial locomotion beyond that dictated by traditional friction on variable surfaces, robots too need not only multi-functional feet, but feet which can also tolerate slipping.

To date there are a number of terrestrial robots including miniature jumping robots [82, 100, 176], miniature walking/running robots [66, 85], and advanced large-scale legged robots [5, 19, 133, 139], which show very high performance with relatively simple point-contact feet; slip recovery has also been demonstrated through the use of high-performance computers, sensors, and actuators [19]. However, as the robot dynamics increase, the interaction time decreases, making active adaptability difficult, as both nature and robots have limited computational power and actuation speed. So whereas organisms making deliberate slow steps can search for, and properly grasp, secure foot holds [108], as the locomotion becomes dynamic, mechanical intelligence built into the structure becomes important [138]. Currently, no work has focused on the implications of foot morphology and behavior to the friction of the foot on diverse surfaces.

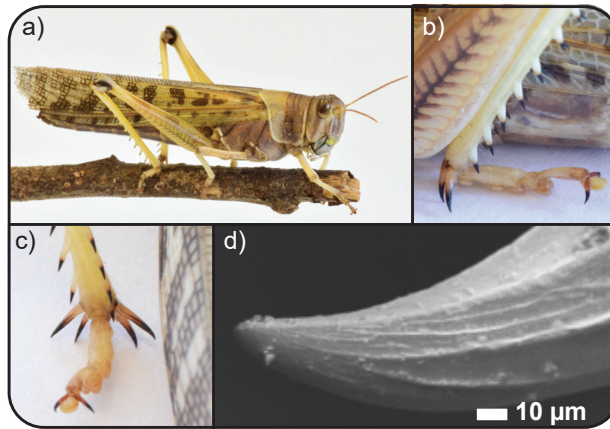


Figure 4.1: Photos of **a)** desert locust (*Schistocerca gregaria*), **b)** the configuration of the adhesive pads and tibia spines with the leg compressed (side view), and **c)** the four tibia spines (rear view). **d)** Scanning electron microscope (SEM) image of a spine tip.

Identifying morphological traits which enhance surface friction can help develop robots' ability to move dynamically through unstructured terrestrial environments without additional computational load.

While others have studied the desert locust's (*Schistocerca gregaria*) jumping behavior from many viewpoints, such as morphological [14, 47, 48, 57, 68], dynamical [31], and neurological [32, 61, 109] aspects, we are exploring the surface interactions of their feet during dynamic terrestrial locomotion. This is because of a particular feature suggesting that these organisms operate at the limits of their frictional capabilities on a wide variety of surfaces.

Desert locusts have developed a buckling region [13] in their knee to adsorb jumping energy in the event of a slip, which is used to avoid damaging the leg. We hypothesize that for natural selection to have created such a region, slips must be very common during jumping. Furthermore, instead of reducing the jumping power to reduce the possibility of slips, a buckling region was created to accommodate them. This feature suggests an ecological pressure to continue advancing the locust's jumping performance and therefore the mechanisms which support it - this makes sense, as the jumping behavior in the desert locust is used to escape danger [56] and the hind leg morphology shows striking similarities to that of the forelegs but with adaptations for jumping and to better interact with the surface Appendix L. These mechanisms and the slipping

behavior will be the focus of this work.

We specifically explored the threat avoidance jumping behavior of desert locusts to elucidate key morphological traits, which contribute to, and enhance, their surface friction; Materials and methods Appendix K. We challenged the locusts to jump, with their maximum energy, off a variety of both manufactured and natural surfaces and observed the interactions of the feet with each. Desert locusts have adhesive pads on their feet [110], which they use for climbing on smooth surfaces. However, they also possess four spines on their tibia, which we posited can interact with the surface during jumping and enhance their friction on rough surfaces.

Scansorial robots using either spines [38, 107, 113] or gecko-inspired adhesives [17, 55, 72, 95] have demonstrated the frictional ability of each of these attachment mechanisms on rough and smooth surfaces, respectively. However, since the desert locust has both adhesive foot pads and spines, we hypothesize that their feet have been not only optimized for smooth and rough surfaces but also dynamic attachment to each. They may however show specialization for one or the other, so to isolate certain traits of the spines and pads, surfaces were selected with differing roughness and surface hardness, including glass, wood, sandstone, and mesh. The smooth glass was selected to significantly reduce the spines' ability to interact strongly with the surface, whereas the mesh was selected to only allow spine-based mechanical interlocking. The wood and sandstone represent potential natural materials that the desert locust may come in contact with in their natural environment and thus show specialization. We observed both the slipping and re-engagement behavior of the feet on each surface to determine the characteristics and probability of these events. We also analyzed the morphology of their feet for clues about how they may interact with each surface.

As nature can alter more than just the roughness of the surface, we posited that the adhesive pads may also show some specialization for hydrophobic, such as the leaves of *Regnellidium diphyllum*, or hydrophilic, such as the leaves of *Alocasia odora*, surfaces [46, 73, 74]. This is because the smooth adhesive pads of the desert locust secrete an emulsion of "lipidic nano-

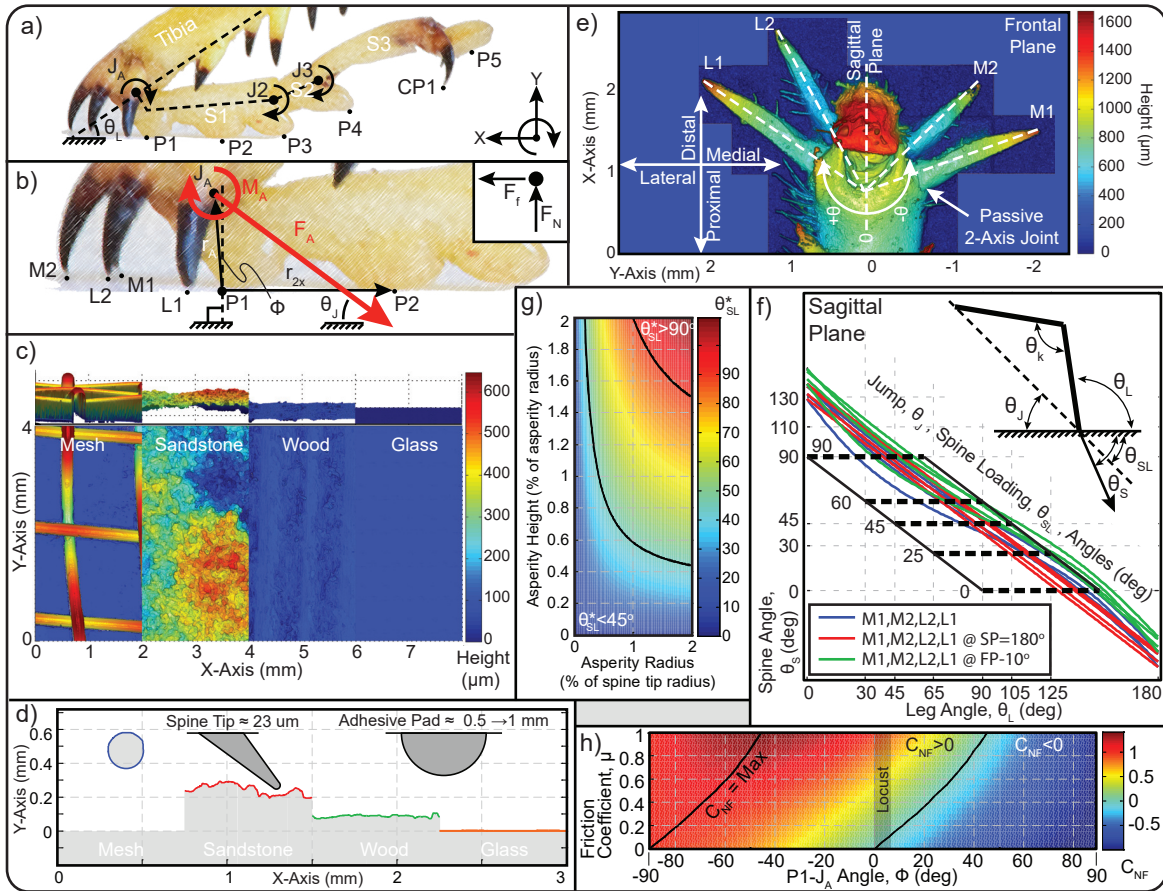


Figure 4.2: **a)** Breakdown of the desert locust’s foot morphology. **b)** Free-body diagram of the spines and segment  $S1$  adhesive pads. **c)** 3D Surface profilometer (Keyence - VK-X200) images of mesh, sandstone, wood, and glass (hydrophilic). Only the hydrophilic glass surface is shown, as the surface chemistry does not significantly alter the surface roughness. **d)** Roughness profiles along with the average spine tip radius and approximate adhesive pad diameter. **e)** Tibia spines with foot removed (3D surface profilometer (Keyence - VK-X200) image). **f)** Spine contact angle in the sagittal-plane for, the initial,  $180^\circ$  to sagittal-plane, and frontal-plane angle minus  $10^\circ$  configurations of the passive two-axes joint angles. **g)** Effective spine loading angle increase,  $\theta_{SL}^*$ , with lines at  $\theta_{SL}^* = 45^\circ, 90^\circ$ . **h)** Normal vs. frictional load coefficient,  $C_{NF} = \mu \cos(\phi) - \sin(\phi)$  from equation (4.2). The two lines represent the maximum coefficient,  $C_{NF} = \max$ , and that of the transition between passive adhesive pad loading and unloading,  $C_{NF} = 0$ ; passive unloading when  $C_{NF} < 0$ .

droplets dispersed in an aqueous liquid” [153] passively during the deformation of its sponge-like cuticle, as with other insects [41]. To isolate the pad behavior, smooth glass was selected. Through altering the surface chemistry, both hydrophobic and hydrophilic glass surfaces were created. The slipping behavior could then be observed on homogeneous surfaces with only a

difference in their wettability.

## 4.2 Locust: Morphological Results and Discussion

The desert locust (female  $2.32 \pm 0.31$  g, male  $1.67 \pm 0.14$  g;  $t(30)=10.0$ ,  $p=0.00$ ), shown in Fig. 4.1a, has 4 spines (Figs. 4.1b,c) with average tip radii of  $23.3 \pm 13.4$   $\mu\text{m}$  (Fig. 4.1d) and 5 adhesive foot pads (Figs. 4.1b,c). The spines (M1, M2, L1, L2) are connected to the tibia, whereas the adhesive pads (P1, P2, P3, P4, P5) reside on segments (S1, S2, S3) of the foot, as seen in Figs. 4.2a,b.

The selected materials include hydrophobic glass (contact angles of  $94.7^\circ/84.0^\circ$ ), hydrophilic glass (contact angles of  $32.6^\circ/21.6^\circ$ ), wood (sawn pine), sandstone, and mesh (steel). Figure 4.2c presents 3D surface profilometer (Keyence - VK-X200) images of each surface and Fig. 4.2d presents the relative sizes of the spine tips and adhesive pads in relation to the surfaces of the materials. The arithmetic mean area roughness,  $S_a$  (asperities), arithmetic mean line roughness discretized by the average spine tip radius,  $R_a$  (friction), and height range of each material are listed in Table 4.1. The wide range of possible jumping angles requires more than the traditional frictional model,  $\mu = 1/\tan \theta_J$ , which exceeds a necessary coefficient of friction of  $\mu = 1$  as the jumping angle is reduced below  $\theta_J = 45^\circ$ . Thus necessitating a transition to increasing the effective contact angle (spines), mechanical interlocking (spines), and adhesion (adhesive pads) to combat slipping.

### 4.2.1 Spine: Surface Interaction

The locust's spines protrude from the distal end of the tibia (Fig. 4.2e) defined by two characteristic angles measured from the leg's sagittal and frontal-planes as shown in Table 4.2. Comparing the sagittal-plane angles of the corresponding medial and lateral spines, M1, L1 ( $t(18)=2.44$ ,  $p=0.03$ ), and M2, L2 ( $p=0.03$  and  $t(17)=2.86$ ,  $p=0.01$ ), shows low significant differences in the angles, whereas the frontal-plane angles only show a significant difference, albeit low, between M1 and L1 ( $t(18)=2.85$ ,  $p=0.01$ ); indicating only minor probability of spine asymmetry. How-

Table 4.1: Summary of surface roughness properties

Material	Properties		
	$S_a$ ( $\mu\text{m}$ )	$R_a$ * ( $\mu\text{m}$ )	Maximum Height ( $\mu\text{m}$ )
Glass †	0.02	0.01	0.19
Wood (pine)	10.60	0.68	212.07
Sandstone	75.13	1.16	581.12
Screen (steel)	174.26	1.15	665.39

\* Discretized by average spine tip radius of 23  $\mu\text{m}$ .

†The transparency and reflectivity may have added noise to the measurements.

ever, the angles do indicate that all the spine will be oriented to interact with the surface during jumping.

Table 4.2: Spine characteristics

Spine	Angles to Leg Planes *	
	Sagittal Plane	Frontal Plane
M1	$-136.8 \pm 9.1^\circ$	$41.0 \pm 7.9^\circ$
M2	$-155.3 \pm 9.5^\circ$	$42.6 \pm 12.6^\circ$
L2	$144.1 \pm 8.0^\circ$	$47.7 \pm 8.4^\circ$
L1	$126.3 \pm 10.1^\circ$	$51.2 \pm 8.8^\circ$

\* The angles are measured from the specified planes.

Figure 4.2f shows the relationship between leg,  $\theta_L$ , spine,  $\theta_S$ , jumping,  $\theta_J$ , and spine loading,  $\theta_{SL} = \theta_J$ , angles; where  $\theta_S \leq 0$  indicates the spine tip is not longer able to interact with the surface. Each spine is not fixed in position, but connected to the tibia by a passive two-axes joint (Fig. 4.2e). The joints give the spines the freedom to change their sagittal-plane angle from the initial positions (Table 4.2) to nearly  $180^\circ$  (Fig. 4.2f, SP= $180^\circ$ ). This suggests that the spines can passively locate stable positions on the surface as they are loaded. These joints also allow for approximately minus  $10^\circ$  of rotation in the frontal-plane (Fig. 4.2f, FP= $10^\circ$ ). Therefore, as the spines are loaded, their effective spine angle is reduced, broadening the leg angle range over which they can interact with the surface. This joint will also include some damping, which

can be used to reduce the impulse caused by the spine re-engaging after a slip; increasing the chance of a successful re-engagement. Figure 4.2f shows that locusts have developed spines that can interact with the surface even in extreme cases; for example, a horizontal jump ( $\theta_J = 0^\circ$  and initial  $\theta_L = 90^\circ$ ) results in spine angles of  $\theta_S \in [38.8^\circ, 59^\circ]$ , permitting strong surface interaction. Spine placement however, typically only allows the more distal medial and lateral spines to interact with the surface.

The performance of spines is strongly related to the roughness characteristics of the surface, spine angle  $\theta_S$ , and spine loading angle  $\theta_{SL}$ . Building off the asperity interaction model presented in [35], we have included surfaces with overhanging asperities and, for our purposes, will calculate an effective increase to the spine loading angle for round asperities as:

$$\theta_{SL}^* = \cos^{-1}(1 - (P_p P_s)/(1 + P_s)) \quad (4.1)$$

where  $P_s \in [0, \infty]$  is the asperity radius as a percent of the spine tip radius and  $P_p \in [0, 2]$  is the asperity height as a percent of the asperity radius (Fig. 4.2g). Mechanical interlocking occurs at  $\theta_{SL} + \theta_{SL}^* \geq 90^\circ$  whereas  $\theta_{SL} + \theta_{SL}^* < 90^\circ$  reduces the required friction coefficient; for example,  $S_a(\text{wood}) = 10.6 \mu\text{m} \Rightarrow P_s = 10.6/23.3$  results in effective increase in the spine loading angles of  $\theta_{SL}^*(P_p = 2) = 68^\circ$  and  $\theta_{SL}^*(P_p = 1) = 46.6^\circ$  requiring a friction coefficient  $\mu = 0.40$  and  $\mu = 0.95$ , respectively, for a horizontal jump ( $\theta_J = 0^\circ$ ). A friction coefficient of  $\mu = 0.40$  is within generally achievable limits demonstrating that even at extreme jumping angles the locust's spines greatly enhance the surface friction. We expect the spines to find asperities with increasing likelihood on the wood, sandstone, and mesh. The glass, however, does not produce any usable asperities and therefore the adhesive pad performance can be isolated.

## 4.2.2 Adhesive Pads: Surface Interaction

Before jumping, the locust folds its foot under the tibia (Figs. 4.2a,b), which allows the adhesive pads to interact with the surface. We posit that segment  $S1$  is configured such that pad  $P1$  passively preloads the second two pads ( $P2$  and  $P3$ ) during jumping. Using the morphology and

summing the torques about pad  $P1$  yields an expression for the torque on segment  $S1$  as follows,

$$\begin{aligned} M_A + F_A \sin \theta_J r_A (\mu \cos \phi - \sin \phi) + \sigma A_p r_A \cos \phi \\ = R_p r_{2x} + R_p (r_{3x}/r_{2x}) r_{3x} \end{aligned} \quad (4.2)$$

where  $F_A$  is the ankle force,  $M_A$  is the ankle torque,  $R_p$  is the reaction force at pad  $P2$ ,  $R_p (r_{3x}/r_{2x})$  is the reaction force at pad  $P3$ , and  $r_{2x}$  and  $r_{3x}$  are the  $x$ -distances between pads  $P1$ - $P2$  and  $P1$ - $P3$ , respectively. The frictional,  $\mu F_A \sin \theta_J$ , and adhesive,  $\sigma A_p$ , forces have been substituted in to relate the applied horizontal force to that supported by the surface friction. The left side is then related to the applied loads and the right side, the passive loading of the adhesive pads; where the jumping angle range  $\theta_J \in [0, 90^\circ]$ ,  $P1$ - $J_A$  angle range  $\phi \in [-90^\circ, 90^\circ]$  ( $\phi > 0$  is in the  $+x$ -direction), and the friction coefficient  $\mu$  determine the loading behavior.

The only way equation (4.2) can produce a negative torque, unloading the adhesive pads, is for the normal vs. frictional load coefficient,  $C_{NF} = (\mu \cos \phi - \sin \phi)$ , to be less than zero,  $C_{NF} < 0$ ; assuming the adhesion is attractive. Fig. 4.2h presents the relationship between the friction coefficient,  $\mu$ , and the  $P1$ - $J_A$  angle,  $\phi$ , where the optimal  $P1$ - $J_A$  angle is  $\phi = \tan^{-1}(-1/\mu)$  and the transition between loading and unloading is governed by  $\phi = \tan^{-1} \mu$ . Thus demonstrating that the locust can preload its pads passively, as seen in Fig. 4.2h, under nearly any coefficient of friction. The highly deformable adhesive pads makes exact measurement of the angle difficult; however, under load,  $\phi$  approaches zero. Applied ankle torque,  $M_A$ , can be used to increase the pad loading for additional adhesion, whereas pads  $P4$  and  $P5$  will generally not contribute.

### 4.2.3 Multi-Surface Foot

So the desert locust has developed feet for robust jumping locomotion on both rough and smooth surfaces but with different loading conditions; the spines attached directly to the tibia receive the majority of the jumping force, whereas the adhesive pads attached to the foot receive a much smaller amount. Its important to note that the pads make contact with the surface first and are slightly deformed before the spines make contact. We propose this difference corresponds

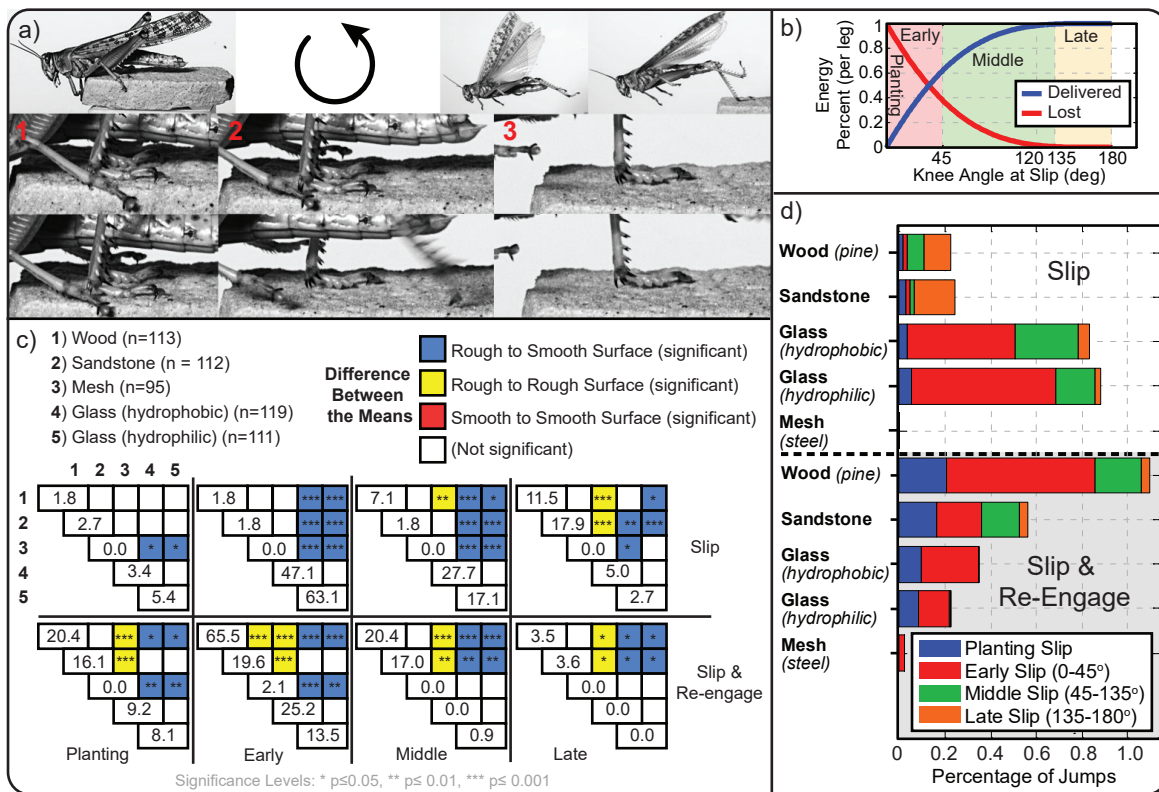


Figure 4.3: **a)** Example of a jumping trial with slips highlighted, including minor asperity failure slip and re-engagement (right foot), slip (left foot), and slip and re-engagement (right foot). **b)** The percent of the jumping energy dissipated or delivered given a slip at a particular knee angle,  $\theta_K$ . **c)** A significance matrix comparing all the combinations of materials divided into slip type and knee angle,  $\theta_K$ , range. The diagonals are the mean values for each surface. **d)** Percent of jumps where slips occur both with and without re-engagement. **Note:** Slip events are counted separately for each leg.

to the particular needs of each attachment mechanism. Spines effectively increase the contact angle between the foot and surface, reducing but still requiring traditional load-based friction; for interlocking, the maximum friction is a function of the yield strength of the spine material. Whereas, pad-based adhesion is a function of normal preload; however, the load required is typically, at least, an order-of-magnitude less than the tangential force produced for flat adhesives and greater than that for structured adhesives [70, 94, 161]. In this way, the locust may have developed a strategy, whereby, the spines receive the majority of the force to maximize their friction and chance of interlocking, and the adhesive pads, needing less preload, are directly loaded with a much lower force, relying instead on the passive loading to saturate the preload.

The combination of adhesive pads and jointed spines, as evolved in the desert locust, presents a multi-functional foot with embodied mechanical intelligence for passive adaptation to a wide variety of surfaces.

### 4.3 Locust: Experimental Results and Discussion

The locust's feet however are not perfect, as evident by their adaptations for slipping. Fig. 4.3a presents 3 different slips within a single jump: (1) right foot minor asperity failure and re-engagement, (2) left foot slip, and (3) right foot slip and re-engagement (Supplementary Materials Video). Using a high speed camera (VisionResearch, Phantom v641) to compare performance, we analyzed the number of slips and re-engagements per foot over approximately 100 experimental trials for each test surface (Materials and Methods).

The experimental results are separated first into slips, where the foot leaves the surface (termed: slip), and slips, where the foot re-engages the surface (termed: slip and re-engage). These categories are further divided into the surface materials and the knee angle ranges at which the slips occurred. The knee angle is divided into 4 ranges which bound the amount of jumping energy lost,  $E_L$ : planting ( $E_L \approx 100\%$ ), early ( $E_L \in [38, 100]\%$ ), middle ( $E_L \in [0.6, 38]\%$ ), and late ( $E_L \in [0, 0.6]\%$ ) slips; as seen in Fig. 4.3b. A planting slip occurs when the locust initiates a jump without the feet in contact with the surface and a slip occurs before the foot comes to rest; this unknown behavior broadens the applicability of the foot design to dynamic attachment.

Figure 4.3c presents a significance matrix, comparing all the combinations of surfaces divided into slip type and knee angle,  $\theta_K$ , range. The diagonals are the mean values for each surface with each slip on each leg counted separately; the standard deviations are generally on the order of the means due to the high probability ( $1.0 \pm 0.9$ ) of secondary slips after a re-engagement. Whereas, Fig. 4.3d presents the slip events separated in the same manner as the significance matrix, but arranged to show the variability among the different surfaces. These two figures provide the information necessary to make some conclusions about the adaptability and specialization of the

locust's foot as well as glean inspiration for concepts to improve robot locomotion.

### 4.3.1 Spine: Slip vs. Re-engagement

The spines are able to adapt to a variety of rough surfaces, both with roughness less than (wood  $S_a = 10.6 \mu\text{m}$ ) and greater than (sandstone  $S_a = 75.13 \mu\text{m}$ ) the spine tip radius ( $23.3 \mu\text{m}$ ), as evident by the similar mean slips between wood ( $0.22 \pm 0.44$ ) and sandstone ( $0.24 \pm 0.47$ ) ( $t(222)=0.3$ ,  $p=0.74$ ). However, as would be expected, the smaller asperities are less stable and result in more slipping, as evident by the significantly different mean slip and re-engagements for wood ( $1.10 \pm 1.13$ ) and sandstone ( $0.56 \pm 0.89$ ) ( $t(212)=4.0$ ,  $p=0.00$ ). This reinforces that spine interactions are roughness dependent, but also that the locust's spines are well developed to find and hold asperities after a slip, resulting in minimal loss of jumping energy.

### 4.3.2 Adhesive Pads: Slip vs. Re-engagement

Re-engagement of adhesive pads poses a particular challenge, as the transition between static and dynamics regimes tends to reduce the interaction strength, making re-engagement impossible. However, re-engagement is observed in the planting, early, and middle knee angle,  $\theta_K$ , ranges, with similar mean values on the hydrophobic ( $0.47 \pm 0.73$ ) and hydrophilic ( $0.30 \pm 0.51$ ) ( $t(154)=1.8$ ,  $p=0.07$ ) glass surfaces. The locust's leg morphology and the catapult type jump are similar to the MultiMo-Bat, which has previously been shown to produce increasing force over the jumping cycle, up to approximately a knee angle of  $\theta_K = 120^\circ$  when lift-off occurs [159, 160]. This increase in applied force in addition to the locust's active ankle joint,  $M_A$ , may be compensating for the reduced interaction strength, making the observed re-engagement of the adhesive pads possible.

### 4.3.3 Spines vs. Adhesive Pads

The desert locust, having both spines and adhesive pads, shows specialization towards spine base friction for jumping, as evident by the significantly lower amount of slips on the wood

( $0.22\pm 0.44$ ), sandstone ( $0.24\pm 0.47$ ), and mesh ( $0.0\pm 0.0$ ), as compared to the hydrophobic glass ( $0.83\pm 0.66$ ) and hydrophilic glass ( $0.88\pm 0.70$ ); no slips were observed for the mesh. The significance matrix shows pervasive significant differences in the means for early and middle slips between rough and smooth surfaces; however, not for planting and late slips. Planting though is unique, in that it is the most dynamic region, and the similar means suggest that both the spines and adhesive pads have equal difficulty in successfully interacting with the surface at high velocities. The drop-off in significance in the means of late slips can be attributed to the loss of spine interaction, due to the leg angle, and potential lift-off which occurs around a knee angle of  $120^\circ$  for a catapult type jump with this leg morphology [159].

#### **4.3.4 Creating vs. Locating Asperities**

The spines show specialization towards locating asperities rather than creating them, as evident by the decreasing number of mean slips in the first three knee angle regions for wood ( $1.17\pm 1.17$ ) vs. sandstone ( $0.59\pm 0.90$ ) ( $t(210)=4.2$ ,  $p=0.00$ ) and sandstone vs. mesh ( $0.02\pm 0.14$ ) ( $t(118)=6.6$ ,  $p=0.00$ ), ordered from lowest to highest roughness and asperity height. We would expect a very low number of slips on the soft wood if the locust was able to penetrate the surface to enhance the friction. Surface profilometer (Keyence - VK-X200) scans of the wood surface also shows no indication of penetration; however, only destructive penetration or plastic deformation would be observed after the jump was completed. The low slips on mesh also demonstrates the relative strength and stability of these two types of mechanical interactions, mechanical interlocking being much higher.

#### **4.3.5 Hydrophobic vs. Hydrophilic Surfaces**

The adhesive pads do not show a specialization for hydrophobic or hydrophilic surfaces as evident by the similar mean slips,  $0.83\pm 0.66$  and  $0.88\pm 0.70$  ( $t(224)=0.6$ ,  $p=0.57$ ), and similar mean slip and re-engagements,  $0.34\pm 0.66$  and  $0.23\pm 0.46$  ( $t(212)=1.6$ ,  $p=0.11$ ); this corroborates results by [42] for climbing aphids and confirms a supposition by [153] for locusts. Further more,

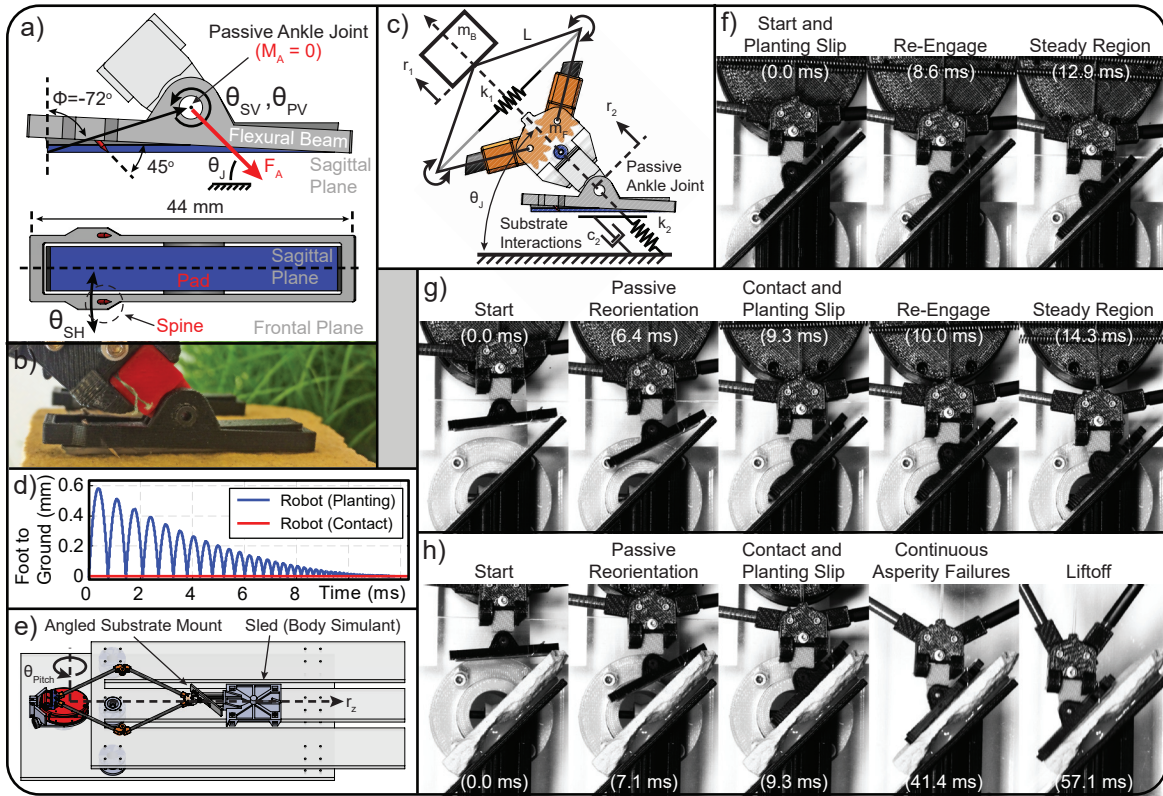


Figure 4.4: **a)** CAD drawing of the SLIP foot design with the degrees-of-freedom of the spines,  $\theta_{SV}$  and  $\theta_{SH}$ , and pad,  $\theta_{PV}$ , labeled. **b)** Photo of constructed SLIP foot. **c)** Free-body diagram and **d)** the simulated jumping response of the MultiMo-Bat with integrated SLIP foot, focused on the ground impact and resulting bouncing behavior for the planting and contact type jumps. The geared leg joints ensure synchronization and axially applied force. **e)** Jumping rig for deterministic testing and observation of the foot-surface interaction, which is dynamically similar to that of the MultiMo-Bat. **f)** Contact jump snapshots on a glass surface. **g)** Planting jump snapshots on a glass surface. **h)** Planting jump snapshots on a sandstone surface.

this suggests that the wettability of the surface does not effect the adhesive properties during the highly dynamic jumping locomotion. Coalescence of the emulsion can lead to a surface film and reduce friction [43, 44], therefore it is most likely stable, allowing a number of capillary bridges [16, 87] between the foot and surface to form, enhance friction through contact pinning and viscous forces.

## 4.4 Robot: Biologically Inspired Design

While jumping locomotion does not preclude static surface engagement, locusts exhibit both planting jumps and surface re-engaging behaviors, indicating that the locust's foot design may have broader applicability to robot locomotion, as these behaviors necessitate dynamic surface engagement. Extracting the features and functions of the locust's foot discussed previously, the simplest interpretation is used to develop a robotic multi-Surface Locust Inspired Passively-adaptable (SLIP) foot for the MultiMo-Bat, a vampire bat-inspired integrated multi-modal jumping-gliding robot [159, 160].

### 4.4.1 SLIP Foot

The SLIP foot, Figs. 4.4a,b, incorporates all the features extracted from the locust's foot. The spines are steel pins mounted at a  $45^\circ$  angle and attached to flexural beams (cross section  $1 \times 3$  mm ( $w \times h$ )) - material modulus experimentally determined in Appendix N - which allow sufficient freedom to move both horizontally  $\theta_{SH} = \pm 4.8^\circ$  ( $\pm 1$  mm) and vertically,  $\theta_{SV}$ , to find asperities and strong enough to penetrate soft surfaces to create its own asperities. The elastomeric adhesive pads (Smooth-On, Ecoflex 00-20) are dry, employing instead van-der-Waals forces to eliminate the difficulty of maintaining a fluid on the feet. The pad is symmetric about the ankle joint, with  $\phi \approx -72^\circ$ , thus ensuring passive pad loading. The rotational dynamics of the adhesive pad,  $\theta_{PV}$ , and spines,  $\theta_{SV}$ , are decoupled from each other as well as the leg,  $\theta_L$ , allowing each to passively orient to the surface throughout the jump, including during slipping. The loading of the spines and adhesive pad is similar to that of the locust, where the pad must be deformed for the spines to engage the surface. However, as the adhesive pad has a thickness of 1 mm and 100% tensile modulus of 55.2 kPa, initial deformation of the distal region opposite the spines requires little force, allowing the spines to interact immediately.

To investigate the potential benefits of an energy absorbing region, similar in function to the locust's buckling region [13], a two-body jumping simulation was developed; as seen in

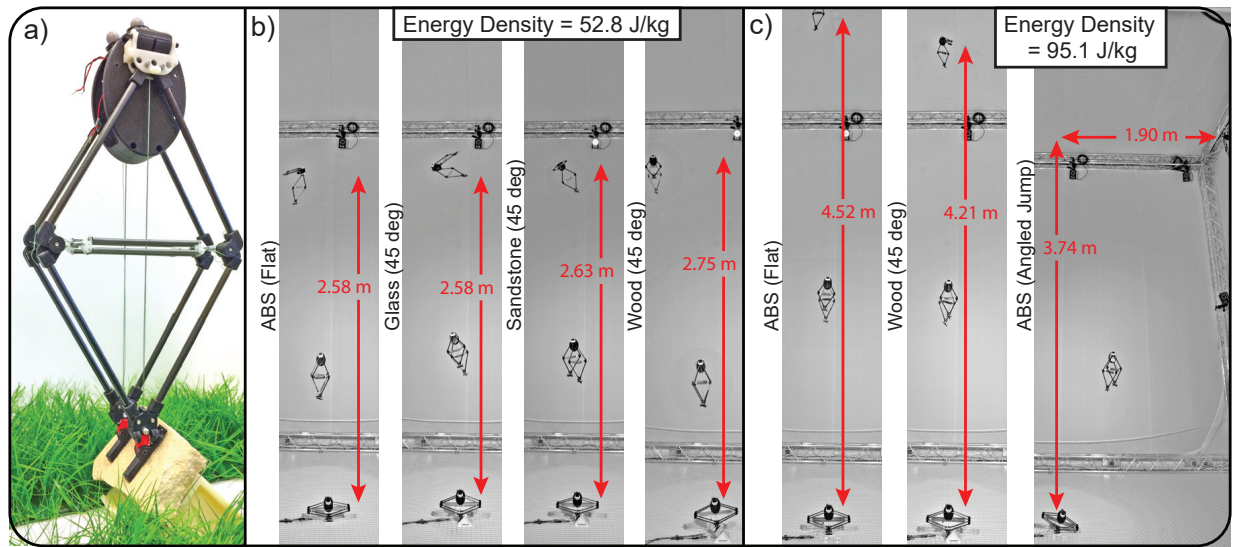


Figure 4.5: **a)** Photo of the jumping-gliding robot, MultiMo-Bat, with the wings removed on the  $\theta_J = 45^\circ$  sandstone surface. **b)** Jumping energy density set to 52.8 J/kg; complete robot trials on flat (ABS) and angled (glass, sandstone, wood) surfaces. **c)** Jumping energy density set to 95.1 J/kg; complete robot trials on flat (ABS), angled (wood) surfaces, and angled jumping (ABS). **Notes:** Motion capture system (Vicon, Vantage) was used for positional data. Angled jump measurements were taken at the last tracked position.

Fig. 4.4c, where the dynamic equations are shown in Appendix M. The leg compliance caused by the driving spring, similar to series elastic actuation [115], provides significant energy absorption from impacts. However, in addition, integrated into the kinematic chain of the leg and foot are several 3D-printed ABS (Stratasys uPrintSE Plus, ABSplus) components, which have a relatively low coefficient of restitution,  $COR = 0.8929$ ; experimentally determined in Appendix N. This acts as the buckling region in the locust's leg, dissipating some of the impact energy of the foot,  $c_2$ , which reduces bouncing, facilitating surface interaction, Fig. 4.4d; other effects such as adhesion, interlocking, and the elastomer foot pads will add additional damping, whereas the foot mass,  $m_F$ , is directly related to the bouncing amplitude and should be minimized.

Finally, inspiration is taken from planthopper (*Issus*) nymphs, which use biologically created gears [23], to synchronize the two sides of the robot's legs, ensuring the force produced is along the center-of-mass axis, as seen in Fig. 4.4c.

## 4.4.2 Experimental Results and Discussion

To experimentally characterize the performance of the SLIP foot, a specific series of trials were conducted at a jumping angle of  $\theta_J = 45^\circ$ , at which point the necessary friction coefficient is difficult to achieve using the traditional friction model. A dynamically similar jumping rig, Fig. 4.4e, was used to facilitate observation (VisionResearch, Phantom v641) of the foot and uniform testing Appendix M compares the dynamics of the robot and the jumping rig). The testing sequence is as follows: glass, sandstone, wood, and glass, where 10 trials are conducted for first the planting and then contact type jumps on each surface in the sequence; where the approximate foot impact velocity is 3.4 m/s and 0 m/s, respectively (Supplementary Materials Video). The order is designed to challenge the SLIP foot, as no modifications or cleaning is conducted between trials; the glass and sandstone can dull or damage the spines, whereas, the sandstone and wood can contaminate and damage the adhesive. The order ensures that each material is tested after the SLIP foot has undergone jumps which can reduce the performance of the primary attachment mechanism.

The robot shows much more deterministic jumping behavior than that of the locust. Table 4.3 presents the behaviors observed on each material in the sequence; where all 10 jumps within each category show the same behavior. The SLIP foot shows no slips albeit some slipping and re-engaging is observed. The glass surface trials all present a planting slip and re-engagement as the preload is increasing after which good surface adherence is achieved (Figs. 4.4f,g). The planting jumps on sandstone show a behavior not observed in the locust trials, that is of repetitive minor asperity failures over approximately a 1.5 to 2.5 cm distance (Fig. 4.4h); observed as approximately linear scratches in the sandstone. Resulting in only a minor loss of energy. Both jump types on wood and contact jumps on sandstone show no slipping and present the best behavior with strong surface interaction.

Comparing with the locust trials, we would expect the best performance to be achieved on the sandstone surface, however, the SLIP foot is supporting significantly larger loads. This results

Table 4.3: Robot Experimental Jumping Results

<b>Surface<sup>†</sup></b>	<b>Planting Jump (n=10 ea.)</b>	<b>Contact Jump* (n=10 ea.)</b>
Glass	Planting Slip+Re-engage	Planting Slip+Re-engage
Sandstone	Slip+Re-engage (Continuous)	No Slip
Wood	No Slip (Penetration)	No Slip (Penetration)
Glass <sup>‡</sup>	Planting Slip+Re-engage	Planting Slip+Re-engage

\* Zero preload.

<sup>†</sup>Listed in the experimental order.

<sup>‡</sup>The foot is not altered or cleaned.

in a change in behavior where, unlike the locust, the spines are easily able to penetrate the wood surface creating very stable mechanical interlocks. The cohesion of the sandstone surface, which easily supported the locust’s tip loading, can however, only support the relatively low dynamic interactions of the contact type jumps, but fails during the highly dynamic impacts of the planting type jumps; this issue can be eliminated by increasing the number of spines to reduce the tip loading. The observed deviation from exactly linear scratches demonstrates the spines’ ability to adapt their position and the foot’s ability to maintain surface interaction during slipping. The SLIP foot also shows much improved smooth surface friction over that of the locust. The similarity of the slipping behavior between planting and contact type jumps is an indication of the importance of the passive loading behavior and not impact loading. This is because both jump types begin with zero preload, and both require an extended preloading period before sufficient adhesion is created to resist slipping.

It is difficult to observe bouncing as the expected size scale is relatively small, although no obvious interface separation from the surface was observed. However, during planting jumps, small oscillations can sometimes be observed not at the interface but in the foot itself, which may indicate the expected minor bouncing. These oscillations are damped within a few cycles due to the added damping of the entire kinematic chain with integrated low COR components and the soft elastomer foot pads.

The decoupling of the rotational dynamics of the adhesive pad and spines is crucial to the

performance of the SLIP foot; several coupled variants were tested and showed significant slipping. This is primarily due to the spine friction transitioning from static to dynamic, caused by torque oscillations produced as a result of the passive loading of the adhesive pad (Supplementary Materials Video).

Finally, the SLIP feet were tested on the MultiMo-Bat (Fig. 4.5a) to validate the system integration and performance. The MultiMo-Bat was tested first on a flat ABS surface and then on angled ( $\theta_J = 45^\circ$ ) glass, sandstone, and wood surfaces (Fig. 4.5b), where the behavior matches that of the constrained jumping rig trials. The MultiMo-Bat produces a maximum jumping height of 2.75 m with similar jumping heights for all cases, where the jumping energy density (J/kg) is approximately equal to the jumping rig. Increasing the jumping energy density by 80% (Fig. 4.5c), propels the MultiMo-Bat up to the maximum height of 4.52 m. Continued slipping is observed on the angled wood surface due to the significant increase in tip loading; however, the passive confirmation of the SLIP foot allows the MultiMo-Bat to extract sufficient energy to propel itself up to heights greater than 4 m. In these cases, the surfaces were angled however, Fig. 4.5c also demonstrates that we can control the jump angle of the robot. Thus, whether the surface is angled or the desired locomotion direction, the SLIP feet can strongly interact with a wide range of surfaces to support dynamic locomotion.

## 4.5 Chapter Summary

Analysis of the locust's slipping behavior shows how likely is to slip during dynamic terrestrial locomotion such as jumping. However, because of this, the locust has developed a number of impressive adaptations to hold and, when a slip does occur, to re-engage the surface, minimizing the amount of dissipated energy and still enabling a successful jump. The locust's foot morphology has significant mechanical intelligence embodied therein, which provide both the spines and adhesive pads with the necessary loading conditions to maximize their ability to contribute to the friction on a wide variety of surfaces.

Through inspiration from and interpretation of the locust's morphology and behavior, we developed a robotic foot, which is capable of passively adapting and interacting with a wide variety of surfaces under a range of dynamic conditions from zero velocity contact type jumps to the high velocity impacts of planting type jumps. In the event of slipping, as seen in both sandstone (52.8 J/kg) and wood (95.1 J/kg), the SLIP foot can maintain sufficient surface friction, propelling the MultiMo-Bat to heights greater than 4 meters. Future work will focus on a more rigorous characterization of the individual effects of the adhesive pads and spines to surface friction and slipping.

For a robot to locomote in an unstructured terrestrial environment, a key component is that which interacts with the environment itself. Here we have presented not only a multi-surface foot but also the concepts necessary for passively interacting, through embodied mechanical intelligence, with a wide variety of surfaces under a wide range of dynamic conditions; and thus, as with the locust, can free up computational power for other tasks. These concepts can be directly integrated into existing robots with point-contact type feet and the current state-of-the-art robotic systems, as the embodied mechanical intelligence make them fully self contained; as seen with the MultiMo-Bat, which employs them as shoes. Building on the concepts, future work may look at adding a two degrees-of-freedom ankle joint and multi-directional adhesive pads and spines to better align and interact with an even wider range of surfaces. This study of the locust's feet highlights the significance of embodied intelligence to the biological system and hopefully inspires further study of embodied intelligence in locomotion design.

# Chapter 5

## Summary

### 5.1 Thesis Summary

To the author's knowledge, at the onset of this research, this is the first time integration of locomotion modes has been studied for robot development. This work serves to highlight the key abstractions associated with integrated multi-modal locomotion and the potential benefits gained by this concept. We presented a number of different MultiMo-Bat's with varying capabilities from significant embodied mechanical intelligence to high energy density actuation to feet specialized for strong interaction with both rough and smooth surfaces, all of which, allows the MultiMo-Bat to reach some of the greatest heights seen in both robots and biological organisms. The concepts presented are not specialized to the MultiMo-Bat, but in fact, the MultiMo-Bat is simply an application and proof-of-concept of the discovered, analyses, developed, experimentally verified, and presented concepts; each of which has broad applicability within the field of miniature robot mobility as well as the larger scientific community.

### 5.2 Current and Future Research

#### Active Control - Tail

It has been show by other groups that the addition of a tail can assist in controlling aerial phases of the robot through shifting angular momentum between the tail and body of the robot. This concept however, requires a tail capable of producing angular momentum on the order of the en-

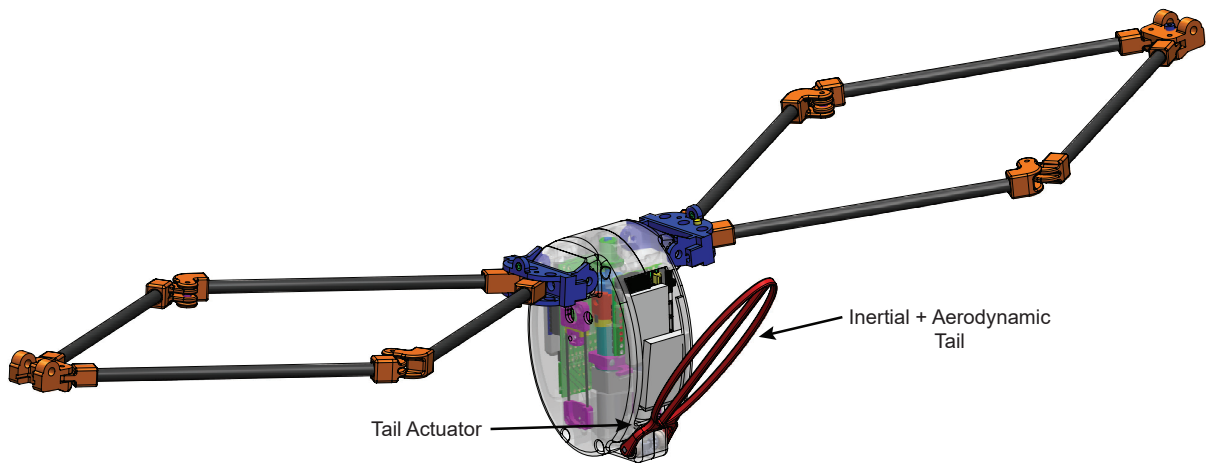


Figure 5.1: MutliMo-Bat with combined inertial and aerodynamic tail.

tire system and thus constitutes a significant additional mass. The high level of inertial coupling between the jumping and gliding modes prohibits such an addition. Therefore, the dynamics of the system will be used instead to increase the effect of a tail.

A tail has the potential to significantly improve the multi-modal locomotion as it can assist during nearly all phases of operation. Through contact with the ground the tail can orient the body prior to the jump to control the jumping direction. During the coast phase the high velocity airflow provide significant potential for creating control torques and, held at a constant angle, control forces to modify the coast phase trajectory and prepare for the coming gliding phase. During gliding flight, the tail can be used to stabilize the glide resulting in increase glide performance.

Development of the 1-axis tailed MultiMo-Bat, Fig. 5.1, is currently ongoing with focus placed on determining the optimal initial angle and gliding trajectory which will be maintained through active tail control. The tail will be co-designed along with the controller ensuring the necessary control authority over each phase of locomotion.

### **Active Control - Wing Deformation**

Current and future work will investigate coast and gliding phase control through wing deformation. Using shape memory alloy (SMA) actuators integrated into the airfoils can allow for

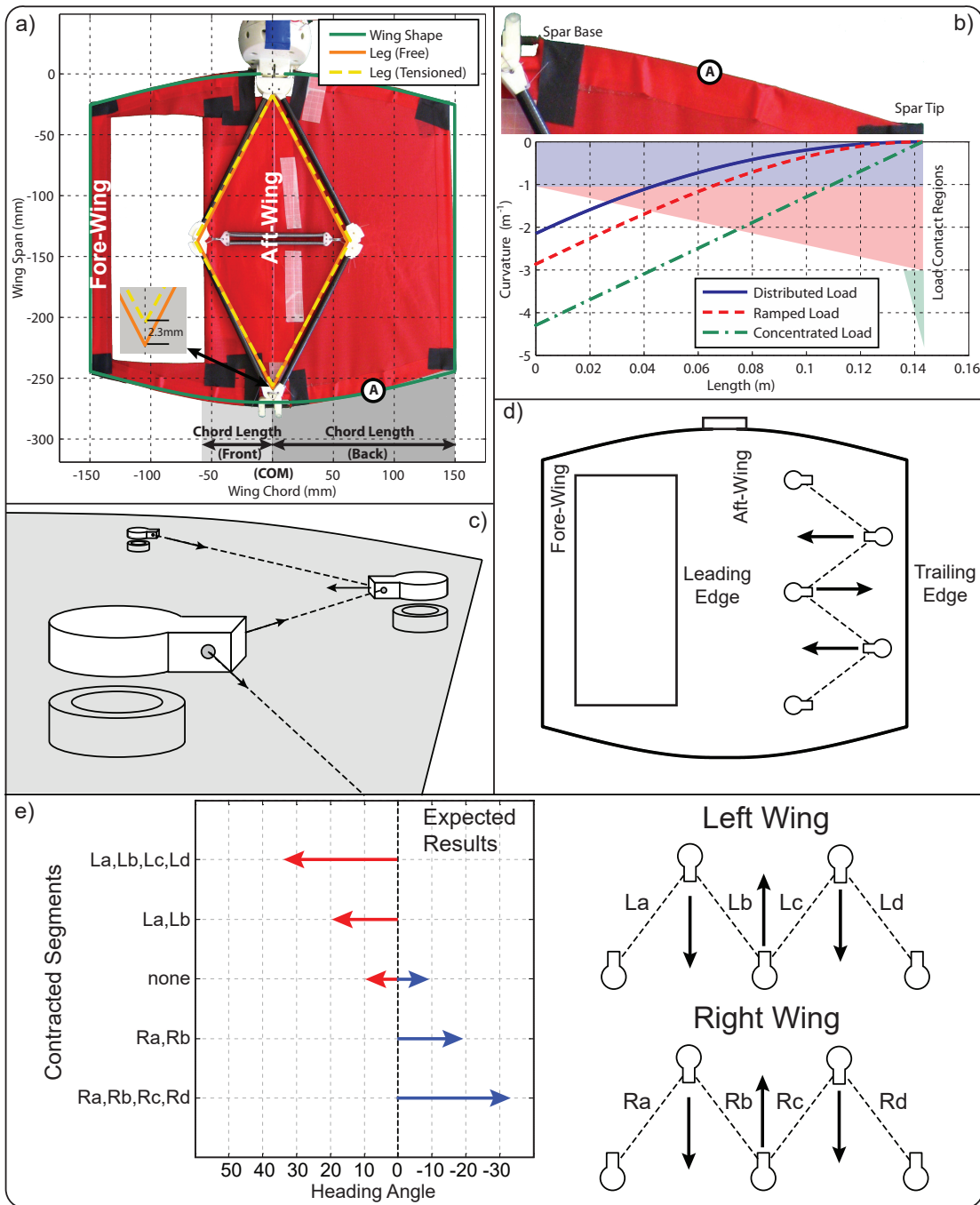


Figure 5.2: **a)** The current wing design produces two airfoils small fore-wing and larger aft-wing. **b)** Shape is controlled by the tension profile. **c)** Magnetic wing clamps for variable deformations without wing modification. **d)** Magnetic wing clamps positioned to pull on the trailing edge. **e)** Expected results of the presented deformations, however, preliminary experimental results show a reduction in gliding distance.

lift/drag asymmetry through independent deformation of portions of the airfoils.

The original wing design remains constant, Fig. 5.2a, however, as the wing shape itself is a function of the designed tension profile, Fig. 5.2b, modification of the tension causes modification of the wing shape, and thus the aerodynamic characteristics. To facilitate testing of various control strategies, magnetic wing clamps are developed through which shape memory alloy wire may be routed, Fig. 5.2c. The clamps are easily reconfigured without effecting the wing. The clamps may be positioned in a number of ways however, as the center-of-mass position in relation to the leading edge has previously been shown to have a significant effect initial placement will try to vary the leading edge position through modification of the trailing edge, Fig. 5.2d; direct leading edge deformation is difficult as the four-bar legs come in contact with this section of the airfoil and therefore make attachment less reliable.

Initial experiments were conducted with the configuration presented in Fig. 5.2d with the experimental deformations shown in Fig. 5.2e. However, instead of altering the heading of the MultiMo-Bat as expected the preliminary results showed only a significant variation in gliding distance. Therefore further study is necessary for directional control of gliding however, the preliminary result may still be promising as the landing area may not always be observable until the MultiMo-Bat is in the coast phase. Thus the MultiMo-Bat, on observation of a danger in the expected landing area, could arrest its glide and parachute back to the jumping position. Preliminary experiments also show the fore-wing as a major contributor to the gliding behavior, therefore small variations in this wing may have more significant effects on the robot's flight.

### **Active Control - High Level Tasks**

Future work will investigate higher level control within the integrated locomotion design strategy by leveraging the perspective of each mode. The latest MultiMo-Bat has an on-board controller, radio, IMU, camera, and extension for GPS. The complete sensor suite will allow the MultiMo-Bat to observe and measure the environment from both the elevated perspective for targeting, path planning, and air measurements while ground level observation has the potential to capture

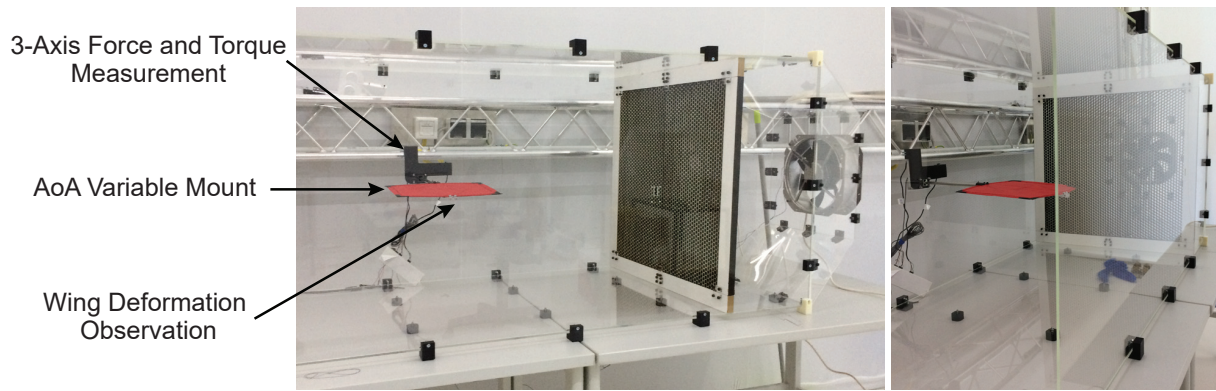


Figure 5.3: Experimental wing tunnel for observation, characterization, and optimization of the highly deformable airfoils during flight conditions.

higher resolution data about the terrestrial environment.

### **Enhanced Gliding Performance**

Currently we are exploring methods for improving the gliding performance through characterization and optimization of the collapsible airfoils developed in this work. The major difference between traditional and the developed collapsible airfoils is the tensioning of the wing membrane. This creates the potential to vary the wing shape during initial design as well as dynamically due to differing angles-of-attack (AoA) during flight. To observe the behavior in a controlled fashion a wind tunnel, Fig. 5.3, has been developed where the aerodynamic forces and airfoil shape can be simultaneously measured.

### **Jumping on Granular Media**

Currently, in addition to exploring the effects of jumping on hard surfaces, I am also considering those surfaces which might deform under the jumping load. Granular media is such a surface and poses a significant challenge as it acts much more like a liquid than a solid, as seen in Fig. 5.4, but is actually neither. This difference may result in dynamic behaviors which exhibit characteristics of both. Groups have studied a number of different aspects of locomotion on granular media from both the jamming approach to encourage a more solid surface behavior to swimming. However, the highly dynamic jumping behavior of the locust may elucidate additional,

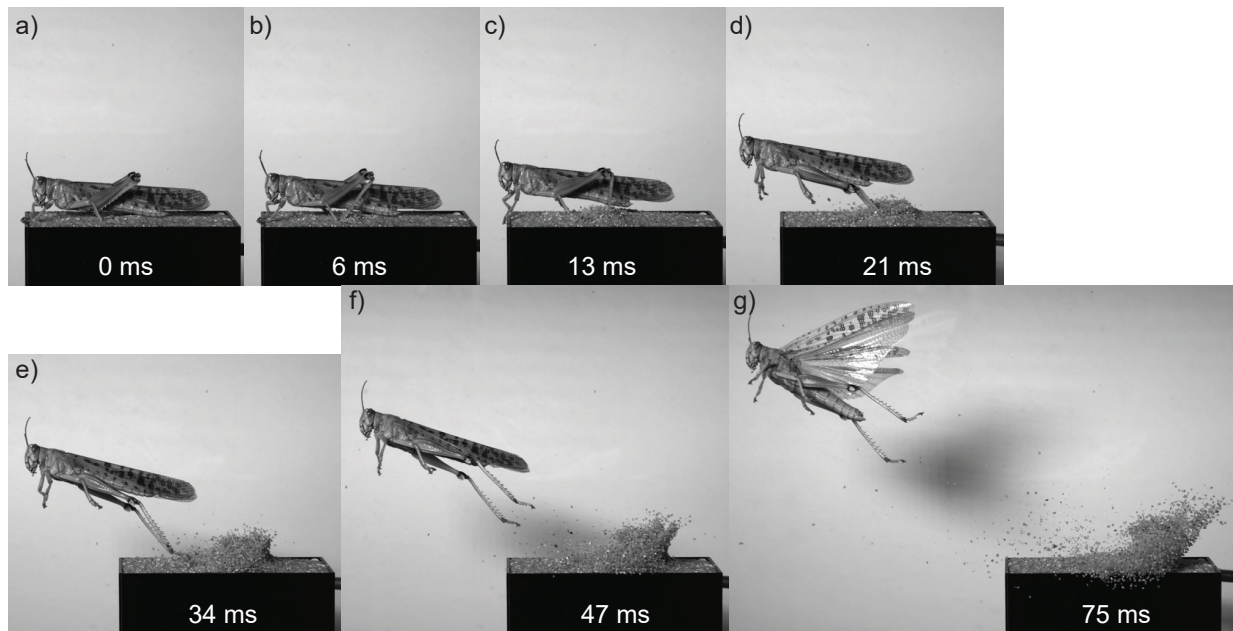


Figure 5.4: Desert locust jumping on unpacked sand where the behavior of the surface appears to act like a liquid.

as of yet, unknown characteristic and design concepts for improving the mobility of miniature robots.

### 5.3 Publications

- Woodward, M. A. and Sitti, M. (2011). Design of a miniature integrated multi-modal jumping and gliding robot. *IEEE/RSJ International Conference on Intelligent Robots and Systems*, pages 556-561 (**JTCF Novel Technology Paper Award for Amusement Culture Finalist**)
- Woodward, M. A. and Sitti, M. (2014). MultiMo-Bat: A biologically inspired integrated jumping-gliding robot. *International Journal of Robotics Research*, 33(Sept):1511-1529 (**Top 5 Most Read Articles 2014 IJRR**)
- Woodward, M. A. and Sitti, M. (accepted). Universal Custom Complex Magnetic Spring Design Methodology. *Transactions on Magnetics*
- Woodward, M. A. and Sitti, M. (under review). Tailored Magnetic Springs for Detwinning

of Shape Memory Alloy Actuated Robotic Mechanisms. *Transactions on Robotics*

- Woodward, M. A. and Sitti, M. (submitting). A Slippery World: how the desert locust's approach to slipping can inspire dynamic robots.
- Woodward, M. A. and Sitti, M. (in process). The Desert Locust's Highly Dynamic Interactions with Granular Media.
- Kim H., Woodward, M. A., and Sitti, M. (under review). Enhanced Non-Steady Gliding Performance of the MultiMo-Bat Through Optimization of the Center-of-Pressure and Onset Orientation. *ICRA 2018*

# Appendix

## Appendix A Preliminary Prototypes and Experiments

### A.1 Modular Independent Jumping Mode

Initial research aimed to add a jumping locomotion mode to a previously developed wall climbing robot, called Waalbot [95, 96]. This robot used gecko inspired fibrillar adhesive pads to climb on smooth surfaces however, these surfaces were not continuous and therefore jumping was a possible method for overcoming obstacles between them.

As the robot already existed the developed jumping mode was created around the necessity to combine it with the existing system. Therefore, the jumping mode was developed to be modular so the components could be assembled in different configurations such that their effect on the robot was minimized. The jumping mode consists of two main subsystems: the energy storage system and the jumping leg. To allow for maximum flexibility the connection between these components was selected to be a cable as it could be routed as necessary to fit within the confines of the robot. To facilitate testing, the two subsystems were combined into a self contained robot which later saw the addition of passively deployed wings, as seen in Figs. A.1 and A.2. However, the ability to be reconfigured was preserved throughout the development. For this system the springs were used directly as the jumping leg and the cable directly compressed them. The energy storage system consisted of a transmission to increase the mechanical advantage and a cam to linearize the required torque during the energy storage process. The energy was released at a fixed point through the removal of two teeth from the final transmission gear set. Once reached

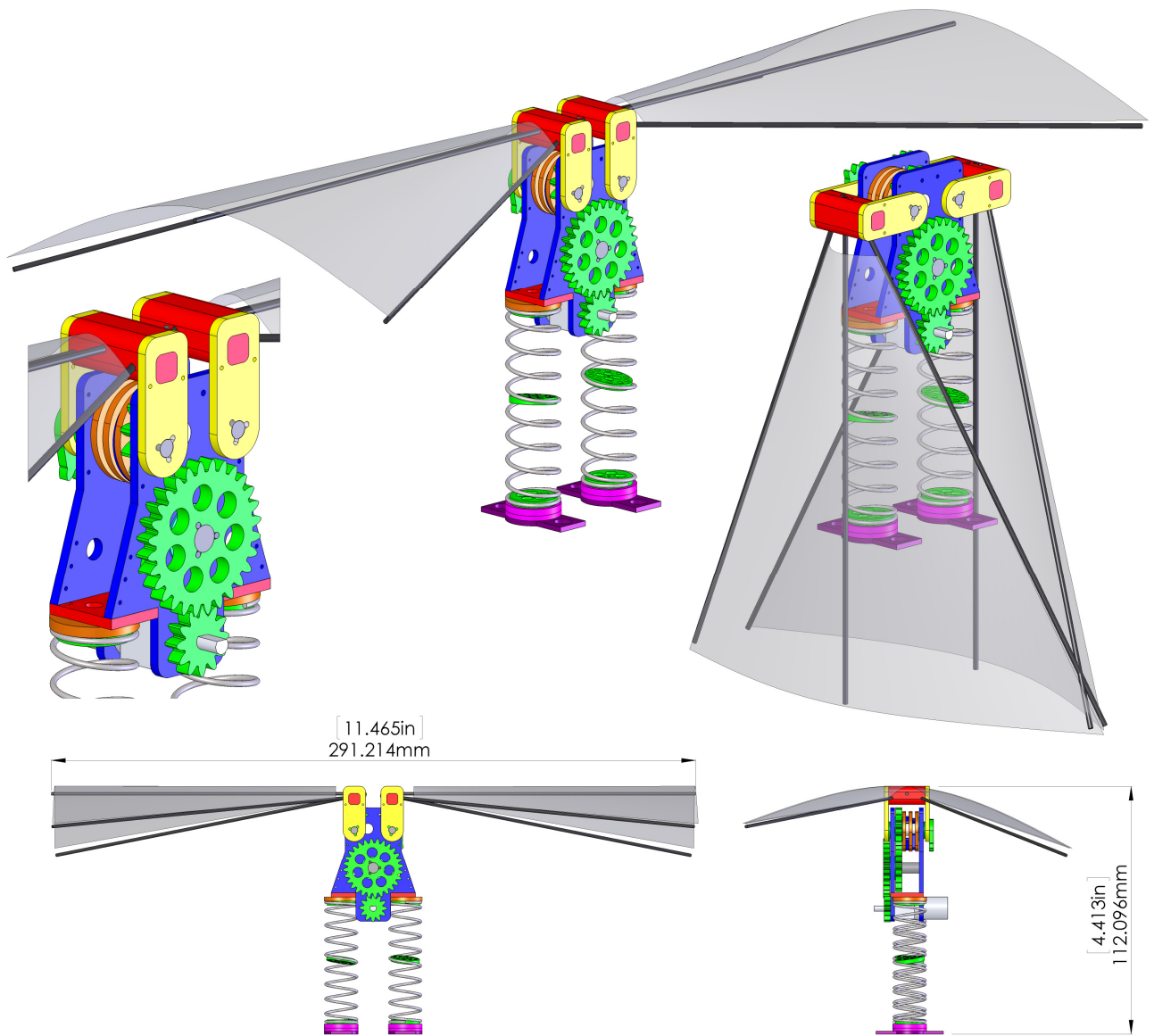


Figure A.1: The CAD model of the first generation jumper is shown with the wings in the deployed and folded states. All components are manufactured from acrylic sheets with the exception of the red wing mounts which are 3D printed significantly reducing cost of manufacturing.

the cam was able to spin freely releasing the stored energy. The entire system was designed to be miniaturized and manufactured in metal to increase strength and significantly reduce the size allowing for easier addition to the existing robot. The current prototype is constructed primarily from laser cut acrylic sheets to reduce cost with the wing mounts 3D printed.

Even with miniaturization the combination would have significantly reduced the performance

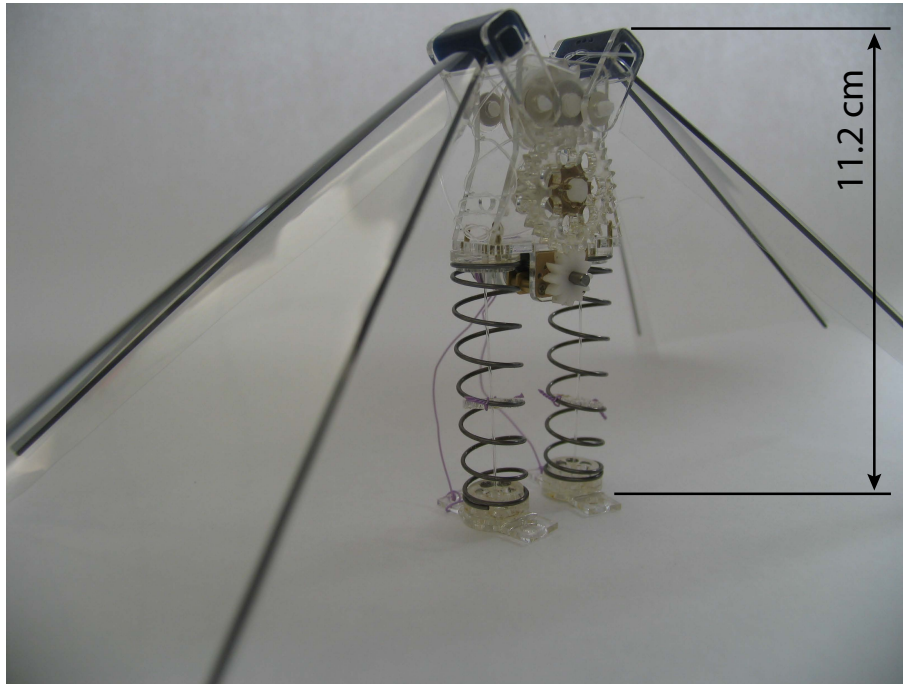


Figure A.2: A photograph of the first generation jumper is shown with thin wires from the motor attached to the feet. The robot is positioned on two conductive pads which provide power to compress the springs. This configuration eliminates the possible effects of the power tether during the jump and coast phases. The wing membranes are constructed from mylar sheets.

of the existing system while producing a jumping mode with performance not sufficient for obstacles of any reasonable size. To achieve the successful combination of these two modes it was realized that the development of an entirely new system would have been required.

This prototype demonstrated several concepts that were carried into future generation of jumping robots. First, the use of cables to store energy in elastic elements allows for significant flexibility in the mounting of the two subsystems. Second, the primary issue with the combination of the two modes was the added mass of the new system of which much of the support structure was duplicated. This caused a significant increase in system mass which reduced performance of all the modes. Finally, the addition and experimental verification of passively deployed asymmetric wings which produced directional gliding proved the potential of this concept and is carried into later prototypes. Also coast phase stability was initially seen with the addition of the wings on the prototype.

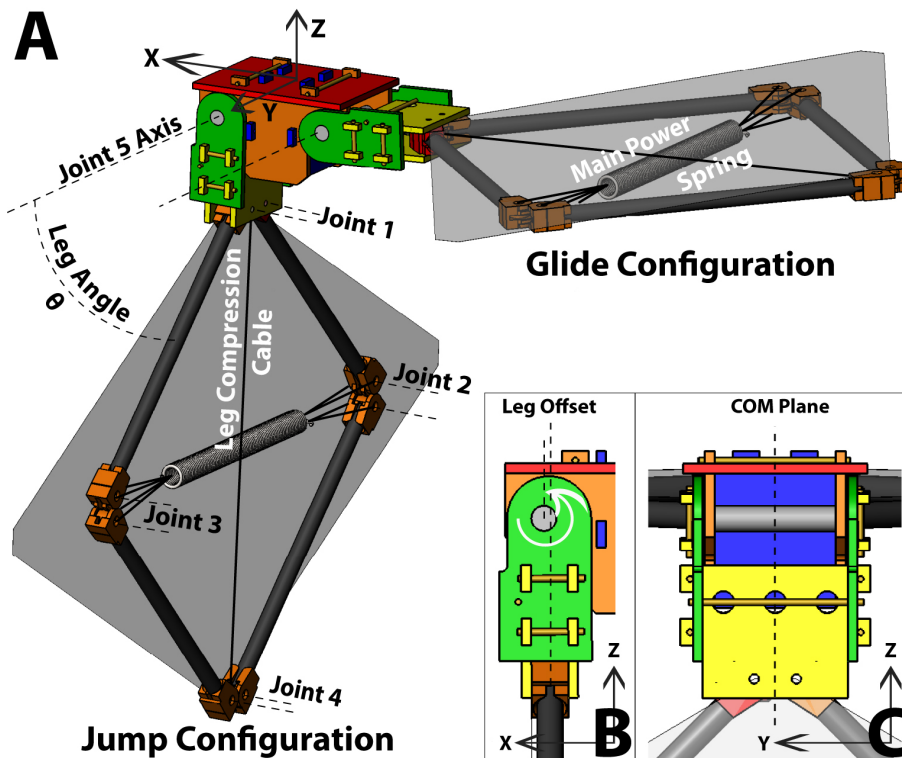


Figure A.3: A) Concept shown with one leg in the jumping configuration and one in the gliding configuration. Joints 1-4 are responsible for the leg extension/retraction whereas Joint 5 is responsible for the transition between jumping and gliding configuration. B) Leg offset utilized for configuration change. C) The  $x - z$  COM plane positioned at the center of the leg assembly.

## A.2 Proof-of-Concept Integrated Jumping and Gliding Robot

Two prototypes have been constructed to test the viability and performance of the proposed jumping and gliding robot concept. Each one is designed to facilitate the testing of key aspects of the overall system.

The first prototype is designed for testing the integration strategy, coast phase stability, and the transition from the jumping configuration to the gliding configuration (Figs. A.3 and A.4a). To facilitate these experiments the overall system performance is reduced to allow for testing in indoor confined environments. The prototype weighs 72 g and is capable of maximum jumps of approximately 1.7 m, which is sufficient for the analysis of all aforementioned behaviors. The additional structures required to generate the gliding mode consist of the wing membrane, carbon fiber support, and elastic element for tensioning the wing (Fig. A.4a). These components result

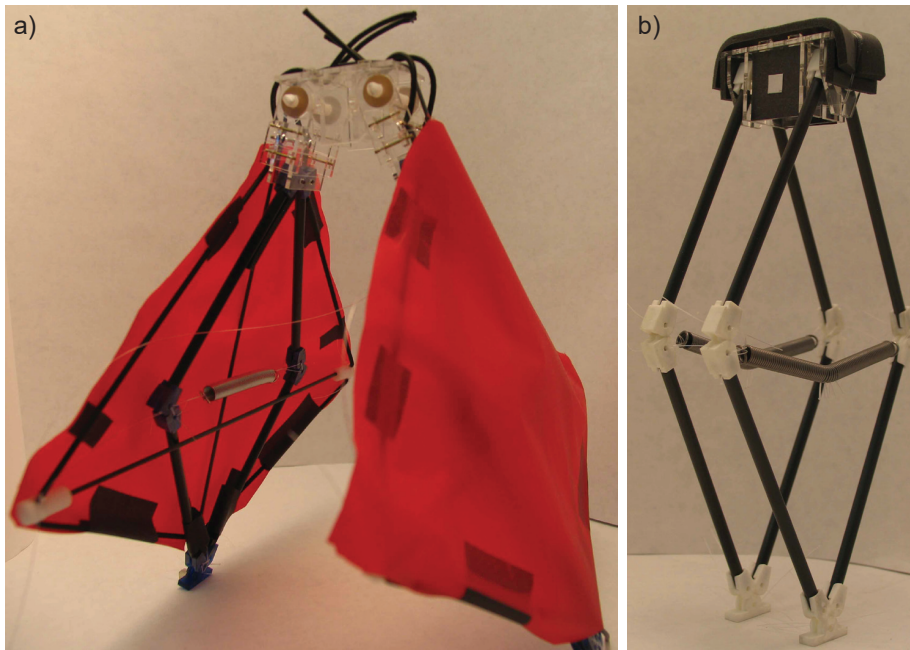


Figure A.4: **a)** Prototype exhibiting both jumping and gliding locomotion modes. Shown with its legs positioned between the jumping and gliding states. **b)** High performance jumping prototype. Shown with molded joints.

Table A.1: Prototype Specification

Subsystems	Prototypes	
	Jumping and Gliding	Jumping
Jumping Mode Structure (g)	49	37
Gliding Mode Structure (g)	16	NA
Power Springs (g)	7	14
Energy Storage (g)	20	20
<b>Robot (g)</b>	<b>92</b>	<b>85</b>
Performance		
Experimental Mass (g)	72	55
Lift-off Velocity (m/s)	5+ (exp), 7.1 (sim)	12.9 (sim)
Jumping Height (m)	1.7 (exp)	6+ (sim)

\* Simulated values (sim) and experimental values (exp). The simulated value are calculated using the single DOF jump phase dynamic model with the parameters for the particular prototype.

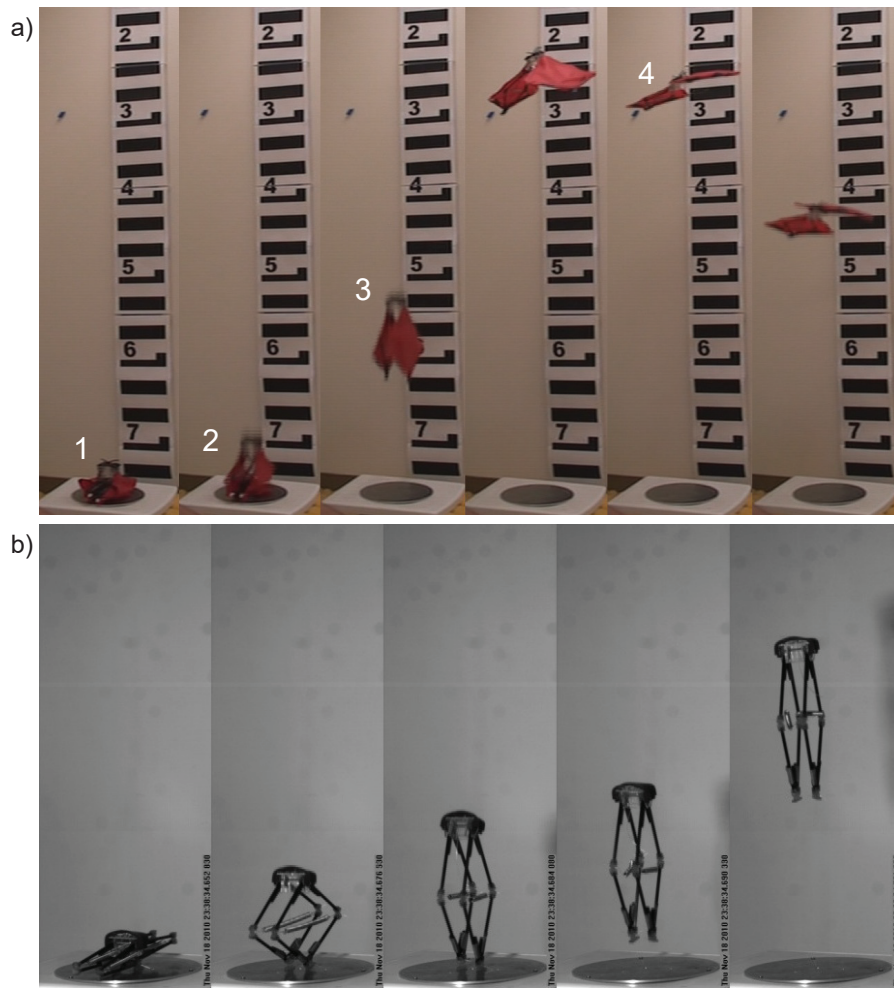


Figure A.5: **a)** Snapshots from the jumping movie of the jumping-gliding robot in operation: a.1 Shows the end of the energy storage phase, a.2 the jumping phase, a.3 the coasting phase, and a.4 the gliding phase. **b)** Earlier prototype of the robot presented in Fig. A.4b.

in a total added mass to the system of 16 g. The prototype was tested both with, Fig. A.5a, and without the additional wing structures to determine the overall effect of the integration strategy. The result is a reduction in jumping height due to the added mass however, the structure is able to stabilize the prototype during the coast phase and the passive conversion between locomotion modes is successfully proven.

The second prototype is designed to test the maximum jumping performance of the system, therefore, the wing components were not included (see Fig. A.4b). The experiential trials (Fig. A.5b) of the first generation of this prototype highlighted the joints as a major weak point

of the robot. These which were subsequently switched to soft-molded joints. This prototype will test the structural strength and behavior of the system under high loads. This is important because the system is concerned with weight reduction and therefore must operate much closer to the limits of the components to achieve maximum performance in all locomotion modes. Testing of the individual four-bars under full load has been successful. This system utilizes optimized springs capable of storing 3 J of energy at a minimum weight of 7 g each. This prototype weighs 55 g and is capable of maximum jumps of greater than 6 m with the possibility of further increasing the power.

## Appendix B Derivation of the Spring Design Equations

The relationship between the yield strength and the wire diameter has been empirically determined as

$$S_{ys} = \frac{R}{\xi} Qd^b \quad (\text{B.1})$$

where  $Q$  and  $b$  are fitting parameters associated with the material and  $d$  is the wire diameter used to calculate the ultimate tensile stress,  $S_{ut} = Qd^b$  [101]. The ultimate shear stress is approximately equal to a constant percentage,  $R$ , of the ultimate tensile stress and a safety factor,  $\xi$ . The second difference is associated with the fact that the rod is coiled and not straight which adds a direct shear component and creates a stress concentration on the inner most edge of the cross-section of the wire. The shear stress profile can be calculated as the sum of the torsional shear stress plus the direct shear stress. Assuming the wire has a circular cross-section the maximum shear stress in the cross-section of the spring is

$$\tau_M = K_w \frac{8FD}{\pi d^3}, \quad K_w = \frac{4C-1}{4C-4} + \frac{0.615}{C} \quad (\text{B.2})$$

where  $F$  is the force at full extension of the spring and  $D$  is mean coil diameter. To account for the curvature, Wahl's Factor,  $K_w$ , which also includes the direct shear factor, is typically substituted into the equation yielding the maximum stress in the coil; which is a function of the

spring index  $C = D/d$  [101]. To ensure maximum energy storage, the maximum shear stress in the coil is set equal to the yield stress of the material,  $\tau_M = S_{ys}$ . Then, eq. B.2 is solved for the applied force,  $F$ , and substituted it into the standard equation for calculating the spring constant of a helical extension spring. This combined equation can then be solved analytically for the mean coil diameter,  $D$ , as a function of the length ratio,  $L_r$ , and the wire diameter,  $d$  such that

$$D_1 = \frac{d}{4} + \frac{\sqrt{C_1 + C_2 + 150d^2}}{20\sqrt{6}} + \frac{\sqrt{2C_1 - C_2 + 300d^2 + \frac{3\sqrt{3}d(173C_1 + 10^4d^2)}{10\sqrt{2}\sqrt{C_1 + C_2 + 150d^2}}}}{20\sqrt{6}} \quad (\text{B.3})$$

$$C_1 = \frac{400GL_r d^2}{\pi S_{ys}}, \quad C_2 = \frac{10^{1/3} \left( 10^{1/3} C_3^2 + 20GL_r d^4 (200GL_r + 1257\pi S_{ys}) \right)}{\pi C_3 S_{ys}} \quad (\text{B.4})$$

$$C_3 = \left( GL_r d^6 \left( -8(10^4)G^2 L_r^2 + 2.046(10^6)GL_r \pi S_{ys} + 6.642(10^5)\pi^2 S_{ys}^2 \right) - 3GL_r d^6 \sqrt{3\pi S_{ys}} \right. \\ \left. \sqrt{-1.66(10^{10})G^3 L_r^3 + 1.231(10^{11})G^2 L_r^2 \pi S_{ys} + 4.184(10^{10})GL_r \pi^2 S_{ys}^2 + 1.634(10^{10})\pi^3 S_{ys}^3} \right)^{1/3}$$

where the length ratio,  $L_r = y/(L_m \lambda)$ , is a function of the spring extension,  $y$ , the maximum mounting length of the spring,  $L_m$ , and a reduction factor,  $\lambda = 1 \rightarrow 0$ , which reduces the free length of the spring to a percentage of the available mounting length.

The final parameters for the design are the required energy,  $E$ , to be stored and the number of springs,  $n$ , used to store it. Using eq. B.2 again, and substituting in  $F = 2E/(ny)$ , the mean coil diameter,  $D$ , can be found as a function of  $E$  and  $n$  as

$$D_2 = \frac{-146dE + 25n\pi d^3 y S_{ys} + \sqrt{4.149(10^5)d^2 E^2 - 4.730(10^4)n\pi d^4 y E S_{ys} + 625n^2 \pi^2 d^6 y^2 S_{ys}^2}}{800E} \quad (\text{B.5})$$

# Appendix C Airfoil CFD

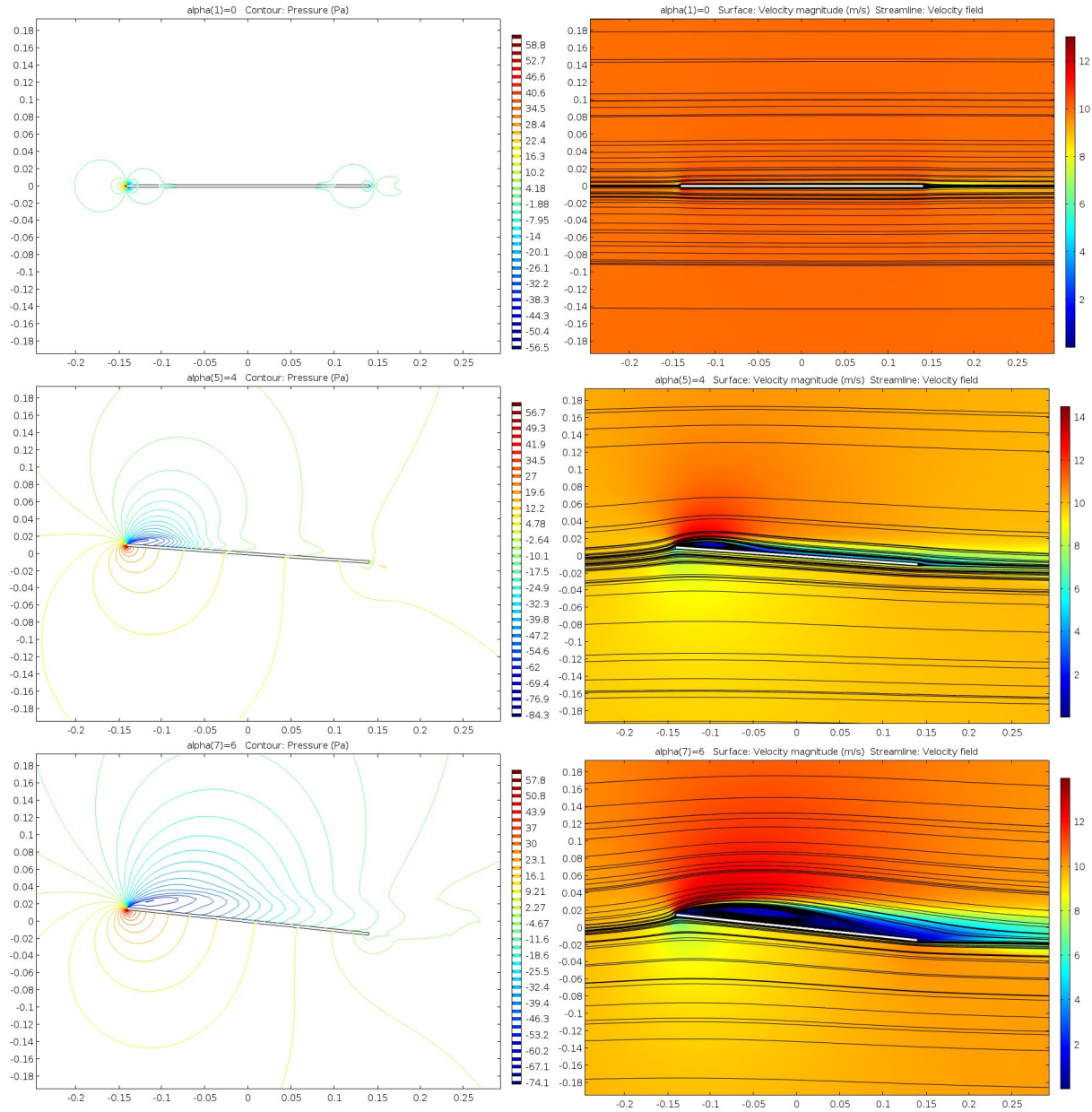


Figure C.1: **Left)** Relative pressure and **Right)** velocity and stream lines in the simulated space. The development of the pressure and velocity distribution over the airfoil is shown through the three subsequent angles-of-attack of 0, 4, and 6 degrees. Data generated via Comsol CFD.

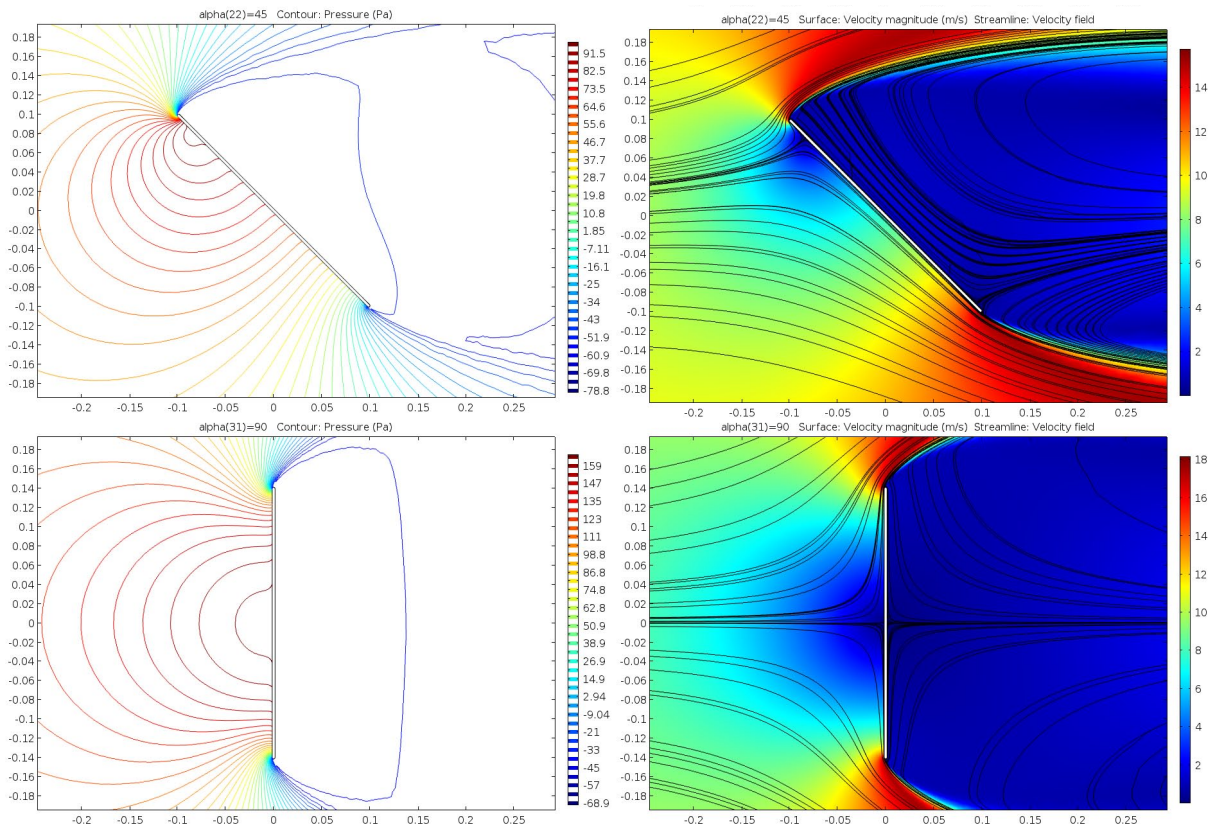


Figure C.2: **Left)** Relative pressure and **Right)** velocity and stream lines in the simulated space. The AoAs of 45 degrees and 90 degrees demonstrate the fully stalled regime where the velocity distribution over the upper side of the airfoil approaches zero and the pressure magnitude becomes symmetric. Data generated via Comsol CFD.

# Appendix D MultiMo-Bat CAD Drawings

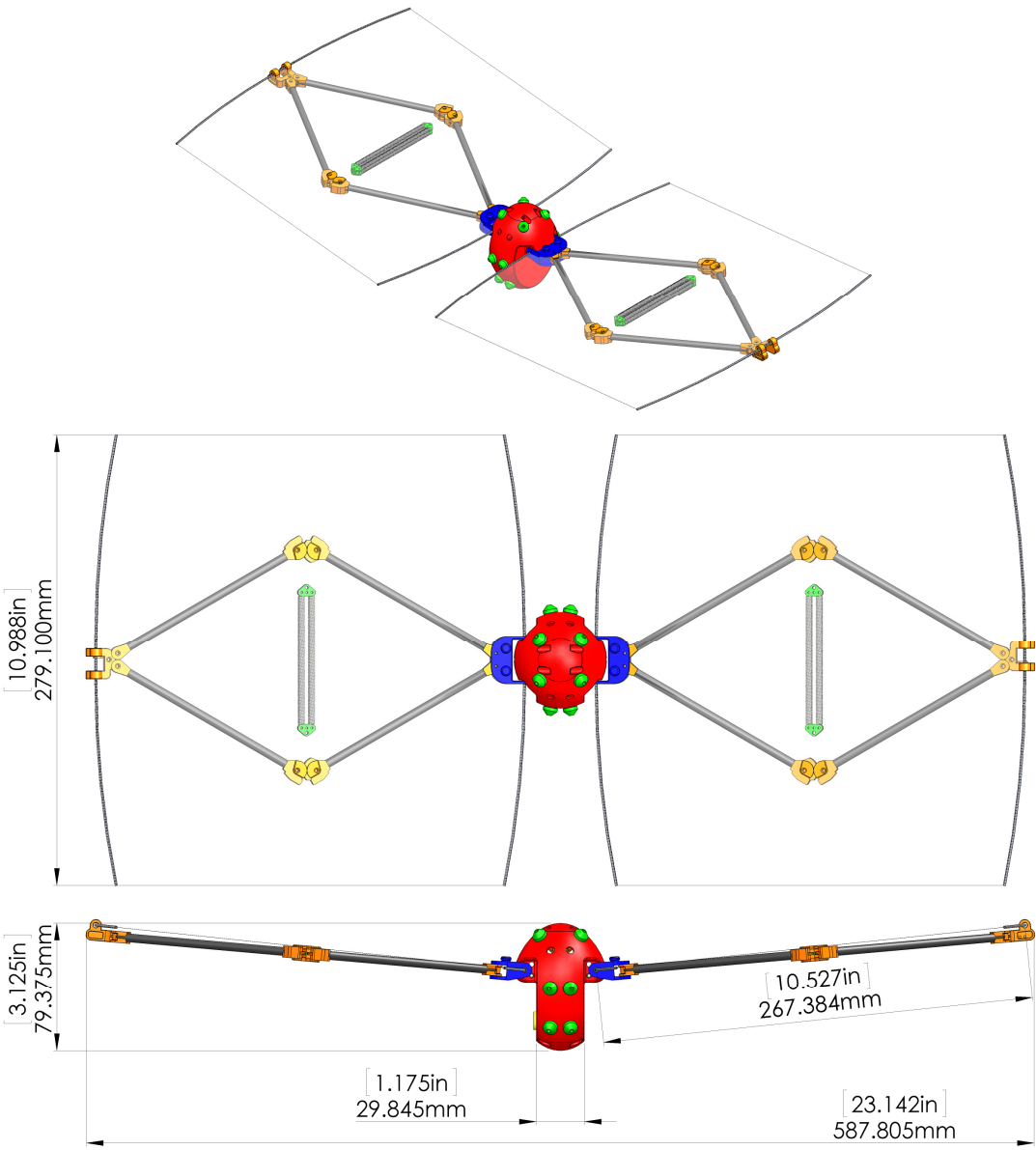


Figure D.1: Gliding configuration. CAD drawings presenting the characteristic dimensions of the MultiMo-Bat.

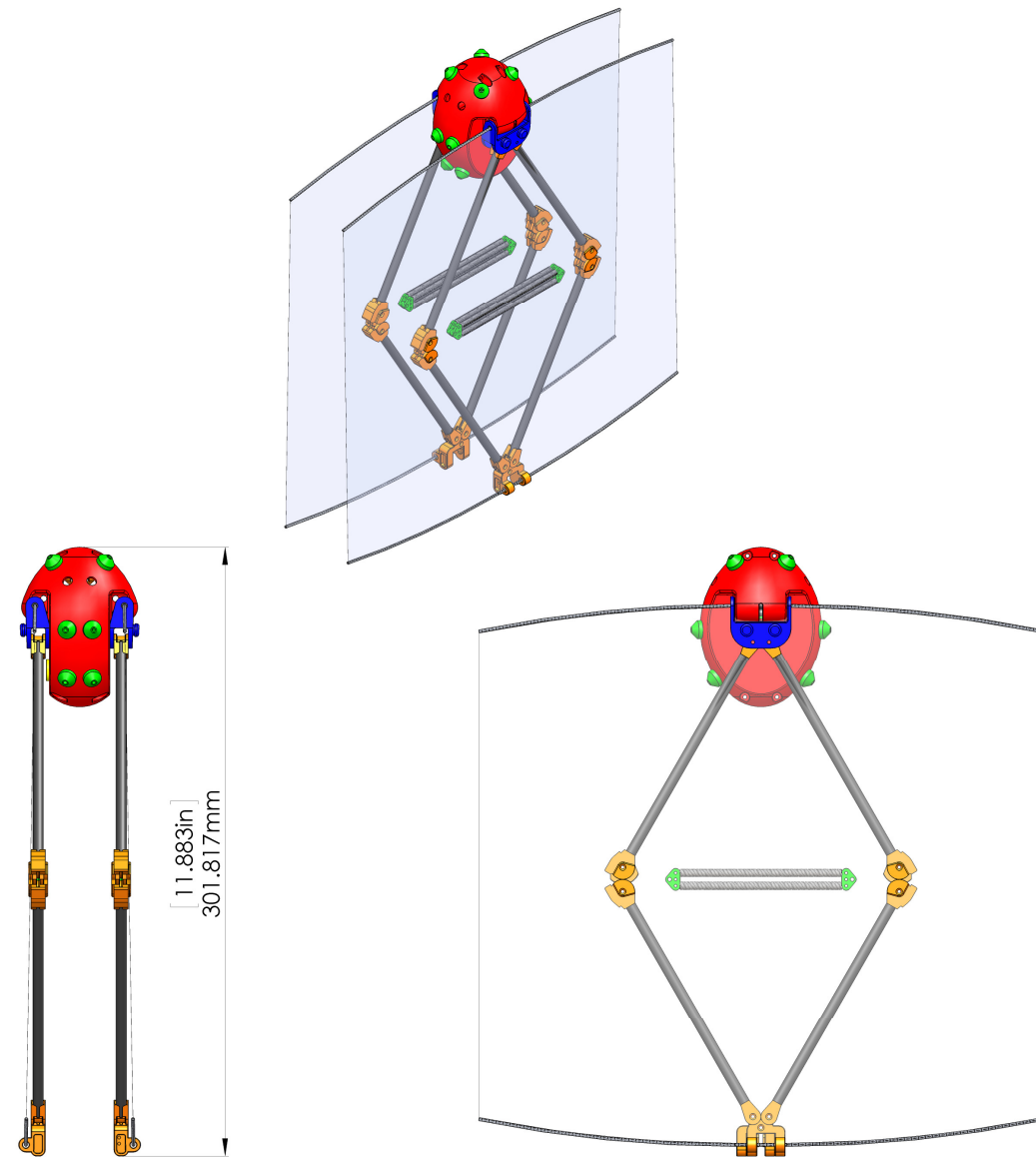


Figure D.2: Jumping configuration. CAD drawings presenting the characteristic dimensions of the MultiMo-Bat.

## Appendix E Manufacturing: Soft Molding Process

As stated throughout the work, integration inherently results in increased component functionality. This tends to increase the complexity of the components and therefore the complexity of their manufacturing. Standard machining techniques become impossible to use as they are not physically capable of creating the component features necessary. Utilizing 3D printed parts solves this issue however; the material possibilities are limited by those available to the 3D printer. A soft molding process allows for a much larger set of materials removing the reliance on the quality of the 3D printer material. This process significantly reduces the cost of development as only a single 3D printed master is required for each part. The soft molding process does reduce the possible features which can be created however, due to the soft mold, can still create features impossible through standard machining.

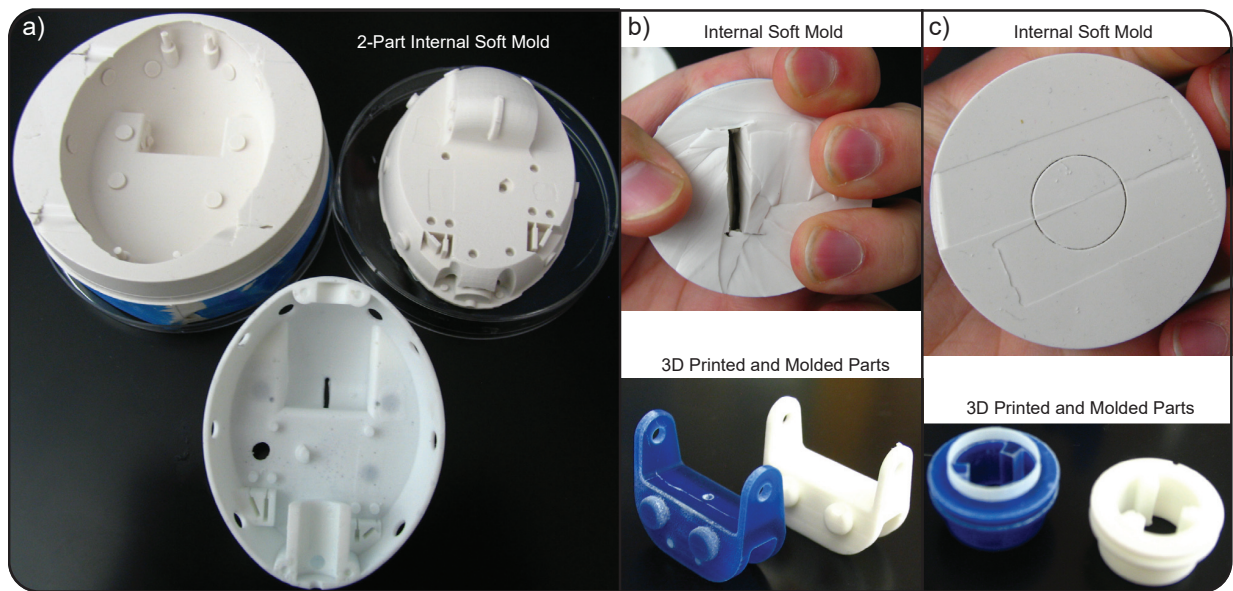


Figure E.1: **a)** The body component requires a two part soft-mold to produce the required features. The shoulder **(b)** and the reel **(c)** are shown in addition to their 3D printed masters and soft-molds.

## **E.1 Procedure**

The soft-molding process begins once the component is designed as molding features must be added to the component before 3D printing. All through holes must be removed through the addition of thin membranes which divide the holes in half and remove the connection between the ends for demolding purposes. The high functionality typically also results in all sides of the component containing features and thus must be accurately molded. Therefore, the part is suspended in the mold resulting in the necessity to add features which hold the component away from all exterior surfaces of the mold.

The part is then secured to the base of a disposable plastic cup. Two part, high tear strength silicone rubber is then mixed and degassed. This is then poured into the cup and degassed again. Once cured, a razor blade is used to cut open the mold exposing the part inside. Through deformation of the mold, the part is separated from the mold before demolding process begins. Once all surfaces are separated from the mold, demolding is achieved by applying a force to the underside while expanding the opening and slowly working the component out.

The remolding process is similar however a rigid material is used. Once the material is mixed and degassed the opening of the mold is expanded and the material poured through the opening; being careful not to create air bubbles as you pour. The demolding process is the same as discussed above.

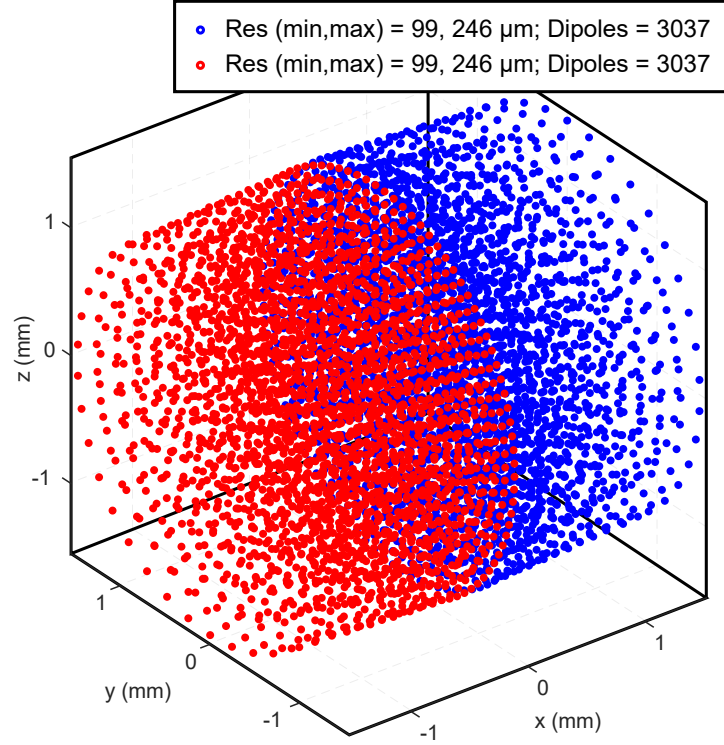


Figure F.1: Aligned configuration of two 3.2 mm magnets showing the distribution of dipoles within each; represented as the red and blue points. The dipole resolution is highest near the contact point enhancing the accuracy of the calculated solution. In this case the magnets are discretized into 3037 dipoles each.

## Appendix F Distributed Dipole Model

The magnetic force-displacement curves are calculated using a distributed amperian model (MATLAB). The procedure begins by first specifying the magnet geometries; these are then discretized into thousands of small volumes, each with a magnetic dipole at the center; as seen in Fig. F.1. The magnetic field produced by a single dipole is derived as [52],

$$B_{u,v}(\vec{r}_{u,v}, \vec{m}_u) = \frac{\mu_0 \|\vec{m}_u\|}{4\pi \|\vec{r}_{u,v}\|^3} \left( 3(\hat{m}_u \cdot \hat{r}_{u,v})\hat{r}_{u,v} - \hat{m}_u \right) \quad (\text{F.1})$$

where  $\vec{m}_u$  represents the magnetic moment of a single dipole in the red (Fig. F.1) magnet and  $\vec{r}_{u,v}$  is the distance vector between one red and one blue (Fig. F.1) dipole. Then the force between the

two dipoles is calculated from the equation  $F = \nabla(\vec{m}_v \cdot B_{u,v})$  as

$$g(\vec{r}, \vec{m}_u, \vec{m}_v) = \frac{3\mu_0 \|\vec{m}_u\| \|\vec{m}_v\|}{4\pi \|\vec{r}_{u,v}\|^4} \left( \hat{r}_{u,v}(\hat{m}_u \cdot \hat{m}_v) + \hat{m}_u(\hat{r}_{u,v} \cdot \hat{m}_v) + \hat{m}_v(\hat{r}_{u,v} \cdot \hat{m}_u) - 5\hat{r}_{u,v}(\hat{r}_{u,v} \cdot \hat{m}_u)(\hat{r}_{u,v} \cdot \hat{m}_v) \right) \quad (\text{F.2})$$

where,  $\vec{m}_v$  represent the magnetic moment of a blue (Fig. F.1) dipole. The net forces between magnets are then calculated as the sum of the forces between the set of dipoles in each magnet; the example in Fig F.1 requires the sum of the interaction between all 3037 dipoles. One of the magnets is then displaced and the procedure is repeated to produce the magnetic force curves.

## Appendix G Internal Energy Storage Mechanism Characterization

The internal energy storage mechanism with SMA actuated clutch was characterized to understand its power requirements and load capabilities.

### Experimental Setup

The complete internal energy storage mechanism is assembled into a MultiMo-Bat body. This body is identical to that of the full system however it allows access and observation of the internal component during the testing phase. The body plus overhead rod is also configured to create the bidirectional forces, just as in the full system, while allowing the pulling force to be directed to only one side; this facilitates experimentation and can be seen in Fig. G.1b. To modify the load on the motor, a large container is connected to the main cables coming from the internal energy storage mechanism. Though the addition of measured quantities of water to the container, the load can be easily modified over a large range.

A power supply delivering 11 volts is used as the current source. To ensure accurate current delivery to the DC motor the complete control circuitry including DC motor driver (pololu carrier board, TI DRV8833 chip) with a current sensor (Pololu carrier board, Allegro +/-15.5 A ACS711

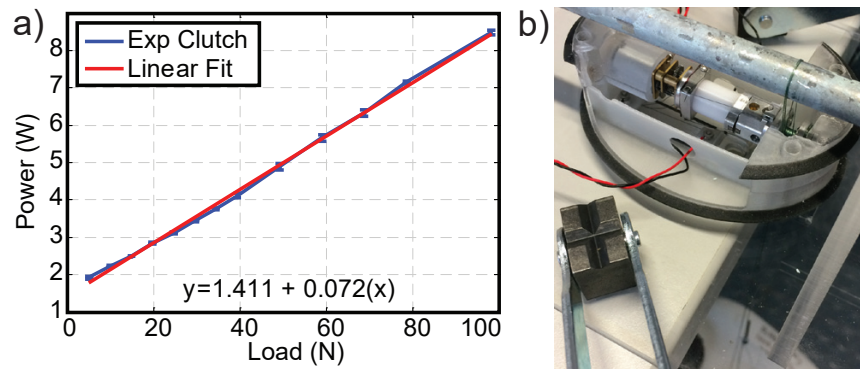


Figure G.1: **a)** Power vs. load characterization of the internal energy storage mechanism, including a linear fit to the data. **b)** Experimental testing setup.

chip) on the input to the motor is used. The activation and deactivation signals comes directly from the micro-controller.

### Experimental Procedure

The procedure begins with the simultaneous activation of the robot controller and the data acquisition system (Labview + National Instruments: USB X series multifunction DAQ). The robot controller waits just over 6 seconds before activating the motor. The activation lasts 3 seconds over which the load is observed to lift off the ground. The activation ceases while data acquisition continues for approximate 4 additional seconds. This provides both a zero point at the beginning and end of the data collection. The motor was tested under 13 different constant loads which span a large region of its operating range including: 522, 1022, 1522, 2022, 2522, 3022, 3522, 4022, 5022, 6022, 7022, 8022, and 10022 g.

### Results

The characterization results in a linear relationship between the motor current and the applied load. To calculate this relationship each applied load was tested five times. The measured data is an analog voltage reading from the current sensor through which the current is calculated as,

$$I = 36.7 \frac{V_{out}}{V_{CC}} - \frac{36.7}{2} \quad (G.1)$$

where  $V_{out}$  is the voltage signal from the sensor and  $V_{CC}$  is the supply voltage [112]. The data is then convert to power  $W$  and force  $N$  and using a least-squares approach, a linear function  $y = c_0 + c_1x$  was fit to the data resulting in,

$$y = 1.411 + 0.072x \quad (G.2)$$

where  $x$  is in units of  $N$ ,  $c_0$  is the y-axis intercept, and  $c_1$  is the slope.

## Appendix H Small Segment Set Example

### Segment Matrix

The 20 segments shown in Fig. 3.14, evaluated at  $k = 20$  points, are combined into the  $\mathbf{S}$  matrix below; where each column represents a single segment with untis of force in grams. The individual segment forces are doubled representing 2 magnet sets to allow for force equalization during manufacturing.

$${}^{20}\mathbf{S} = \begin{bmatrix} -141.5 & -173.2 & -185.9 & -233.9 & -88.5 & -107.0 & -114.6 & -143.2 & -174.0 & -215.0 & -231.1 & -292.2 & 508.5 & 674.0 & 743.2 & 1021.4 & 358.9 & 492.5 & 548.4 & 777.5 \\ -132.4 & -161.7 & -173.5 & -217.9 & -73.4 & -88.5 & -94.8 & -118.1 & -168.4 & -207.7 & -223.1 & -282.0 & 467.9 & 625.4 & 691.1 & 956.8 & 336.8 & 465.1 & 518.9 & 740.0 \\ -122.3 & -149.1 & -159.8 & -200.7 & -56.4 & -67.6 & -72.4 & -89.8 & -162.2 & -199.7 & -214.4 & -270.6 & 433.6 & 583.9 & 646.6 & 901.2 & 316.6 & 440.0 & 491.8 & 705.5 \\ -111.1 & -135.2 & -145.0 & -181.6 & -37.4 & -44.6 & -47.8 & -59.2 & -155.3 & -190.8 & -204.9 & -258.1 & 403.6 & 547.4 & 607.4 & 852.0 & 298.2 & 416.9 & 466.9 & 673.6 \\ -98.8 & -119.7 & -128.3 & -160.4 & -16.6 & -19.8 & -21.2 & -26.3 & -147.7 & -181.1 & -194.3 & -244.8 & 377.0 & 514.8 & 572.4 & 807.9 & 281.2 & 395.5 & 443.8 & 643.9 \\ -84.8 & -102.5 & -109.9 & -137.2 & 5.6 & 6.7 & 7.1 & 8.8 & -139.3 & -170.5 & -182.9 & -230.0 & 353.2 & 485.4 & 540.7 & 767.8 & 265.6 & 375.7 & 422.3 & 616.3 \\ -69.3 & -83.5 & -89.5 & -111.3 & 27.2 & 32.5 & 34.8 & 43.1 & -130.0 & -158.7 & -170.2 & -213.7 & 331.6 & 458.6 & 511.9 & 731.1 & 251.1 & 357.3 & 402.3 & 590.4 \\ -51.9 & -62.0 & -66.4 & -82.4 & 47.1 & 56.3 & 60.3 & 74.8 & -119.7 & -145.7 & -156.3 & -196.1 & 311.9 & 434.0 & 485.4 & 697.3 & 237.6 & 340.1 & 383.7 & 566.1 \\ -32.3 & -38.6 & -41.3 & -51.2 & 65.2 & 78.4 & 84.0 & 104.3 & -108.2 & -131.5 & -141.0 & -176.5 & 293.8 & 411.4 & 460.9 & 666.0 & 225.1 & 324.0 & 366.1 & 543.2 \\ -11.1 & -13.3 & -14.2 & -17.6 & 81.1 & 98.0 & 105.0 & 131.0 & -95.4 & -115.5 & -123.8 & -154.8 & 277.2 & 390.5 & 438.3 & 636.9 & 213.4 & 308.9 & 349.7 & 521.7 \\ 11.1 & 13.3 & 14.2 & 17.6 & 95.4 & 115.5 & 123.8 & 154.8 & -81.1 & -98.0 & -105.0 & -131.0 & 261.8 & 371.0 & 417.2 & 609.7 & 202.5 & 294.7 & 334.2 & 501.3 \\ 32.3 & 38.6 & 41.3 & 51.2 & 108.2 & 131.5 & 141.0 & 176.5 & -65.2 & -78.4 & -84.0 & -104.3 & 247.6 & 352.9 & 397.6 & 584.2 & 192.3 & 281.4 & 319.7 & 482.1 \\ 51.9 & 62.0 & 66.4 & 82.4 & 119.7 & 145.7 & 156.3 & 196.1 & -47.1 & -56.3 & -60.3 & -74.8 & 234.4 & 336.0 & 379.2 & 560.3 & 182.7 & 268.8 & 305.9 & 463.8 \\ 69.3 & 83.5 & 89.5 & 111.3 & 130.0 & 158.7 & 170.2 & 213.7 & -27.2 & -32.5 & -34.8 & -43.1 & 222.1 & 320.1 & 361.9 & 537.7 & 173.7 & 257.0 & 292.9 & 446.5 \\ 84.8 & 102.5 & 109.9 & 137.2 & 139.3 & 170.5 & 182.9 & 230.0 & -5.6 & -6.7 & -7.1 & -8.8 & 210.6 & 305.3 & 345.8 & 516.5 & 165.3 & 245.8 & 280.7 & 430.0 \\ 98.8 & 119.7 & 128.3 & 160.3 & 147.7 & 181.1 & 194.3 & 244.8 & 16.6 & 19.8 & 21.2 & 26.3 & 199.9 & 291.3 & 330.5 & 496.4 & 157.3 & 235.2 & 269.0 & 414.3 \\ 111.1 & 135.2 & 145.0 & 181.6 & 155.3 & 190.8 & 204.9 & 258.2 & 37.4 & 44.6 & 47.8 & 59.2 & 189.8 & 278.2 & 316.2 & 477.4 & 149.9 & 225.2 & 258.0 & 399.4 \\ 122.3 & 149.1 & 159.9 & 200.7 & 162.2 & 199.7 & 214.4 & 270.6 & 56.4 & 67.6 & 72.4 & 89.8 & 180.4 & 265.8 & 302.6 & 459.4 & 142.8 & 215.7 & 247.5 & 385.2 \\ 132.4 & 161.8 & 173.5 & 217.9 & 168.4 & 207.7 & 223.1 & 281.9 & 73.4 & 88.5 & 94.8 & 118.1 & 171.5 & 254.1 & 289.8 & 442.3 & 136.2 & 206.7 & 237.6 & 371.6 \\ 141.5 & 173.2 & 185.9 & 233.8 & 174.0 & 215.0 & 231.1 & 292.3 & 88.5 & 106.9 & 114.6 & 143.2 & 163.2 & 243.1 & 277.7 & 426.0 & 129.9 & 198.1 & 228.1 & 358.7 \end{bmatrix} \quad (H.1)$$

### Desired force

The  ${}^d\vec{f}$  represents the desired forces along the motion axis which creates the tailored magnetic spring shown in Fig. 3.17.b.

$${}^d\vec{f} = [150.0 \ 137.2 \ 127.4 \ 120.3 \ 116.2 \ 115.0 \ 116.6 \ 121.1 \ 128.5 \ 138.8 \ 152.0 \ 168.0 \ 186.9 \ 208.7 \ 233.4 \ 261.0 \ 291.4 \ 324.7 \ 360.9 \ 400.0]^T \quad (H.2)$$

## Segment Quantity

The  $\vec{q}$  represents the initial calculated quantities for the tailored magnetic spring shown in Fig. 3.17.b when no dimensionality reduction is performed.

$$\vec{q} = [0.8 \quad -1.2 \quad -0.3 \quad 0.4 \quad -0.0 \quad 60.5 \quad -56.1 \quad -3.1 \quad -4.2 \quad 37.7 \quad -28.7 \quad -2.5 \quad -3937.2 \quad -13697.9 \quad 19495.2 \quad -2678.5 \quad -10011.2 \quad 87547.4 \quad -85614.9 \quad 8885.1]^T \quad (\text{H.3})$$

## Family of Analytical Solutions

Varying the number of evaluation points,  $k$ , and the dimensionality reduction percent,  $P_\lambda$ , can generate a family of solutions. Fig. H.1 presents 650 solutions generated from  ${}^{20}\mathbf{S}$  for the monostable tailored magnetic spring in Fig. 3.17.

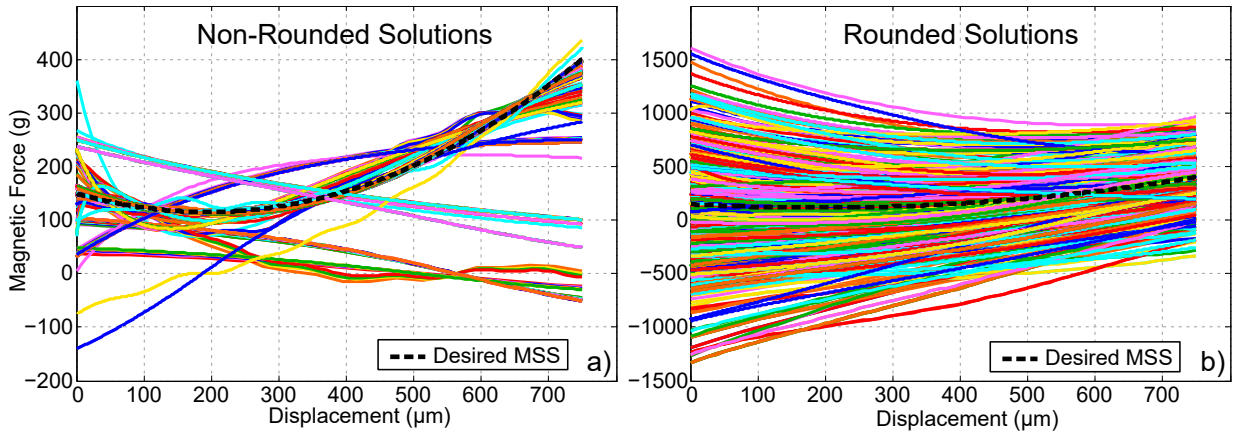


Figure H.1: **a)** The non-rounded and **b)** rounded solutions for the monostable tailored magnetic spring. There are a total of 650 solutions presented.

## Appendix I Robot Controller

The robot controller is designed around the integrated strategy, where both mass and volume are minimized through the development of a custom PCB. This PCB integrates a number of carrier boards for specific functions such as microcontroller (Arduino, Pro Mini 328 or Teensy 3.1), motor drivers (Pololu, DRV8833 Dual Motor Driver Carrier), IMU (Pololu, AltIMU-10 v4

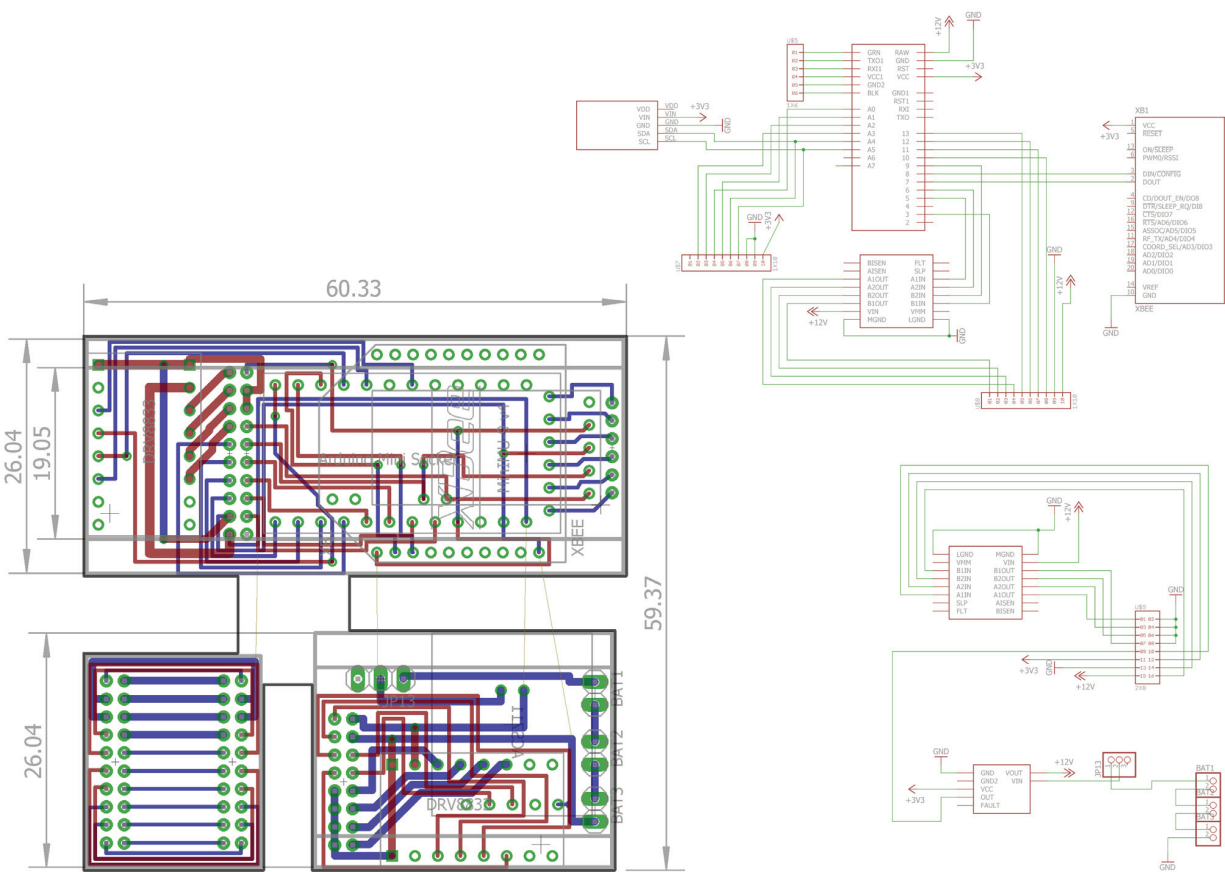


Figure I.1: Robot controller PCB and schematic views.

Gyro, Accelerometer, Compass, and Altimeter), and wireless communication (XBee, Series 1 - 1mW with PCB Antenna).

Figure I.1 presents the PCB design and schematic views of the robot controller which is designed to operate on 3 series connected polymer lithium ion batteries (Sparkfun Electronics) at a total voltage of 11.1 V. Sufficient additional I/O ports are included for camera and GPS integration as needed.

## Appendix J Experimental Testing Facility

Miniature robots and biological organisms require dedicated experiential testing areas as the setups must remain constant throughout the testing period. The nature of complex high performance robotic systems which operate very close to the structural limits of their components.



Figure J.1: **a)** Inside the experimental testing facility. **b)** Outside the experimental testing facility.

Therefore, requiring small redesigns throughout the initial testing periods to optimize the design before the necessary experimental trials can begin. The non-deterministic and complex behavior of organisms requires significantly more data to formulate conclusions and their own free will requires significant initial experiential observation to configure the experiential tests in such a way which encourages the organism to exhibit the desired behavior. Both these systems can require as long as a month or more to obtain sufficient data for proper analysis.

Observation by high speed video, motion capture, and computer vision systems are all facilitated by well lit uncluttered environments, Fig J.1a. However, I had to create this environment within a large highly cluttered room, Fig J.1b. To achieve this, first the heavily damaged and uneven floor was sanded, leveled, and painted with a diffuse reflective white color. Diffusion of the light minimizes the chance of bright spots, which could mask regions of the experiential

space and hinder observation; it also help to even the lighting. I then designed a  $11\text{m}\times 5\text{m}\times 5\text{m}$  ( $L\times W\times H$ ) truss structure covered first in an inner diffuse reflective and stretchable material to further reflect light and eliminate wrinkling of the surfaces. The outer layer is designed to eliminate the propagation light between the inside and outside, thus eliminating shadows inside and shielding the outside from the high intensity lights. The room is maintained as a semi-clean room to preserve the aforementioned qualities.

The observation equipment inside consists of a motion capture system (Vicon, Vantage V5) with 420 fps at 5 MP, high speed camera (Vision Research, Phantom v641) with 1450 fps at 2560 x 1600 pixels, and high intensity LED light sources (Messring, M=Light LED) with intensities of constant 100,000 and pulsed 250,000 lumen. The maximum observation volume of these systems is  $5\text{m}\times 5\text{m}\times 5\text{m}$ .

## **Appendix K Materials and Methods**

### **Desert Locusts (*Schistocerca gregaria*)**

The locusts were obtained from a local pet store and housed in a terrarium with heat lamp and plentiful food supply. Any stress or nutritional deficiency was abated by a acclimation period of no less than 5 days, where no experimental trials were conducted. Grass was the main source of food provided to the locusts.

### **Experimental Preparation of Desert Locusts**

The desert locusts were transferred from their main terrarium to an empty acrylic terrarium with a heat lamp and thermometer. The locusts, being cold blooded, were warm up to an average temperature of 30.5 °C before transferring them to the testing terrarium. This process also allowed them to clean their adhesive pads; especially important before smooth surface trials.

### **Experimental Setup for Capturing Locust Jumps**

An acrylic box was constructed to contain the locusts after each jump, while allowing unrestricted viewing of the event. In the center a small platform was placed on which the surface and angle could be modified for testing various parameters of the locust's jump. The platform dimensions were specifically selected to encourage the locust to align itself in particular directions. This helped to improve the accuracy of the captured data.

### **Test Surface Preparation**

The hydrophilic glass was prepared by cleaning a glass slide with varying polarity solvents; the sequence was as follows: acetone, IPA, deionized water, and argon gas for drying. To fabricate the hydrophobic glass, the surface chemistry of some of the cleaned glass slides was altered through a silanization process as follows: air plasma, immersion in butylamine and methoxy(dimethyl) octadecylsilane, and condensation at 80 °C. The advancing and receding contact angles were measured using a Krüss-Drop Shape Analyzer. The wood, sandstone, and

steel mesh were purchased from a local hardware store and cut to proper size. The wood is smooth cut pine, chosen for its relative softness.

### **Imaging of Test Surfaces and Locust Morphology**

The surface and locust foot morphology plots were generated with a high-resolution 3D surface profilometer (Keyence - VK-X200) with  $x$ –axis and  $y$ –axis resolutions of 1390 nm and  $z$ –axis resolutions of 0.1 nm.

### **Statistical Testing**

The reported statistical values were obtained from two-sample two-tailed t-tests, where significance is defined as  $p \leq 0.05$  with a null hypothesis of equal mean values. The effective degrees of freedom were approximated with the Welch-Satterthwaite equation.

## **Appendix L Locust Adaptation to Jumping**

The morphology of the locust's hind legs used for jumping, exhibit striking similarity to that of the 4 forelegs Fig. L.2. The forelegs also have 4 jointed tibia spines and 3 segment feet with 3 adhesive pads on the first segment,  $S1$ ; however, their configurations and sizes are different. The spines are smaller, conical shaped, and pointed more distally than in the hind legs, and the adhesive pad have no separation between pads  $P1$  and  $P2$ . These morphological similarities add additional evidence to the hypothesis of the locust's continued adaptation towards enhanced jumping performance.

## **Appendix M Dynamics: Robot and Jump Test Rig**

To analyze the potential for bouncing as the foot makes contact with the surfaces, a jumping rig was developed which simulates the dynamics of the robot but within a more observable configuration. The configuration, Fig. M.3a, was designed to be dynamically similar to that

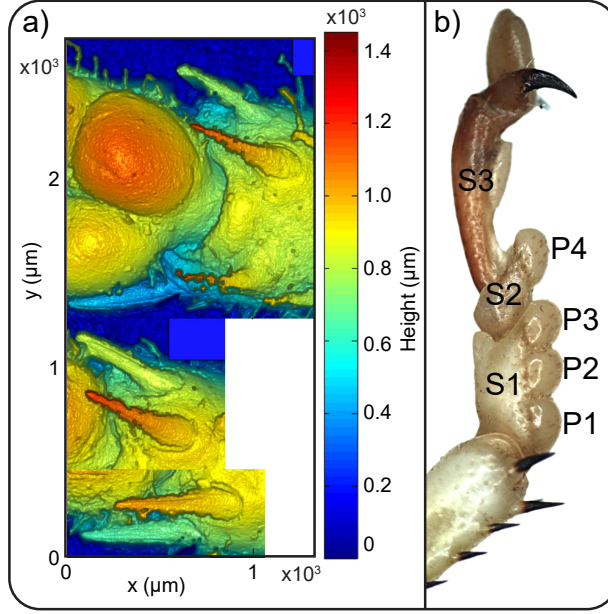


Figure L.2: The forelegs of the locust are morphologically similar to the hind legs, albeit with different configurations and sizes. Adding evidence to the existence of an ancestor with equal fore and hind legs. **a)** 3D surface profilometer images of the underdeveloped spines and associated joints, at the base. **b)** Photo of the locust foreleg with components labeled.

of the robot which is governed by,

$$\begin{aligned}
 m_B \ddot{r}_1 &= 2k_1 \left( L^2 - \left( \frac{r_1 - r_2}{2} \right)^2 \right)^{0.5} \\
 m_F \ddot{r}_2 &= -2k_1 \left( L^2 - \left( \frac{r_1 - r_2}{2} \right)^2 \right)^{0.5} - k_2 r_2 - c_2 \dot{r}_2,
 \end{aligned} \tag{M.1}$$

whereas the jumping rig is governed by,

$$\begin{aligned}
 m_B \ddot{r}_1 &= -k_2(r_1 - r_2) - c_2(\dot{r}_1 - \dot{r}_2) \\
 m_F \ddot{r}_2 &= 2k_1 \left( L^2 - \left( \frac{r_2}{2} \right)^2 \right)^{0.5} + k_2(r_1 - r_2) + c_2(\dot{r}_1 - \dot{r}_2),
 \end{aligned} \tag{M.2}$$

where  $r_1$  and  $r_2$  represent to position of the two masses, main body,  $m_B = 55.4$  g, and foot,  $m_F = 4.8$  g. The robot's  $k_1 = 291.2$  N/m and  $L = 135.8$  mm are the stiffness of the main power spring and the leg length, respectively. The ground interaction is governed by  $k_2 = 10^9$  N/m and  $c_2 = 88.4$  Ns/m, which are the stiffness and damping coefficient, respectively. Note: all values represent half of the robot as only one leg is being tested. The ground stiffness was chosen to be arbitrarily large compared to  $k_1$  whereas the damping coefficient  $c_2$  was calculated from the

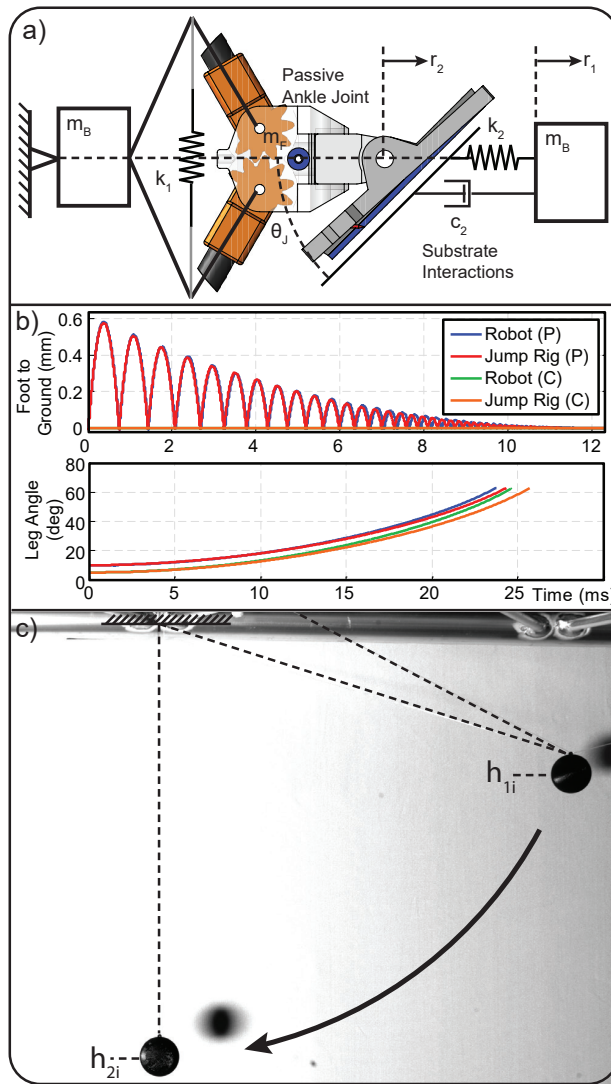


Figure M.3: **a)** The free body diagram of the jumping rig for comparison to the robot. **b)** Dynamic comparison between the jumping rig and the robot. Both the bouncing of the foot and jumping behavior are presented to show the similarity. Note: P=planting jump, C=contact jump. **c)** A pendulum setup was used to experimentally determine the coefficient of restitution of the 3D printed ABS plastic (Stratasys, ABSplus).

experimentally determined coefficient of restitution,  $COR = 0.8929$ , of the 3D printed ABS material (Stratasys uPrintSE Plus, ABSplus); discussed in (Supplementary Materials Appendix N).

A comparison of the dynamics, Fig. M.3b, shows good agreement between the magnitude and damping responses of the testing rig and the robot with only a small variation in the bouncing frequency of the foot.

## Appendix N Material Properties: Experimental

Two properties of the 3D-printed ABS material (Stratasys, ABSplus) were determined experimentally including: coefficient of restitution and Young's modulus.

The coefficient of restitution was experimentally calculated by colliding two equal spheres together and comparing the energy before and after the collision. Figure M.3c shows the testing setup for determining the COR of the material; where the two spheres are identical and the height potential energy before and after the collision is used to calculate the COR,  $COR = 0.8929$ .

The Young's modulus of the material was experimentally tested to obtain the modulus for thin small sections. The manufacturing process of the uPrintSE (Stratasys) results in significant differences between bulk and small sections. The test consisted of two printed cantilever beams with dimensions (LxWxH): 40x1x3 mm and 40x3x1 mm. Each was loaded and the deformation measured. Using the Euler-Bernoulli beam theory, the Young's moduli for each configuration was calculated as, 173.25 MPa and 164.77 MPa, respectively.

# Bibliography

- [1] Agashe, J. S. and Arnold, D. P. (2009). A study of scaling and geometry effects on the forces between cuboidal and cylindrical magnets using analytical force solutions. *Journal of Physics D: Applied Physics*, 42(9):099801–099801. 3.1
- [2] Alexander, R. M. (2003). *Principles of Animal Locomotion*. Princeton University Press. 1.1
- [3] Allag, H. and Yonnet, J.-p. (2009). 3-D Analytical Calculation of the Torque and Force Exerted Between Two Cuboidal Magnets. *IEEE Transactions on Magnetics*, 45(10):3969–3972. 3.1
- [4] Altenbach, J. S. (1979). *Locomotor Morphology of the Vampire Bat - Desmodus Rotundus*. 2.2
- [5] Ananthanarayanan, A., Azadi, M., and Kim, S. (2012). Towards a bio-inspired leg design for high-speed running. *Bioinspiration & Biomimetics*, 7(4):046005. 4.1
- [6] Armour, R., Paskins, K., Bowyer, A., Vidyasagar, A., Zufferey, J.-c., Floreano, D., Desbiens, A. L., Pope, M. T., Christensen, D. L., Buschmann, T., Ewald, A., and Twickel, A. V. (2015). A locust-inspired miniature jumping robot. *Bioinspiration & Biomimetics*, 10(6):66012. 2.1
- [7] Armour, R., Paskins, K., Bowyer, A., Vincent, J., Megill, W., and Bomphrey, R. (2007). Jumping robots: a biomimetic solution to locomotion across rough terrain. *Bioinspiration & biomimetics*, 2(3):65–82. 1.1, 2.1, 2.10
- [8] Arnold, D. P. (2007). Review of microscale magnetic power generation. *IEEE Transactions on Magnetics*, 43(11):3940–3951. 3.1
- [9] Azukizawa, T., Yamamoto, S., and Matsuo, N. (2008). Feasibility Study of a Passive Magnetic Bearing Using the Ring Shaped Permanent Magnets. *IEEE Transactions on Magnetics*, 44(11):4277–4280. 3.1
- [10] Bancel, F. (1999). Magnetic nodes. *Journal of Physics D: Applied Physics*, 2155(32):2155–2161. 3.2
- [11] Barth, J., Megnin, C., and Kohl, M. (2012). A Bistable Shape Memory Alloy Microvalve With Magnetostatic Latches. *Journal of Microelectromechanical Systems*, 21(1):76–84. 3.1
- [12] Bartlett, N. W., Tolley, M. T., Overvelde, J. T. B., Weaver, J. C., Mosadegh, B., Bertoldi, K., Whitesides, G. M., and Wood, R. J. (2015). Robot Powered By Combustion. *Science*, 349(July):161–165. 3.1
- [13] Bayley, T. G., Sutton, G. P., and Burrows, M. (2012). A buckling region in locust hindlegs contains resilin and absorbs energy when jumping or kicking goes wrong. *The Journal of Experimental Biology*, 215(Pt 7):1151–61. 4.1, 4.4.1
- [14] Bennet-Clark, H. C. (1975). The energetics of the jump of the locust *Schistocerca gregaria*. *Journal of Experimental Biology*, 63(1):53–83. 1.1, 4.1
- [15] Bennet-Clark, H. C. and Lucey, E. C. (1967). The jump of the flea: a study of the energetics and a model of the mechanism. *Journal of Experimental Biology*, 47(1):59–67. 1.1

- [16] Bibette, J., Mason, T. G., Gang, H., Weitz, D. A., and Poulin, P. (1993). Structure of adhesive emulsions. *Langmuir*, 9(12):3352–3356. 4.3.5
- [17] Birkmeyer, P., Gillies, A. G., and Fearing, R. S. (2012). Dynamic Climbing of Near-Vertical Smooth Surfaces. *IEEE/RSJ International Conference on Intelligent Robots and Systems*. 4.1
- [18] Boston Dynamics (2013). SandFlea. 2.1, 2.10
- [19] Boston Dynamics (2017). [www.bostondynamics.com/](http://www.bostondynamics.com/). 4.1
- [20] Bouendeu, E., Greiner, A., Smith, P. J., and Korvink, J. G. (2011). A low-cost electromagnetic generator for vibration energy harvesting. *IEEE Sensors Journal*, 11(1):107–113. 3.1
- [21] Boxerbaum, a. S., Shaw, K. M., Chiel, H. J., and Quinn, R. D. (2012). Continuous wave peristaltic motion in a robot. *The International Journal of Robotics Research*, 31(3):302–318. 3.1
- [22] Burrows, M. (2007). Kinematics of jumping in leafhopper insects (Hemiptera, Auchenorrhyncha, Cicadellidae). *Journal of Experimental Biology*, 210(Pt 20):3579–89. 1.1
- [23] Burrows, M. and Sutton, G. (2013). Interacting gears synchronize propulsive leg movements in a jumping insect. *Science*, 341(6151):1254–6. 4.4.1
- [24] Castano, A., Behar, A., and Will, P. M. (2002). The Conro modules for reconfigurable robots. *IEEE/ASME Transactions on Mechatronics*, 7(4):403–409. 3.1
- [25] Cheng, S. S. and Desai, J. P. (2015). Towards high frequency actuation of SMA spring for the neurosurgical robot - MINIR-II. *2015 IEEE International Conference on Robotics and Automation (ICRA)*, pages 2580–2585. 3.1
- [26] Cho, H. W., Yu, J. S., Jang, S. M., Kim, C. H., Lee, J. M., and Han, H. S. (2012). Equivalent magnetic circuit based levitation force computation of controlled permanent magnet levitation system. *IEEE Transactions on Magnetics*, 48(11):4038–4041. 3.1
- [27] Cho, K. J. and Asada, H. (2005). Multi-axis SMA actuator array for driving anthropomorphic robot hand. *Proceedings - IEEE International Conference on Robotics and Automation*, 2005(April):1356–1361. 3.1
- [28] Cho, K.-J. and Asada, H. H. (2006). Architecture Design of a Multiaxis Cellular Actuator Array Using Segmented Binary Control of Shape Memory Alloy. *IEEE Transactions on Robotics*, 22(4):831–843. 3.1
- [29] Christensen, D. L., Hawkes, E. W., Suresh, S. A., Ladenheim, K., and Cutkosky, M. R. (2015). uTugs: Enabling microrobots to deliver macro forces with controllable adhesives. *Robotics and Automation (ICRA), 2015 IEEE International Conference on*, pages 4048–4055. 3.1
- [30] Churaman, W. a., Currano, L. J., Morris, C. J., Rajkowski, J. E., and Bergbreiter, S. (2012). The First Launch of an Autonomous Thrust-Driven Microrobot Using Nanoporous Energetic Silicon. *Journal of Microelectromechanical Systems*, 21(1):198–205. 2.1, 2.10
- [31] Cofer, D., Cymbalyuk, G., Heitler, W. J., and Edwards, D. H. (2010a). Control of tumbling during the locust jump. *Journal of Experimental Biology*, 213(19):3378–3387. 4.1
- [32] Cofer, D., Cymbalyuk, G., Heitler, W. J., and Edwards, D. H. (2010b). Neuromechanical simulation of the locust jump. *Journal of Experimental Biology*, pages 1060–1068. 4.1
- [33] Conway, J. T. (2013). Forces Between Thin Coils With Parallel Axes Using Bessel Functions. *IEEE Transactions on Magnetics*, 49(9):5028–5034. 3.1
- [34] Cugat, O., Delamare, J., and Reyne, G. (2003). Magnetic Micro-Actuators and Systems (MAGMAS). *IEEE Transactions on Magnetics*, 39(6):3607–3612. 3.1
- [35] Dai, Z., Gorb, S. N., and Schwarz, U. (2002). Roughness-dependent friction force of the

- tarsal claw system in the beetle *Pachnoda marginata* (Coleoptera, Scarabaeidae). *The Journal of Experimental Biology*, 205:2479–2488. 4.2.1
- [36] De Graef, M. and Beleggia, M. (2009). General magnetostatic shapeshape interaction forces and torques. *Journal of Magnetism and Magnetic Materials*, 321(15):L45–L51. 3.1
- [37] Dermitzakis, K., Carbajal, J. P., and Marden, J. H. (2011). Scaling laws in robotics. *Procedia Computer Science*, 7:250–252. 2.8
- [38] Desbiens, A. L., Asbeck, A. T., and Cutkosky, M. R. (2011). Landing, perching and taking off from vertical surfaces. *The International Journal of Robotics Research*, 30(3):355–370. 4.1
- [39] Desbiens, A. L., Pope, M., Berg, F., Teoh, Z. E., Lee, J., and Cutkosky, M. (2013). Efficient Jumpgliding : Theory and Design Considerations. *IEEE International Conference on Robotics and Automation*, pages 4436–4443. 2.1, 2.10
- [40] Desbiens, A. L., Pope, M. T., Christensen, D. L., Hawkes, E. W., and Cutkosky, M. R. (2014). Design principles for efficient, repeated jumpgliding. *Bioinspiration & biomimetics*, 9(2):025009. 2.1
- [41] Dirks, J.-H. and Federle, W. (2011). Mechanisms of fluid production in smooth adhesive pads of insects. *Journal of the Royal Society, Interface / the Royal Society*, 8(January):952–960. 4.1
- [42] Dixon, A. F. G., Croghan, P. C., and Gowing, R. P. (1990). The mechanism by which aphids adhere to smooth surfaces. *The Journal of Experimental Biology*, 152(1):243–253. 4.3.5
- [43] Dresselhuis, D. M., van Aken, G. A., de Hoog, E. H. A., and Cohen Stuart, M. A. (2008). Direct observation of adhesion and spreading of emulsion droplets at solid surfaces. *Soft Matter*, 4(6):1147. 4.3.5
- [44] Dubey, S., Sharma, G., Shishodia, K., and Sekhon, G. (2005). A study of lubrication mechanism of oilinwater (O/W) emulsions in steel cold rolling. *Industrial Lubrication and Tribology*, 57(5):208–212. 4.3.5
- [45] Felton, S., Tolley, M., Demaine, E., Rus, D., and Wood, R. (2014). A method for building self-folding machines. *Science*, 345(6197):644–646. 3.1
- [46] Feng, L., Li, S., Li, Y., Li, H., Zhang, L., Zhai, J., Song, Y., Liu, B., Jiang, L., and Zhu, D. (2002). Super-hydrophobic surfaces: From natural to artificial. *Advanced Materials*, 14(24):1857–1860. 4.1
- [47] Gabriel, J. M. (1985a). THE DEVELOPMENT OF THE LOCUST JUMPING MECHANISM. *Journal of Experimental Biology*, (118):327–340. 4.1
- [48] Gabriel, J. M. (1985b). THE DEVELOPMENT OF THE LOCUST JUMPING MECHANISM PERFORMANCE. *Journal of Experimental Biology*, 326:313–326. 4.1
- [49] Gafford, J., Ranzani, T., Russo, S., Aihara, H., Thompson, C., Wood, R., and Walsh, C. (2016). Snap-on robotic wrist module for enhanced dexterity in endoscopic surgery. *IEEE International Conference on Robotics and Automation*, pages 4398–4405. 3.1
- [50] Gao, J., Yan, G., Wang, Z., He, S., Xu, F., Jiang, P., and Liu, D. (2015). Design and Testing of a Motor-Based Capsule Robot Powered by Wireless Power Transmission. *IEEE/ASME Transactions on Mechatronics*, 4435(c):1–1. 3.1
- [51] Gardiner, J. D. and Nudds, R. L. (2011). No apparent ecological trend to the flight-initiating jump performance of five bat species. *Journal of Experimental Biology*, 214:2182–8. 2.2
- [52] Griffiths, D. J. (2008). *Introduction to Electrodynamics*. Pearson Education, Inc., San Francisco, third edition. 3.2, Appendix F
- [53] Haines, C. S., Lima, M. D., Li, N., Spinks, G. M., Foroughi, J., Madden, J. D., Kim,

- S. H., Fang, S., Jung de Andrade, M., Goktepe, F., Goktepe, O., Mirvakili, S. M., Naficy, S., Lepro, X., Oh, J., Kozlov, M. E., Kim, S. J., Xu, X., Swedlove, B. J., Wallace, G. G., and Baughman, R. H. (2014). Artificial muscles from fishing line and sewing thread. *Science*, 343(6173):868–872. 3.1
- [54] Hawkes, E. W., Christensen, D. L., and Cutkosky, M. R. (2015). Vertical dry adhesive climbing with a 100 bodyweight payload. *IEEE International Conference on Robotics and Automation*, 2015-June(June):3762–3769. 3.1
- [55] Hawkes, E. W., Eason, E. V., Asbeck, A. T., and Cutkosky, M. R. (2013). The Gecko’s toe: Scaling directional adhesives for climbing applications. *IEEE/ASME Transactions on Mechatronics*, 18(2):518–526. 4.1
- [56] Hawlena, D., Kress, H., Dufresne, E. R., and Schmitz, O. J. (2011). Grasshoppers alter jumping biomechanics to enhance escape performance under chronic risk of spider predation. *Functional Ecology*, 25(1):279–288. 4.1
- [57] Heitler, W. J. (1977). THE LOCUST JUMP. *Journal of Experimental Biology*. 4.1
- [58] Ho, T. and Lee, S. (2010). Design and implementation of an SMA-actuated jumping robot. *IEEE/RSJ International Conference on Intelligent Robots and Systems*, pages 3530–3535. 3.1
- [59] Ho, T. and Lee, S. (2012). A Novel Design of a Robot That Can Jump and Roll with a Single Actuator. *IEEE/RSJ International Conference on Intelligent Robots and Systems*, pages 908–913. 2.1, 3.1
- [60] Hoover, A. M., Steltz, E., and Fearing, R. S. (2008). RoACH: An autonomous 2.4g crawling hexapod robot. *IEEE/RSJ International Conference on Intelligent Robots and Systems*, pages 26–33. 3.1
- [61] Hoyle, G. (1957). The Leap of the Grasshopper. *Scientific America*, pages 30–35. 4.1
- [62] Hwang, D. and Higuchi, T. (2016). A Planar Wobble Motor with a XY Compliant Mechanism Driven by Shape Memory Alloy. *IEEE/ASME Transactions on Mechatronics*, 21(1):302–315. 3.1
- [63] Ijspeert, A. J. (2014). Biorobotics: using robots to emulate and investigate agile locomotion. *Science*, 346(6206):196–203. 3.1
- [64] Inc, D. A. (2014). Dyna Alloy Inc. 3.6, 3.3
- [65] Janssen, J. L. G., Paulides, J. J. H., Compter, J. C., and Lomonova, E. A. (2010). Three-dimensional analytical calculation of the torque between permanent magnets in magnetic bearings. *IEEE Transactions on Magnetics*, 46(6):1748–1751. 3.1
- [66] Jayaram, K. and Full, R. J. (2016). Cockroaches traverse crevices, crawl rapidly in confined spaces, and inspire a soft, legged robot. *Proceedings of the National Academy of Sciences*, pages 1–6. 3.1, 4.1
- [67] Jung, G. P., Koh, J. S., and Cho, K. J. (2011). Meso-scale compliant gripper inspired by caterpillar’s proleg. *IEEE International Conference on Robotics and Automation*, pages 1831–1836. 3.1
- [68] Katz, S. L. and Gosline, J. M. (1993). ONTOGENETIC SCALING OF JUMP PERFORMANCE IN THE AFRICAN DESERT LOCUST ( SCHISTOCERCA GREGARIA ). *Journal of Experimental Biology*, 111:81–111. 4.1
- [69] Kim, B., Lee, S., Park, J. H., and Park, J. O. (2005). Design and fabrication of a locomotive mechanism for capsule-type endoscopes using shape memory alloys (SMAs). *IEEE/ASME Transactions on Mechatronics*, 10(1):77–86. 3.1
- [70] Kim, S., Aksak, B., and Sitti, M. (2007). Enhanced friction of elastomer microfiber adhesives with spatulate tips. *Applied Physics Letters*, 91(22):89–92. 4.2.3

- [71] Kim, S., Hawkes, E., Cho, K., Jolda, M., Foley, J., and Wood, R. (2009). Micro artificial muscle fiber using NiTi spring for soft robotics. *IEEE/RSJ International Conference on Intelligent Robots and Systems*, pages 2228–2234. 3.1
- [72] Kim, S., Spenko, M., Trujillo, S., Heyneman, B., Santos, D., and Cutkosky, M. R. (2008). Smooth vertical surface climbing with directional adhesion. *IEEE Transactions on Robotics*, 24(1):65–74. 4.1
- [73] Koch, K. and Barthlott, W. (2009). Superhydrophobic and superhydrophilic plant surfaces: an inspiration for biomimetic materials. *Philosophical Transactions of the Royal Society*, 367(1893):1487–509. 4.1
- [74] Koch, K., Bhushan, B., and Barthlott, W. (2009). Multifunctional surface structures of plants: An inspiration for biomimetics. *Progress in Materials Science*. 4.1
- [75] Kode, V. R. C. and Cavusoglu, M. C. (2007). Design and Characterization of a Novel Hybrid Actuator Using Shape Memory Alloy Invasive Surgery Applications. *IEEE/ASME Transactions on Mechatronics*, 12(4):455–464. 3.1
- [76] Koh, J. S. and Cho, K. J. (2010). Omegabot: Crawling robot inspired by *Ascotis Selenaria*. *IEEE International Conference on Robotics and Automation*, pages 109–114. 3.1
- [77] Koh, J.-S. and Cho, K.-J. (2013). Omega-Shaped Inchworm-Inspired Crawling Robot With Large-Index-and-Pitch (LIP) SMA Spring Actuators. *IEEE/ASME Transactions on Mechatronics*, 18(2):419–429. 3.1
- [78] Koh, J. S., Jung, S. P., Noh, M., Kim, S. W., and Cho, K. J. (2013). Flea inspired catapult mechanism with active energy storage and release for small scale jumping robot. *IEEE International Conference on Robotics and Automation*, pages 26–31. 2.1, 3.1
- [79] Koh, J.-s., Yang, E., Jung, G.-P., Jung, S.-P., H, S. J., Lee, S.-I., Jablonski, P. G., Wood, R. J., Kim, H.-Y., and K-J, C. (2015). Jumping on water: Surface tension dominated jumping of water striders and robotic insects. *Science*, 349(6247):517–522. 2.1, 3.1
- [80] Kohut, N. J., Hoover, A. M., Ma, K. Y., Baek, S. S., and Fearing, R. S. (2011). MEDIC: A legged millirobot utilizing novel obstacle traversal. *IEEE International Conference on Robotics and Automation*, pages 802–808. 3.1
- [81] Kovac, M., Fauria, O., Zufferey, J.-C., and Floreano, D. (2011). The EPFL jumpglider: A hybrid jumping and gliding robot with rigid or folding wings. *IEEE International Conference on Robotics and Biomimetics*, pages 1503–1508. 2.1, 2.10
- [82] Kovac, M., Fuchs, M., Guignard, A., Zufferey, J.-C., and Floreano, D. (2008). A miniature 7g jumping robot. *IEEE International Conference on Robotics and Automation*, pages 373–378. 2.1, 2.10, 3.1, 4.1
- [83] Kovac, M., Schlegel, M., Zufferey, J.-C., and Floreano, D. (2009a). A miniature jumping robot with self-recovery capabilities. *IEEE/RSJ International Conference on Intelligent Robots and Systems*, pages 583–588. 2.1, 2.10
- [84] Kovac, M., Schlegel, M., Zufferey, J.-C., and Floreano, D. (2009b). Steerable miniature jumping robot. *Autonomous Robots*, 28(3):295–306. 2.1, 2.10
- [85] Lambrecht, B. G. A., Horchler, A. D., and Quinn, R. D. (2005). A Small , Insect-Inspired Robot that Runs and Jumps. *IEEE/RSJ International Conference on Intelligent Robots and Systems*, (April):40–45. 2.1, 4.1
- [86] Lan, C. C., Lin, C. M., and Fan, C. H. (2011). A self-sensing microgripper module with wide handling ranges. *IEEE/ASME Transactions on Mechatronics*, 16(1):141–150. 3.1
- [87] Lee, M., Kim, B., Kim, J., and Jhe, W. (2015). Noncontact friction via capillary shear interaction at nanoscale. *Nature Communications*, 6:7359. 4.3.5
- [88] Lee, Y. P., Kim, B., Lee, M. G., and Park, J.-o. (2004). Locomotive mechanism design

- and fabrication of biomimetic micro robot using shape memory alloy. *IEEE International Conference on Robotics and Automation*, pages 5007–5012 Vol.5. 3.1
- [89] Li, F., Bonsignori, G., Scarfogliero, U., Chen, D., Stefanini, C., Lui, W., Dario, P., and Fu, X. (2009). Jumping mini-robot with bio-inspired legs. *IEEE International Conference on Robotics and Biomimetics*, pages 933–938. 2.1
- [90] Majidi, C., Shepherd, R. F., Kramer, R. K., Whitesides, G. M., and Wood, R. J. (2013). Influence of surface traction on soft robot undulation. *The International Journal of Robotics Research*, 32(13):1577–1584. 3.1
- [91] Mao, S., Dong, E., Xu, M., Jin, H., Li, F., and Yang, J. (2013). Design and development of starfish-like robot: Soft bionic platform with multi-motion using SMA actuators. *IEEE International Conference on Robotics and Biomimetics*, (December):91–96. 3.1
- [92] Menciassi, A., Gorini, S., Moglia, A., Pernorio, G., Stefanini, C., and Dario, P. (2005). Clamping tools of a capsule for monitoring the gastrointestinal tract problem analysis and preliminary technological activity. *Proceedings - IEEE International Conference on Robotics and Automation*, 2005(April):1309–1314. 3.1
- [93] Mengelkamp, J., Ziolkowski, M., Weise, K., Carlstedt, M., Brauer, H., and Hauelsen, J. (2015). Permanent Magnet Modeling for Lorentz Force Evaluation. *IEEE Transactions on Magnetics*, 51(7). 3.2
- [94] Murphy, M. P., Aksak, B., and Sitti, M. (2009). Gecko-inspired directional and controllable adhesion. *Small*, 5(2):170–175. 4.2.3
- [95] Murphy, M. P., Kute, C., Menguc, Y., and Sitti, M. (2011). Waalbot II: Adhesion Recovery and Improved Performance of a Climbing Robot using Fibrillar Adhesives. *The International Journal of Robotics Research*, 30(1):118–133. 3.1, 4.1, A.1
- [96] Murphy, M. P. and Sitti, M. (2007). Waalbot: An agile small-scale wall-climbing robot utilizing dry elastomer adhesives. *IEEE/ASME Transactions on Mechatronics*, 12(3):330–338. A.1
- [97] Nakamura, Y., Matsui, A., Saito, T., and Yoshimoto, K. (1995). Shape-memory-alloy active forceps for laparoscopic surgery. *IEEE International Conference on Robotics and Automation*, 3:2320–2327. 3.1
- [98] Nawroj, A. I., Swensen, J. P., and Dollar, A. M. (2015). Design of mesoscale active cells for networked, compliant robotic structures. *IEEE International Conference on Intelligent Robots and Systems*, 2015-Decem:3284–3289. 3.1
- [99] Nguyen, K. T., Ko, S. Y., Park, J. O., and Park, S. (2015). Terrestrial Walking Robot With 2DoF Ionic PolymerMetal Composite (IPMC) Legs. *IEEE/ASME Transactions on Mechatronics*, 20(6):2962–2972. 3.1
- [100] Noh, M., Kim, S.-w., An, S., Koh, J.-S., and Cho, K.-J. (2012). Flea-Inspired Catapult Mechanism for Miniature Jumping Robots. *IEEE Transactions on Robotics*, 28(5):1007–1018. 2.1, 2.10, 3.1, 4.1
- [101] Norton, R. L. (2006). *Machine Design - An Integrated Approach*. Pearson Prentice Hall. Appendix B, Appendix B
- [102] Onal, C. D., Tolley, M. T., Wood, R. J., and Rus, D. (2015). Origami-Inspired Printed Robots. *IEEE/ASME Transactions on Mechatronics*, 20(5):2214–2221. 3.1
- [103] Orekhov, V., Hong, D. W., and Yim, M. (2010). Actuation mechanisms for biologically inspired everted toroidal robots. *IEEE/RSJ International Conference on Intelligent Robots and Systems*, pages 2535–2536. 3.1
- [104] Paden, B., Groom, N., and Antaki, J. F. (2003). Design Formulas for Permanent-Magnet Bearings. *Journal of Mechanical Design*, 125(4):734. 3.1

- [105] Patronik, N. A., Ota, T., Zenati, M. A., and Riviere, C. N. (2009). A miniature mobile robot for navigation and positioning on the beating heart. *IEEE Transactions on Robotics*, 25(5):1109–1124. 3.1
- [106] Patt, P. J. (1985). Design and Testing of a Coaxial Linear Magnetic Spring with Integral Linear Motor. *IEEE Transactions on Magnetics*, MAG-21(5):1759–1761. 3.1
- [107] Paul, S., Mckenzie, C., and Parness, A. (2012). 2012 IEEE International Conference on Robotics and Automation Video Summary of D . R . O . P . The Durable Reconnaissance and Observation Platform. pages 3535–3536. 4.1
- [108] Pearson, K. and Franklin, R. (1984). Characteristics of Leg Movements and Patterns of Coordination in Locusts Walking on Rough Terrain. *The International Journal of Robotics Research*, 3:101–112. 4.1
- [109] Pearson, K. G., Gynther, I. C., and Heitler, W. J. (1986). Coupling of flight initiation to the jump in locusts. *Journal of Comparative Physiology A*, 158(1):81–89. 4.1
- [110] Perez Goodwyn, P., Peressadko, A., Schwarz, H., Kastner, V., and Gorb, S. (2006). Material structure, stiffness, and adhesion: Why attachment pads of the grasshopper (*Tettigonia viridissima*) adhere more strongly than those of the locust (*Locusta migratoria*) (Insecta: Orthoptera). *Journal of Comparative Physiology A: Neuroethology, Sensory, Neural, and Behavioral Physiology*, 192(11):1233–1243. 4.1
- [111] Petruska, A. J. and Abbott, J. J. (2013). Optimal Permanent-Magnet Geometries for Dipole Field Approximation. *IEEE Transactions on Magnetics*, 49(2):811–819. 3.2
- [112] Pololu (2015). Pololu.com. Appendix G
- [113] Pope, M. T., Kimes, C. W., Jiang, H., Hawkes, E. W., Member, S., Estrada, M. A., Kerst, C. F., Roderick, W. R. T., Han, A. K., Christensen, D. L., and Cutkosky, M. R. (2016). A Multimodal Robot for Perching and Climbing on Vertical Outdoor Surfaces. *IEEE Transactions on Robotics*, 33(1):1–11. 4.1
- [114] Porez, M., Boyer, F., and Ijspeert, A. J. (2014). Improved Lighthill fish swimming model for bio-inspired robots: Modeling, computational aspects and experimental comparisons. *The International Journal of Robotics Research*, 33(10):1322–1341. 3.1
- [115] Pratt, G. A. and Williamson, M. M. (1995). Series elastic actuators. *IEEE/RSJ International Conference on Intelligent Robots and Systems*, 1(1524):399–406. 4.4.1
- [116] Rajkowski, J. E., Gerratt, A. P., Schaler, E. W., and Bergbreiter, S. (2009). A multi-material milli-robot prototyping process. *IEEE/RSJ International Conference on Intelligent Robots and Systems*, pages 2777–2782. 3.1
- [117] Rakotoarison, H. L., Yonnet, J., and Delinchant, B. (2007). Using Coulombian Approach for Modeling Scalar Potential and Magnetic Field of a Permanent Magnet With Radial Polarization. *IEEE Transactions on Magnetics*, 43(4):1261–1264. 3.1
- [118] Ravaud, R., Lemarquand, G., Lemarquand, V., and Depollier, C. (2008). Analytical Calculation of the Magnetic Field Created by Permanent-Magnet Rings. *IEEE Transactions on Magnetics*, 44(8):1982–1989. 3.1
- [119] Rentschler, M. E., Dumpert, J., Platt, S. R., Iagnemma, K., Oleynikov, D., and Farritor, S. M. (2006). Modeling, analysis, and experimental study of in vivo wheeled robotic mobility. *IEEE Transactions on Robotics*, 22(2):308–321. 3.1
- [120] Riskin, D. K., Bertram, J. E. a., and Hermanson, J. W. (2005). Testing the hindlimb-strength hypothesis: non-aerial locomotion by Chiroptera is not constrained by the dimensions of the femur or tibia. *Journal of Experimental Biology*, 208:1309–19. 2.2
- [121] Riskin, D. K., Parsons, S., Schutt, W. A., Carter, G. G., and Hermanson, J. W. (2006). Terrestrial locomotion of the New Zealand short-tailed bat *Mystacina tuberculata* and the

common vampire bat *Desmodus rotundus*. *Journal of Experimental Biology*, 209:1725–1736. 2.2

- [122] Robertson, W., Cazzolato, B., and Zander, A. (2005). A Multipole Array Magnetic Spring. *IEEE Transactions on Magnetics*, 41(10):3826–3828. 3.1
- [123] Rossi, C., Coral, W., Colorado, J., and Barrientos, A. (2011). A motor-less and gear-less bio-mimetic robotic fish design. *IEEE International Conference on Robotics and Automation*, pages 3646–3651. 3.1
- [124] Rus, D. and Tolley, M. T. (2015). Design, fabrication and control of soft robots. *Nature*, 521(7553):467–475. 3.1
- [125] Saha, C. R., O’Donnell, T., Wang, N., and McCloskey, P. (2008). Electromagnetic generator for harvesting energy from human motion. *Sensors and Actuators A: Physical*, 147(1):248–253. 3.1
- [126] Scarfogliero, U., Stefanini, C., and Dario, P. (2006). A bioinspired concept for high efficiency locomotion in micro robots: the jumping Robot Grillo. *IEEE International Conference on Robotics and Automation*, (May):4037–4042. 2.1
- [127] Scarfogliero, U., Stefanini, C., and Dario, P. (2007). Design and Development of the Long-Jumping Grillo Mini Robot. *IEEE International Conference on Robotics and Automation*, (April):10–14. 2.1
- [128] Scarfogliero, U., Stefanini, C., and Dario, P. (2009). The use of compliant joints and elastic energy storage in bio-inspired legged robots. *Mechanism and Machine Theory*, 44(3):580–590. 2.1
- [129] Schutt, W. A., Altenbach, J. S., Chang, Y. H., Cullinane, D. M., Hermanson, J. W., Muradali, F., and Bertram, J. E. (1997). The dynamics of flight-initiating jumps in the common vampire bat *Desmodus rotundus*. *Journal of Experimental Biology*, 200:3003–12. 2.2, 2.10
- [130] Selvaggi, J. P., Salon, S., Kwon, O., Chari, M. V. K., and Debortoli, M. (2007). Computation of the External Magnetic Field , Near-Field or Far-Field , From a Circular Cylindrical Magnetic Source Using Toroidal Functions. *IEEE Transactions on Magnetics*, 43(4):1153–1156. 3.1
- [131] Seo, J. M., Ro, J. S., Rhyu, S. H., Jung, I. S., and Jung, H. K. (2015). Novel hybrid radial and axial flux permanent-magnet machine using integrated windings for high-power density. *IEEE Transactions on Magnetics*, 51(3). 3.1
- [132] Seok, S., Onal, C. D., Cho, K.-J., Wood, R. J., Rus, D., and Kim, S. (2013). Meshworm: A Peristaltic Soft Robot With Antagonistic Nickel Titanium Coil Actuators. *IEEE/ASME Transactions on Mechatronics*, 18(5):1485–1497. 3.1
- [133] Seok, S., Wang, A., Chuah, M. Y., Hyun, D. J., Lee, J., Otten, D. M., Lang, J. H., and Kim, S. (2014). Design Principles for Energy-Efficient Legged Locomotion and Implementation on the MIT Cheetah Robot. *IEEE/ASME Transactions on Mechatronics*, 20(3):1117–1129. 4.1
- [134] Sfakiotakis, M., Kazakidi, A., Evdaimon, T., Chatzidaki, A., and Tsakiris, D. P. (2015). Multi-arm robotic swimmer actuated by antagonistic SMA springs. *IEEE International Conference on Intelligent Robots and Systems*, 2015-Decem:1540–1545. 3.1
- [135] Shepherd, R. F., Ilievski, F., Choi, W., Morin, S. a., Stokes, a. a., Mazzeo, a. D., Chen, X., Wang, M., and Whitesides, G. M. (2011). Multigait soft robot. *Proceedings of the National Academy of Sciences*, 108(51):20400–20403. 3.1
- [136] Sitti, M., Menciassi, A., Ijspeert, A., Low, K. H., and Kim, S. (2013). Survey and Introduction to the Focused Section on Bio-Inspired Mechatronics. *IEEE/ASME Transactions on Mechatronics*, 18(2):409–418. 1.1
- [137] Song, Y. S. and Sitti, M. (2007). Surface Tension Driven Biologically Inspired Water

- Strider Robots: Theory and Experiments. *IEEE Transactions on Robotics*, 23(3):578–589. 3.1
- [138] Spagna, J. C., Goldman, D. I., Lin, P.-C., Koditschek, D. E., and Full, R. J. (2007). Distributed mechanical feedback in arthropods and robots simplifies control of rapid running on challenging terrain. *Bioinspiration & Biomimetics*, 2(1):9–18. 4.1
- [139] Sprowitz, A., Tuleu, A., Vespignani, M., Ajallooeian, M., Badri, E., and Ijspeert, a. J. (2013). Towards dynamic trot gait locomotion: Design, control, and experiments with Cheetah-cub, a compliant quadruped robot. *The International Journal of Robotics Research*, 32(8):932–950. 4.1
- [140] Stoeter, S. A. and Papanikolopoulos, N. (2005). Autonomous stair-climbing with miniature jumping robots. *IEEE Transactions on Systems, Man, and Cybernetics*, 35(2):313–325. 2.1
- [141] Strang, G. (2006). *Linear Algebra and its Applications*. Thomson Brooks/Cole, Belmont, CA, fourth edition. 3.4, 3.11
- [142] Strickler, T. L. (1978). *Functional Osteology and Myology of the Shoulder in the Chiroptera*. 2.2
- [143] Tanaka, T. and Hirose, S. (2008). Development of Leg-wheel Hybrid Quadruped AirHopper. *IEEE/RSJ International Conference on Intelligent Robots and Systems*, pages 22–26. 2.1
- [144] Teymoori, S., Rahideh, A., Moayed Jahromi, H., and Mardaneh, M. (2016). Two-Dimensional Analytical Magnetic Field Prediction for Consequent-Pole Permanent Magnet Synchronous Machines. *IEEE Transactions on Magnetics*, 9464(c):1–1. 3.1
- [145] Thomas, A. L. R. and Taylor, G. K. (2001). Animal flight dynamics I. Stability in gliding flight. *Journal of theoretical biology*, 212(3):399–424. 2.3.1
- [146] Tian, L. L., Ai, X. P., and Tian, Y. Q. (2012). Analytical model of magnetic force for axial stack permanent-magnet bearings. *IEEE Transactions on Magnetics*, 48(10):2592–2599. 3.1
- [147] Torres-Jara, E., Gilpin, K., Karges, J., Wood, R. J., and Rus, D. (2010). Composable Flexible Small Actuators Built from Thin Shape Sheets. *IEEE Robotics and Automation Magazine*, (December). 3.1
- [148] Troisfontaine, N., Bidaud, P., and Morel, G. (1997). A new inter-phalangeal actuator for dexterous micro-grippers. *Proceedings of International Conference on Robotics and Automation*, 2(May). 3.1
- [149] Tsukagoshi, H., Sasaki, M., Kitagawa, A., and Tanaka, T. (2005). Jumping Robot for Rescue Operation with Excellent Traverse Ability. *IEEE International Conference on Advanced Robotics*, pages 841–848. 2.1, 2.10
- [150] Urata, J., Yoshikai, T., Mizuuchi, I., and Inaba, M. (2007). Design of high D.O.F. mobile micro robot using electrical resistance control of shape memory alloy. *IEEE/RSJ International Conference on Intelligent Robots and Systems*, pages 3828–3833. 3.1
- [151] Vokoun, D., Beleggia, M., Heller, L., and Šittner, P. (2009). Magnetostatic interactions and forces between cylindrical permanent magnets. *Journal of Magnetism and Magnetic Materials*, 321(22):3758–3763. 3.1
- [152] Vokoun, D., Tomassetti, G., Beleggia, M., and Stachiv, I. (2011). Magnetic forces between arrays of cylindrical permanent magnets. *Journal of Magnetism and Magnetic Materials*, 323(1):55–60. 3.1
- [153] Vötsch, W., Nicholson, G., Müller, R., Stierhof, Y.-D., Gorb, S., and Schwarz, U. (2002). Chemical composition of the attachment pad secretion of the locust *Locusta migratoria*. *Insect Biochemistry and Molecular Biology*. 4.1, 4.3.5

- [154] Weber, T. A. and Macomb, D. J. (1989). On the equivalence of the laws of Biot Savart and Ampere. *American Journal of Physics*. 3.1
- [155] Werfel, J., Petersen, K., and Nagpal, R. (2014). Designing Collective Behavior in a Termite-Inspired Robot Construction Team. *Science*, 343(February):754–759. 3.1
- [156] West, G. B., Brown, J. H., and Enquist, B. J. (1997). General Model for the Origin of Allometric Scaling Laws in Biology. *Science*, 276(April):122–126. 2.9
- [157] Wimsatt, W. A. (1970). *Biology of Bats*. 2.2
- [158] Woodward, M. A. (2011). NanoRobotics Laboratory. 2.3.1
- [159] Woodward, M. A. and Sitti, M. (2011). Design of a miniature integrated multi-modal jumping and gliding robot. *IEEE/RSJ International Conference on Intelligent Robots and Systems*, pages 556–561. 2.7.3, 3.1, 4.3.2, 4.3.3, 4.4
- [160] Woodward, M. A. and Sitti, M. (2014). MultiMo-Bat: A biologically inspired integrated jumping-gliding robot. *The International Journal of Robotics Research*, 33(September):1511–1529. 3.1, 3.6, 3.7, 3.9, 4.3.2, 4.4
- [161] Wu-Bavouzet, F., Cayer-Barrioz, J., Le Bot, A., Brochard-Wyart, F., and Buguin, A. (2010). Effect of surface pattern on the adhesive friction of elastomers. *Physical Review E - Statistical, Nonlinear, and Soft Matter Physics*, 82(3):1–9. 4.2.3
- [162] Yamada, A., Mameda, H., Mochiyama, H., and Fujimoto, H. (2010). A Compact Jumping Robot utilizing Snap-through Buckling with Bend and Twist. *IEEE/RSJ International Conference on Intelligent Robots and Systems*, pages 389–394. 2.1, 2.10
- [163] Yamada, A., Wataril, M., Mochiyama, H., and Fujimoto, H. (2007). A Jumping Robot based on the Closed Elastica. *International Symposium on Micro-NanoMechatronics and Human Science*, pages 604–609. 2.1
- [164] Yang, D., Mosadegh, B., Ainla, A., Lee, B., Khashai, F., Suo, Z., Bertoldi, K., and Whitesides, G. M. (2015). Buckling of Elastomeric Beams Enables Actuation of Soft Machines. *Advanced Materials*, 27(41):6323–6327. 3.1
- [165] Yang, X., Cao, Y., Liu, S., Wang, Y., Dong, G., and Yang, W. (2014). Optimization Design of a Vibration-Powered Generator With Annular Permanent Magnetic Spring and Soft Magnetic Pole. *IEEE Transactions on Applied Superconductivity*, 24(3):1–4. 3.1
- [166] Yim, S. and Sitti, M. (2012). Design and rolling locomotion of a magnetically actuated soft capsule endoscope. *IEEE Transactions on Robotics*, 28(1):183–194. 3.1
- [167] Yonnet, J.-P. (1978). Passive magnetic bearings with permanent magnets. *IEEE Transactions on Magnetics*, MAG-14(5):803–805. 3.1
- [168] Yoshida, E., Kokaji, S., Murata, S., Kurokawa, H., and Tomita, K. (1999). Miniaturized self-reconfigurable system using shape memory alloy. *Proc. of the Int. Conf. on Intelligent Robots and Systems (IROS)*, 3:1579–1585. 3.1
- [169] Yoshida, E., Murata, S., Kokaji, S., Kamimura, A., Tomita, K., and Kurokawa, H. (2002). Get Back in Shape. *IEEE Robotics and Automation Magazine*, (December):54–60. 3.1
- [170] Yung, K. W., Landecker, P. B., and Villani, D. D. (1998). An Analytic Solution for the Force Between Two Magnetic Dipoles. *Magnetic and Electrical Separation*, 9(1):39–52. 3.2
- [171] Zhang, Q., Wang, Y., and Kim, E. S. (2015). Electromagnetic Energy Harvester With Flexible Coils and Magnetic Spring for 1–10 Hz Resonance. *Journal of Microelectromechanical Systems*, pages 1–14. 3.1
- [172] Zhang, T., Qian, F., Li, C., Masarati, P., Hoover, a. M., Birkmeyer, P., Pullin, a., Fearing, R. S., and Goldman, D. I. (2013). Ground fluidization promotes rapid running of a lightweight robot. *The International Journal of Robotics Research*, 32(7):859–869. 3.1

- [173] Zhang, Z. G., Yamashita, N., Gondo, M., Yamamoto, A., and Higuchi, T. (2008). Electrostatically actuated robotic fish: Design and control for high-mobility open-loop swimming. *IEEE Transactions on Robotics*, 24(1):118–129. 3.1
- [174] Zhao, J., Xi, N., Gao, B., Mutka, M. W., and Xiao, L. (2010). Design and testing of a controllable miniature jumping robot. *IEEE/RSJ International Conference on Intelligent Robots and Systems*, pages 3346–3351. 2.1
- [175] Zhao, J., Xi, N., Gao, B., Mutka, M. W., and Xiao, L. (2011). Development of a controllable and continuous jumping robot. *IEEE International Conference on Robotics and Automation*, pages 4614–4619. 2.1, 2.10
- [176] Zhao, J., Xu, J., Gao, B., Xi, N., Cintr, F. J., Mutka, M. W., and Xiao, L. (2013). MSU Jumper: A Single-Motor-Actuated Miniature Steerable Jumping Robot. *IEEE Transactions on Robotics*, 29(3):602–614. 2.1, 2.10, 4.1
- [177] Zhao, J., Yang, R., Xi, N., Gao, B., Fan, X., Mutka, M. W., and Xiao, L. (2009). Development of a miniature self-stabilization jumping robot. *IEEE/RSJ International Conference on Intelligent Robots and Systems*, pages 2217–2222. 2.1
- [178] Zhao, J., Zhao, T., Xi, N., Mutka, M. W., and Xiao, L. (2015). MSU Tailbot : Controlling Aerial Maneuver of a Miniature-Tailed Jumping Robot. *IEEE/ASME Transactions on Mechatronics*, pages 1–12. 3.1